

UC Berkeley

UC Berkeley Electronic Theses and Dissertations

Title

Mapping and manipulating optoelectronic processes in emerging photovoltaic materials

Permalink

<https://escholarship.org/uc/item/5kb5v0r7>

Author

Leblebici, Sibel

Publication Date

2016

Peer reviewed|Thesis/dissertation

Mapping and manipulating optoelectronic processes in emerging photovoltaic materials

By

Sibel Yontz Leblebici

A dissertation submitted in partial satisfaction of the
requirements for the degree of

Doctor of Philosophy

in

Engineering – Materials Science and Engineering

in the

Graduate Division

of the

University of California, Berkeley

Committee in charge:

Doctor Alexander Weber-Bargioni, Co-Chair

Professor Ting Xu, Co-Chair

Professor Junqiao Wu

Professor Ana Arias

Spring 2016

Mapping and manipulating optoelectronic processes in emerging photovoltaic materials

Copyright 2016

By

Sibel Yontz Leblebici

Abstract

Mapping and manipulating optoelectronic processes in emerging photovoltaic materials

by

Sibel Yontz Leblebici

Doctor of Philosophy in Engineering - Materials Science and Engineering

University of California, Berkeley

Doctor Alexander Weber-Bargioni, Co-Chair

Professor Ting Xu, Co-Chair

The goal of the work in this dissertation is to understand and overcome the limiting optoelectronic processes in emerging second generation photovoltaic devices. There is an urgent need to mitigate global climate change by reducing greenhouse gas emissions. Renewable energy from photovoltaics has great potential to reduce emissions if the energy to manufacture the solar cell is much lower than the energy the solar cell generates. Two emerging thin film solar cell materials, organic semiconductors and hybrid organic-inorganic perovskites, meet this requirement because the active layers are processed at low temperatures, e.g. 150 °C. Other advantages of these two classes of materials include solution processability, composed of abundant materials, strongly light absorbing, highly tunable bandgaps, and low cost.

Organic solar cells have evolved significantly from 1% efficient devices in 1989 to 11% efficient devices today. Although organic semiconductors are highly tunable and inexpensive, the main challenges to overcome are the large exciton binding energies and poor understanding of exciton dynamics. In my thesis, I optimized solar cells based on three new solution processable azadipyrrromethene-based small molecules. I used the highest performing molecule to study the effect of increasing the permittivity of the material by incorporating a high permittivity small molecule into the active layer. The studies on two model systems, small donor molecules and a polymer-fullerene bulk heterojunction, show that Frenkel and charge transfer exciton binding energies can be manipulated by controlling permittivity, which impacts the solar cell efficiency.

Hybrid organic-inorganic perovskite materials have similar advantages to organic semiconductors, but they are not excitonic, which is an added advantage for these materials. Although photovoltaics based on hybrid halide perovskite materials have exceeded 20% efficiency in only a few years of optimization, the loss mechanisms are not understood but critical to systematically improve the efficiency towards the theoretical limit. Thus, I correlated morphology to local power conversion efficiency determining properties by mapping local short circuit current, open circuit voltage, and dark drift current in state-of-the-art methylammonium lead iodide solar cells with sub-30 nm spatial resolution using photoconductive atomic force microscopy. I found, within individual grains, spatially-correlated heterogeneity in short circuit current and open circuit voltage. This heterogeneity is attributed to a facet-dependent density of trap states. These results imply that controlling crystal grain and facet orientation will enable a systematic optimization of hybrid halide perovskite photovoltaics.

Table of Contents

List of Acronyms and Symbols	iii
Acknowledgements	vi
Introduction.....	1
1 Motivation.....	2
2 Photovoltaic fundamentals	6
2.1 Solar cell efficiency	7
2.2 Shockley-Queisser limit: detailed balance	8
3 Organic solar cells.....	10
3.1 Photocurrent generation in organic solar cells	11
3.2 History of organic solar cells: materials and device architectures	13
3.3 Technical challenges in organic solar cells	16
4 Hybrid organic-inorganic perovskite solar cells	27
4.1 Hybrid organic-inorganic perovskite material properties	29
4.2 Short history of perovskite solar cells	31
4.3 Perovskite solar cell operation	33
4.4 Advantages of hybrid perovskite solar cells.....	34
4.5 Challenges of hybrid perovskite solar cells.....	37
5 Solar cell characterization techniques.....	41
5.1 Power conversion efficiency	42
5.2 Solar cell quantum efficiency	42
5.3 Scanning probe microscopy	43
Exciton manipulation in organic solar cells.....	51
6 Solution processable azadipyrrromethene electron donors for planar heterojunction solar cells	52
6.1 Introduction	53
6.2 Materials and instrumentation	53
6.3 Device fabrication	54
6.4 Material properties	55
6.5 Organic solar cells	59
6.6 Conclusions	61
7 Increasing organic solar cell efficiency by increasing permittivity to reduce exciton binding energy.....	62

7.1 Introduction	63
7.2 Materials and methods.....	63
7.3 Results and discussion.....	65
7.4 Conclusion.....	74
8 Controlling charge transfer exciton binding energy in organic bulk heterojunction photovoltaics	75
8.1 Introduction	76
8.2 Film and device formation	77
8.3 Film characterization	78
8.4 Results and discussion.....	78
8.5 Conclusion.....	85
9 Exciton mobility and charge transfer in organic solar cell bulk heterojunctions from femtosecond stimulated Raman spectroscopy	87
9.1 Introduction	88
9.2 Experimental methods.....	89
9.3 Data processing	90
9.3 Results and discussion.....	94
9.4 Conclusion.....	99
Optoelectronic processes limiting power conversion efficiency in perovskite photovoltaics	102
10 Facet-dependent photovoltaic efficiency variations in single hybrid halide perovskite grains	103
10.1 Introduction	104
10.2 Sample preparation and device performance	105
10.3 Python image analysis	105
10.4 Conductive atomic force microscopy	106
10.5 First principles calculations.....	112
10.6 Results and discussion.....	113
10.7 Conclusion.....	128
Conclusions and outlook	129
Bibliography	132

List of Acronyms and Symbols

ADPM	Azadipyrromethene
AFM	Atomic force microscopy
BCP	Bathocuproine
BF2-ADPM	B,F ₂ -chelated azadipyrromethene
BHJ	Bulk heterojunction
BO-ADPM	B,O-chelated azadipyrromethene
BOS	Balance of systems
CA	Camphoric anhydride
cAFM	Conductive atomic force microscopy
CBM	Conduction band minimum
CIGS	Copper indium gallium selenide
CT	Charge transfer
ΔE_{DA}	Energy offset between donor HOMO and acceptor LUMO
$\Delta LUMO$	LUMO level offset
DA	Donor-acceptor
DFT	Density functional theory
DSSC	Dye-sensitized solar cells
EBIC	Electron beam induced current
EDS	Energy dispersive x-ray spectroscopy
E_{eb}	Exciton binding energy
EHP	Electron hole pair
EL	Electroluminescence
EQE	External quantum efficiency
ES	Excited state
FA	Formamidinium
FC	Franck-Condon
FF	Fill factor
FSRS	Femtosecond stimulated Raman spectroscopy
FTO	Fluorine doped tin oxide
FWHM	Full width at half maximum
GS	Ground state
HOMO	Highest occupied molecular orbital
HTL	Hole transport layer
I_D	Dark drift current

IPES	Inverse photoelectron spectroscopy
I_{SC}	Short circuit current
ITO	Indium doped tin oxide
IQE	Internal quantum efficiency
IV	Current-voltage
J_{SC}	Short circuit current density
J - V	Current density-voltage
KPFM	Kelvin probe force microscopy
LED	Light emitting diode
LUMO	Lowest unoccupied molecular orbital
OFET	Organic field effect transistor
OLED	Organic light emitting diode
OSC	Organic solar cell
MA	Methylammonium
MDMO-PPV	Poly[2-methoxy-5-(3',7'-dimethyloctyloxy)-1,4-phenylene vinylene]
MEH-PPV	Poly[2-methoxy-5-(2'-ethyl-hexyloxy)-1,4-phenylene vinylene]
η_A	Absorption efficiency
η_{ED}	Exciton diffusion efficiency
η_{ES}	Exciton separation efficiency
η_T	Carrier transport efficiency
η_{CC}	Carrier collection efficiency
NREL	National Renewable Energy Laboratory
P3HT	Poly(3-hexylthiophene-2,5-diyl)
PCBM	[6,6]-phenyl C61 butyric acid methyl ester
PCE	Power conversion efficiency
PEDOT:PSS	Poly(3,4-ethylenedioxythiophene)-poly(styrenesulfonate)
PL	Photoluminescence
PPV	Poly(p-phenylenevinylene)
P_{MAX}	Maximum power point
PS	Polystyrene
PTIR	Photothermal induced resonance
rms	Root-mean-square
SCLC	Space-charge limited current
SOC	Spin-orbit coupling
spiro-OMeTAD	2,2',7,7'-tetrakis(N,N-di-p-methoxyphenylamine)-9,9'-spirobifluorene
SPM	Scanning probe microscopy

SSSE	Solid state solvation effect
STM	Scanning tunneling microscopy
STS	Scanning tunneling spectroscopy
TEM	Transmission electron microscopy
THF	Tetrahydrofuran
TiO ₂	Titanium dioxide
TOF	Time-of-flight
UPS	Ultraviolet photoelectron spectroscopy
VBM	Valence band maximum
V_{oc}	Open circuit voltage
wt%	Weight percent
XAS	X-ray absorption spectroscopy
XES	X-ray emission spectroscopy

Acknowledgements

Most importantly, I would like to thank my loving family. They have always been encouraging and supportive, and especially so while I have been working on my Ph.D. Baba, thank you for your initial advice when I started graduate school, “A Ph.D. is like a marathon, pace yourself.” Anne, thank you for always being there to help me prepare for presentations, helping me improve my writing skills, and keeping my sanity as I have been working on this dissertation. And, Leyla, thank you for always telling me you are proud of me.

I would like to thank my two wonderful research advisors, Biwu Ma and Alex Weber-Bargioni, who have had an enormously positive impact on my Ph.D. experience. Biwu taught me how to ask the right questions and when my research was a compelling story to be published. He also always had his door open and was happy to discuss research at any time. Alex has been incredibly flexible in allowing me to join his group while continuing my previous research and in allowing me to switch research directions only one year later. Working with Alex has also significantly boosted my self-confidence because he reminds me that my work is challenging and has an impact. I also strongly value his dedication to empowering women in science. Both Alex and Biwu showed me how much fun doing research can and should be.

My work on organic solar cells would not be possible without the help and support of Teresa Chen and Steve Shelton. I am grateful for Teresa’s constant patience, availability, and teaching me all aspects of making, optimizing, and characterizing organic solar cells. Also, Steve and Teresa’s friendship made my daily life enjoyable.

I would like to acknowledge the entire Weber-Bargioni group, including those involved in the larger optoelectronics group, who I have enjoyed working with and learned so much from. Specifically, Sebastian and Sara’s company made the hours spent working at the AFM much more entertaining. Also, Nick and Jiye were always available to answer my questions and give me suggestions on my research.

I would like to thank my qualifying exam and dissertation committee members, Professors Xu, Wu, Dubon, Arias, and Yang, for their feedback throughout my Ph.D. tenure. I would also like to acknowledge Professor Angus Rockett at University of Illinois for encouraging me to pursue a Ph.D. and providing me with useful advice along the way.

The staff members and scientists at the Molecular Foundry have made my day-to-day life so much easier and have been available to answer my many questions. Specifically, I would like to thank Adam Schwartzberg, Frank Ogletree, Ed Wong, Virginia Altoe, and Liana Klivansky.

And last but not least, I would like to thank my friends, classmates, and colleagues who have always been there for me both professionally and personally. Amy, Evan R., Alex L., Changyi, Andrew, Evan O., Claire, Dom, and Teresa W. thank you for being there for me through all the ups and downs, and I look forward to more good times together.

Introduction

Chapter 1

Motivation

The goal of the work presented in this dissertation is to understand and overcome optoelectronic processes that limit power conversion efficiency (PCE) in emerging second generation solar cells. Developing forms of efficient and inexpensive energy generation from non-greenhouse gas producing sources is a major scientific and technological goal today. Climate scientists unanimously agree that the earth's atmosphere is warming due to greenhouse gas emissions and have established, through the United Nations Paris climate agreement in 2015, a target of less than 1.5 °C warming above pre-industrial levels to prevent catastrophic effects. Thus, renewable energy sources need to be harnessed to meet this goal (1). According to the Energy Information Administration, the world energy consumption in 2012 was approximately 17.5 TW and continuously rising. We need to put in place renewable energy sources that can provide sufficient energy for the growing world population. The sun is the most abundant renewable energy resource with 6500 TW of available power worldwide, which is significantly greater than wind or hydroelectric at 1700 and 1.9 TW of available power worldwide (2). Fortunately, the cost of solar energy has been steadily decreasing, as exemplified in Figure 1.1 showing residential photovoltaic costs. The decrease in cost has stemmed from reductions in module costs, balance of systems (BOS) costs such as inverters and racking, and soft costs like permitting and installation labor (3). Non-module costs have decreased by 20% since 2012 (Figure 1.1) because of increased system size and module efficiency. As module efficiency increases the \$/W cost will decrease, assuming the module costs stays constant, and the BOS costs will decrease because fewer modules are needed for the same power generated; BOS costs and installation costs generally scale with system area.

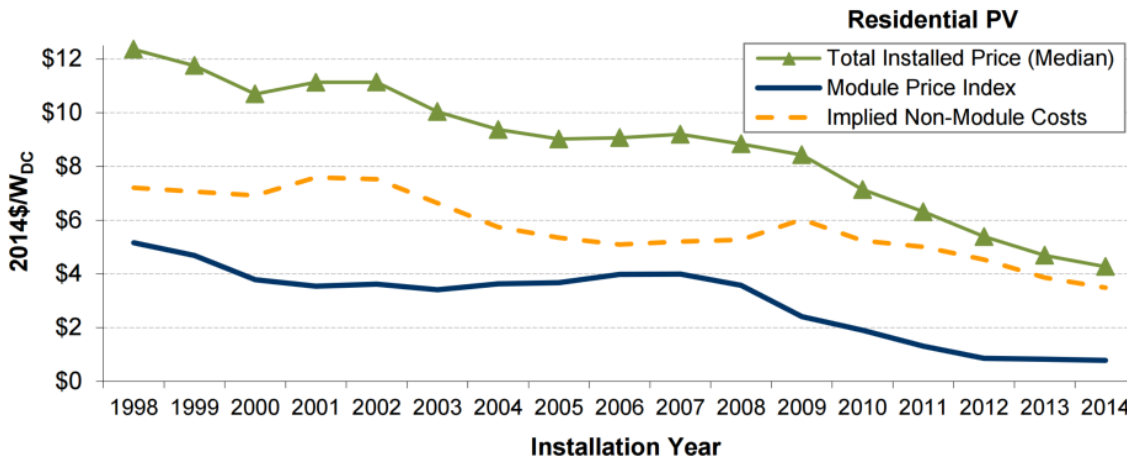


Figure 1.1. Decreasing cost of residential photovoltaics from 1998 to 2014. From Ref. (3).

For photovoltaic adoption to be widespread and to displace electricity from natural gas power plants, photovoltaic systems need to achieve a \$1/W cost for residential rooftop systems. At \$1/W, the cost of electricity from solar would be less than or equal to the cost of electricity from other sources (4). Currently, the primary challenge in reaching this cost target is the BOS costs. BOS costs in \$/W can be reduced by increasing the power that the solar cell generates while keeping the cost and the size of the solar panel the same. For reference, the mean module efficiency for residential and non-residential systems in 2014 was 16.0% (3).

Another significant consideration for a rapid adoption of solar technology to reduce greenhouse gas emissions is the energy input to make the solar panels. The energy input can be assessed in terms of energy payback time, which is the time needed for a photovoltaic panel to generate the energy equivalent to the energy used for manufacturing. The photovoltaic energy payback time is dependent on the manufacturing steps needed to produce the panel and the solar cell efficiency. Figure 1.2 shows energy payback times for different types of solar technologies. Monocrystalline silicon panels have the longest energy payback time because the silicon active layer is thick, and it is energy intensive to purify the silicon and saw the silicon boule into wafers (5). Existing thin-film photovoltaics, such as gallium selenide (CIGS) and cadmium telluride (CdTe), have a lower payback time because very little active material is needed in the solar cell; however, the growth substrate and the film-deposition process contribute significantly to the input energy for traditional thin-film photovoltaics (6).

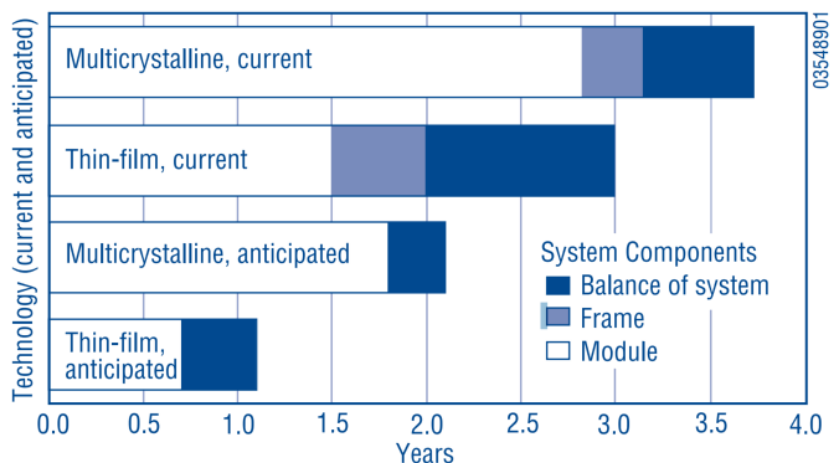


Figure 1.2. Energy payback time for anticipated and existing photovoltaic systems. From Ref. (6).

There is an urgent need to develop materials for solar cells that would require little energy input to manufacture and simultaneously result in high efficiency solar cells. These solar materials would then have short energy pay back periods. Additionally, because they would require less energy to produce, the solar cells should be less expensive assuming abundant materials are used.

There are two emerging thin film photovoltaic materials that fit these requirements that I am interested in: organic semiconductors and hybrid organic-inorganic perovskite materials (7). These anticipated thin film solar cells are expected to require less energy to produce than traditional silicon or existing inorganic thin film solar cells. And, these two classes of photovoltaic materials are solution processable at room temperature onto glass or plastic substrates. Thus, the greatest embodied energy for these photovoltaic modules will likely be the encapsulation (5).

Organic semiconductors are of interest because there exist a wide variety of conjugated molecules and polymers that are highly tunable through synthetic means. As a result, optoelectronic properties in these materials can be adjusted to achieve high efficiency solar cells.

Nature, through its use of photosynthetic light-harvesting complexes, is an excellent example of how effective conjugated organic systems can be at converting light into energy (8). However, like these naturally existing complexes, synthetic organic semiconductors form excitons rather than electron hole pairs (EHPs) upon light absorption. Manipulating the excitons transport and dissociation efficiency is the main challenge in maximizing organic solar cell (OSC) performance. Thus, the first part of my dissertation is focused on the studying exciton binding energy and manipulating it in model OSC systems.

Hybrid perovskite photovoltaic materials have all the advantages of traditional thin film solar cells while also being solution processable and having high PCEs. Perovskite solar cells have rapidly achieved efficiencies over 20% (9). But, to systematically increase beyond this efficiency, the loss mechanisms in these materials need to be better understood to overcome them. Thus, I established a characterization technique to measure current and voltage at the length scales of critical optoelectronic processes in operating perovskite solar cells, which enabled me to identify a major loss mechanism in these materials.

The following dissertation is organized as follows. Chapter 2 describes the fundamentals of photovoltaics. Chapter 3 provides background on the history of OSCs and challenges to achieving high PCEs. Chapter 4 is a summary of perovskite materials and the main achievements and challenges in the field of perovskite photovoltaics. Chapter 5 describes the main techniques used to characterize the solar cell materials studied in my dissertation. The subsequent sections are the scientific output. First, I will describe a new set of small molecules for OSCs and approaches to control the Frenkel and CT state excitons to improve PCE. The last section serves to identify local loss mechanisms in perovskite photovoltaics. All the scientific output chapters represent a published, peer-reviewed article or a manuscript for publication of which I am one of the main authors. Finally, a conclusion chapter summarizes my results.

Chapter 2

Photovoltaic fundamentals

For a thorough introduction to solar cell physics and materials, refer to the following references: Refs. (10, 11). The fundamentals described here provide background for the contents of this dissertation.

2.1 Solar cell efficiency

The PCE of a solar cell is determined by the ratio of power generated to input solar power. For terrestrial solar cells, the standard incident solar spectrum is the AM1.5G spectrum. The PCE is determined by measuring a current-voltage (IV) curve under standard illumination using a solar simulator at room temperature. The IV curve under illumination can be approximated as the superposition of the IV curve for the solar cell diode in the dark and the light-generated current. As shown in Figure 2.1, the IV curve provides the key metrics needed to determine the PCE of the solar cell.

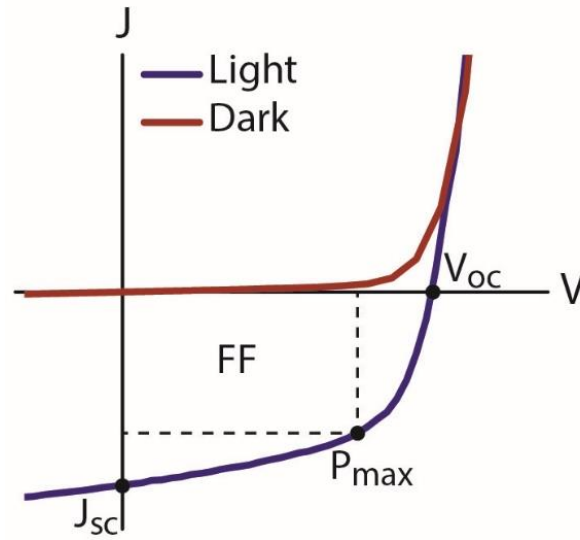


Figure 2.1. An example solar cell IV in the dark and under illumination. The open circuit voltage (V_{OC}), short circuit current density (J_{SC}), and maximum power point (P_{MAX}) are shown.

The solar cell PCE is given by the following equation:

$$\eta = \frac{P_{MAX}}{P_{in}} = FF \frac{I_{SC} V_{OC}}{P_{in}}$$

where P_{MAX} is the power density delivered at the maximum power point, P_{in} is the incident illumination power, I_{SC} is the short circuit current, V_{OC} is the open circuit voltage, and FF is the fill factor. The standard P_{in} for reporting PCE is 1 kW/m². I_{SC} is the current at zero applied bias. V_{OC} is the voltage at which the current is equal to zero; measuring these parameters locally also provides information about the effects of film morphology and composition in heterogeneous materials. FF, often referred to as the squareness of the IV curve, is given by the ratio of the maximum power point (P_{MAX}) to the product of I_{SC} and V_{OC} :

$$FF = \frac{P_{MAX}}{I_{SC} V_{OC}}.$$

Two other useful efficiency metrics for solar cells are external quantum efficiency (EQE) and internal quantum efficiency (IQE). EQE is a spectral measurement of photocurrent

generation at zero bias: the ratio of carriers collected to incident photons. The integral of the EQE spectrum over the photon energy range is J_{SC} (10):

$$J_{SC} = q \int b_s(E) EQE(E) dE$$

where q is the electronic charge and $b_s(E)$ is the incident spectral photon density. Similarly, IQE is the ratio of carriers collected to the photons absorbed by the solar cell. IQE is calculated using the following equation:

$$IQE(E) = \frac{EQE(E)}{A(E)} = \frac{EQE(E)}{1 - R(E) - T(E)}$$

where $A(E)$ is the absorption, which can be calculated from reflection, $R(E)$, and transmission, $T(E)$, spectra. The EQE and IQE spectra provide information about the efficiency of charge separation and collection in the device across all visible wavelengths. By measuring the IV curve under illumination and in the dark along with IQE, the source of low efficiency in the solar cell can be diagnosed.

2.2 Shockley-Queisser limit: detailed balance

In 1961, William Shockley and Hans Queisser developed the detailed balance efficiency limit for p-n junction solar cells (12). Detailed balance refers to the fact that the photon emission rate of from the solar cell is equal to the photon absorption rate, keeping the concentration of electrons in the material constant (10). The basis of detailed balance for solar cells is that the cell and the sun act as blackbodies. Based on their model, we now have the Shockley-Queisser limit which provides the maximum theoretical efficiency for a single junction solar cell with a given bandgap. Their theory is based on a series of assumptions for a single bandgap p-n junction solar cell (12). The assumptions are:

1. Both the sun and the solar cell are perfect blackbodies.
2. Photons with energy greater than the bandgap of the semiconductor are absorbed and generate one EHP. The quantum efficiency is 100%.
3. All carriers thermalize to the conduction and valence band edges.
4. The only form of recombination is radiative.
5. Charge carriers have infinite mobility, meaning they are all collected.

The two forms of energy loss in their model are that photons with energy less than the bandgap are not absorbed and only a fraction of the energy from high energy photons is converted because of carrier thermalization to the band edges. As a result, the bandgap is the most important factor for determining theoretical maximum solar cell efficiency. The maximum efficiency as a function of bandgap is shown in Figure 2.2. The highest theoretical efficiency for terrestrial solar cells is 33.7% at a 1.34 eV bandgap. The curve is not smooth because of the shape of the AM1.5G solar spectrum.

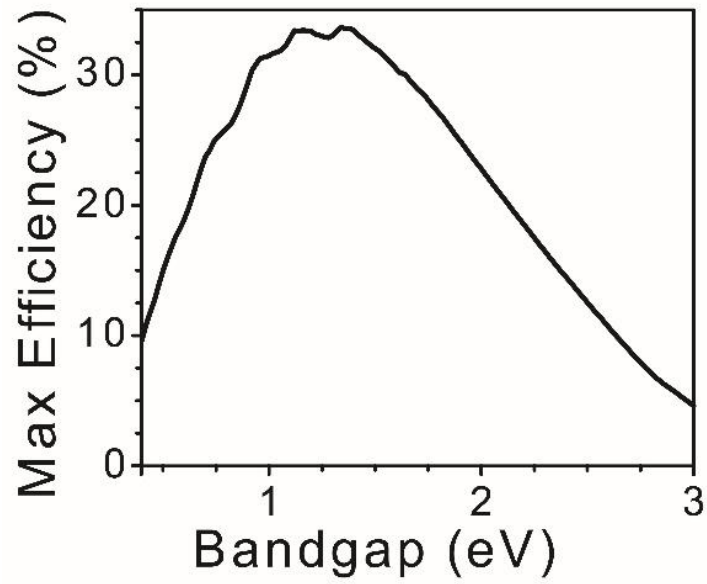


Figure 2.2. Shockley-Queisser maximum solar cell efficiency based on the AM1.5G solar spectrum.

Based on the Shockley-Queisser assumptions, solar cell materials must be engineered to have a bandgap ideally suited for the solar spectrum (near either 1.3 or 1.5 eV), reduced non-radiative recombination, and high mobility to achieve high PCEs.

Chapter 3

Organic solar cells

OSCs with high efficiency have the ability to replace fossil fuels for energy production due to their low cost and, more importantly, the low energy input needed to produce the solar panels compared to inorganic solar materials (7, 13). OSCs fall into the category of second-generation photovoltaics because they are based on thin films of a strongly absorbing material and can be processed directly onto large substrates. Existing thin film solar cells are fabricated with inorganic active materials such as CdTe or CIGS, but OSCs have the advantage that they do not require high-temperature processing and can be fabricated on a wider range of substrates, such as plastics (14). Thus, OSCs can be used in novel applications because they are lightweight and flexible (15, 16). Another advantage of OSCs is that the active small molecules or polymers have highly tunable properties via their chemical structures that can be altered through chemical synthesis (17).

High input energy is not required for OSCs because the organic semiconductors are often solution processable, and the embodied energy of the active layer is low because only very thin films are needed. Solution processability enables both low temperature and high throughput processing of the active layer through spin coating, blade coating, spray coating, dip coating, printing, and various forms of roll-to-roll processing (18, 19). The films can afford to be very thin because the optical absorption in organic semiconductors is very high and broad (14). Organic semiconductors can approach 100% absorption at film thicknesses from 100 – 200 nm because of their large extinction coefficients over the visible wavelength range (20).

Although OSCs have many advantages, several challenges still remain. Most importantly, the efficiency of OSCs still lags behind that of other thin film solar technologies (9). Below I will describe the technical challenges that need to be overcome to increase the efficiency of OSCs. Another challenge is the sensitivity of organic semiconductors to oxygen, which hinders long term stability of OSCs. However, significant advancements in encapsulation to improve stability and increase the lifetime of OSCs have been achieved (21, 22). For a more detailed overview of the advantages and challenges in OSCs, refer to these review articles: Refs. (14, 23, 24).

3.1 Photocurrent generation in organic solar cells

OSCs are excitonic solar cells, meaning that excitons, bound EHPs, are formed upon absorption. In contrast to inorganic semiconductors, where highly delocalized Wannier Mott excitons are formed at low temperatures, highly localized Frenkel excitons form in organic semiconductors at room temperature; Frenkel excitons have a significantly higher binding energy than Wannier-Mott excitons. This is a consequence of organic semiconductors being composed of mostly non-covalently bonded carbon, which has fewer and more tightly bound electrons, and results in a low static dielectric constant (23). Most organic semiconductors have a relative permittivity of 3, whereas silicon has a permittivity of 12. As a result, the excitons formed in organic semiconductors can have binding energies as high as 1 eV (25). In order to separate the exciton, a type II heterojunction is required (Figure 3.1) to provide a driving force for dissociation (26). Additionally, due to the exciton binding energy (E_{eb}), the optical bandgap and transport bandgap are not equal. The transport bandgap is the difference between the highest occupied molecular orbital (HOMO) and lowest unoccupied molecular orbital (LUMO), but the optical bandgap is the transport bandgap minus E_{eb} (27).

The process of photocurrent generation is complex, but the basic steps are described in Figure 3.1. Incident light is absorbed in the donor or acceptor material and generates a Frenkel exciton. This exciton then diffuses until it either recombines or reaches an interface between the donor and acceptor materials. If it reaches this interface, and if the LUMO level offset (ΔLUMO) between the donor and acceptor is greater than E_{eb} , the exciton will dissociate. Now, the electron is in the acceptor and the hole in the donor, but because of their proximity immediately after dissociation, a charge transfer (CT) exciton forms at the donor-acceptor (DA) interface (28). This process of exciton dissociation is still widely debated (29, 30), but after the CT state dissociates, the free electron and hole are transported to their respective electrodes. Reducing Frenkel and CT exciton binding energies would result in more efficient exciton dissociation and would allow for a smaller ΔLUMO , allowing for higher V_{OC} and I_{SC} . Because the photocurrent generation can be described in these steps, the EQE and IQE can be described as the product of the efficiency of these steps:

$$EQE = \eta_A \cdot IQE = \eta_A \eta_{ED} \eta_{ES} \eta_T \eta_{CC}$$

where η_A is the absorption efficiency, η_{ED} is the exciton diffusion efficiency, η_{ES} is the exciton separation efficiency, η_T is the carrier transport efficiency, and η_{CC} is the carrier collection efficiency (31). For a more in depth overview of photocurrent generation, please see Ref. (30).

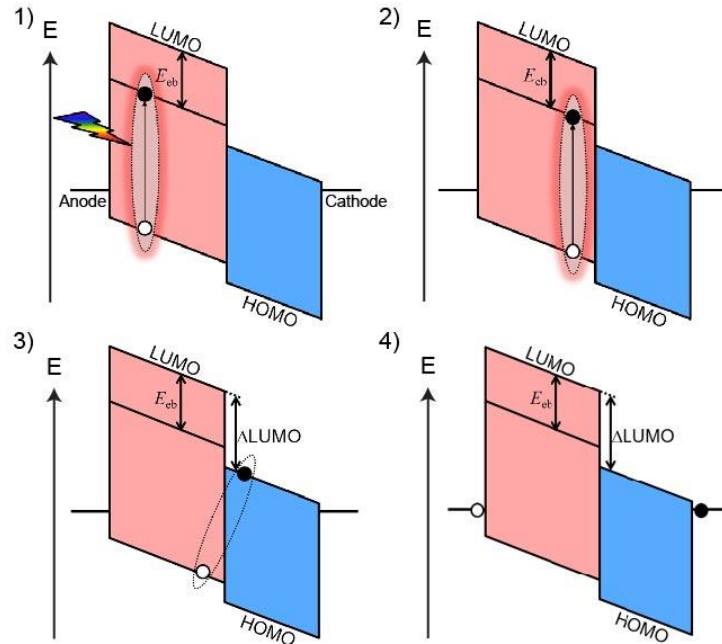


Figure 3.1. Photocurrent generation process in OSCs with a type II heterojunction shown on an energy level diagram at short circuit conditions. The electron donor is in pink and the acceptor is in blue. 1) The donor absorbs a photon and generates an exciton with a binding energy, E_{eb} . 2) The exciton diffuses to the interface with the acceptor. 3) Because the ΔLUMO is greater than E_{eb} , the exciton dissociates and the electron is donated to the acceptor. 4) After the CT state dissociates, the free electron and hole are transported and collected at the electrodes. Formally, the two-particle HOMO-LUMO energy levels should not be on the same energy diagram as the single-particle exciton, however this representation is commonly used.

3.2 History of organic solar cells: materials and device architectures

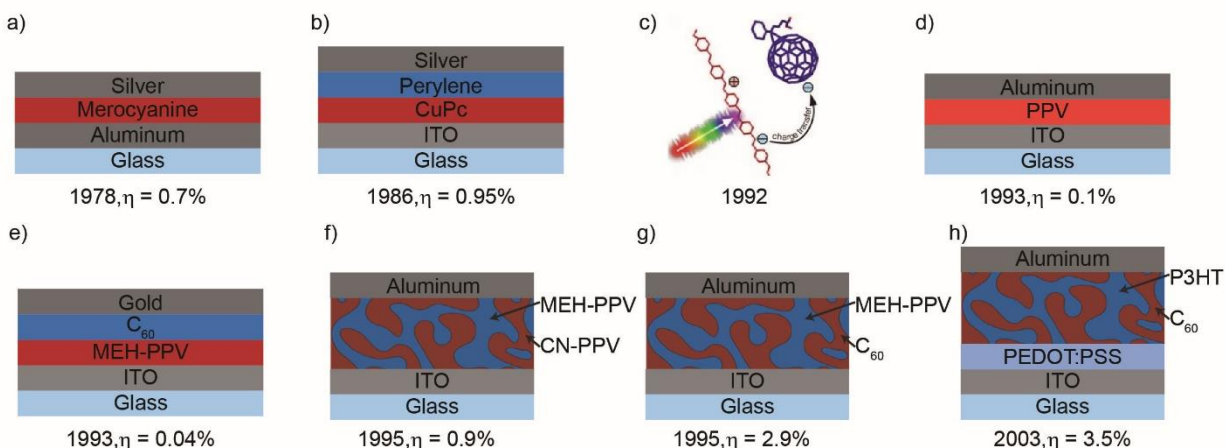


Figure 3.2. The early history of OSCs. a) 1978: Single junction thermally evaporated small molecule solar cell (32). b) 1986: Planar heterojunction made up of two thermally evaporated small molecules: copper phthalocyanine (CuPc) and a perylene derivative, using indium doped tin oxide (ITO) as the transparent electrode (33). c) 1992: Photoinduced charge transfer between poly(p-phenylenevinylene) (PPV) and [6,6]-phenyl C61 butyric acid methyl ester (PCBM) was discovered (34, 35). d) 1993: Single junction solution processed polymer solar cell (36). e) 1993: Thermally evaporated planar heterojunction with poly[2-methoxy-5-(2'-ethyl-hexyloxy)-1,4-phenylene vinylene] (MEH-PPV) and PCBM (37). f) 1995: Bulk heterojunction (BHJ) composed of solution processable polymers, MEH-PPV and cyano-PPV (CN-PPV) (38). g) 1995: BHJ composed of solution processed MEH-PPV and PCBM (39). h) 2003: Prototypical polymer-fullerene BHJ solar cell with poly(3-hexylthiophene-2,5-diyl) (P3HT) and PCBM (40). The transparent electrode, ITO, is enhanced with poly(3,4-ethylenedioxythiophene)-poly(styrenesulfonate) (PEDOT:PSS).

Research on the properties of organic semiconductors began in the 1960s, but first attempts at making OSCs resulted in low efficiencies because they were fabricated with only one small molecule dye layer between two metal electrodes, as shown in Figure 3.2a (24, 32). Having different work function electrodes was not sufficient to overcome the E_{eb} . Interest in OSCs accelerated when Tang reported an OSC with 1% efficiency in 1986 (Figure 3.2b) (33). Tang's device was composed of a two-layer structure of small dye molecules that were thermally evaporated and sandwiched between electrodes. This structure is known as a planar heterostructure or a bilayer device. Until 1993, only small molecules based on dyes were being used in OSCs (24). These small molecules were not highly soluble but could easily be deposited using thermal evaporation. Some of the most commonly used small molecules are shown in Figure 3.3.

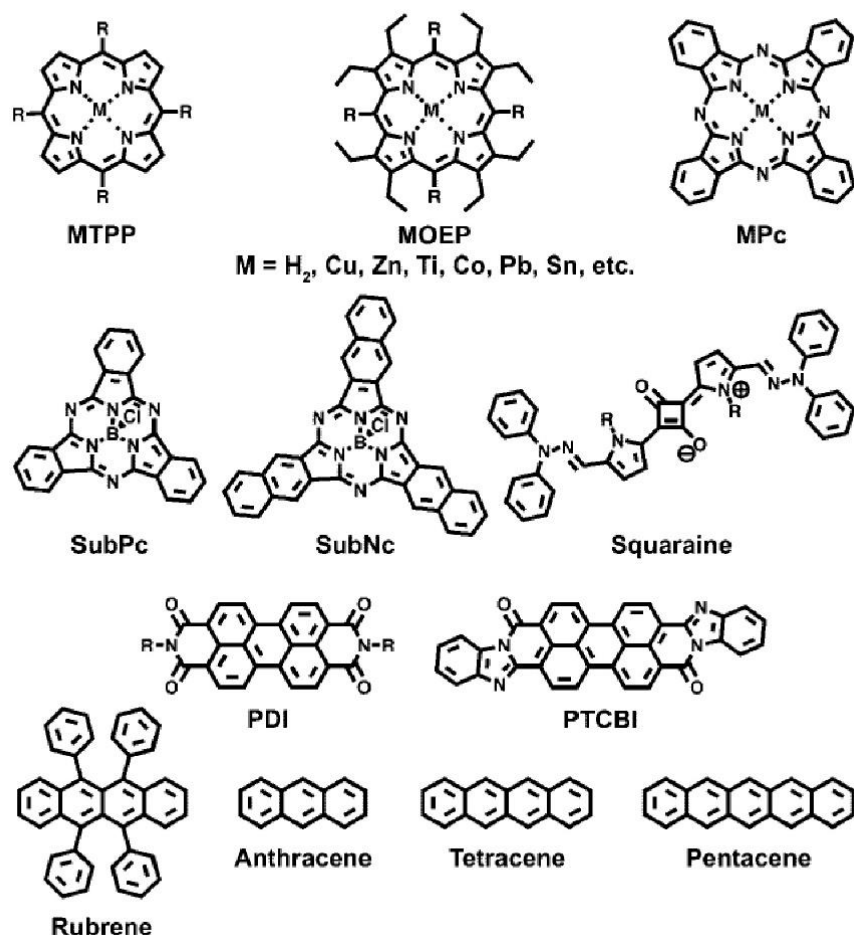


Figure 3.3. Chemical structures of many common conjugated small molecules. From Ref. (23).

In 1993 and 1994, the first reports of single junction conjugated polymer solar cells, as shown in Figure 3.2d, were published but with efficiencies less than 0.1% (24, 36). Initially, these OSCs had very low efficiency because of low material quality and purity (41). However, conjugated polymers are advantageous because they are solution processable in organic solvents allowing for high throughput processing. The chemical structures of several commonly used semiconducting polymers are shown in Figure 3.4. Around that same time, a major breakthrough in OSCs was the discovery of photoinduced electron transfer from semiconducting polymers to fullerenes (Figure 3.2c), indicating that excitons can be dissociated at the interface between polymers and C_{60} (34). This observation led to planar heterojunctions of solution processed conjugated polymers and thermally evaporated C_{60} , which is shown in Figure 3.2e (37, 42). In 1995, several groups began forming all polymer BHJs (Figure 3.2f), an interpenetrating network of phase separated donor and acceptor materials (38, 43). The BHJ design overcomes the challenge of making planar heterojunctions that are sufficiently thick for full light absorption and thin enough to ensure that excitons can diffuse to the DA interface before recombining. To take advantage of both the BHJ device structure and highly efficient electron transfer between polymers and C_{60} , a more soluble form of C_{60} was needed. In 1995, Hummelen et al. synthesized PCBM, a highly soluble derivative of C_{60} that is still the most commonly used acceptor material

today (44). Later that year, the first report of a polymer-fullerene BHJ device (Figure 3.2g) was published in which solar cells with 2.9% PCE were fabricated (39). The next major advancement in OSCs was the P3HT:PCBM BHJ device (Figure 3.2h) first reported in 2002 with relatively low efficiency, but quickly the efficiency was enhanced to 3.5% through thermal annealing (40, 45).

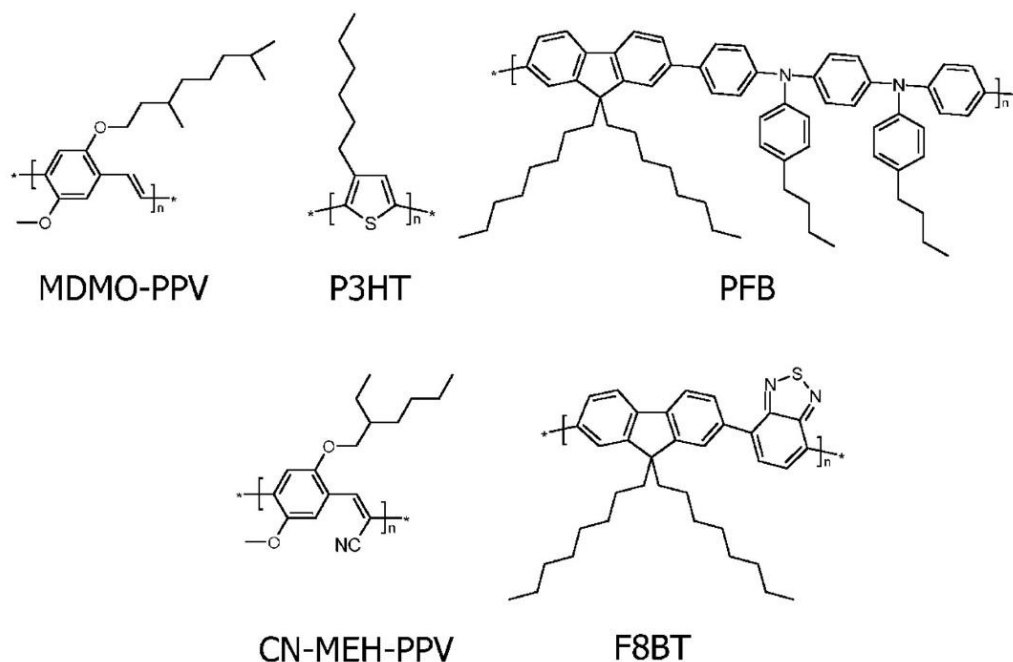


Figure 3.4. Chemical structures of common conjugated polymers. From Ref. (24).

It was not until 2006, that solution processable small molecules were developed for BHJ devices (46–49). The chemical structures of prominent solution processable small molecules are shown in Figure 3.5. Small molecules are advantageous because they do not have variations in solubility, molecular weight, or polydispersity that are problematic for polymer semiconductors (50). These factors also suggest that it is less challenging to purify small molecules. Additionally, synthesizing small molecules is generally considered to be easier than conjugated polymers (51). Small conjugated molecules also have the advantage that they often self-assemble into semicrystalline domains; as a result, they have higher carrier mobilities, but form lower-quality, rough films (46). Today, both polymer and small molecule OSCs have achieved PCEs over 10% (52).

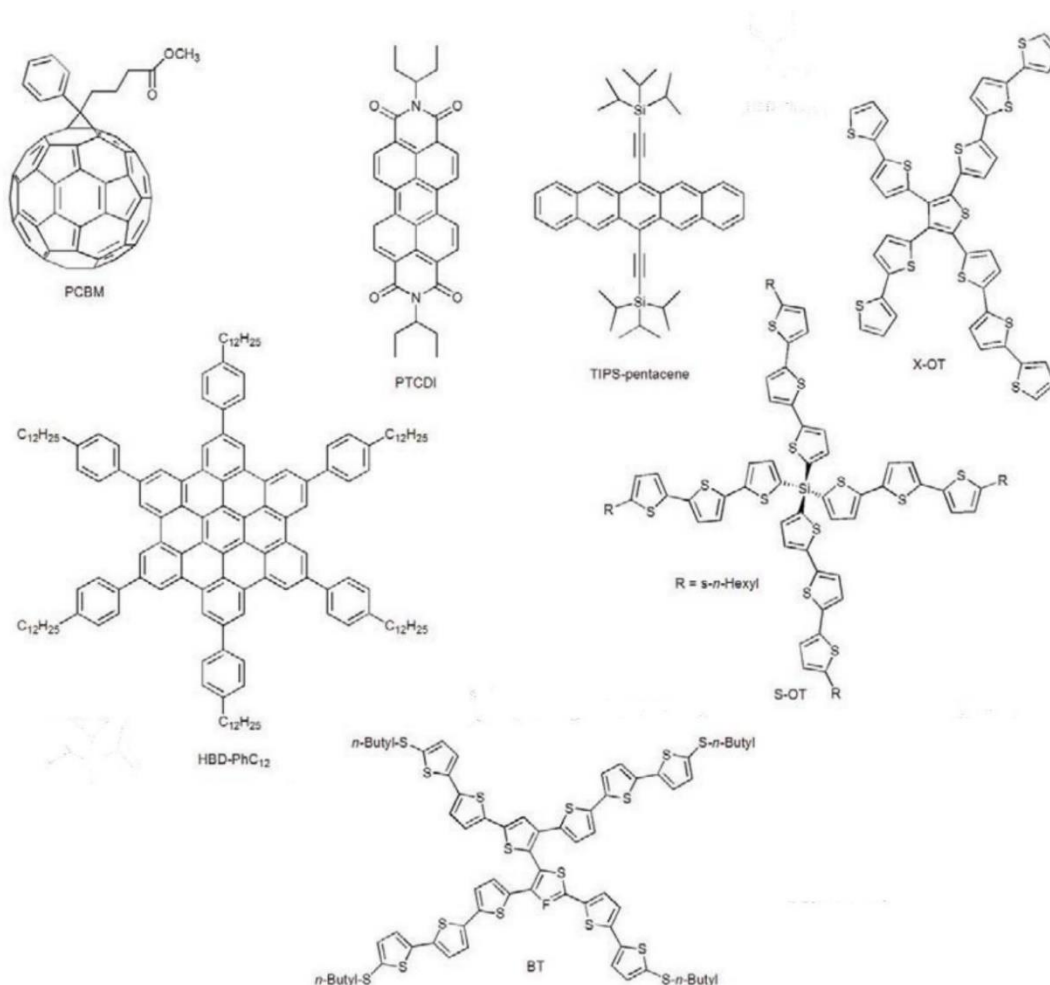


Figure 3.5. Examples of solution processable small molecules for OSCs. Adapted from Ref. (51).

3.3 Technical challenges in organic solar cells

There remain several major challenges to improve the efficiency of OSCs: poor control over phase separation in BHJ devices, high exciton binding energies, an incomplete understanding of CT states, and low carrier mobility. Each of the challenges and how one may overcome them is discussed below.

3.3.1 Poor control of phase separation

The phase separated domains of the donor and acceptor materials need to be approximately 10 - 20 nm in size because of short (5 - 10 nm) exciton diffusion lengths. Additionally, the BHJ film needs to possess continuous domains to transport carriers to the electrodes. By simply mixing the donor and acceptor components in solution before spin coating the solution onto a substrate, the two phases will separate if the donor and acceptor are dissimilar and if at least one component is semicrystalline. Within the solution, polymers often already begin to form different types of conformations depending on the solvent used, based on Flory-Huggins theory (53). The conformation of the polymer in solution will dictate the nucleation and growth process of the BHJ domains when the solvent evaporates from the solution while on the substrate. After the solvent has evaporated, the polymer chains or small molecules are fixed and

no longer have the ability to diffuse. In order to improve crystallinity and form larger phase domains, thermal or solvent annealing can be used to allow the species to be mobile. Careful control of the annealing temperature or solvent annealing time are required to prevent the domains from becoming too large (54). Much of the optimization of phase morphology is done through trial-and-error processing. Processing parameters that are used to control the phase separation and domain size include solvent, DA ratio, solution concentration, solvent additives, and thermal or solvent annealing. The solvent choice is incredibly important because the solubility of the polymers and small molecules is determined by their chemical structure, which also determines their miscibility with each other. Also, the boiling point of the solvent determines the amount of time the organic semiconductors domains have to grow and crystallize in solution on the substrate (55).

The most common methods to characterize phase separation include atomic force microscopy (AFM), transmission electron microscopy (TEM), and grazing-incidence wide-angle x-ray scattering. More techniques are described in the review article by Huang et al. (56). Of the three characterization techniques, only AFM for understanding phase separation will be described here due to its relevance to this dissertation. A detailed description of AFM is provided in Chapter 5. AFM is a useful technique because it provides information about the topography of the film and often phase separation. Phase separation can be observed using AFM phase images, which is a measure of local adhesion between the AFM tip and sample and can distinguish different materials in tapping mode AFM. One limitation of AFM is that only the surface is probed, but cross-sectional AFM imaging can overcome this if creating the cross-section does not modify the morphology. In 2001, AFM was used for the first time to understand the relationship between phase separation and BHJ device performance (57). Shaheen et al. found that the phase segregation in BHJ films was larger when using toluene compared to chlorobenzene (Figure 3.6). Due to these smaller domains and greater DA interfacial area, the PCE increased when devices were fabricated with chlorobenzene. High quality topography and phase images of as-cast and annealed P3HT and P3HT:PCBM BHJ films were measured by Dante et al. (58) to show that fiber like networks form when P3HT is annealed at 150 °C (Figure 3.7). Controlling phase separation is still a challenge in OSCs because optimization is performed by trial-and-error. To improve device performance, a better understanding of the relationships between fabrication conditions, microstructure, and device performance are needed.

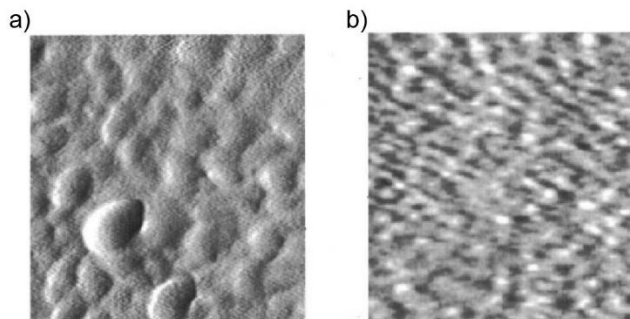


Figure 3.6. AFM topography images of poly[2-methoxy-5-(3',7'-dimethyloctyloxy)-1,4-phenylene vinylene (MDMO-PPV):PCBM BHJ films spin cast from (a) toluene and (b) chlorobenzene. The smaller features when spin cast from chlorobenzene suggest that the phase domains are much smaller. Adapted from Ref. (57).

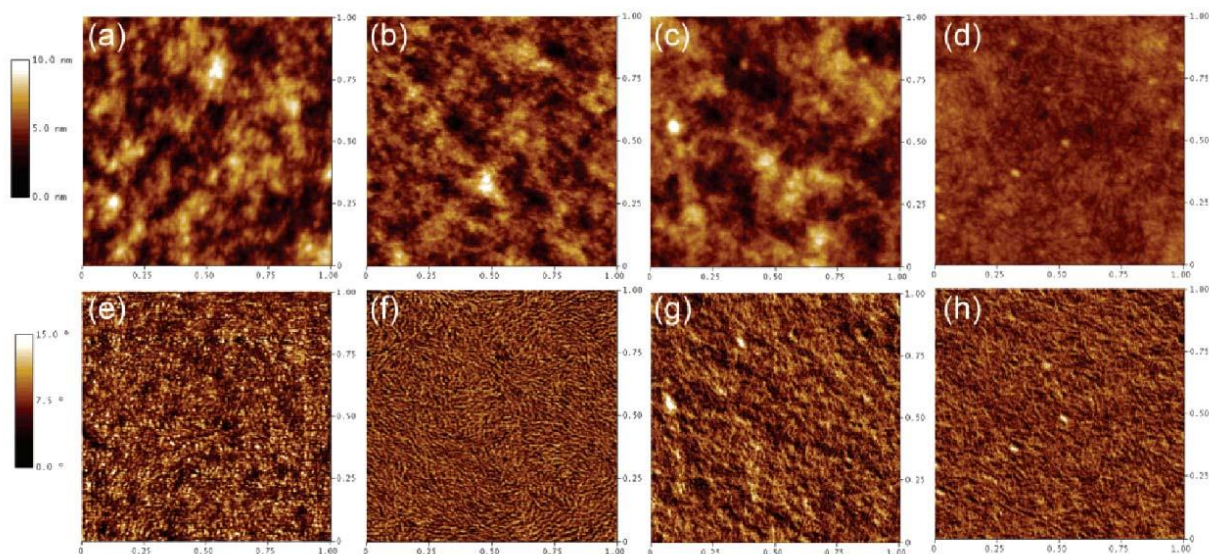


Figure 3.7. AFM topography (a-d) and phase images (e-h) of as cast P3HT (a,e), annealed P3HT (b,f), as-cast P3HT:PCBM (c,g), and annealed P3HT:PCBM (d,h). Adapted from Ref. (58).

3.3.2 High exciton binding energy

As mentioned earlier, OSCs are excitonic devices, meaning that excitons rather than free carriers are generated upon light absorption. E_{eb} in organic semiconductors is large due in part to the low permittivity but also due to electron-lattice interactions. When excitons are formed, there is an associated bond rearrangement due to the relaxation of the neighboring molecular structure. These electron-lattice interactions also increase E_{eb} (30). The need to split excitons into free carriers leads to two disadvantages: excitons will recombine in 100 ps to 1 ns if not dissociated, and energy is lost in the dissociation process. E_{eb} ranges from 1.4 to 0.2 eV in common organic semiconductor materials (25). In OSCs, a ΔLUMO greater than E_{eb} is required to dissociate the exciton. But, a large ΔLUMO results in reduced V_{OC} and is therefore undesirable (59). One approach to circumvent this limitation is to reduce E_{eb} , thereby simultaneously achieving efficient exciton separation with a small ΔLUMO and thus realizing enhanced PCEs for OSCs.

Based on a back-of-the-envelope calculation by Koster et al., η_{ES} can be enhanced from 27% to 67% by decreasing E_{eb} by only 0.1 eV for a fixed $\Delta LUMO$ (60).

The exciton binding can be approximated using scanning tunneling spectroscopy (STS), the combination of inverse photoelectron spectroscopy (IPES) and ultraviolet photoelectron spectroscopy (UPS), or x-ray emission and absorption spectroscopy (XES and XAS). These techniques measure the HOMO and LUMO levels of the material and compare that value to the energy required to create an exciton. The exciton formation energy, or optical band gap (E_{OP}) can be determined using UV–visible absorption spectroscopy or photoluminescence (PL). Thus, $E_{eb} = (LUMO - HOMO) - E_{OP}$. To determine the HOMO and LUMO levels using STS, a scanning tunneling microscope (STM) is used, in which the bias on the tip is adjusted to tunnel electrons between the tip and the local density of states. The bias at which no current tunnels defines the band gap. STS can be performed by either maintaining a constant distance between the tip and the sample or maintaining a constant tunneling current. As shown in Figure 3.8a, the HOMO and LUMO levels are defined by the steep edges in the relative tip height, defining a bandgap of 3.2 eV (61). This band gap is then compared to the absorption spectra of the molecule in Figure 3.8b, which reveals an optical bandgap of roughly 2.9 eV; the resulting E_{eb} is then 0.3 eV.

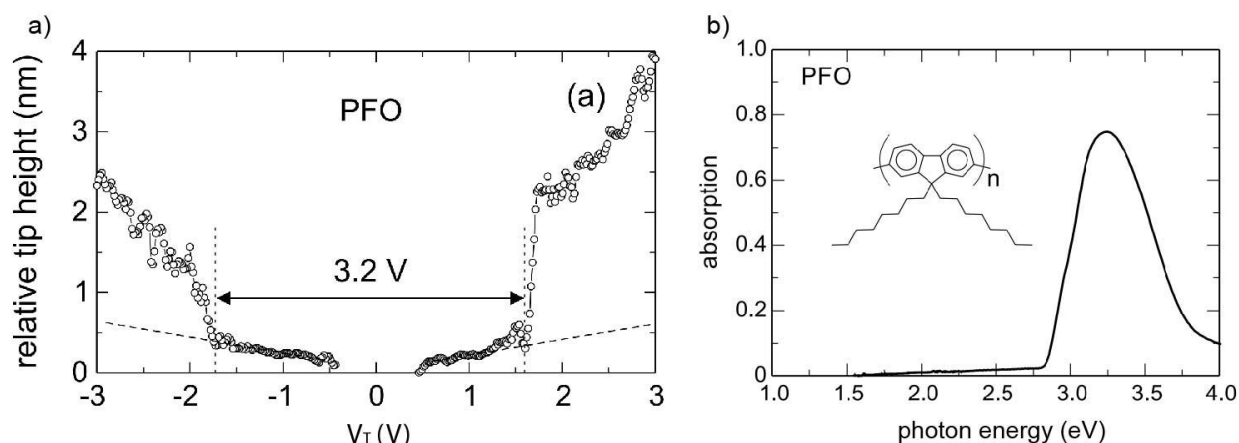


Figure 3.8. Determining E_{eb} with STS and UV-vis absorption spectroscopy in poly[(2-methoxy-5-dodecyloxy)-1,4-phenylenevinylene-co-1,4-phenylenevinylene] (PFO). a) STS spectrum showing a HOMO-LUMO gap of 3.2 eV. b) UV-vis absorption spectra of PFO with the molecular structure. Adapted from Ref. (61).

IPES measures the LUMO level by injecting electrons from a collimated beam into the high energy unoccupied states and measuring the energy of the photons emitted when the electron decays to a lower energy unoccupied state. UPS measures the HOMO level by measuring the energy of an electron removed from the HOMO or core level by exciting it with ultraviolet light. The UPS and IPES spectra for CuPc are shown in Figure 3.9. The HOMO-LUMO band gap is determined by the difference in energy of the UPS and IPES peaks nearest to the fermi level. Again the optical gap is measured with UV-vis absorption spectroscopy, and the difference between the HOMO-LUMO gap and the optical gap is E_{eb} .

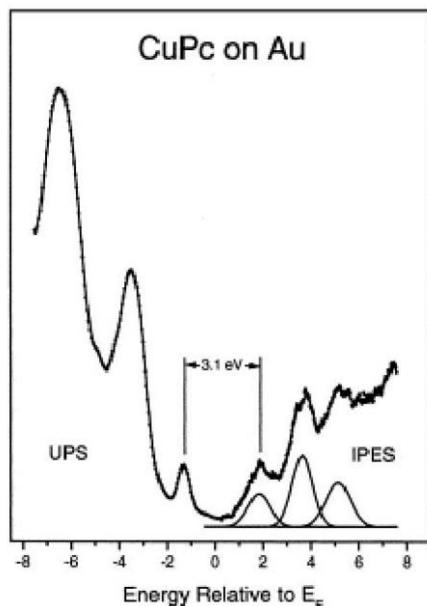


Figure 3.9. UPS and IPES spectra of CuPc. UPS and IPES are used to determine the HOMO-LUMO band gap to calculate E_{eb} .

Similar to UPS and IPES, XAS and XES measure the HOMO and LUMO levels in thin films. A schematic for XAS and XES is shown in Figure 3.10a. In the case of XAS, x-rays are absorbed in the material by a core electron state that is excited to an unoccupied orbital; the onset of absorption defines the LUMO energy. Now that a hole remains in the core level, an electron from the occupied orbitals can relax to that energy and release an x-ray. This process is the working principle of XES, which provides information about the HOMO energy. XAS and XES spectra for a star-shaped oligothiophene molecule are shown in Figure 3.10b (62). The main challenge in measuring the band gap with STM, UPS and IPES, or XAS and XES is that highly specific and expensive equipment or synchrotron light sources are needed.

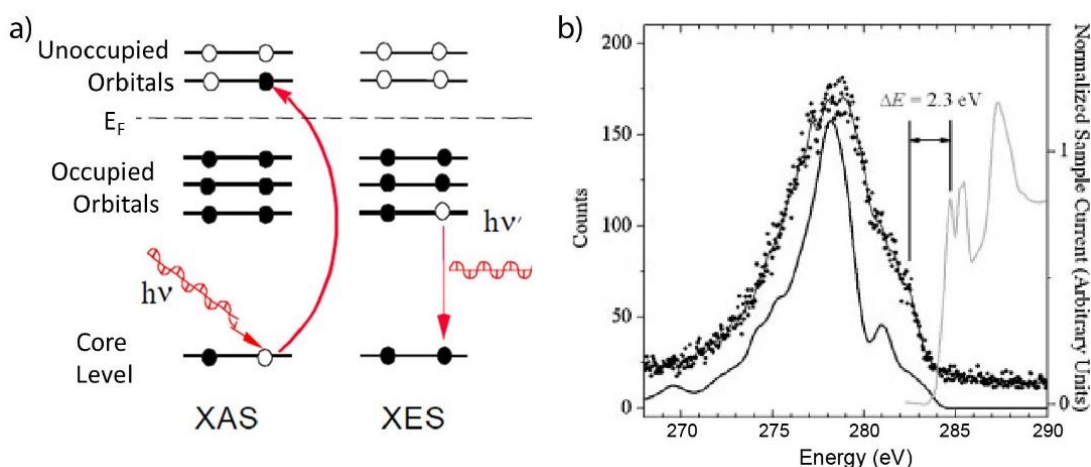


Figure 3.10. X-ray absorption and emission spectroscopy to determine HOMO-LUMO gap. a) Schematic of the x-ray absorption and emission processes. b) The XAS, XES, and simulated XES spectra for a star-shaped oligothiophene molecule. Adapted from Ref. (62).

Exciton dissociation is a critical process in OSCs, without it no photocurrent would be generated. Exciton dissociation and recombination are often described by Onsager-Braun theory, which applies to both singlet and CT excitons. In Onsager's theory, the probability that the exciton will escape its Coulomb attraction and generate free carriers is dependent on the competing rates of dissociation and recombination. A critical component of the theory is the Coulomb capture radius, r_c , which is the distance at which the Coulomb attraction equals $k_B T$ (63).

$$r_c = \frac{e^2}{4\pi\epsilon_r\epsilon_0 k_B T}$$

The probability that the electron will escape the Coulomb capture radius depends on the electric field applied, the distance of the charges, and the temperature of the system. The effect of an electric field on the electrostatic interactions of an electron is shown in Figure 3.11a. When Braun modified Onsager's theory in 1984, he also considered the lifetime of the exciton (30, 64). In the Onsager-Braun model the escape probability is defined as

$$P(E) = k_d(E)\tau(E)$$

where $P(E)$ is the escape probability, $\tau(E)$ is the lifetime of the CT state, $k_d(E)$ is the dissociation rate, and E is the electric field. Based on Onsager's original model, the dissociation rate is dependent on the electric field and the Coulomb capture radius.

$$k_d(E) = \frac{3\mu e}{4\pi\epsilon_r\epsilon_0 a^3} \exp\left(\frac{-\Delta E}{k_B T}\right) \left[1 + b + \frac{b^2}{3} + \frac{b^3}{18} + \dots\right]$$

where μ is the charge mobility, ϵ_r is the relative permittivity, a is the distance between the charges, ΔE is the Coulomb attraction defined as $e^2/4\pi\epsilon_r\epsilon_0 a$, b is $e^2 E/8\pi\epsilon_r\epsilon_0 k_B^2 T^2$, and the final bracket is a first-order Bessel function (30). The escape probability as a function of distance between the electron and hole and the applied electric field is shown in Figure 3.11b (64).

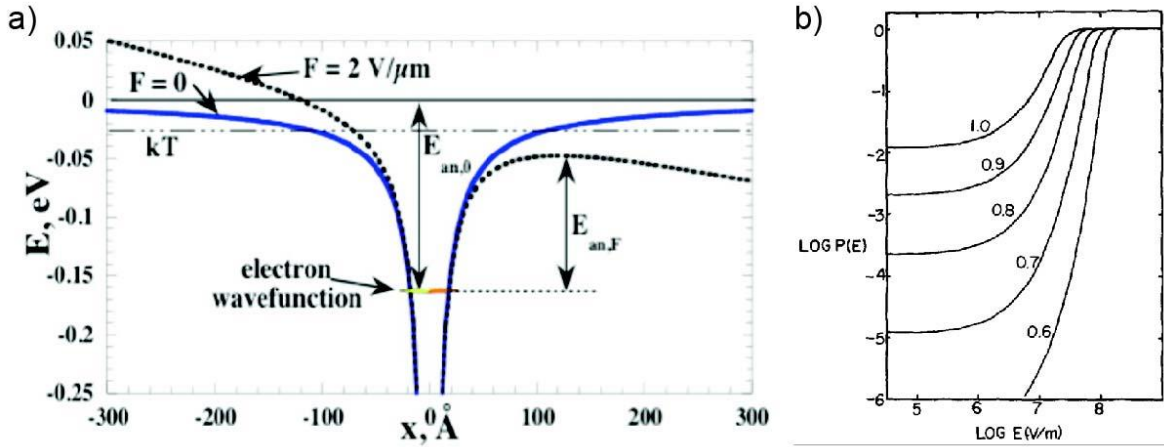


Figure 3.11. Onsager-Braun model for exciton dissociation and recombination. a) Electrostatic interactions in an organic semiconductor with permittivity of 4. The diagram shows the effect zero electric field ($F=0$) (blue line) and how the energy landscape changes when a field of $F=2$ V/ μm is applied (black, dashed line). From Ref. (23). b) The escape probability ($P(E)$) for an electron as a function of electric field (E). Each line represents a different distance between the electron and hole. The materials parameters are a mobility of 1×10^{-4} m²/Vs, relative permittivity of 3, temperature of 300 K, and exciton lifetime of 10 ns. From Ref. (64).

Many strategies have been reported to reduce E_{eb} in organic semiconductor films for OSCs (65–77). In Chapters 7 and 8, the strategy of blending the active layer with a high permittivity small molecule will be discussed. In this chapter, two of the more common and interesting methods from literature will be described. One method to reduce E_{eb} is to increase the permittivity of the BHJ by increasing the PCBM content due to the higher permittivity of PCBM. From the Onsager-Braun model, it is apparent that the permittivity of the material plays a critical role in the Coulomb capture radius and the exciton dissociation probability. By increasing the permittivity, the electron and hole are screened and interact less. PCBM has relative permittivity of 4, which is higher than the relative permittivity of 3 for most organic semiconductors. By increasing the ratio of fullerene to polymer in MDMO-PPV:PCBM BHJ OSCs from 1:1 to 1:4, the permittivity increases and contributes to the increase in photocurrent (76). Similarly, the permittivity in N,N0-bis(1-naphthyl)-N,N-diphenyl-1,1-biphenyl-4,4-diamine (NPD):C₆₀ increases linearly from 2.8 to 4 by increasing the C₆₀ fraction from 0 to 1. As a result, J_{SC} increases as more C₆₀ is added to the film (75). Another method to overcome E_{eb} in OSCs is to enhance exciton dissociation using electric fields (30). As described by the Onsager-Braun model, the exciton dissociation probability is largely dependent on the electric field. Yuan et al. poled ferroelectric polymers to generate electric fields across the BHJ layer to increase η_{ES} and reduce exciton recombination. In P3HT:PC₇₀BM BHJ devices with thin ferroelectric polymer layers at the electrodes, J_{SC} increases from approximately 10 to 12 mA/cm² (66).

3.3.3 Poor understanding of charge transfer states

Another challenge for OSCs is the several competing explanations for the mechanism of CT exciton dissociation. There is still significant debate in the field of OSCs on the mechanism for CT state dissociation (78). CT states are formed after the singlet exciton dissociates at the DA interface, but the electron in the acceptor and the hole in the donor are within close enough proximity to interact and form a CT state exciton. If simply considering the capture radius of an electron in an organic semiconductor with a permittivity of 3.5, the capture radius must be 16 nm for the CT state to dissociate at room temperature (78). Based on this simple electrostatic model, CT state dissociation should be very unlikely, however many OSC systems have dissociation efficiencies of 100%. Without fully understanding this critical step in photocurrent generation, OSC materials and devices cannot be rationally optimized.

Three main parameters are commonly considered important for CT state dissociation: excess photon energy, long-range material order, and electric fields. Many authors claim that free carriers are spontaneously generated after exciton dissociation due to hot CT excitons (79–82). High energy CT states, also referred to as hot CT states, are predicted to be more delocalized than low energy CT states, as a result the electron and hole are farther apart and can dissociate spontaneously compared to the lowest energy CT state (83). Additionally, the electron will be thermally hot when it transfers from the donor to the acceptor due to the $\Delta LUMO$. η_{ES} may be dependent on the amount of excess thermal energy of the electron (30). In one study of hot excitons, photocurrent generation was compared in films of MEH-PPV:C₆₀ that were irradiated either with below band gap photons to directly excite the CT states at the DA interface or with above band gap photons to generate excitons which would dissociate at the DA interface. The authors found that the CT states were more localized when directly excited compared to when they were generated through above gap excitation. As a result, the excess CT state energy was necessary for greater photocurrent generation (84). Similar results were found in highly efficient PCPDTBT:PCBM BHJs (85). In contrast, Lee et al. found that the quantum yield of carrier

photogeneration is the same for carrier generation through exciton formation and by directly exciting the CT states in P3HT:PCBM BHJs (86). The topic of hot exciton dissociation is still debated.

Long range order is considered a critical property for efficient exciton dissociation. As described by Onsager-Braun theory, high carrier mobility increases the probability of escaping the Coulomb capture radius (30). Long range order often leads to enhanced carrier mobility, as seen by an increase in mobility and carrier generation after annealing P3HT:PCBM BHJ devices to form more crystalline P3HT domains. Additionally, an increase in crystallinity from annealing results in more delocalized CT states. By modeling the photocurrent as a function of applied bias, Mandoc et al. found that the electron and hole in the CT state were separated by 0.78 nm before annealing and 1.2 nm after annealing (87). The CT state delocalization is likely caused by greater orbital overlap after annealing and less DA intermixing at the domain boundary (30). Thus, enhanced order in the donor and acceptor domains leads to higher CT state dissociation efficiencies.

Finally, electric fields are predicted by Onsager-Braun theory to facilitate CT state dissociation by reducing the Coulomb potential. The effect of electric fields on CT state separation is often measured in PL quenching experiments. CT states are expected to be dominated by radiative recombination, so, if the CT excitons dissociate, the intensity of the PL will decrease. Thus, the CT exciton dissociation efficiency under an electric field can be monitored via PL intensity. Veldman et al. found that the PL is quenched in P3HT:PCBM BHJ films when an external bias is applied to the system (77). Similarly, Ali et al. observed that the PL intensity is reduced as the magnitude of the field increases in an all small molecule BHJ (88), as shown in Figure 3.12. Nayak et al. point out that spontaneous exciton dissociation through hot excitons and the effect of electric field on the dissociation probability are very material specific; not all materials will have the same mechanism for charge generation at the DA interface (78). As a result, the mechanism for CT state generation needs to be determined for any new DA system in order to enhance the dissociation efficiency and improve PCE.

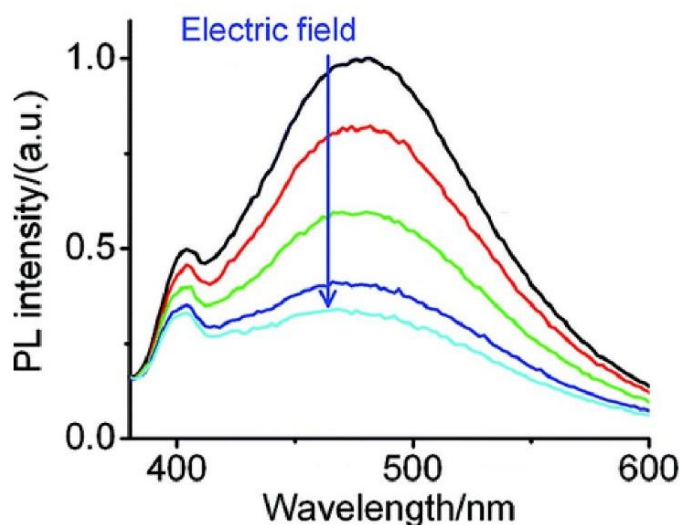


Figure 3.12. PL quenching in small molecule BHJ films. The electric field is increased from 0 to 20 V. Greater PL quenching due to an applied electric field supports the Onsager-Braun model for CT state dissociation. Adapted from Ref. (88).

3.3.4 Low charge carrier mobility

Once the excitons are dissociated into free carriers, high electron and hole mobilities are needed to efficiently transport the carriers to the electrodes before recombination. Drift mobility, μ , is described by v , the velocity of charge carriers, and E , the strength of the electric field applied to the material as shown in the equation: $\mu = \frac{v}{E}$. Carrier mobility in organic semiconductors needs to be improved for solar cell applications to allow for thicker active layers, so more light can be absorbed. If the mobility is low and the active layer is thick, many of the generated carriers will not reach the electrodes before recombining. Mobility is also important for other applications of organic semiconductors such as organic light emitting diodes (OLEDs) and organic field effect transistors (OFETs). For OSCs, mobility in the direction perpendicular to the substrate is most important, thus it will be focused on here.

Unlike covalently bonded inorganic semiconductors, organic semiconductors consist of molecules weakly bound by van der Waals forces, hydrogen bonding, and π - π interactions. As a result, the charges are localized and delocalized bands only form when molecules pack to form crystals with strong π -orbital overlap (89). Due to the localized states in disordered organic semiconductor films, hopping transport, rather than band transport, is considered the primary charge transport mechanism (90). Hopping transport is a sequential redox process in which electrons are transferred to a neutral molecule through the LUMO and holes are transferred through the HOMO (91). On the other hand, band-like transport behavior and high mobility values have been observed in single organic crystals at low temperatures (92). Significant progress has been made to improve the mobility of organic semiconductors. In the 1980's the highest recorded mobilities were around $10^{-5} \text{ cm}^2/\text{V}\cdot\text{s}$ while researchers have now achieved mobilities above $40 \text{ cm}^2/\text{V}\cdot\text{s}$ (93).

Another important aspect of charge transport in organic semiconductors is anisotropy. In liquid-crystalline or single crystal molecular semiconductor films, the overlap of π -orbitals occurs along specific directions due to the generally flat shape of the conjugated molecules (94). In disordered small molecule films, less anisotropy is observed because of the random orientation of π -orbitals; however, due to short range order, some anisotropy does still exist (95). In general, the packing structure in molecular semiconductors has a strong effect on the mobility, and small changes in intermolecular orientations can cause a significant change in carrier mobility (94).

One of the challenges associated with mobility in organic semiconductors is accurately measuring the mobility. There are numerous methods for measuring mobility, but the most commonly used for measuring transport perpendicular to the substrate are time-of-flight (TOF) and space charge limited current (SCLC) measurements. It is also common to measure in-plane mobility through the analysis of OFETs. For both the TOF and SCLC methods, the organic material of interest is sandwiched between two electrodes. The TOF measurement is conducted such that one of the electrodes is transparent, and through it the semiconductor is irradiated with a short laser pulse (96). The laser pulse generates a transient photocurrent near one electrode and the applied bias causes the electrons or holes to drift across the sample to be collected at the other electrode. The current measured as a function of time is used to determine transit time, τ , which is the time required for the photogenerated charges to drift across the sample (97). As shown in Figure 3.13, τ is determined from the nondispersive photocurrent or from the double

logarithmic plot of the dispersive photocurrent. The following equation is used to calculate the mobility, μ , from the transit time

$$\mu = \frac{d^2}{V\tau},$$

where d is the sample thickness, V is the applied voltage, and τ is the transit time (91).

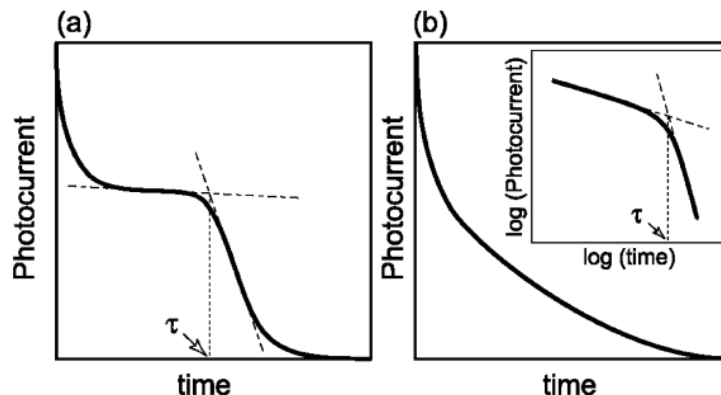


Figure 3.13. Typical transient photocurrent plots of (a) a nondispersive and (b) dispersive photocurrent. The double logarithmic plot is shown in the inset. Adapted from Ref (91).

For SCLC mobility measurements, current density-voltage (J - V) measurements are used to determine the mobility. Given sufficient injection of holes (electrons), the high density of carriers results in the formation of an electric field gradient, which limits the transport of holes (electrons) due to the space charge that accumulates; the current measurement under these conditions is SCLC, which is described by Child's Law

$$J = \frac{9}{8} \epsilon_r \epsilon_0 \mu \frac{V^2}{L^3},$$

where ϵ_r is the relative permittivity of the semiconductor, ϵ_0 is the permittivity of free space, μ is mobility, V is the voltage applied, and L is the thickness of the semiconductor film. For this equation to be valid, it is assumed that the mobility is field independent (98). However, due to the disorder found in organic semiconductors, the mobility is generally found to be field dependent, which is described by the Mott-Gurney equation

$$J = \frac{9}{8} \epsilon_r \epsilon_0 \mu_0 \frac{V^2}{L^3} \exp(0.89\gamma\sqrt{E}) \frac{V^2}{L^3},$$

where μ_0 is the zero-field mobility, E is the electric field, and γ is the field dependence prefactor (98). The work function of the electrodes must be matched with either the HOMO or LUMO of the material to form hole-only and electron-only devices, respectively. And, to probe the bulk of the material, the electrodes must form ohmic contacts (99).

The organic semiconductor carrier mobility is dependent on a variety of factors. The main factors that still pose a challenge are molecular structure and packing, disorder, and impurities. The structure of the molecule or polymer will greatly influence how the π -orbitals overlap and thus the molecular disorder and packing (100). Even in semicrystalline organic semiconductor films, polymorphism can cause significant long-range disorder (93). Impurities are also a major concern because they can lead to trap states and increase molecular disorder. Impurities can be caused by low material purity but also by any remaining solvent in the film from solution processing (93).

OSCs are an interesting technology because of their low embodied energy, high tunability, low cost, mechanical flexibility, and ease of processing. Although significant progress has been made

in understanding photocurrent generation in OSCs and increasing their efficiency, many issues such as high E_{eb} , low carrier mobility, and poor control of phase separation still remain. In 2015, the highest National Renewable Energy Laboratory (NREL) certified efficiency for a single junction OSCs is only 11.5% (101). OSCs may still have an advantage for niche applications that require flexible, colorful, or partially transparent solar cells. However, OSCs are quickly being overshadowed by hybrid organic-inorganic perovskite solar cells, which have similar advantages to OSCs but in only a few years of research have a PCE of 21.0% (101).

The work in this dissertation is focused on two of the large challenges for OSCs: reducing exciton binding energy and further understanding CT state dissociation. To reduce the binding energy of Frenkel and CT state excitons, I increased the permittivity of donor and BHJ films, respectively. And to better understand the importance of hot excitons for charge separation, we utilized ultrafast time-resolved spectroscopy to observe exciton mobility.

Chapter 4

Hybrid organic-inorganic perovskite solar cells

Hybrid organic-inorganic perovskite solar cells, also referred to as organometallic perovskites, have made an extraordinary entrance in the field of solar cell research. The rapid progress in solar cell efficiency and understanding of these materials is unprecedented for a solar material. The increase in solar cell efficiency over time compared to other thin film solar technologies is shown in Figure 4.1. This rapid progress is partly due to the similarities between perovskite solar cells and OSCs and dye sensitized solar cells (DSSCs) (102). Perovskite solar cells are solution-processable, are tunable, are composed of abundant materials, and have PCEs over 20% (9). Although they have sufficiently high efficiencies on their own, perovskite solar cells are considered a strong match to silicon or other thin film solar materials for high efficiency tandem solar cells (103).

Perovskite solar cells are also considered thin film devices, and, like OSCs, they require very little energy to produce. The energy payback time for perovskite solar cells is similar to OSCs because they are solution processable and are deposited at room temperature (104). For the perovskite lattice to self-assemble, the initial precursors must be annealed together on the substrate but at relatively low temperatures (e.g. 150 °C). Although the efficiencies have already reached 20%, there remain many challenges for processing perovskite solar cells such as their sensitivity to moisture, low melting temperature, and solubility in polar solvents. Another general concern about perovskite solar cells is that the most commonly studied material contains lead, though replacing the lead is an active area of research. Incredible progress has been made to increase the efficiency in perovskite solar cells, but basic understanding of the material properties is lagging behind. It is critical to understand the loss mechanisms on their native length scales to allow for systematic solar cell optimization.

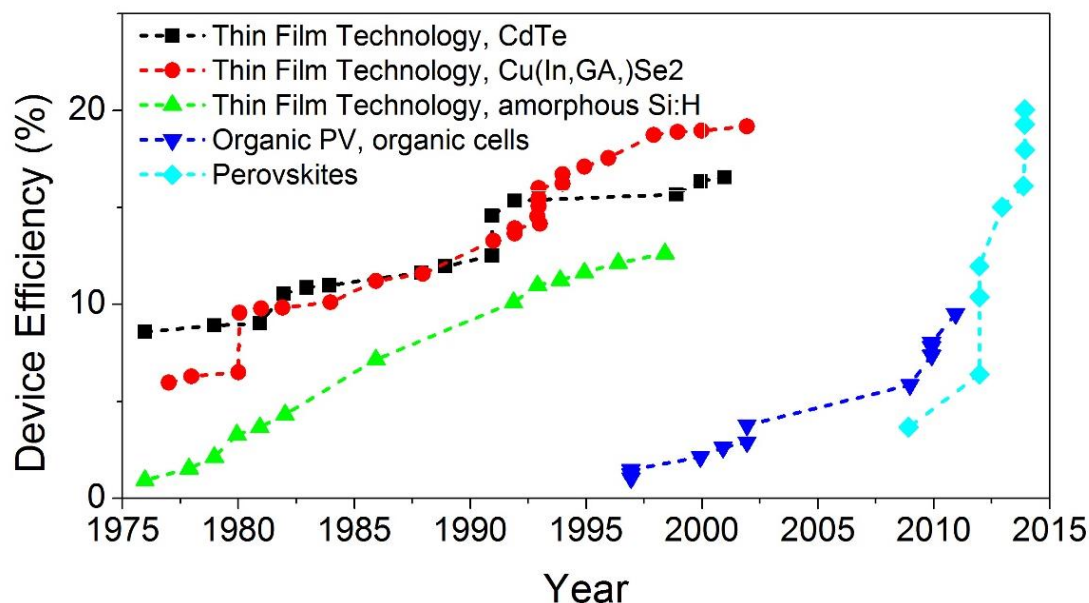


Figure 4.1. Record solar cell PCEs for thin film technologies over time. The slope of the perovskite solar cells is significantly steeper than other thin film technologies. This plot is courtesy of the National Renewable Energy Laboratory, Golden, CO.

4.1 Hybrid organic-inorganic perovskite material properties

4.1.1 Crystal structure and composition

The perovskite crystal structure has the formula ABX_3 , where A and B are cations of different sizes and X is an anion. In this ionic crystal, the A atoms are larger than the B atoms, and the unit cell can be cubic, orthorhombic, or tetragonal. The structure of the perovskite unit cell is shown in Figure 4.2. Traditionally, perovskite materials such as barium titanate and strontium titanate have been of interest because they have high dielectric constants and are often ferroelectric or superconducting (105–107). These emerging hybrid perovskite materials are composed of inorganic and organic ions. For solar applications, lead halide perovskites have been the most commonly studied hybrid perovskites. Lead halide perovskites have molecular cations in the A position, which are commonly methylammonium (MA) (CH_3NH_3^+), ethylammonium ($\text{CH}_3\text{CH}_2\text{NH}_3^+$), or formamidinium (FA) ($\text{CH}_2\text{CH}=\text{CH}_2^+$) (102). The smaller cation is commonly lead and the anion is a halide (I^- , Br^- , Cl^-). See Figure 4.2 for typical ions used in hybrid organic-inorganic halide solar cells. The band gap is determined by the inorganic components and their bond length and angle. For reference, MAPbI_3 , the prototypical perovskite for solar cells, has a band gap of approximately 1.5 eV (108). By changing the organic cation size, the bond angle between B and X will change and incur a slight change in the band gap. Additionally, the bandgap energy can be altered more significantly by changing the inorganic ions, where the s- and p-orbitals determine the nature and energy of the conduction band minimum (CBM) and valence band maximum (VBM) (109). In addition to having a tunable bandgap, the absorption coefficient of lead halide perovskites is very high; MAPbI_3 has an absorption coefficient on the order of 10^5 cm^{-1} , which is similar to inorganic semiconductor materials such as GaAs (Figure 4.3) (110). The electronic properties of perovskite semiconductors are also dependent on the crystal structure (111); lead halide perovskite materials have several crystal phase transitions. The most common MAPbI_3 perovskite has a transition from orthorhombic-to-tetragonal crystal structure at 162 K and a tetragonal-to-cubic transition at 327 K (112).

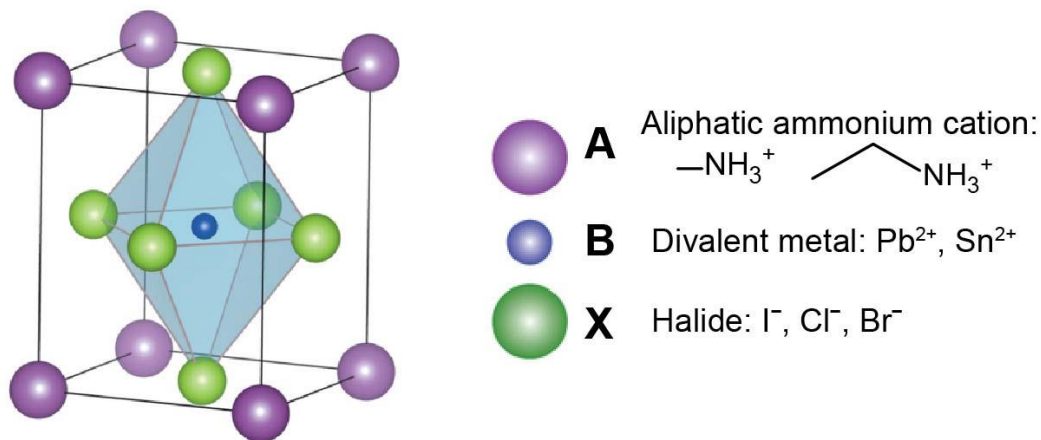


Figure 4.2. ABX_3 perovskite crystal structure. Typical ions for hybrid organic inorganic halide perovskites for solar cells are shown. Adapted from Ref. (113).

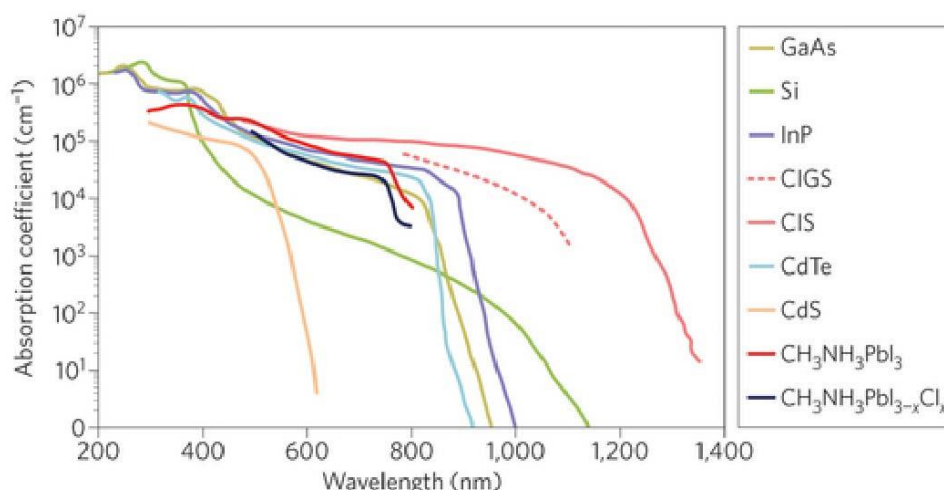


Figure 4.3. Comparing absorption coefficients of many solar absorber materials. Lead halide perovskites have similar absorption coefficients to established solar materials such as CdTe and GaAs. Adapted from Ref. (102).

Mixed halide and mixed cation perovskites have also been extensively studied, such as $\text{MAPbI}_{3-x}\text{Cl}_x$, $\text{MAPbI}_{3-x}\text{Br}_x$, and $\text{FA}_{0.9}\text{Cs}_{0.1}\text{PbI}_3$ (114, 115). But, specifically with mixed halide perovskites, care needs to be taken that the composition is stable. Though many reports of $\text{MAPbI}_{3-x}\text{Cl}_x$ have been published, no chlorine has been detected in such films (116–118). Originally, it was assumed that the Cl^- doping enhanced the efficiency of perovskite solar cells. However, Cl^- in the precursor solution improves the quality of the perovskite films formed during solution processing by slowing down the growth process (118). Another concern with mixed halides is rapid segregation of the two ions to across the thickness of the film to form separate phases, as is found in the segregation of $\text{MAPbI}_{3-x}\text{Br}_x$ into MAPbI_3 and MAPbBr_3 under 1-sun illumination (119, 120). The stability of hybrid perovskites needs to be established before they can be used for solar applications.

4.1.2 Material processing

Lead halide perovskite films are formed by combining the inorganic constituent, such as PbI_2 or PbCl_2 , with the organic constituent, such as methylammonium iodide (MAI) or methylammonium chloride (MACl). In a one-step solution process, the inorganic and organic precursor salts are combined in an organic solvent, spin coated onto a substrate, and thermally annealed. By optimizing the annealing time and temperature, the film quality can be improved using a one-step solution process. Similarly, dual-source thermal evaporation can be used to grow very uniform lead halide perovskite films. For large area films, ultra-sonic spray-coating has also been employed (121). However, it has been established that a two-step solution process generally yields more uniform films and better performing perovskite solar cells (122). In a two-step process, the inorganic precursor (e.g. PbI_2) is first deposited via spin coating from solution or thermal evaporation, and then exposed to either a vapor or solution of the organic component (e.g. MAI). To finalize the formation of the perovskite, the film is then annealed (121). Using a vapor assisted solution process results in smoother films because the initial inorganic film is not partially dissolved during the incorporation of the organic component (123). All of these processing techniques generate polycrystalline films. Single crystals can also be grown but they

are often too thick to use in solar cell devices, though they are useful for understanding fundamental material properties (124–126).

4.2 Short history of perovskite solar cells

Hybrid organic-inorganic perovskites do not have a long history. Halide perovskites were first investigated as materials for light emitting diodes (LEDs) in 1995, but not considered for solar cells because of the lead content (102). Not until 2009 were halide perovskite nanoparticles (NPs) used in solar cells as sensitizers in DSSCs. The DSSCs consisted of porous titanium dioxide (TiO_2) infiltrated with MAPbI_3 NPs that were formed in solution and had an efficiency of 3.8% (127). However, this efficiency was considered low compared to the 11% DSSCs at the time. The efficiency was improved to 6.5% in 2011 (Figure 4.4a), but the DSSCs were still unstable because the perovskite dissolved in the polar liquid electrolyte (109, 128). Because of this instability, a solid state hole transport layer (HTL) was used instead of the liquid electrolyte; spiro-OMeTAD (2,2',7,7'-tetrakis(N,N-di-p-methoxyphenylamine)-9,9'-spirobifluorene) had been successfully used in other DSSCs because it can infiltrate the porous TiO_2 during spin coating (102). Using spiro-OMeTAD in perovskite NP sensitized DSSCs resulted in an efficiency of 9.7% and enhanced the device stability (Figure 4.4b) (129).

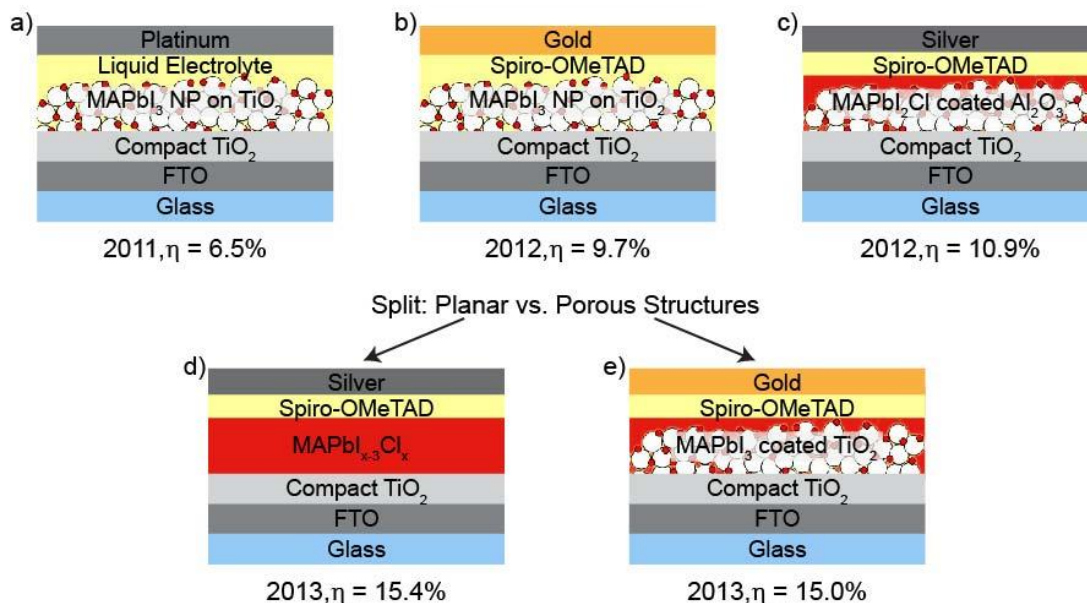


Figure 4.4. Early history of hybrid organic-inorganic perovskite solar cells. a) 2001: MAPbI_3 perovskite NPs were first used as sensitizers in DSSCs but were unstable due to the solubility of the perovskite in the liquid electrolyte (128). Fluorine doped tin oxide (FTO) is the transparent electrode. b) 2012: The efficiency of MAPbI_3 NP sensitized DSSCs was improved by using a solid state HTL, spiro-OMeTAD (129). c) 2012: By replacing the porous TiO_2 with Al_2O_3 , fully infiltrating the porous layer with MAPbI_2Cl , and including a capping layer of MAPbI_2Cl , the efficiency was enhanced to 10.9% (130). d) 2013: A 15.4% efficient planar $\text{MAPbI}_{x-3}\text{Cl}_x$ solar cell was fabricated with a high quality film by using dual-source thermal evaporation (113). e) 2013: By using a two-step process of forming the MAPbI_3 within the porous TiO_2 layer, the efficiency of porous devices was improved to 15% (122).

Then in 2012, the seminal paper from Snaith and co-workers brought perovskite solar cells to the forefront of solar research (130). There were several major advances reported in this publication that led to future advancements in perovskite solar cells. First, a 7.6% efficient solar cell was achieved using a thin perovskite absorber layer on top of the TiO_2 in addition to infiltrating the TiO_2 with the perovskite (130). This efficiency enhancement was also due to using a mixed halide perovskite ($\text{MAPbI}_{3-x}\text{Cl}_x$). More importantly, Lee et al. discovered that the TiO_2 electron transport layer could be replaced by an Al_2O_3 porous layer for a solar cell with an efficiency of 10.9%, as shown in Figure 4.4c (130). V_{OC} was enhanced when using the wide bandgap Al_2O_3 scaffold because the energy loss from transferring the electron from the perovskite to the TiO_2 was eliminated. But, more importantly, it led to the understanding that the perovskite is an ambipolar conductor. To emphasize this, a 1.8% efficient solar cell was fabricated without the scaffold layer (130). These results split the researchers in the field of perovskite solar cells into two groups: those fabricating devices with a porous scaffold layer and those fabricating planar perovskite devices. Progress in enhancing the efficiency of perovskite solar cells was made by both groups. In 2013, 15% efficient solar cells were established by improving the quality of the perovskite material. In the area of planar perovskite solar cells, the quality of the perovskite film was enhanced by using dual-source thermal evaporation of PbCl_2 and $\text{CH}_3\text{NH}_3\text{I}$ (Figure 4.4d). The perovskite forms a more uniform film when using thermal evaporation compared to a single step solution process for planar devices, leading to efficiencies over 15% (113). The improved film quality is shown in Figure 4.5. Grätzel and co-workers established a two-step solution process by first infiltrating the porous TiO_2 with PbI_2 solution and then converting it to the perovskite by spin coating the $\text{CH}_3\text{NH}_3\text{I}$ solution (Figure 4.4e). The two-step process results in improved morphology of the perovskite within the TiO_2 because it prevents the formation of perovskite precipitates in solution (122).

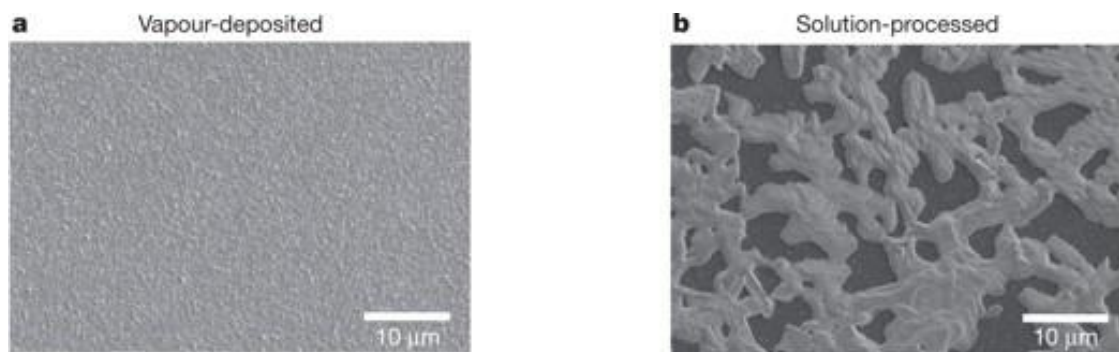


Figure 4.5. Comparison of $\text{MAPbI}_{3-x}\text{Cl}_x$ film quality using dual source vapor deposition (a) or one-step solution processing (b). The non-uniformity and pin-holes in the solution processed film significantly reduce the solar cell efficiency. Adapted from (113).

In 2014, the quality of the perovskite material continued to improve and more significant research into the basic properties of lead halide perovskites was established. The next major improvement in device performance was in 2014, when Yang and co-workers reported a 19.3% efficient planar perovskite device. This efficiency boost was due to reduced defects in the perovskite film and transport layers with improved energy level alignment (131). Further

efficiency advancements have focused on optimizing the composition of the perovskite material by experimenting with different organic cations and ratios of halides (132). Currently, in 2016, the highest efficiency for perovskite solar cells is 21.02%, which was certified by NREL (101). Theoretically, the maximum efficiency of a 1 μm thick MAPbI_3 solar cell in a planar configuration is predicted to be 26% (109, 133).

4.3 Perovskite solar cell operation

The two types of perovskite solar cell structures, porous and planar, operate as p-i-n devices (114). In both cases, incident photons generate EHPs in the perovskite absorber. The carriers then diffuse or drift to their respective electron and hole transport layers. Figure 4.6 demonstrates the photocurrent generation mechanism in both types of architectures and provides a schematic of the energy levels in the solar cell. TiO_2 is most commonly used to accept the electrons from the perovskite and spiro-OMeTAD is used to collect the holes. This mechanism for photocurrent generation has been directly observed via electron beam induced current (EBIC) microscopy (134). When the device architecture employs a mesoporous TiO_2 scaffold infiltrated with perovskite, the electrons only need to diffuse an average of 10 nm reach the perovskite- TiO_2 interface and transfer to the TiO_2 . As a result, the mixed TiO_2 /perovskite layer can be as thick as needed for maximum light absorption and the quality of the perovskite material is not as critical for electron transport (135). However, by employing a planar architecture, the challenge associated with the interface between the TiO_2 perovskite is eliminated. But, in the planar structure, the perovskite film needs to be of high quality to allow for long carrier diffusion lengths and lifetimes to ensure that the carriers reach their respective transport layers.

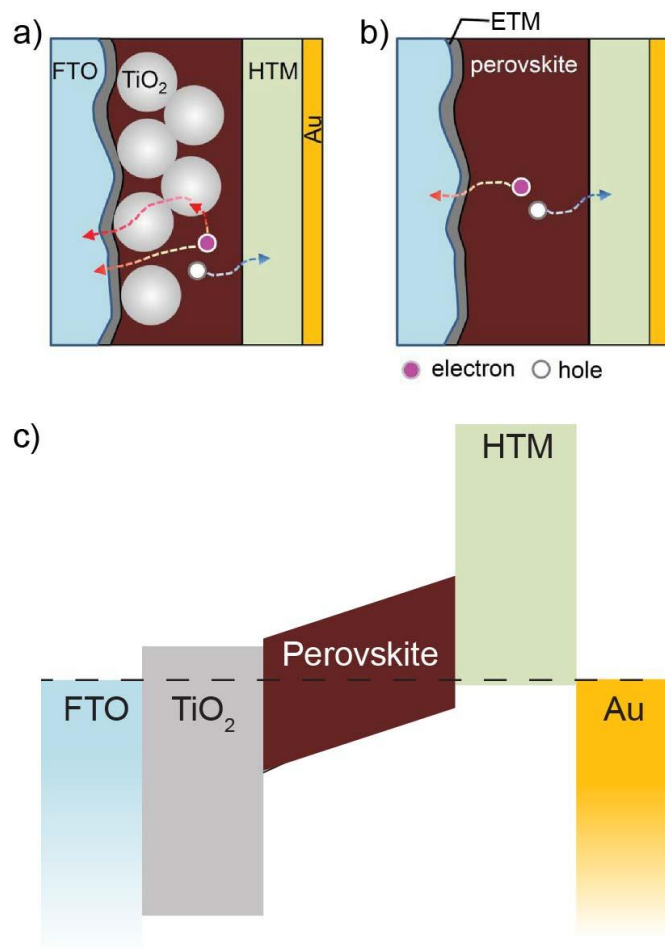


Figure 4.6. Photocurrent generation in perovskite solar cells. a) Photocurrent generation pathway in devices with a porous TiO₂ scaffold begins with formation of an EHP in the perovskite material. The electron is then transferred to the TiO₂ scaffold or diffuses directly to the electron transport material (ETM). The hole diffuses to the hole transport material (HTM). The electron and hole are then collected by their respective electrodes, usually fluorine doped tin oxide (FTO) and gold. b) In the planar device structure, the EHP is formed in the perovskite layer. Then due to long diffusion lengths, the electron and hole are collected by the transport layers and the electrodes. c) Solar cell energy band diagram under short circuit conditions. Adapted from Ref. (102, 109).

4.4 Advantages of hybrid perovskite solar cells

4.4.1 The fascination with hybrid perovskites

There are several key materials properties that have allowed for hybrid organic-inorganic perovskite solar cells to achieve high efficiencies at a rapid rate. One is the ease of material processing (104, 122, 136). The knowledge gained through low temperature solution and vapor processing techniques used for OSCs and DSSCs was easily adapted to hybrid perovskite thin films. As a result, high quality perovskite thin films were easily grown using the equipment already available in labs that were fabricating OSCs. Perovskite films could easily be fabricated

to measure basic material properties and rapidly optimized for solar cells, which led to hybrid perovskites becoming a disruptive new solar material. Another basic property that allows for high efficiency is strong light absorption. As mentioned earlier, lead halide perovskites have absorption coefficients on the same order of magnitude as other direct bandgap semiconductors used for solar cells, such as GaAs and CdTe (110). As a result, the perovskite films can be approximately 300 nm thick and absorb 95% of incident sunlight.

4.4.2 Long carrier lifetime and high mobility

Planar perovskite solar cells can achieve high efficiencies with roughly 300 nm thick films because of the long carrier lifetimes and high mobilities. Two articles simultaneously published in *Science* reported 100 nm or longer carrier diffusion lengths in lead halide perovskites. These results were particularly surprising because solution processed polycrystalline materials generally suffer from short diffusion lengths. In the work by Snaith and co-workers, PL lifetime measurements (Figure 4.7a) were used to determine that MAPbI₃ and MAPbI_{3-x}Cl_x have carrier lifetimes (both electron and hole) on the order of 300 ns to microseconds, thus diffusion lengths of 100 nm and 1 μm respectively (137). It was later determined that the lower diffusion length in the pure iodide perovskite was due to poor material quality, not composition (102). Similarly, Xing et al. used transient PL and femtosecond transient optical spectroscopy to study MAPbI₃ (Figure 4.7b) and found that electrons and holes have diffusion lengths of 130 and 90 nm respectively (138). Both of these results suggest that 200 nm films do not require a nanoporous TiO₂ scaffold because the carrier diffusion lengths are sufficient for efficient collection at the electron and hole transport layers in the planar device architecture.

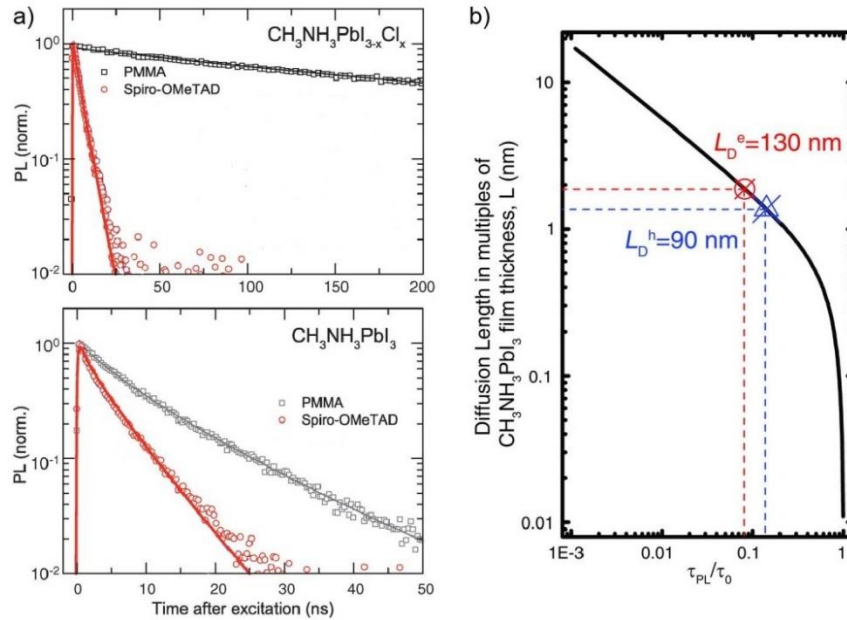


Figure 4.7. Measuring carrier diffusion lengths in lead halide perovskites. a) Time resolved PL showing the PL decay time for MAPbI_{3-x}Cl_x (top) and MAPbI₃ (bottom) with a surface passivation layer (PMMA) or a quenching layer (spiro-OMeTAD). Diffusion models are fit to the PL quenching data to determine the carrier diffusion lengths. Adapted from Ref. (137). b) Dependence of carrier diffusion length on PL lifetime quenching ratios (τ_{PL}/τ_0). The electron and hole diffusion lengths in MAPbI₃ were calculated as 130 and 80 nm respectively. Adapted from Ref. (138).

Long diffusion lengths in lead halide perovskites imply high carrier mobility and low recombination rates. The carrier mobility in MAPbI₃ is on the order of 10 cm²/V·s for electrons and holes, with the hole mobility being slightly lower than the electron mobility (139–141). Also, it was observed that bimolecular and monomolecular, meaning trap and impurity assisted, recombination rates are very low in these materials (139). The low monomolecular recombination rate is likely due to the low defect density in MAPbI₃. The defect density in single crystal and polycrystalline MAPbI₃ are 10¹⁰ and 10¹⁶/cm³ respectively (114). Several studies have found that defects and grain boundaries have very little influence on the electronic properties of polycrystalline perovskite films. Density functional theory (DFT) calculations to study vacancy defects, such as PbI₂, MAI and elemental defects, suggest that the defects either generate states outside of the perovskite bandgap or shallow states near the band edges (102). These results help to explain why solution processed perovskite films have long carrier lifetimes. However, several groups have experimentally found evidence for detrimental surface trap states in perovskite thin films (142–144), demonstrating the limitations of DFT calculations. Similar to point defects, grain boundaries have little to no effect on the electronic structure of polycrystalline lead halide perovskites (102, 114). Grain boundaries studied by kelvin probe force microscopy (KPFM), have only a 45 meV surface potential difference from the grains in the dark, and the surface potential difference reduces under illumination (145). Having benign grain boundaries is a significant advantage compared to other polycrystalline solar cell materials (e.g. Si, CdTe, CIGS), which require additional processing steps to reduce the negative effects of grain boundaries (114).

4.4.3 Bandgap tunability

Hybrid organic-inorganic perovskites also have the advantage that the band gap is highly tunable by adjusting the components in the crystal (146, 147). Adjusting the band gap is critical for achieving the ideal band gap for single junction or tandem devices. Many experts in the field of perovskite solar cells believe that the ideal commercialization pathway is to fabricate tandem solar cells with established solar materials such as silicon or CIGS (103, 114, 135). For example, to form a tandem solar cell with silicon, the ideal band gap for a top cell is 1.75 eV. McMeekin et al. successfully tuned the perovskite band gap to approximately 1.75 eV by adjusting the ratio of iodide to bromide and FA to cesium, with a final composition of FA_{0.83}Cs_{0.17}Pb(I_{0.6}Br_{0.4})₃ (120). Figure 4.8 shows the change in absorption spectra and photographs of the films as the ratio of iodide to bromide changes. Although perovskites are highly tunable, it is critical to ensure that the materials are stable under operating temperatures and 1-sun illumination.

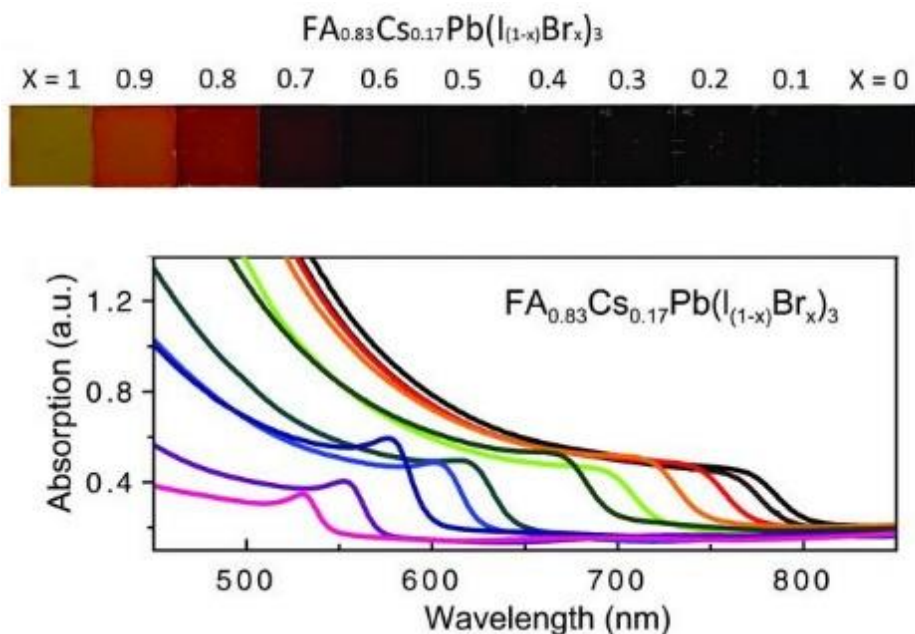


Figure 4.8. Tunability of hybrid organic-inorganic perovskite films. Photographs of perovskite films (top) with increasing ratio of bromide to iodide and the accompanying UV-vis absorption spectra (bottom).

4.5 Challenges of hybrid perovskite solar cells

Although perovskites have several attributes necessary for high efficiency solar cells, many challenges exist in making these materials suitable for commercialization. Phase change between tetragonal and cubic at solar cell operating temperatures, as mentioned above, is one major concern. Additionally, many cite that the presence of lead in the material may prevent adoption of perovskite solar cells (135). However, the successes of CdTe solar modules and the fact that the European legislation on toxic substances is less stringent for lead compared to cadmium suggests that lead content may not be a problem for perovskite module commercialization (102). Because perovskites are highly tunable, replacing the lead is also an option. Non-toxic hybrid perovskite materials with tin instead of lead have begun to show promise, with a reasonable performance of roughly 6% PCE reported, but are still lagging behind lead based perovskites (148, 149).

4.5.1 Hysteresis in current voltage curve

The largest concern for perovskite solar cell commercialization is the instability of the material. In 2014, the first major reports on the observed hysteresis in the perovskite IV curve were published (150, 151). In perovskite solar cells, the shape of the IV curve varies significantly based on the direction and rate of the voltage sweep, as shown in Figure 4.9a. Additionally, the degree of hysteresis also depends on light soaking time and the properties and thickness of the electron and hole transport layers (150). Not only does hysteresis bring into question the stability of the perovskite material, but also creates a challenge in measuring accurate solar cell efficiencies. *Nature Materials* has established a checklist for photovoltaic research that requires information regarding scan rate and direction, light soaking conditions, and stabilized maximum

power point current density measurements (152). This checklist ensures that the results can be reproduced and that the reported efficiency is accurate. An example of stabilized current and efficiency measurements are shown in Figure 4.9b. Other *Nature* journals are also requiring the use of this check-list, which will likely become the standard for all perovskite solar cell research.

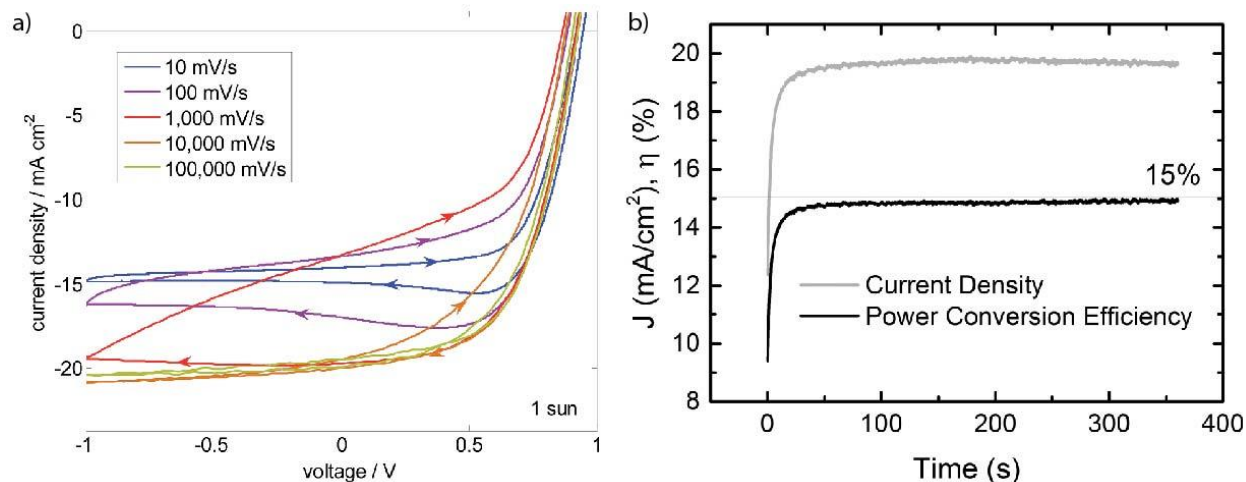


Figure 4.9. Hysteresis in perovskite solar cells. a) IV curves of porous TiO₂ MAPbI₃ solar cells. The arrows indicate the sweep direction and the sweep rate was varied from 10 to 100,000 mV/s. The hysteresis is more significant for intermediate voltage sweep rates. Adapted from Ref. (153). b) Photocurrent density and PCE over time for a porous Al₂O₃ MAPbI₃ solar cell at 0.75 V forward bias. The maximum power point for the measured solar cell is 0.75 V. The solar cell becomes stable in less than 50 s. Adapted from Ref. (150).

4.5.2 Ion migration

Initially, many reports hypothesized that the hysteresis was due to trapping and de-trapping carriers at states near surfaces and interfaces, polarization due to ferroelectric behavior, and the migration of intrinsic or excess ions (150, 151). The research community is now leaning toward ion migration as the main cause of hysteresis (153–158). When an electric field is applied to the perovskite film, regardless of composition, an internal field is created inside the film due to ion migration toward the electrodes (155, 157, 159, 160). This effect was most clearly shown by Yuan et al. when they applied an electric field across lateral perovskite devices and observed directional changes in the photothermal induced resonance (PTIR) and KPFM images, as shown in Figure 4.10. Now that the hysteresis is better understood and more details of ion migration have been uncovered, methods to mitigate ion migration are needed. Several studies have observed that hysteresis is reduced when perovskite grain size increases (158). These results suggest that ion migration through grain boundaries may dominate. Thus, one method to reduce ion migration is to increase grain size. Additionally, tuning the components of the perovskite crystal or fabricating perovskites with greater formation energies can help reduce ion migration (161).

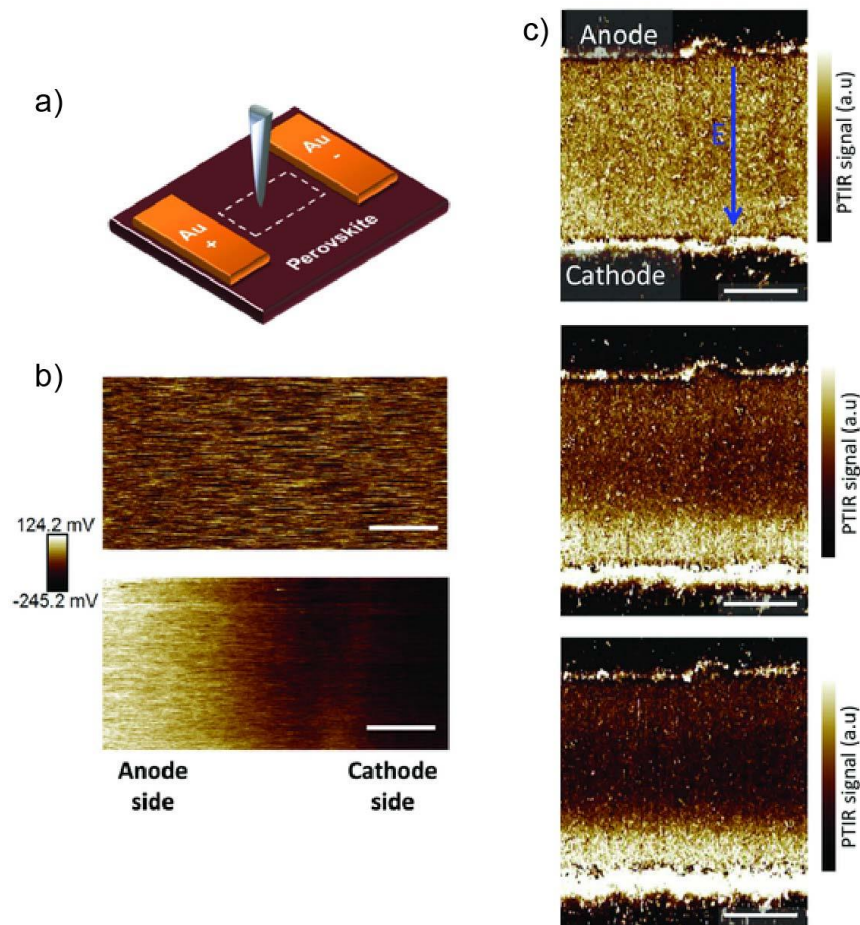


Figure 4.10. Ion migration observed in lateral MAPbI₃ perovskite devices. a) Schematic of device configuration. b) KPFM images of the perovskite film before and after applying a 1.2 V/μm electric field for 100 s. Before applying an electric field, the surface potential is uniform between the electrodes. After the electric field is applied, the surface potential increases on the anode side and decreases on the cathode side. The scale bar is 6 μm. c) PTIR images of perovskite films before (top), 100 s after (middle), and 200 s after (bottom) applying a 1.6 V/μm electric field. The PTIR images show the CH₃ asymmetric deformation absorption of the MA ion. These results suggest that the MA ions are migrating in the film. The scale bar is 20 μm. Adapted from Ref. (156).

4.5.3 Unidentified loss mechanisms

Perovskite solar cells are a highly promising new class of solar cells made with highly tunable, easily processable, low cost materials with a low embodied energy. Although perovskite solar cells could be commercialized as single junction solar cells, they are considered more promising as a top cell for an already commercialized solar materials such as silicon or CIGS. One challenge that currently needs to be addressed is the material stability under solar cell operating conditions. At this stage of research in the area of perovskite solar cells, stability issues are only starting to be addressed and solutions will likely soon be discovered. A more pressing challenge is understanding the loss mechanisms in perovskite solar cells to overcome them and

reach higher PCEs. To understand how morphology is related to reductions in V_{OC} and I_{SC} , two critical performance parameters, I used cAFM to directly measure these parameters in perovskite solar cells on the nanoscale. As described in Chapter 10, there are specific perovskite crystal facets with a high density of surface defects that limit PCE.

Chapter 5

Solar cell characterization techniques

5.1 Power conversion efficiency

PCE is measured by sweeping the bias across the solar cell and measuring the current while illuminating the sample with a solar simulator. In the studies presented in this dissertation, a Thermal-Oriel 300W solar simulator provided AM 1.5G solar illumination at 100 mW cm^{-2} for device testing. As shown in Figure 5.1, this solar simulator uses a xenon arc lamp and filters the light using an AM 1.5G filter to approximately match the solar spectrum. A Keithley 236 source-measure unit was used to measure $J-V$ curves.

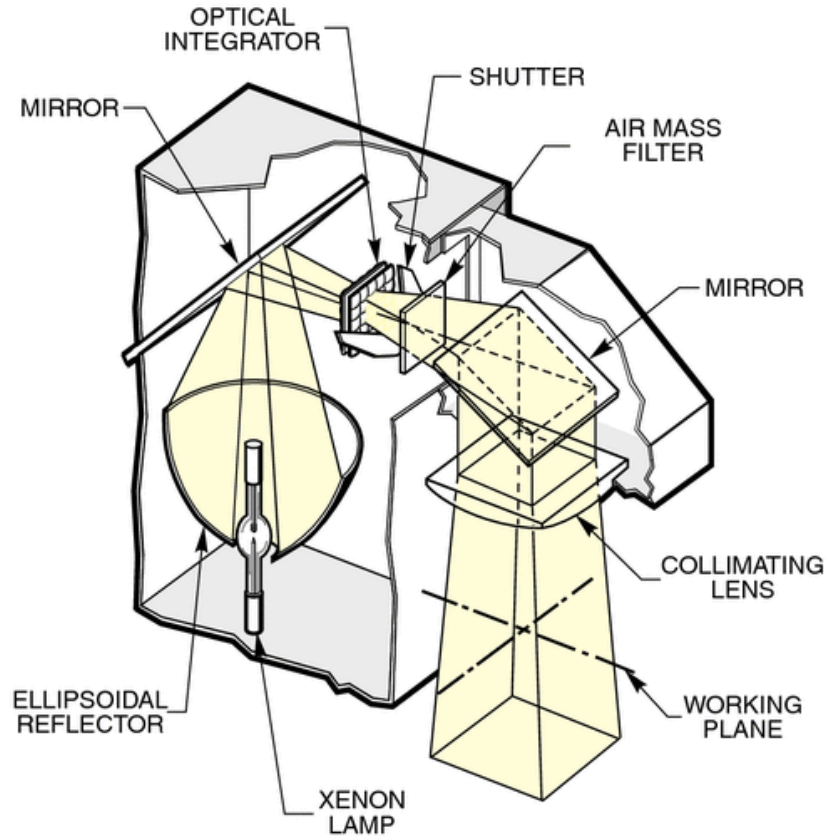


Figure 5.1. Solar simulator schematic. From Newport Corporation.

5.2 Solar cell quantum efficiency

The measurement set up for EQE is shown in Figure 5.2. The light source is a xenon arc lamp. The wavelength of light is swept during the measurement using the monochromator; the filter wheel uses long pass filters to eliminate second harmonics. The light is chopped at 80 Hz and the chopper is connected to the reference port of the lock-in amplifier. The lock-in amplifier measures current at zero bias at each wavelength for the solar cell and the reference diode separately. The reference diode is calibrated by Newport and used to determine the absolute illumination power at each wavelength. Thus, the EQE can be calculated by comparing the current measured by the reference diode and the solar cell at each wavelength. IQE is then calculated as the ratio of the EQE and η_A as a function of wavelength. Spectral reflectance of the full devices for IQE calculations was measured using a CARY 5000 Internal Diffuse Reflectance accessory with an integrating sphere and a polytetrafluoroethylene reference. The absorption (A) was calculated from reflectance (R) measurements, where $A = 1 - R$.

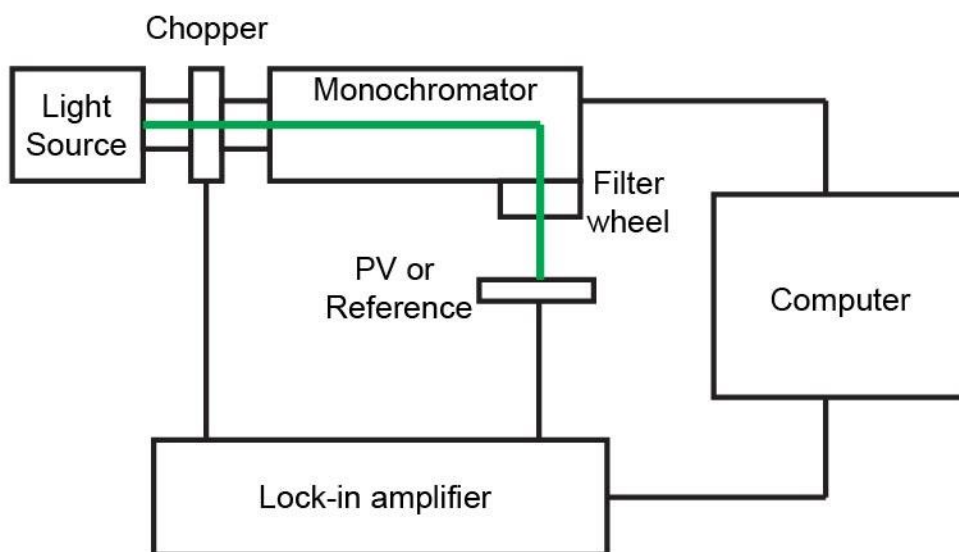


Figure 5.2. Schematic of external quantum efficiency measurement setup. The green line indicates the light pathway. The solar cell (PV) and reference photodiode are measured separately.

5.3 Scanning probe microscopy

The majority of solar cell characterization is done on macroscale samples or devices. For example, the efficiency of solar cells is measured by measuring the IV curve of a macroscale device; carrier behavior and lifetime is studied by measuring light emission on the macroscale; and carrier transport is measured by PL quenching or 4-point probe measurements on the macroscale. However, these measurements all assume that the property of the material measured is relatively homogenous. This assumption is most often not true, and as a result these measurements average over the material properties. Many solar cell materials are polycrystalline and have defects such as dislocations and point defects. Additionally, all solar cell devices consist of interfaces between materials. These inhomogeneities in the solar cell materials and devices are typically on length scales below 10 nm and need to be studied locally to be fully understood. Scanning probe microscopy (SPM) is ideally suited to capture these processes at their native length scales (162). SPM can provide information that will provide deeper understanding of solar materials to then develop materials based on knowledge rather than trial-and-error.

SPM is based on the concept of measuring interactions between a surface and a nano-scale sharp probe that is very close to, or in contact with, that surface. As it is applicable to this dissertation only specific AFM techniques will be discussed in detail. However, there are other useful scanning probe techniques for studying solar cell materials, including KPFM (163–167), spectroscopic imaging (142, 168), EBIC imaging (134, 169), and cathodoluminescence imaging (143, 170), but they will not be discussed here.

5.3.1 Forces in atomic force microscopy

In conventional AFM, the sharp AFM tip or probe, which has a radius of curvature between 2 and 50 nm, is used to measure long-range and short-range forces between the tip and the sample. The dominant long range-force is due to van der Waals forces that exist between atoms without a permanent dipole, which attract each other due to constantly fluctuating dipoles. The force between the tip and the sample is inversely proportional to the distance between the tip and sample squared. At tip-sample distances greater than 1 nm, the attractive van der Waals forces dominate (171). The short-distance force, at distances below 1 nm, is dominated by Pauli repulsion, in which electrons in inner electron shells of the atoms in the tip and the sample repel each other (172). Other forces include electrostatic, capillary, and magnetic forces. The tip-sample interaction is often modeled using the Lennard-Jones potential (shown in Figure 5.3a), which describes both the long-range attractive and short-range repulsive forces. The Lennard-Jones potential is then modified by incorporating the spring constant of the AFM cantilever, which is observed in the AFM force-distance curve (Figure 5.3b). Force-distance curves are measured by bringing the tip toward the sample until a set maximum force, and then pulling the tip away from the sample while measuring the deflection of the tip. The deflection is proportional to the force. This measurement is useful because it describes the stiffness of the cantilever, allows for determining a minimum setpoint for contact mode AFM, and defines the adhesion force between the tip and the sample, as shown in Figure 5.3b.

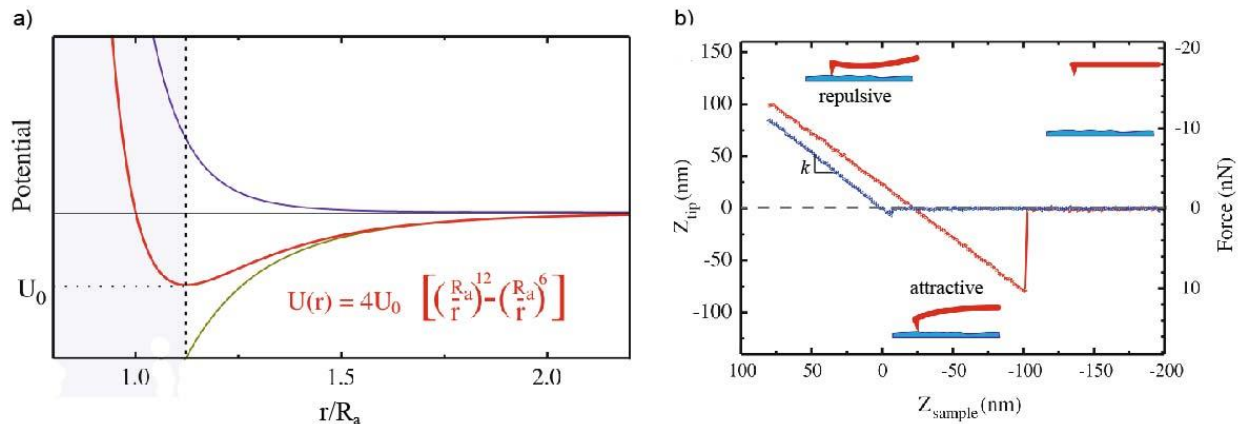


Figure 5.3. AFM tip-sample interactions. a) Lennard-Jones potential describes how the atoms in the tip interact with atoms in the sample as a function of distance. Adapted from Ref. (171). b) Force-distance curve for an AFM tip approaching (blue) and retracting (red) from the sample surface. Z_{tip} is the cantilever deflection and is proportional to the tip-sample force. Z_{sample} is the distance between the tip and the sample measured by the z-piezo. The diagrams inset in the curve show that the tip is in the attractive regime when the deflection is negative and repulsive when the deflection is positive. The spring constant, k , of the cantilever is the slope of the force-distance curve in the repulsive regime. Adapted from Ref. (173).

5.3.2 Atomic force microscopy instrumentation

To detect the tip-sample interaction forces and maintain a constant interaction between the tip and the sample, the AFM instrumentation is designed as follows and as shown in Figure

5.4. In contact mode AFM, the AFM tip sits at the end of a cantilever, which is reflective. A laser reflects off the end of the cantilever onto a four-quadrant photodiode. As the tip deflects to either approach or retract from the sample to maintain a constant interaction force with the sample, the cantilever bends and the reflection of the laser onto the photodiode changes position. The laser reflection position then indicates the height change in the sample topography. Either the tip or the sample will move such that the tip rasters across the area of interest of the sample to generate an image.

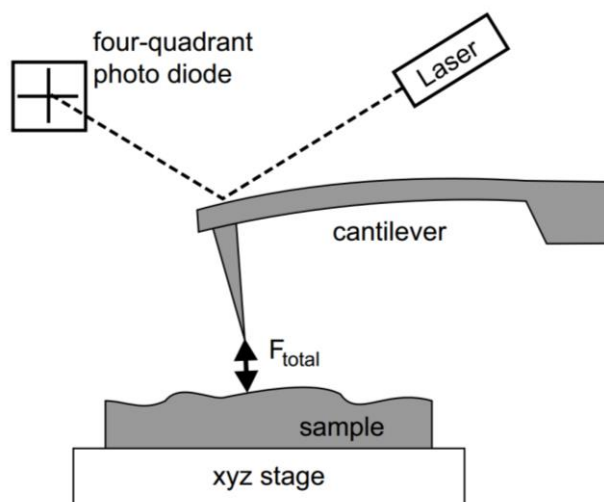


Figure 5.4. AFM instrumentation. The AFM tip is attached to a cantilever with a reflective surface. As the tip deflection changes based on the forces between the tip and the sample, the laser reflection from the cantilever will change position on the photodiode. The sample stage is rastered to form an image. From Ref. (174).

5.3.3 Primary atomic force microscopy scan modes

There are two primary modes of AFM operation: tapping and contact mode. Although, non-contact mode is often considered a third mode, it is often operated as tapping mode. In tapping mode, a piezoelectric element is used to mechanically oscillate the cantilever at a fixed frequency close to its resonance frequency and at a fixed amplitude. The tip oscillation is modified by the tip-sample interaction, which is detected by the photodiode; the forces between the tip and sample change the oscillation amplitude and the frequency of the cantilever (174). These changes are modeled as a damped oscillator. Thus, either the change in amplitude or frequency can be monitored such that the tip-sample distance is adjusted to maintain constant amplitude or frequency respectively. Tapping mode AFM is commonly used to measure surface roughness and topography on the nanoscale and has the advantage that there is minimal damage to the tip and the sample. Tapping mode also allows for phase imaging, where the phase lag between the cantilever driving oscillation and the actual cantilever oscillation is monitored (172). Phase lag is due to elasticity, adhesion, and friction; because these three properties often differ from material to material, two materials can be differentiated in the phase image. Phase image and topography images are measured in parallel, so surface properties can be directly correlated to the topography. Tapping mode AFM is often used to study organic BHJ solar cells to observe

DA phase separation using phase contrast imaging, as shown in Chapter 3. For inorganic solar cells, tapping mode AFM is often used to determine how substrate roughness and processing conditions effect film quality and efficiency (175, 176).

Contact mode, the other main AFM scan mode, measures the deflection of a static cantilever. To maintain a constant cantilever deflection, meaning a constant force between the tip and the sample, while the tip is scanning over the sample, the AFM tip height is adjusted and recorded to generate the topography image. In this scan mode, the tip is in the repulsive regime of the force-distance curve (Figure. 5.3b), so that it is fully in contact with the sample. Because the tip is fully in contact with the surface, large frictional forces can cause damage to the sample and the AFM tip. The sample, particularly if soft, can be indented by the tip. Also, the AFM tip will become blunt over time especially with hard samples. As a result, a minimum possible force to stay in the repulsive regime should be applied when measuring in contact mode. Soft, meaning less stiff, cantilevers are used for contact mode AFM. As shown in Figure 5.5, when an AFM tip approaches the sample, the tip will snap into contact with the sample when the gradient of the attractive force is larger than the stiffness of the cantilever. With a soft cantilever, there is a significant hysteresis in the height at which the tip retracts from the surface due to competition between adhesion and the force due to retracting the tip. Thus, the force for contact mode measurements can be reduced by applying a lower setpoint after the tip has snapped into contact (172). Another challenge in contact mode AFM is that the resolution is limited due to the large contact area that occurs between the tip and the sample when the tip is pressing into the sample surface. However, contact mode does provide very precise topography measurements because repulsive forces are very sensitive to tip-sample distance.

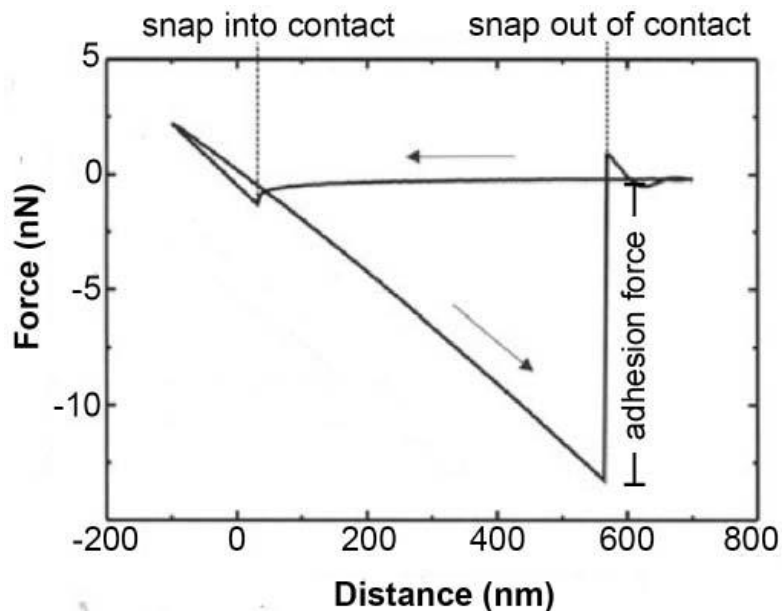


Figure 5.5. Force-distance curve for a soft cantilever used for contact mode measurements. On the approach, when the force gradient becomes greater than the stiffness of the cantilever, the tip snaps into contact with the sample. As the tip retracts, the tip snaps out of contact when the normal force is greater than the adhesion force. Adapted from Ref. (172).

5.3.4 Photoconductive atomic force microscopy

Contact mode AFM is useful for characterizing solar cells because it can be used to measure local current and photocurrent in conductive AFM (cAFM) mode. In cAFM (Figure 5.6), a conductive tip scans the sample in contact mode, a bias is applied between the tip and the sample, and a current amplifier is used to record the current collected at the tip; current is recorded at each pixel in the image. Because topography and current are simultaneously recorded in cAFM, local structure and morphology can be correlated to current generation and transport. The most commonly used conductive AFM tips are platinum coated silicon tips. However, gold coated silicon, platinum silicide, all platinum, and conductive diamond tips are also available for cAFM. Metal coated silicon tips are useful because they can be made with a small tip radius but the coating can wear off depending on the hardness of the sample. Metals tips are also useful because they have low resistance. Alternatively, platinum silicide and conductive diamond tips are useful because they are wear resistant, but they have a higher electrical resistance and larger tip radius. Another important consideration is the work function of the tip material compared to the material being measured especially when characterizing working solar cells. Although AFM is considered a surface technique, cAFM probes where the current flows, which is often in the depth of the material between the bottom contact and the AFM tip when measuring solar cells.

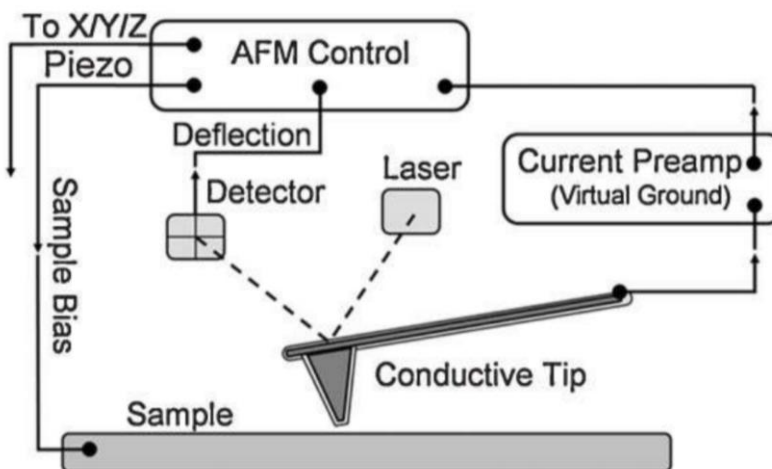


Figure 5.6. Conductive AFM instrumentation. cAFM operates in contact mode, where a constant deflection of the cantilever is maintained. A bias is applied between a conductive AFM tip and the sample. The current is measured through the AFM tip with a current preamplifier. Adapted from Ref. (177).

cAFM is often used to probe conductivity heterogeneity in nanostructured systems. For example, the behavior of grain boundaries in CIGS solar cells has been studied with cAFM (178–180). The study of grain boundaries is inherently challenging because current measured at grain boundaries can be greater simply due to the greater contact area on the sides of the tip when the tip is in the grain boundary. However, Sadewasser et al. carefully measured the dark current in CIGS solar cells and found that current at 50 mV was higher at the grain boundaries than in the grain interiors, as shown in Figure 5.7. The grain boundaries were identified from the topography image and the white circles indicate where the current corresponds to grain

boundaries. Because not all grain boundaries have high current, it is likely that the bright grain boundaries correspond to a specific orientation (180). Further studies on the orientation of the grains and grain boundaries in the same area measured by cAFM could provide valuable design information for higher efficiency solar cells.

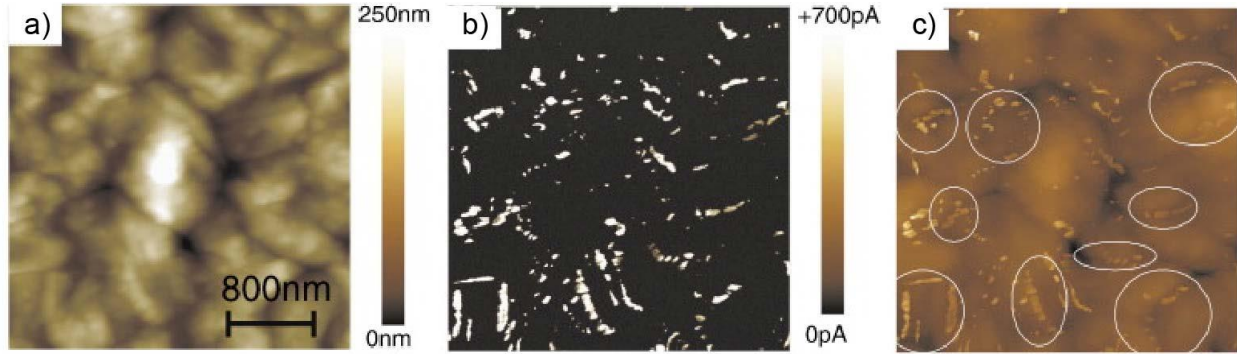


Figure 5.7. cAFM study of grain boundaries in CIGS solar cells. a) Topography b) dark current at 50 mV and c) overlay of dark current on topography images. The circles indicate where the high current corresponds to grain boundaries. Adapted from Ref. (180).

Photocurrent can be measured using cAFM by illuminating a solar cell without the top contact and selecting an appropriate AFM tip to act as the top contact. The sample can be illuminated in several different ways, as shown in Figure 5.8, and the light can either be focused or illuminate a large portion of the sample. Standard AFM tip geometries can be used for bottom and side illumination but a protruding tip, often referred to as an elephant tip, is required for top illumination to prevent shadowing (Figure 5.8b). Additionally, an objective with a 0.4 numerical aperture is ideal for top illumination because the light comes in at a 45 degree angle and prevents shadowing. The sample can be illuminated with a laser or with a white light source.

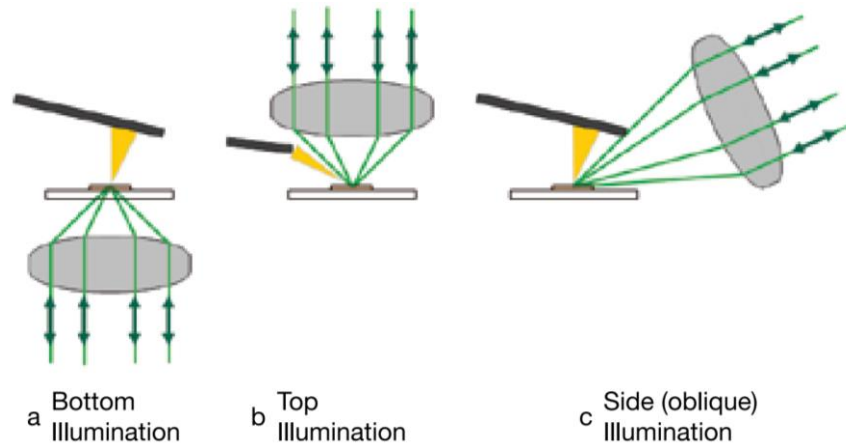


Figure 5.8. Illuminating a sample for photoconductive AFM. Three different types of illumination methods can be used: bottom (a), top (b), and side (c). From Horiba Scientific.

By illuminating the solar cell, I_{SC} can be measured directly at zero bias. Locally measuring photocurrent provides information about charge generation and collection at the

material's surface (181). Also, by sweeping the voltage at a specific position, an IV curve can be measured at the nanoscale. cAFM has been a very useful tool for studying OSCs, where morphology is strongly linked to efficiency (177, 182–185). Ginger and co-workers studied MDMO-PPV:PCBM BHJ solar cells with cAFM because it has previously been observed that the solar cell performance is highly dependent on processing solvent (57). In their cAFM measurements, the sample was illuminated from the bottom with a focused laser (532 nm) spot that has been aligned with the cAFM probe to generate high photocurrent and the Pt cAFM tip acts as the top electrode in the solar cell (186). As shown in Figure 5.9a, the MDMO-PPV:PCBM processed from xylene has topological features approximately of 100 nm, which correspond to PCBM crystallites in the BHJ (182). The photocurrent map reveals current heterogeneity over an order of magnitude (Figure 5.9b); the high current areas are not always associated with PCBM crystallites. To better characterize the film, local IV curves were measured at two different crystallites, square and triangle in Figure 5.9a,b, using cAFM (Figure 5.9c). From these IV curves and cross-sectional SEM images of the MDMO-PPV:PCBM films, Groves et al. conclude that the photocurrent heterogeneity in the PCBM crystallites is due to their vertical position in the BHJ film: if the PCBM crystallite is at the bottom of the film, electron transport to the AFM tip is hindered by low mobility (186). This cAFM study demonstrates the usefulness of electrically probing solar materials on the nanoscale for providing information to improve solar cell design.

SPM is a powerful technique for characterizing solar cells on the nanoscale. Understanding nanoscale properties of solar cells helps to establish the relationships between processing conditions, morphology, and performance. Specifically, AFM and cAFM are useful for characterizing nanostructured solar cell materials such as polycrystalline inorganic solar cells, polycrystalline perovskite solar cells, and BHJ OSCs.

I worked to establish a unique approach-retract scan mode, also known as PinPoint mode developed by Park Systems, for cAFM. Although it is possible to use traditional contact mode AFM to measure photocurrent in soft materials systems such as organic semiconductor films (Figure 5.9), significant challenges arise due to the frictional forces between the AFM tip and the sample as the tip scans across the surface. In the approach-retract scan mode, all friction is eliminated because at each pixel the tip slowly approaches the sample until a specified force between the tip and the sample is reached, then the current and height are recorded, and finally the tip retracts before it moves to the next pixel. When measuring hybrid halide perovskite solar cells this technique was necessary to achieve accurate reproducible images of photocurrent because traditional cAFM current images were ridden with measurement artifacts. The approach-retract scan mode is described in detail in Chapter 10.

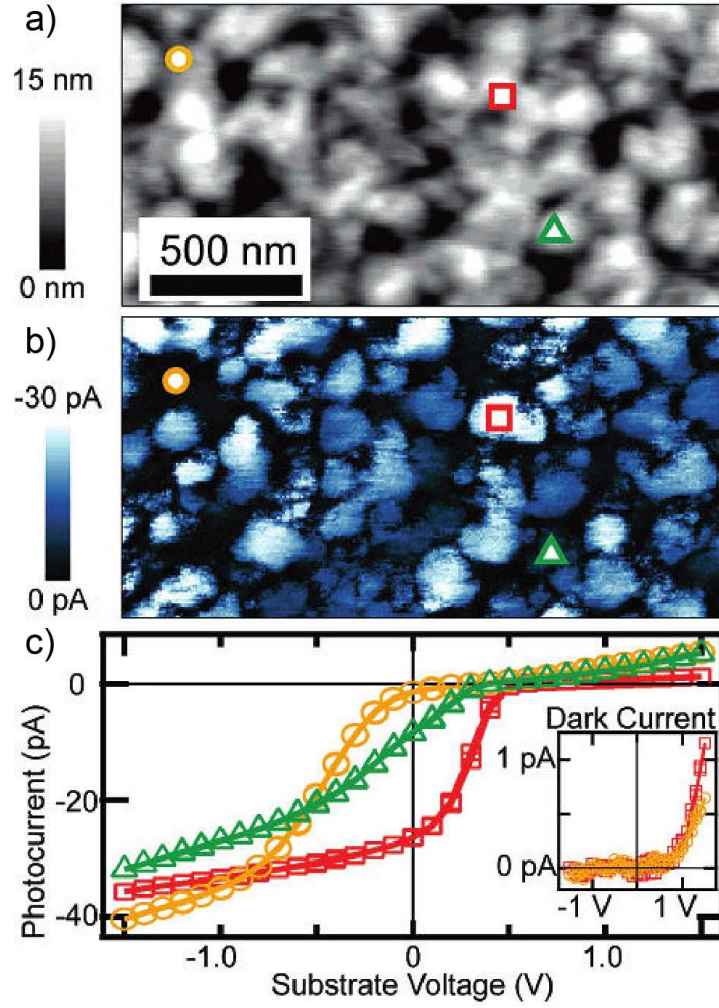


Figure 5.9. cAFM characterization of MDMO-PPV:PCBM BHJ solar cells. a) Topography image of the MDMO-PPV:PCBM film. b) I_{sc} map measured simultaneously with the topography image. A 532 laser was used to illuminate the sample from the bottom. c) IV curves measured locally at the points (circle, square, triangle) marked in the topography and current maps. The inset shows the dark current measurements in those areas. Adapted from Ref. (186).

Exciton manipulation in organic solar cells

Chapter 6

Solution processable azadipyrromethene electron donors for planar heterojunction solar cells

Adapted from Ref (187):

Sibel Y. Leblebici, Luis Catane, David E. Barclay, Tara Olson, Teresa L. Chen, Biwu Ma, *ACS Applied Materials & Interfaces* 2011, **3**, 4469-4474

6.1 Introduction

Previously small molecules, based on dyes, were thermally evaporated, but, by adding solubilizing groups to the small molecules, they can be designed to be solution processable. When developing a new molecule for high efficiency solar cells, the design should allow for simultaneously high J_{SC} and V_{OC} . Since the light harvesting capability of the organic semiconductors represents one of the major factors in determining the J_{SC} , low bandgap materials with high absorption coefficients and strong spectral overlap with solar irradiation are desired (24). For this reason, a variety of near-infrared organic dyes have been explored for OSCs, including phthalocyanines (188–190), subphthalocyanines (191), merocyanines (192), squareaines (193), isoindigos (194, 195), borondipyrromethenes (196), and diketopyrrolopyrroles (197). On the other hand, the V_{OC} is generally considered to be controlled by the energy offset (ΔE_{DA}) between the HOMO of the donor and the LUMO of the acceptor (59), as well as the morphological properties of the DA interface (198). It is not trivial to maintain a high V_{OC} for solar cells with near-infrared materials, or to achieve high J_{SC} and V_{OC} simultaneously, as the reduced bandgap of electron donors often results in lower ΔE_{DA} .

This chapter describes a series of solution processable azadipyrromethene based small molecules, i.e. azadipyrromethene (ADPM), B,F₂-chelated azadipyrromethene (BF₂-ADPM) and B,O-chelated azadipyrromethene (BO-ADPM), used in OSCs for the first time. Due to their facile synthesis, high solubility, high stability, and exceptional photophysical properties with high absorption coefficients ($\sim 10^5 \text{ M}^{-1} \text{ cm}^{-1}$) and fluorescence quantum yields in the near-infrared region (199–201), ADPM based organic dyes have previously been exploited in a diverse range of material and biological applications, such as photosensitizers for photodynamic therapy (202, 203), fluorescent probes for biological imaging (204, 205) and as laser dyes (206). By using these near-infrared dyes as electron donors and C₆₀ as the acceptor, I constructed efficient planar heterojunction OSCs. Of particular interest is the BO-ADPM/C₆₀ bilayer device exhibiting PCEs up to 2.63%, which is attributed to the photocurrent generation into the near-infrared spectrum of up to 845 nm while maintaining high V_{OC} of $\sim 0.8 \text{ V}$.

6.2 Materials and instrumentation

The three ADPM compounds, shown in Figure 6.1, were synthesized following the procedures reported in literature (202, 204). All the reactants and solvents were purchased from either Aldrich or Alfa Aesar, and were used as received. ¹H-NMR measurements were recorded using Bruker Biospin Avance II 500 MHz NMR Spectrometer. Elemental analysis was carried out in a Perkin-Elmer 2400 Series II combustion analyzer. Figure 6.2 shows the synthetic scheme.

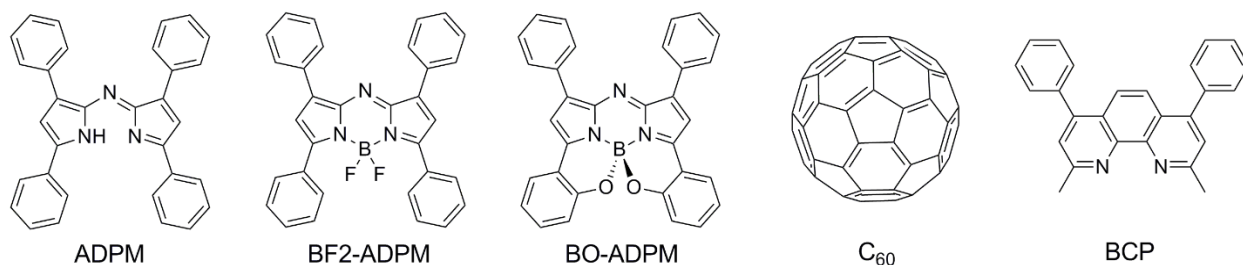


Figure 6.1. Chemical structures of the ADPM dyes and molecules used in OSCs.

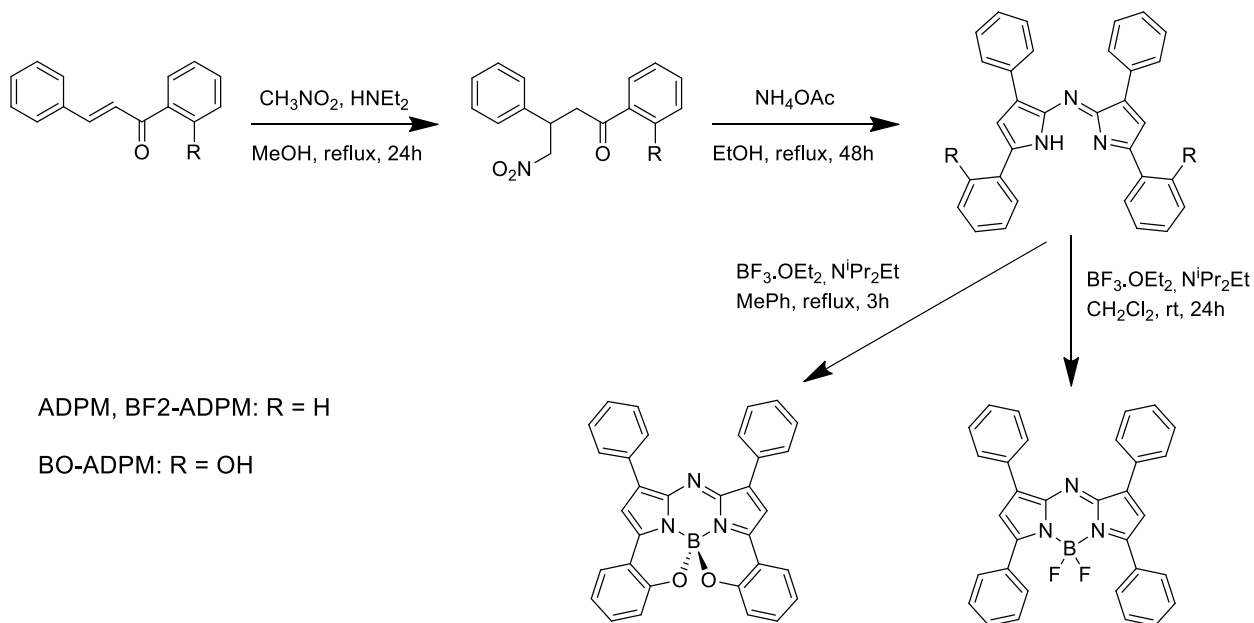


Figure 6.2. Synthesis of ADPM molecules and their boron chelated compounds.

Pre-patterned ITO-coated glass substrates were purchased from Thin Film Devices Inc. Sublimed grade C₆₀ and bathocuproine (BCP) were purchased from Aldrich (Figure 6.1). PEDOT:PSS (Baytron PH 500) was purchased from H. C. Starck. UV-Vis measurements of materials in solution and in film form were conducted with a CARY 5000 UV-Vis-NIR spectrophotometer. Film thickness was measured using a Dektak 150 profilometer. Cyclic voltammetry was performed using a Solartron 1285 potentiostat, wherein a platinum wire acts as the working and counter electrode and a silver wire as the reference electrode. Samples were prepared in dichloromethane solution with 0.1 M tetrabutylammonium hexafluorophosphate as the electrolyte at a scan rate of 100 mV s⁻¹. AFM images were taken on a Veeco Nanoscope V scanning probe microscope in tapping-mode.

6.3 Device fabrication

OSCs were fabricated in a planar heterojunction structure of ITO/PEDOT:PSS/ADPM donor/C₆₀/BCP/Ag. ITO-coated glass substrates were cleaned by successive sonication in soap solution, deionized water, acetone and isopropanol for 15 min at 40 °C and UV ozone cleaned for 10 min. A ~ 40 nm thick PEDOT:PSS layer was prepared by spin casting its aqueous solution onto the cleaned ITO-coated glass substrates at 4000 rpm for 40 s and baked at 140 °C for 20

min. ADPM, BF₂-ADPM, and BO-ADPM were dissolved in chlorobenzene at a concentration of 4 mg/mL. Additionally, BO-ADPM was dissolved in tetrahydrofuran (THF) at 2 mg/mL. All solutions were passed through a 0.2 μm polytetrafluorethylene filter prior to being spin-coated onto the PEDOT:PSS film at 2000 rpm for 60 s. Subsequently, the C₆₀ (45 nm), BCP (10 nm), and Ag (100 nm) were thermally evaporated under high vacuum ($\sim 2 \times 10^{-6}$ mbar) at rates of 1.5, 1.5 and 4 \AA s^{-1} , respectively. The BCP layer acts to block excitons and transport electrons (23). The Ag electrodes defined the devices with a shadow mask of 0.03 cm^2 in area. Hole-only devices were fabricated with the structure of ITO/PEDOT:PSS/ADPM donor/Au. The hole-only devices were used to study hole mobility via the SCLC method.

6.4 Material properties

The solution UV-Vis absorption spectra were recorded in chlorobenzene for all three molecules and also in THF for BO-ADPM (Figure 6.3a). Their corresponding thin film absorption spectra are shown in Figure 6.3b, which were measured on ITO/PEDOT:PSS coated glass substrates. I found that all three ADPM molecules display extremely high extinction coefficients, reaching up to $\sim 1.7 \times 10^5 \text{ M}^{-1} \text{ cm}^{-1}$ in solution and $\sim 1.5 \times 10^4 \text{ cm}^{-1}$ in thin film. Also, significant broadening and a bathochromic shift of the absorption peaks in the thin film were observed, which is considered to be the result of strong molecular π - π interactions due to the flat molecule structures. The red shift of the absorption spectra from ADPM to BF₂-ADPM and BO-ADPM is attributed to the electron-withdrawing nature of the B,F₂ (207) and B,O chelates, as well as the intramolecular B-O ring formation (204). It is worth highlighting that BO-ADPM absorbs in the near-infrared region up to $\sim 800 \text{ nm}$ in solution and $\sim 850 \text{ nm}$ in the thin film regardless of the solvent used. The optical bandgaps for the three materials were determined from the onset of the thin film absorption spectra, which are 1.70 eV for ADPM, 1.59 eV for BF₂-ADPM, and 1.47 eV for BO-ADPM.

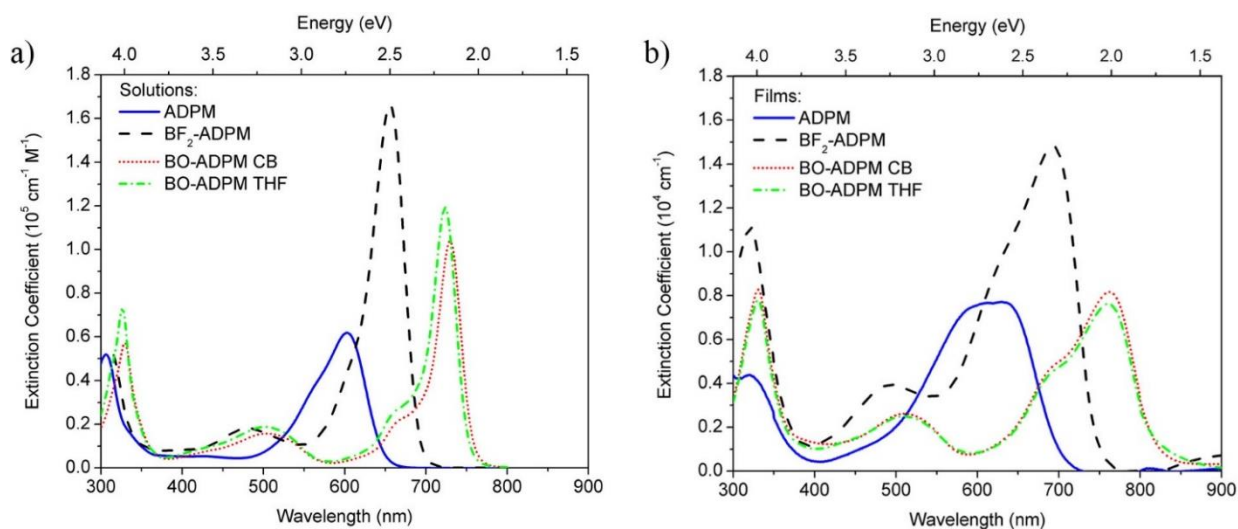


Figure 6.3. Extinction coefficients of ADPM, BF₂-ADPM, and BO-ADPM (a) solutions in and (b) thin films spin cast from chlorobenzene (CB) and THF solvents. The extinction coefficients in the thin films are approximately 10 times smaller than in solution.

Cyclic voltammetry was used to investigate the electrochemical properties of this family of molecules. The cyclic voltammetry curves for the three molecules are shown in Figure 6.4. The oxidation and reduction potentials relative to an internal ferrocene/ferrocenium redox couple

(- 4.8 eV vs. vacuum) translates to electrochemical bandgaps of 1.88 eV, 1.74 eV, and 1.46 eV for ADPM, BF2-ADPM and BO-ADPM, respectively. The trend observed in the electrochemical bandgap values for the three compounds corresponds well to that for the optical bandgaps.

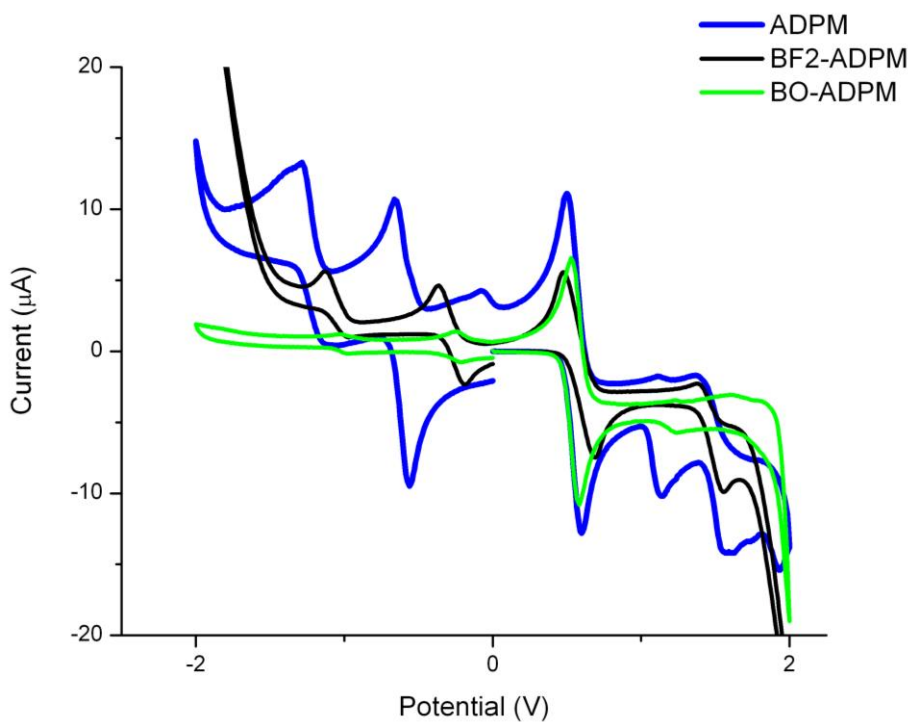


Figure 6.4. Cyclic voltammetry curves for ADPM, BF2-ADPM, and BO-ADPM.

The HOMO and LUMO levels were estimated to be - 5.38 eV and - 3.50 eV for ADPM, - 5.68 eV and - 3.94 eV for BF2-ADPM, and - 5.48 eV and - 4.02 for BO-ADPM. The resulting energy level diagram is shown in Figure 6.5. DFT calculations were performed with the Spartan'08 software package using the B3LYP hybrid functional and the 6-31*G basis set to investigate the electronic properties of these sensitizers. The orbital energy levels in vacuum, minimum energy conformations, and electron density plots are shown in Figure 6.6. The calculations predicted quite consistent results for the energy levels and bandgaps. The HOMO and LUMO levels of these molecules suggest their suitable application as electron donors in OSCs with C₆₀ as the acceptor, which has a HOMO of - 6.2 eV and a LUMO of - 4.5 eV (23).

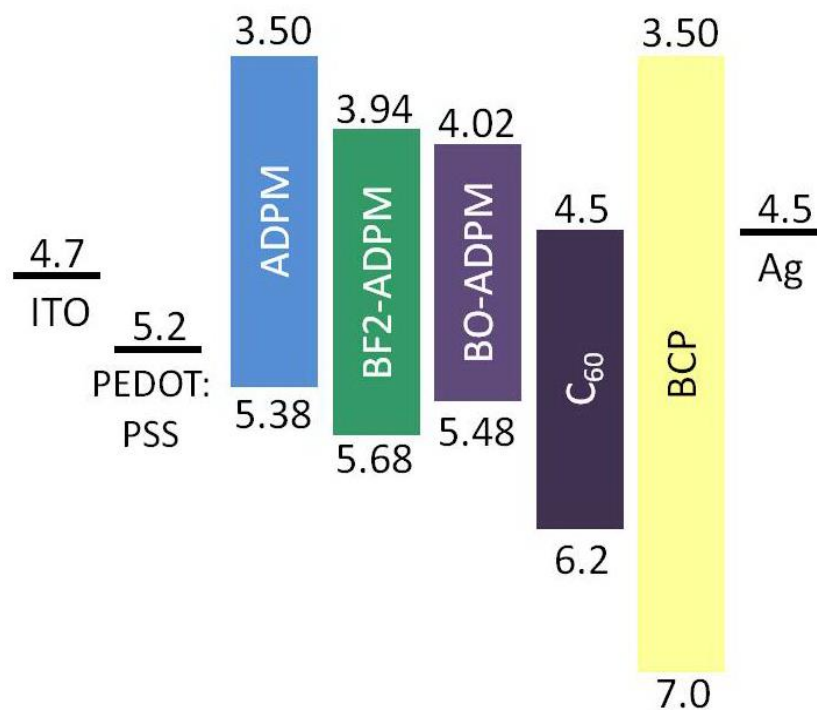


Figure 6.5. Schematic energy levels of organic thin films and electrodes determined from cyclic voltammetry.

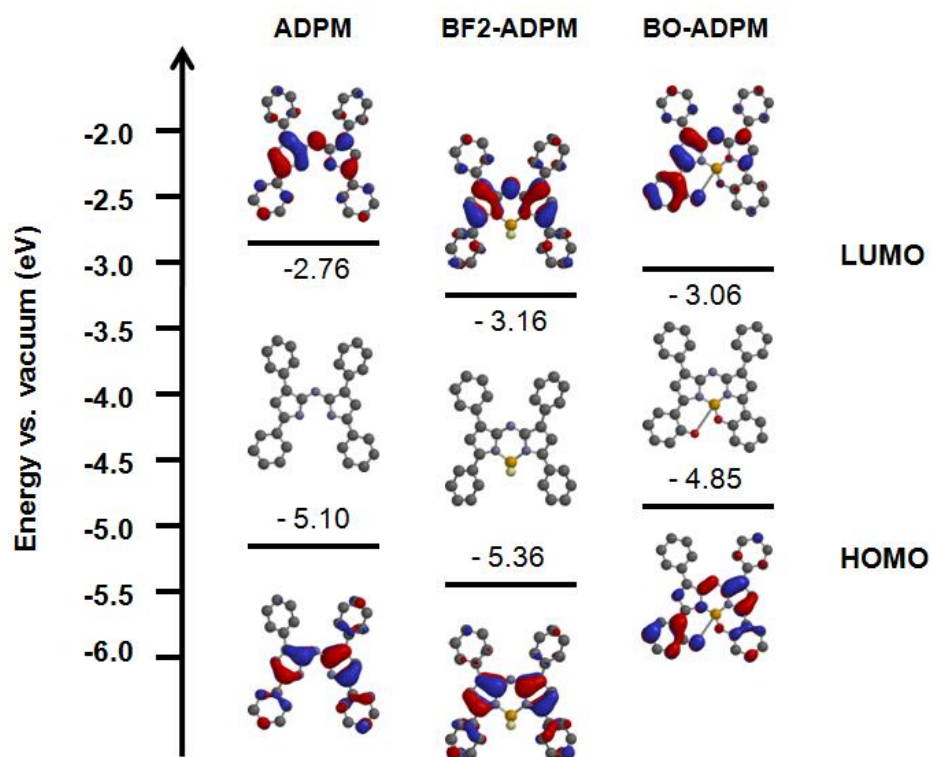


Figure 6.6. HOMO and LUMO surface plots and energy levels calculated via DFT for ADPM, BF2-ADPM, and BO-ADPM.

The hole carrier mobility of the ADPM films was evaluated by SCLC measurements. The SCLC hole-only devices were fabricated with the structure of ITO/PEDOT:PSS/ADPM film/Au, wherein the ADPM films were prepared by spin casting chloroform solutions of ADPM and BF2-ADPM, and chlorobenzene and THF solutions of BO-ADPM. Chloroform was used for ADPM and BF2-ADPM to ensure sufficiently thick films needed for SCLC measurements (> 100 nm). The resulting SCLC hole mobility values are shown in Table 6.1. Thin films of ADPM and BF2-ADPM prepared from chloroform solutions, and BO-ADPM from chlorobenzene solution exhibit very similar mobility values of $1\text{--}2 \times 10^{-4} \text{ cm}^2 \text{ V}^{-1} \text{ s}^{-1}$. While a lower hole mobility of $2.88 \times 10^{-5} \text{ cm}^2 \text{ V}^{-1} \text{ s}^{-1}$ was obtained for BO-ADPM thin films processed in THF. This difference in hole mobility indicates distinct film morphologies for the films prepared via various solvents. It is very likely that the BO-ADPM film from THF is amorphous and the film from chlorobenzene has more crystalline features (198).

Table 6.1. ADPM molecule properties: Photophysical, electrochemical and electronic properties of three ADPM molecules and their thin films.

Compounds	Solution absorption peak (nm) and intensity ($10^5 \text{ M}^{-1} \text{ cm}^{-1}$)	Film absorption peak (nm) and intensity (10^4 cm^{-1})	Film absorption onset (nm)	Film optical bandgap (eV)	HOMO (eV)	LUMO (eV)	Electrochemical bandgap (eV)	Hole mobility ($\text{cm}^2 \text{ V}^{-1} \text{ s}^{-1}$) ^a
ADPM	603, 0.62	627, 0.77	729	1.70	-5.38	-3.50	1.88	1.92×10^{-4}
BF2-ADPM	656, 1.66	693, 1.48	782	1.59	-5.68	-3.94	1.74	1.49×10^{-4}
BO-ADPM	724, 1.19	761, 0.76	845	1.47	-5.48	-4.02	1.46	1.57×10^{-4} (2.88×10^{-5}) ^a

^aFilm processed with THF

The surface morphology of the thin films was studied with tapping mode AFM. Thin films were prepared via spin casting chlorobenzene solutions of all three compounds with an additional BO-ADPM film prepared from THF. The two BO-ADPM and the BF2-ADPM films exhibit uniform and smooth morphologies with root-mean-square (rms) roughness values of 0.29 nm for BF2-ADPM from chlorobenzene (Figure 6.7b), 0.32 nm for BO-ADPM from chlorobenzene (Figure 6.7c), and 0.40 nm for BO-ADPM from THF (Figure 6.7d). In contrast, ADPM forms large crystallites (Figure 6.7a) such that the surface is very rough with rms roughness of 5.7 nm.

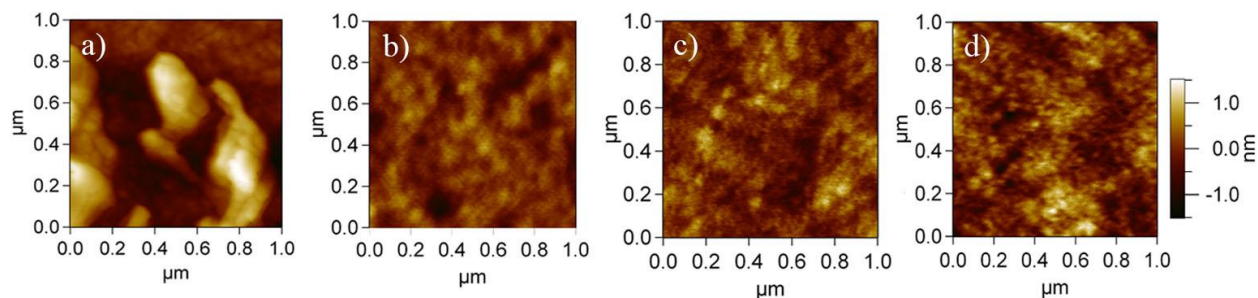


Figure 6.7. Tapping mode AFM images of spin cast films of a) ADPM from chlorobenzene, b) BF2-ADPM from chlorobenzene, c) BO-ADPM from chlorobenzene, and d) BO-ADPM from THF. The height scale for image (a) is 10 times the scale bar.

6.5 Organic solar cells

Simple planar heterojunction solar cells were fabricated with solution processed ADPM thin films as electron donors and vapor deposited C₆₀ as the electron acceptor. As shown in Figure 6.8a, the resulting device structure was ITO/PEDOT:PSS(40 nm)/Donor(8-15 nm)/C₆₀ (45 nm)/BCP(10 nm)/Ag(100 nm).

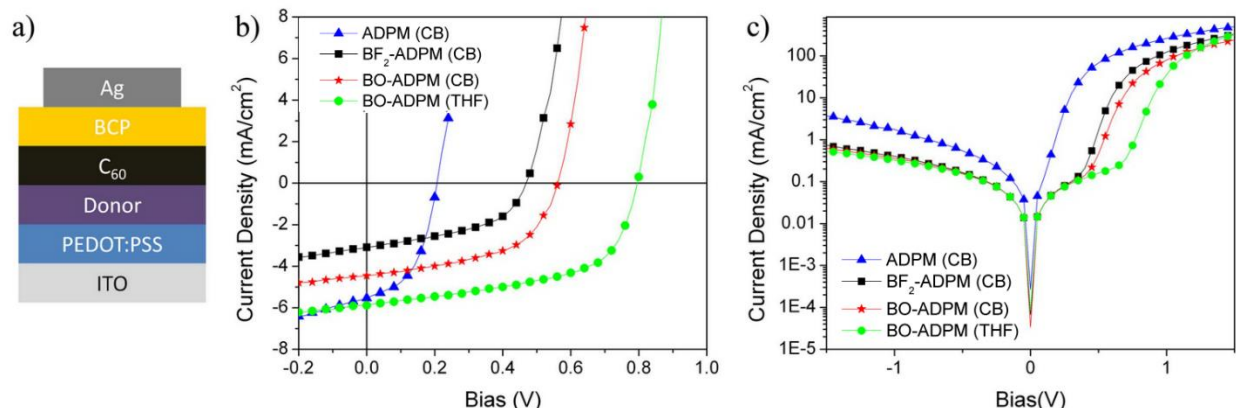


Figure 6.8. Planar heterojunction OSCs with ADPM small molecules. Schematic device architecture (a), J - V characteristics of devices (b) under AM 1.5G simulated 1 sun solar illumination, and (c) in the dark. CB denotes the use of chlorobenzene.

I optimized the device performance by changing the solvents used and the solution concentrations for ADPM donor molecules. The solution processed donor layers were prepared via spin casting solutions at 2000 rpm for 60 s, such that the film thickness was controlled by the solution concentration. I obtained the best performing device with a PCE of 2.63%, wherein the donor layer of ~ 14 nm thick BO-ADPM was prepared from 2 mg/mL solution in THF. In addition, the best ADPM, BF₂-ADPM, and BO-ADPM devices fabricated from chlorobenzene solutions showed PCEs of 0.56, 0.69%, and 1.32% respectively. All devices were negatively affected by thermal annealing.

Figure 6.8b shows J - V curves for the four devices under AM 1.5G simulated solar illumination with an intensity of 100 mW cm⁻². The device characteristics are shown in Table 6.2. As far as the V_{OC} is concerned, the ADPM device exhibited the lowest value, which is consistent with its high HOMO level among three compounds (208). Additionally, the highly crystalline morphology of the ADPM film could result in strong molecular interactions between ADPM and C₆₀ at the DA interface, resulting in enhanced charge recombination (198). Under conditions of high recombination, the forward bias current is high, which results in a reduced V_{OC} . The dark current depends on the recombination in the device. Indeed, the highest dark current density for the ADPM device shown in Figure 6.8c supports our explanation. Compared to the ADPM device, the BF₂-ADPM device exhibited higher V_{OC} and lower J_{SC} , due to the much higher ΔE_{DA} and lower η_{ES} of BF₂-ADPM/C₆₀ (208).

Table 6.2. Device performance characteristics for planar heterojunction solar cells with ADPM donors

Donor layer	Thickness (nm)	V_{oc} (V)	J_{sc} (mA/cm ²)	FF	PCE (%)	Average PCE (%) ^a
ADPM (CB) ^b	8.5	0.207	-5.53	0.487	0.56	0.54
BF2-ADPM (CB)	11.1	0.469	-3.088	0.475	0.69	0.66
BO-ADPM (CB)	12.3	0.562	-4.456	0.527	1.32	1.26
BO-ADPM (THF)	14.3	0.796	-5.882	0.562	2.63	2.53

^a. At least three devices were tested
^b. CB denotes chlorobenzene

For the devices processed with chlorobenzene, the ADPM device showed much higher J_{sc} than the other two donors, although ADPM has the largest bandgap with lowest spectral overlap with solar irradiation. To gain a better understanding of the difference in J_{sc} , I measured EQE spectra for the devices with different donor layers (Figure 6.9). The photocurrent generation for all devices is shown across a broad spectrum up to the near-infrared region, which matches well with the thin film absorption spectra as shown in Figure 6.3b. The low EQEs of $\leq 20\%$ are very typical for planar heterojunction structured OSCs (209). I found that the ADPM/ C_{60} devices exhibited much higher EQE than the other donors. This is not surprising because ADPM/ C_{60} has the highest $\Delta LUMO$, resulting in the highest η_{ES} . Additionally, the less flat molecular structure of ADPM than other molecules could afford larger donor/acceptor distance in the bilayer interfaces leading to higher η_{ES} and subsequently higher J_{sc} (210). It is worth mentioning that the EQE spectra past 800 nm were not measured, due to limitations in our setup.

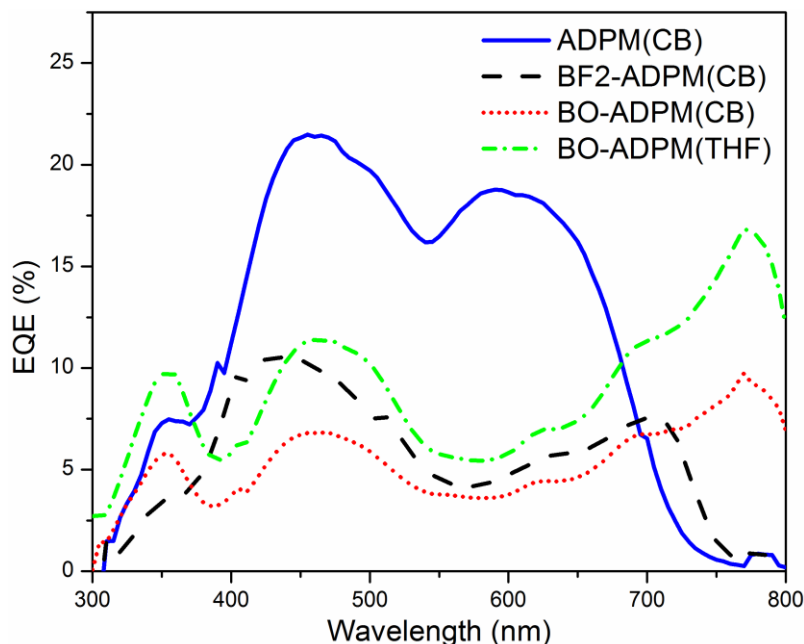


Figure 6.9. EQE spectra for ADPM donor based devices. CB denotes chlorobenzene.

The BO-ADPM device is the most interesting because it has much higher performance than ADPM and BF2-ADPM devices. Also, the device characteristics show a strong dependence on the processing solvent. Both the V_{oc} and J_{sc} increase significantly as a result of changing the

processing solvent from chlorobenzene to THF. As demonstrated previously, a higher boiling point solvent affords improved molecular stacking and strengthened molecule interactions after spin-casting (211–214). In our case, stronger molecular interactions are believed to be present in the thin film processed by chlorobenzene with a boiling point of 131 °C than in the thin film processed by THF with boiling point of 66 °C. The increase in molecular interactions by processing with chlorobenzene is well supported by the increase in hole mobility by an order of magnitude compared to the mobility in films processed from THF. The better alignment of BO-ADPM molecules in the chlorobenzene processed thin film could lead to stronger BO-ADPM/C₆₀ interactions at the DA interface, resulting in higher dark current, compared to processing from THF, as shown in Figure 6.8c. Ultimately, the BO-ADPM device processed with THF possesses weak DA interactions at the interfaces, low dark current, and subsequently high V_{OC} (198), as well as low CT state energy allowing for high η_{ES} and subsequently high J_{SC} (210). Our findings are consistent with observations in other molecular systems, and suggest that obtaining high J_{SC} and V_{OC} simultaneously is possible with control of the thin film electronic and morphological properties (198).

6.6 Conclusions

In conclusion, I demonstrated efficient planar heterojunction OSCs with small molecular weight azadipyrromethenes, a new family of solution processable near-infrared donor materials with high extinction coefficients and broad spectral absorption into the near-infrared region. Of particular interest, a high V_{OC} of ~ 0.8 V has been realized for the BO-ADPM/C₆₀ devices with photocurrent generation up to 850 nm. A PCE of 2.63% is among the highest values for planar heterojunction solar cells with solution processed near-infrared donor layers. In 2011, when the research presented in this chapter was published, the highest PCE for a solution processable small molecule solar cell was approximately 5% (215, 216). This work clearly shows the great potential of the application of ADPM based molecules in OSCs.

Although the efficiency of the BO-ADPM/C₆₀ solar cell is high for a near-infrared donor-fullerene bilayer device, the EQE remains below 20%. Low EQE suggests that many inefficiencies remain within the device. The absorption of visible light is already high because of the optimal bandgap and the large extinction coefficient. I tried enhancing exciton diffusion to the DA interface by fabricating BHJs solar cells composed of BO-ADPM and PCBM. But, these devices had very low performance due to poor phase separation; BO-ADPM is amorphous, which limits control over phase separation. The carrier mobility in BO-ADPM is low, even when processing films from chlorobenzene. Thus, based on this preliminary study of BO-ADPM, I was interested in improving the overall PCE and EQE by enhancing η_{ES} . Increasing η_{ES} is often overlooked as a method of increasing PCE, but it also allows new photophysical mechanisms to be studied in organic semiconductors. The strategy to enhance η_{ES} is discussed in the next chapter.

Chapter 7

Increasing organic solar cell efficiency by increasing permittivity to reduce exciton binding energy

Adapted from Ref (217):

Sibel Y. Leblebici, Teresa L. Chen, Paul Olalde-Velasco, Wanli Yang, Biwu Ma. *ACS Applied Materials & Interfaces* 2013, 5, 10105-10110.

7.1 Introduction

As discussed in Chapter 3, organic semiconductors generate Frenkel excitons with relatively high E_{eb} due to their low dielectric constant, the presence of significant electron-lattice interactions, and electron correlation effects (30, 218). The excitons that diffuse to the DA interface separate into free carriers provided that $\Delta LUMO$ is sufficient to overcome E_{eb} (26, 219, 220): η_{ES} is a function of the difference between E_{eb} and $\Delta LUMO$ (60). Thus, a sufficiently large $\Delta LUMO$ is needed for efficient exciton separation; however, a large $\Delta LUMO$ is undesirable because it results in low V_{OC} (59). By reducing E_{eb} , high η_{ES} and large V_{OC} can be simultaneously achieved. Approaches to increase η_{ES} include adding ferroelectric polymers to the BHJ (65, 66), applying an external electric field (77), and p-type doping (67).

Because E_{eb} is directly related to the Coulombic potential between the electron and hole,

$$E_{eb} = e^2/4\pi\epsilon_0\epsilon_r a$$

where e is the elementary charge, ϵ_0 is the permittivity of vacuum, ϵ_r is the permittivity of the material, and a is the distance between the electron and hole, increasing the permittivity is one strategy to reduce E_{eb} . To this end, Engel et al. have demonstrated an increase in free carrier generation in pentacene as a result of depositing it on high dielectric constant substrates (221) and determining methods to increase the permittivity of organic semiconductors has become increasingly important to pushing the limits of OSCs (60, 222). In this chapter, I demonstrate a simple approach to lowering E_{eb} in organic thin films by blending BO-ADPM with a high dielectric constant molecule, camphoric anhydride (CA). The reason BO-ADPM was used in this study is three-fold. BO-ADPM has intense broad absorption and a narrow band gap of 1.5 eV, which affords photocurrent generation in the near-infrared region when coupled with the acceptor C_{60} (187), as reported in the previous chapter. Also, the EQE values of the BO-ADPM/ C_{60} system are low, which is partially due to the insufficient $\Delta LUMO$ to overcome E_{eb} , leading to a low η_{ES} . Finally, because BO-ADPM is a small molecule that forms amorphous films, I expect CA and BO-ADPM to be miscible. This system therefore serves as a model platform to study the effect of film permittivity on E_{eb} and η_{ES} in OSCs.

7.2 Materials and methods

The molecular structures of BO-ADPM and CA are shown in Figure 7.1a and the band gap alignment for the OSC is shown in Figure 7.1b. The CA energy levels were calculated using DFT. DFT calculations were performed with the Spartan'08 software package using the B3LYP hybrid functional and the 6-31*G basis set.

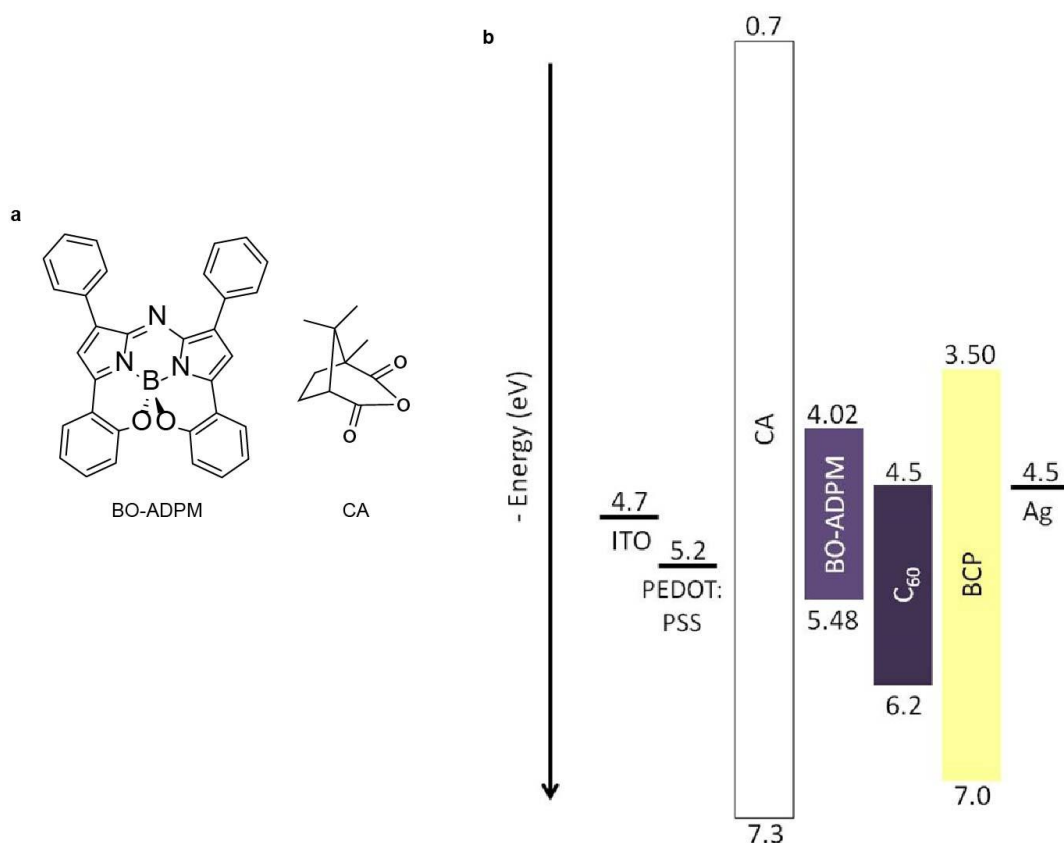


Figure 7.1. Structures and energy levels of materials used in high permittivity OSCs. a) Molecular structures of the donor material BO-ADPM and highly polar molecule CA. b) Energy level schematic of organic thin films and electrodes relative to vacuum.

The synthesis and characterization of BO-ADPM has been reported in the previous chapter (187). Polystyrene (PS), CA, sublimed grade C₆₀, and BCP were purchased from Aldrich. Pre-patterned ITO-coated glass substrates were purchased from Thin Film Devices Inc. PEDOT:PSS (Baytron PH 500) was purchased from H. C. Starck. BO-ADPM:CA films were prepared by spin-casting mixtures of BO-ADPM and CA dissolved in THF at the appropriate ratios to create films with 10, 20, 30, 40, and 50 weight percent (wt%) CA. OSCs were fabricated in a planar heterojunction structure of ITO/PEDOT:PSS(30 nm)/BO-ADPM:CA(20 nm)/C₆₀(35 nm)/BCP(8 nm)/Ag(100 nm). Control devices had a similar structure of ITO/PEDOT:PSS/BO-ADPM:PS/C₆₀(35 nm)/BCP(8 nm)/Ag(100 nm).

Devices were fabricated in the following steps. ITO-coated glass substrates were cleaned by successive sonication in soap solution, deionized water, acetone, and isopropanol for 15 min at 40 °C and UV ozone cleaned for 10 min. PEDOT:PSS was spin-cast onto the cleaned ITO-coated glass substrates and baked at 140 °C for 20 min. BO-ADPM:CA and BO-ADPM:PS solutions in THF (2 mg/mL) were spin-coated onto the PEDOT:PSS film at 2000 rpm for 60 s. Subsequently, C₆₀, BCP, and Ag were thermally evaporated under high vacuum ($\sim 2 \times 10^{-6}$ mbar) at rates of 1, 1, and 2 Å s⁻¹, respectively. The Ag electrodes defined the devices with a shadow mask of 0.03 cm² in area. To observe shifts in the optical band gap in the absence of BO-ADPM aggregation effects, PS:CA matrix films of varying weight ratios were doped with a constant

wt% of BO-ADPM. The films were prepared by spin-casting BO-ADPM:CA:PS solutions in mixtures of 10, 20, 30, 40, and 50 CA wt% with 0.05 wt% BO-ADPM.

Permittivity was measured via impedance spectroscopy of parallel plate capacitors with the structures ITO/BO-ADPM:CA or PS:CA:BO-ADPM (~200 nm)/Au(70 nm) using a Solartron SI 1260 Impedance – Gain/phase Analyzer at an AC level of 0.1 V and no DC bias. The imaginary impedance, $\text{Im}(Z)$, was measured as a function of frequency, f . The permittivity was calculated from the following equation,

$$\epsilon_r(f) = \frac{d}{A\epsilon_0} \frac{-1}{2\pi f \cdot \text{Im}(Z)}$$

where ϵ_0 is the permittivity of vacuum, A is the capacitor area, and d is the distance between the two electrodes.

XES and XAS measurements were conducted at the Advanced Light Source undulator beamline 8.0.1. BO-ADPM:CA films (100 nm) were formed by spin-casting solutions onto Si substrates. We performed a comparative study to address radiation damage concerns. Reliable data were collected with the samples cooled to 90 K by liquid nitrogen and a defocused x-ray beam with a minimum photon dose. In particular, for the lengthy XES measurements, samples were kept itinerant with a programmed motor on a stable cryostat, to prevent the x-ray beam from remaining stationary on the sample surface. Additionally, XAS was remeasured on a spot along the itinerant path of the sample motion after the XES measurement to confirm the samples are free of radiation damage. XAS spectra were collected in both total electron and total fluorescence yield modes, which correspond to a probe depth of several nm and ~ 100 nm, respectively. XES spectra were collected through a Rolland circle soft x-ray spectrometer. The experimental resolution of XES and XAS is about 200 and 80 meV respectively, but the energy position of the spectral leading edges are defined with much better precision, which is typical for soft x-ray spectroscopy. The XES and XAS data shown are normalized to collection time and photon flux monitored by a clean gold mesh. Excitation energy for performing the XES experiments was high above the absorption edge at 310 eV to avoid any resonance effects.

UV-visible absorption measurements of the thin films were conducted with a CARY 5000 UV-Vis-NIR spectrophotometer. PL and PL lifetime were measured using a Horiba Nanolog Spectrofluorometer in a nitrogen protecting environment. AFM images were recorded on a Veeco Nanoscope scanning probe microscope in tapping mode for spin-coated BO-ADPM:CA films on PEDOT:PSS coated ITO/glass substrates. All film thicknesses were measured using a Dektak 150 profilometer. Hole-only devices to determine hole mobility in the BO-ADPM:CA films were fabricated with the structure of ITO/PEDOT:PSS/BO-ADPM:CA/Au.

7.3 Results and discussion

The effect of the CA concentration on the permittivity of the blends of BO-ADPM:CA was studied using impedance spectroscopy. The high solubility and low crystallinity of both BO-ADPM and CA allowed uniform thin films to be prepared via solution processing. As shown in Figure 7.2a, the film's dielectric constant at an AC frequency of 1000 Hz increases linearly with CA wt% from 4.46 for the neat BO-ADPM film to 10.8 for the film with a 1:1 blend ratio. This is similar to the literature reported tuning of the permittivity in red dye DCM2:PS thin films upon CA doping (223). Permittivity as a function of frequency for each CA concentration is shown in

Figure 7.2b. Blending BO-ADPM with CA also resulted in a significant reduction of the film absorption properties, as the high band gap CA molecule does not absorb in the visible light region. Figure 7.2c shows the linear decrease in absorption intensity with the increasing wt% of CA blend films and resulting decrease in BO-ADPM content.

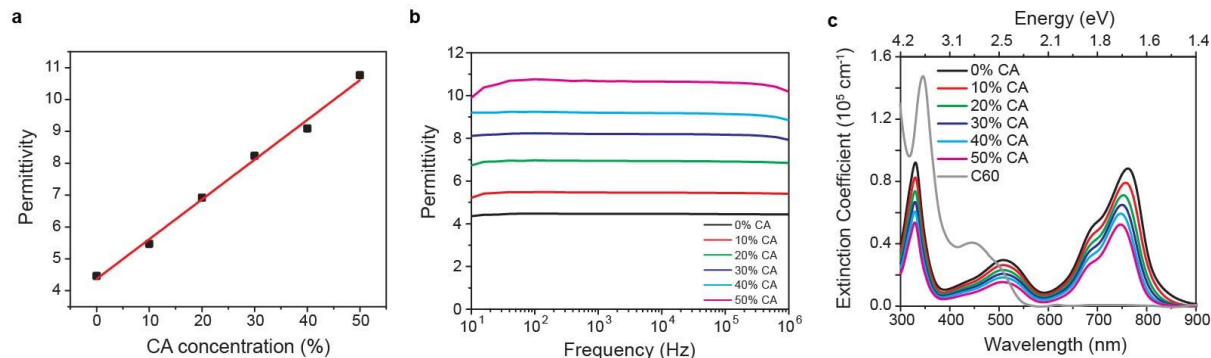


Figure 7.2. Permittivity and extinction coefficient of BO-ADPM:CA films. a) Plot of the relationship between the concentration of CA in blended BO-ADPM:CA films and the permittivity. The line red is a linear fit to the data points. b) Permittivity as a function of frequency for BO-ADPM:CA films with varying weight ratios. c) UV-visible absorption spectra of BO-ADPM:CA blend films at various weight ratios and C₆₀.

Planar heterojunction OSCs were fabricated with solution-processed neat BO-ADPM and blended BO-ADPM:CA thin films as the donor and vapor-deposited C₆₀ as the acceptor, with a structure of ITO/PEDOT:PSS(30 nm)/BO-ADPM:CA(20 nm)/C₆₀(35 nm)/BCP(8 nm)/Ag(100 nm), shown in Figure 7.3a. The J - V curves shown in Figure 7.3b represent the highest efficiency device at each BO-ADPM:CA ratio. The average device characteristics of 6 devices at each ratio, and J_{SC} , V_{OC} , FF, and PCE are listed in Table 1. The results of the BO-ADPM:CA donor devices are contrasted to the BO-ADPM:PS control device data shown in Figure 7.4. As a control, BO-ADPM was blended with PS, a low dielectric constant, non-conductive polymer. The control devices were fabricated using the same processing conditions as the BO-ADPM:CA devices. In the BO-ADPM:PS devices, no change was observed in the V_{OC} upon increased concentration of PS in the donor film and the J_{SC} dropped significantly with increased PS concentration. The device characteristics for the BO-ADPM:PS devices are shown in Table 7.2. It is important to note that all the BO-ADPM:CA devices showed similar J_{SC} values between 4.66 and 5.26 mA cm^{-2} although they possess notably different absorption efficiencies (η_A), as shown in Figure 7.2c. The relatively constant J_{SC} upon decreased η_A suggests an increase in IQE by the improvement of one or more of the remaining photocurrent generation processes, i.e. η_{ED} , η_{ES} , η_T , η_{CC} . To confirm this, IQE spectra were calculated from EQE and reflectance spectra. Indeed, upon increasing the CA concentration, the IQE spectra (Figure 7.3c) show a clear enhancement throughout the entire spectrum from 300 to 800 nm where BO-ADPM absorbs light and contributes to photocurrent. η_{ES} of excitons generated in C₆₀ is also expected to increase slightly due to the increased dielectric constant at the interface with the BO-ADPM:CA donor. Note that the contributions to the IQE from C₆₀ and BO-ADPM are difficult to decouple except in the 600 – 800 nm region, where only the BO-ADPM component contributes to the photocurrent

generation – the improvement in the IQE is seen most clearly in this region. In the BO-ADPM:CA devices, the increase in V_{OC} with increased CA concentration is attributed to the increase in the dipole moment at the interface between the BO-ADPM:CA and C_{60} layers (66, 224).

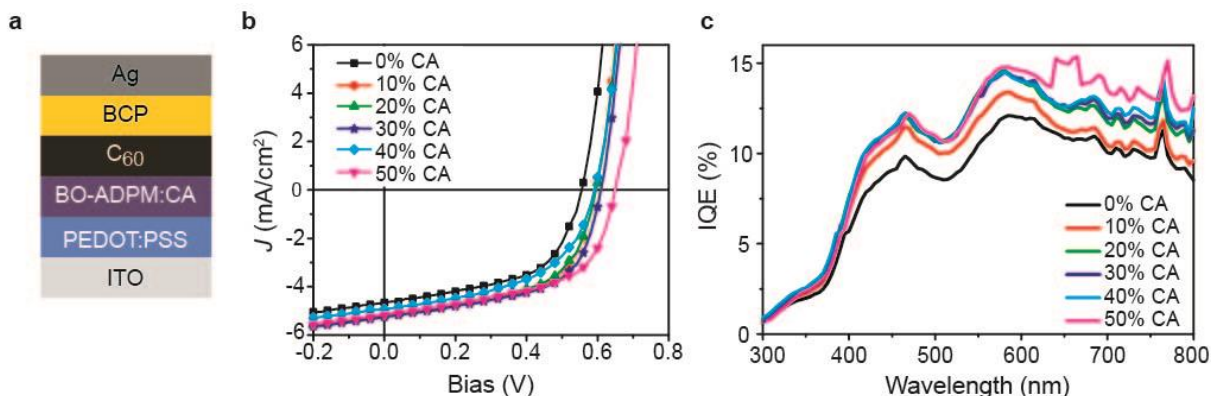


Figure 7.3. Characterization of BO-ADPM:CA/ C_{60} solar cells. a) BO-ADPM:CA/ C_{60} photovoltaic device structure. b) J - V curves of BO-ADPM:CA/ C_{60} devices. c) IQE spectra calculated from reflectance and EQE spectra demonstrating an increase in IQE with increasing CA concentration.

Table 7.1. Photovoltaic performance parameters and hole mobilities of BO-ADPM:CA donor blend solar cells with different weight ratios of CA.

BO-ADPM:CA weight ratio	V_{OC} (V)	J_{SC} (mA/cm ²)	FF (%)	PCE (%)	Hole Mobility (cm ² /V·s)
100:0	0.550 ± 0.006	-4.65 ± 0.13	52.6 ± 4.6	1.34 ± 0.10	4.06×10^{-5}
90:10	0.599 ± 0.005	-4.83 ± 0.26	55.4 ± 1.7	1.61 ± 0.12	-
80:20	0.587 ± 0.015	-4.96 ± 0.15	54.8 ± 1.7	1.60 ± 0.07	1.05×10^{-6}
70:30	0.616 ± 0.007	-4.95 ± 0.26	56.3 ± 0.7	1.72 ± 0.10	-
60:40	0.628 ± 0.017	-4.61 ± 0.19	54.3 ± 1.7	1.57 ± 0.03	2.11×10^{-7}
50:50	0.646 ± 0.022	-4.41 ± 0.42	49.6 ± 7.7	1.43 ± 0.35	-

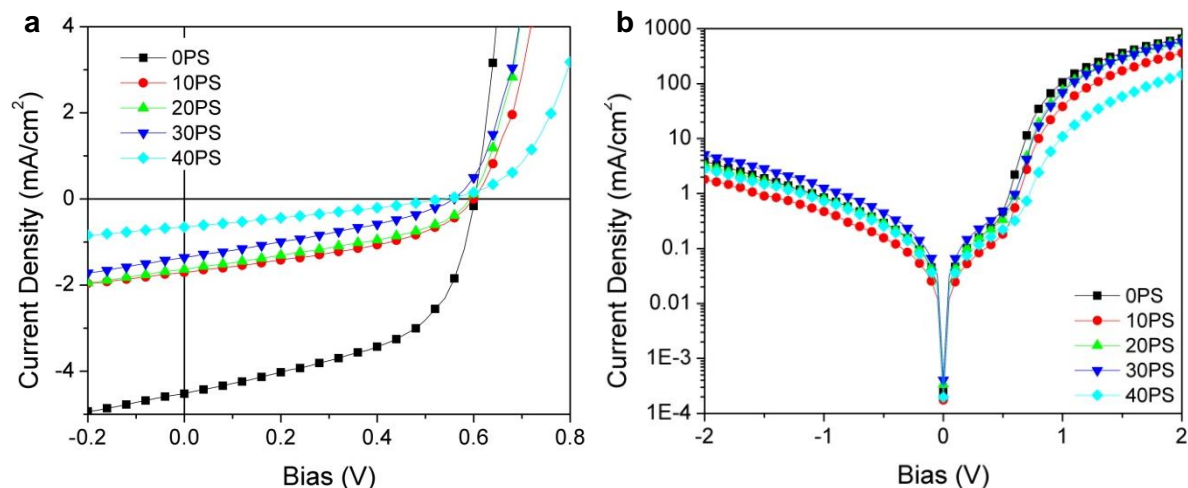


Figure 7.4. J-V characteristics of BO-ADPM:PS/C₆₀ solar cells a) under AM 1.5G solar illumination at 100 mW cm⁻² and b) in the dark.

Table 7.2. Solar cell performance characteristics for BO-ADPM:PS/C₆₀ control devices

wt% PS	V_{OC} (V)	J_{SC} (mA/cm ²)	FF	PCE (%)
0	0.602	-4.52	0.53	1.44
10	0.600	-1.71	0.42	0.43
20	0.592	-1.64	0.39	0.38
30	0.558	-1.36	0.32	0.24
40	0.539	-0.65	0.28	0.10

I studied each photocurrent generation process (η_A , η_{ED} , η_{ES} , η_T , η_{CC}) to determine which are responsible for the increase in IQE. First, the hole carrier mobilities of the BO-ADPM:CA films were determined via SCLC measurements, with mobility values listed in Table 1. As expected, a greater wt% of CA, a non-conducting molecule, in the blended film resulted in lower mobility in the BO-ADPM:CA films and reduced hole transport efficiency. Electron transport efficiency is considered constant, since the same acceptor layer of C₆₀ was used for all the devices. Thus, it is likely that both η_{ED} and η_T worsened or stayed constant, preventing their contribution to the observed increase in IQE. Moreover, because the same electrodes were used, η_{CC} is believed to be very similar for all concentrations of CA. Therefore, the only remaining photocurrent generation process that could possibly be responsible for the increase in IQE is η_{ES} . η_{ES} is influenced by both the morphological and electronic properties of the DA interface. Greater surface roughness of the donor film in planar heterojunction devices creates a larger DA interfacial area, allowing for more exciton separation sites and higher η_{ES} (225, 226). But this is not the case for the BO-ADPM:CA devices. AFM images in Figure 7.5 show that the film topology is not altered by the incorporation of CA, and that the films are extremely smooth, i.e. rms roughness of 0.31 nm for the BO-ADPM neat film and 0.37 nm for the film with 50% CA. Thus, the observed increase in IQE is not believed to be a result of greater DA interfacial area from morphological changes.

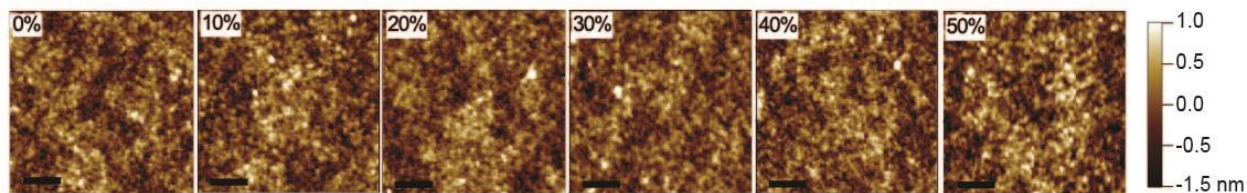


Figure 7.5. Tapping-mode AFM images of BO-ADPM:CA blend films with 10%, 20%, 30%, 40%, 50% CA have rms roughness of 0.31, 0.33, 0.31, 0.34, and 0.37 nm respectively. The scale bar represents 1 μm .

By process of elimination, the only remaining photocurrent generation process contributing to the enhancement of IQE is η_{ES} resulting from the difference between ΔLUMO and E_{cb} . Provided that CA is not chemically bonding to BO-ADPM in the blended films, negligible changes to the BO-ADPM HOMO and LUMO levels are expected. To confirm this hypothesis, we performed synchrotron-based XAS and XES to probe the LUMO and HOMO states respectively. XES experiments, however, require a high x-ray dose and could cause radiation damage when studying organic compounds (62, 227, 228). To address the potential radiation damage issues associated with soft x-ray studies on organic compounds, several radiation tests were performed. All data were collected with a defocused x-ray beam with samples cooled to 90 K. Still, XES requires a high x-ray dose and long measurement times, which leads to severe radiation damage. Our approach to avoid radiation damage is to translate the sample position during the x-ray measurements, through a programmed motorization of a stable low-temperature cryostat. This method has been demonstrated before and our data, shown in Figure 7.6, are consistent with a previous XES radiation damage study (227).

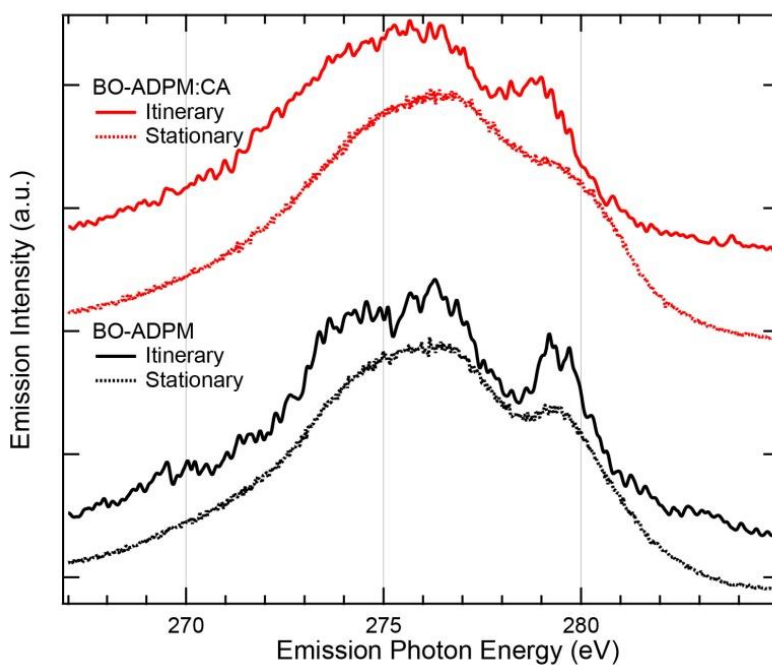


Figure 7.6. Comparison between itinerant and stationary measurements of XES. Significant loss of spectral features is observed in the stationary measurement due to beam damage.

Three sets of XAS measurements, shown in Figure 7.7, were performed to further demonstrate that radiation damage was limited. An initial set of XAS data was collected before any other x-ray exposure, while the sample was cooled with liquid nitrogen, and with a minimum x-ray dose. A second XAS measurement was performed after the itinerary XES measurement to demonstrate that minimal radiation damage occurred. Finally, for comparison, XAS spectra were collected on samples that were damaged by keeping the beam stationary for 5 minutes prior to the measurements. The three sets of comparative XAS studies demonstrate that no obvious radiation damage occurred during our controlled XAS and XES experiments.

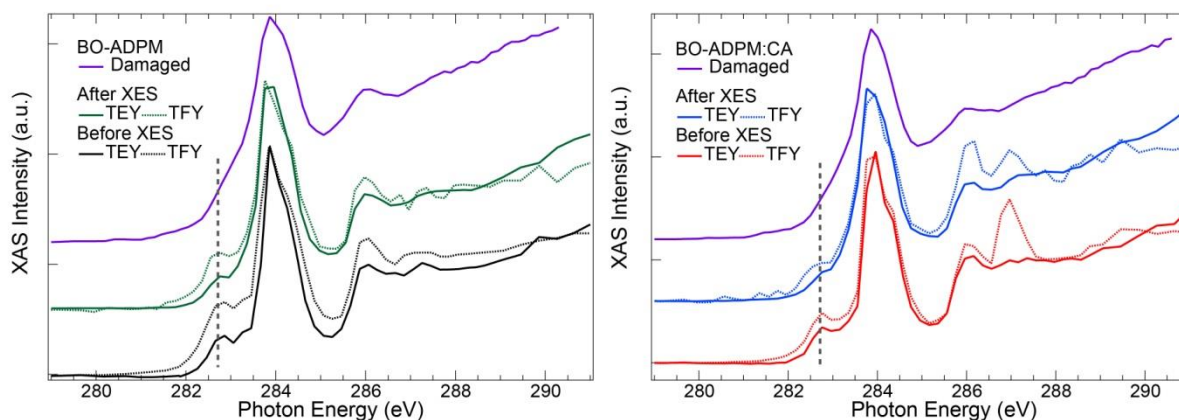


Figure 7.7. Study of film damage during XES measurements. XAS spectra for BO-ADPM and BO-ADPM:CA 50:50 films demonstrating that minimal damage was caused during the itinerary XES measurements.

Figure 7.8a shows that the leading edges of the XAS spectra, which correspond to the LUMO states, remain exactly the same for both the neat BO-ADPM and BO-ADPM:CA 50:50 films. The reliable XES spectra collected with a defocused x-ray beam on an itinerary sample surface cooled to liquid nitrogen temperature is shown in Figure 7.8b. Although the features in the XES spectra are broad due to the intrinsically low count rate of such a technique, the XES leading edges, which correspond to the HOMO states of the two systems, are at the same energy. Analysis on the detailed lineshape of the XES and XAS spectra is not a topic of this work; nonetheless, the soft XES and XAS data strongly suggest that the HOMO and LUMO levels do not change upon addition of CA into the film.

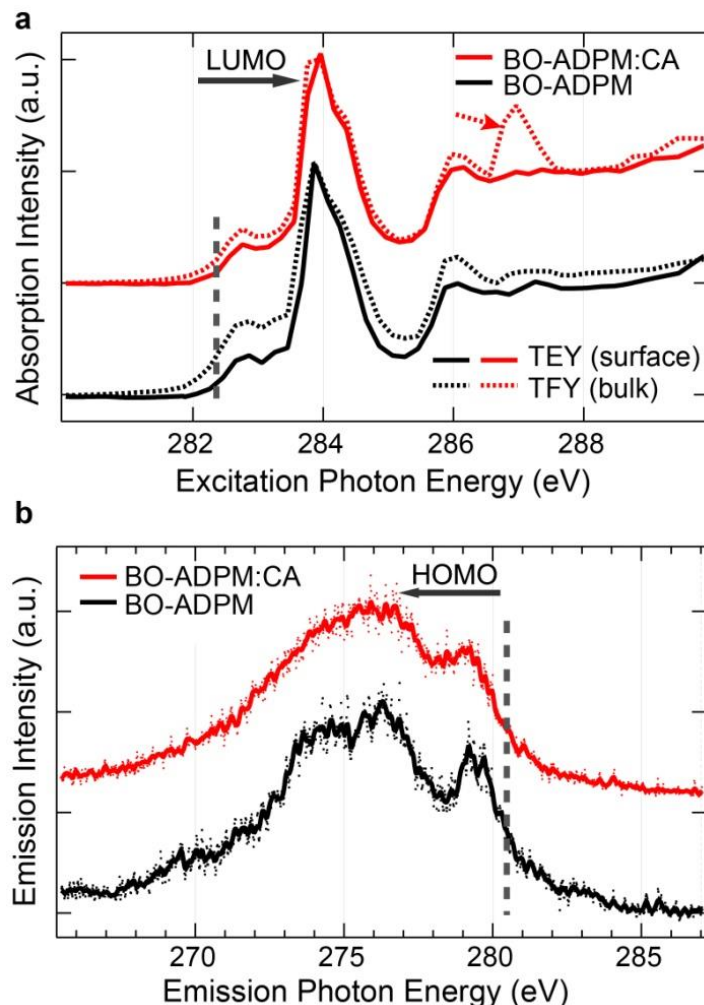


Figure 7.8. HOMO and LUMO levels for BO-ADPM films with and without CA. a) XAS measured in total electron yield (TEY) and total fluorescence yield (TFY) modes provide information about the surface and bulk of the film respectively. The LUMO levels of BO-ADPM and BO-ADPM:CA (50:50 wt%) are shown to be identical with same edge onset energy. The peak at 287 eV indicates a composition variation between the surface and the bulk of the BO-ADPM:CA film. b) XES demonstrates that the edge onset does not differ between neat BO-ADPM and with 50% CA doping. The solid lines are smoothed data.

Absorption and PL spectroscopy were employed to determine the change in E_{eb} . Although absorption spectroscopy is commonly used to estimate the energy of the HOMO-LUMO gap, or transport gap (E_T), of organic semiconductors, it is actually a measure of the optical band gap, E_{op} (27, 229). The optical band gap and transport gap differ by E_{eb} , $E_{eb} = E_T - E_{op}$. The normalized absorption spectra of the BO-ADPM:CA blend films are shown in Figure 7.9a; the blue-shift in the lowest energy absorption peak demonstrates a 32.7 meV increase in E_{op} , which suggests that E_{eb} decreased by 32.7 meV. It is important to note that the blue-shift in the absorption spectra could be partially due to reduced intermolecular π - π interactions as a result of decreased BO-ADPM concentration in the film.

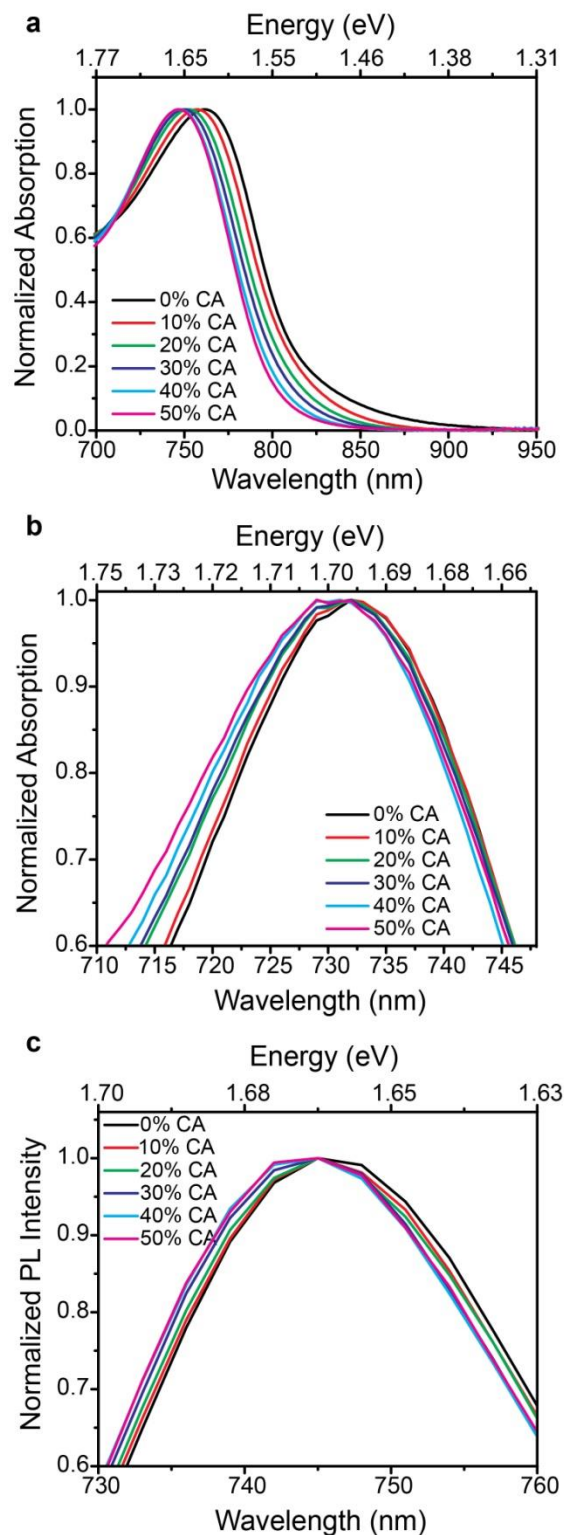


Figure 7.9. Exciton energy shift studied with absorption and PL spectroscopy. (a) Normalized absorption spectra of BO-ADPM:CA, (b) normalized absorption spectra of PS:CA films doped with BO-ADPM, and (c) normalized PL spectra of PS:CA films doped with BO-ADPM show a blue-shift with increasing CA concentration.

To eliminate π - π interaction effects and ensure that the peak shift is in part due to the change in permittivity of the film, absorption and PL spectroscopy of PS:CA films doped with a low and constant concentration of 0.5% BO-ADPM were measured. In the absorption and PL spectra (Figure 7.9b and 7.9c) of BO-ADPM doped PS:CA films, a blue-shift of ~ 7 meV was observed in the absence of BO-ADPM π - π interactions. Unfortunately, the addition of PS significantly reduces the enhancing effect of CA on the permittivity of the film. The BO-ADPM doped PS film without CA has a permittivity of 2.73, which increases to only 5.74 for the doped PS film with 40% CA (see Table 7.3); this is much lower than the permittivity of BO-ADPM:CA films without PS.

Table 7.3. Permittivity at 1000 Hz of the PS:CA matrix films doped with BO-ADPM

CA Concentration (%)	0	10	20	30	40	50
Permittivity	2.73	4.40	5.21	5.14	5.74	4.69

The PL quantum efficiency decreases and the exciton lifetime does not change significantly upon increasing CA concentration, indicating increased nonradiative decay and decreased radiative decay rates, as shown in Figure 7.10. There are two equations that can be used to determine radiative decay (k_R) and nonradiative decay (k_{NR}) rates as a function of lifetime (τ) and quantum efficiency (ϕ):

$$\phi = \frac{k_R}{k_R + k_{NR}} = k_R \tau, \tau = \frac{1}{k_R + k_{NR}}$$

Since τ is almost the same for all the cases, a decreased ϕ means a lowered k_R and an increased k_{NR} . This is not surprising, as the energy shift of the lowest excited state could lead to a higher intersystem cross rate, which quenches the emission (230). These findings support the observed decrease of E_{eb} with increasing film dielectric constant, which leads to higher η_{ES} , though it is difficult to decouple π - π interaction and permittivity effects.

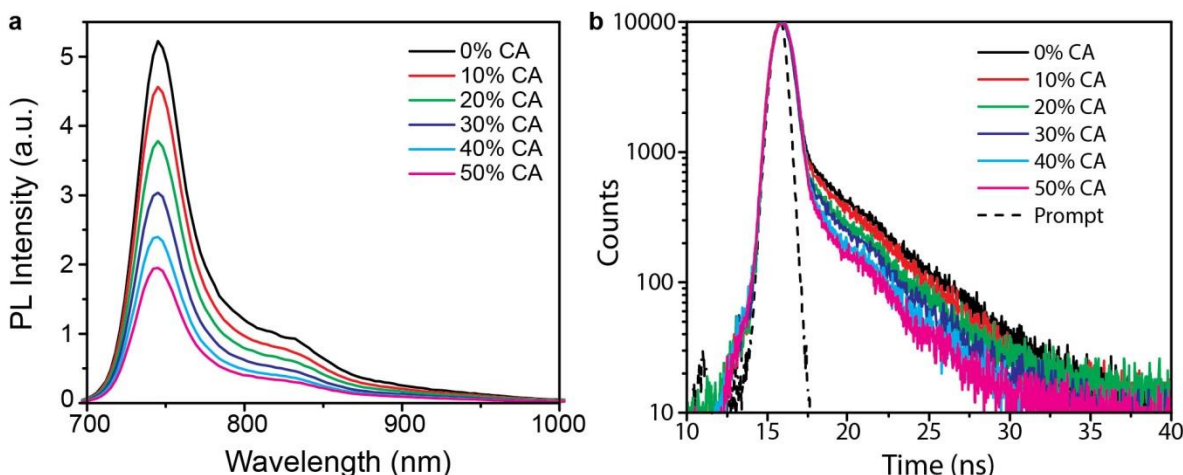


Figure 7.10. PL quenching and lifetime in BO-ADPM:CA films. a) The PL intensity of the BO-ADPM doped PS:CA film decreased as a greater wt % wt % of CA was added to the film. b) PL lifetime measurements show that as the CA concentration increases in the PS:CA films doped with BO-ADPM the lifetime does not change significantly. The PL lifetimes are 3.86, 3.72, 3.48, 3.48, 3.28, and 3.21 ns for 0, 10, 20, 30, 40, and 50 wt% CA films respectively.

7.4 Conclusion

In summary, I have demonstrated enhancement of η_{ES} by decreasing E_{eb} in operating OSCs. The reduced E_{eb} was realized by increasing the donor film permittivity and decreasing the intermolecular π – π interactions, i.e., blending the electron donor BO-ADPM with a high dielectric constant small molecule CA. An increase in IQE across the entire spectrum was achieved, with a 30% increase in IQE at $\lambda = 770$ nm, by increasing the dielectric constant of the donor film from 4.46 to 10.8. Our findings suggest organic semiconductors with high permittivity have great potential in improving the PCE of OSCs. The concept of reducing E_{eb} could be especially meaningful for OSCs with low band gap materials, where $\Delta LUMO$ is often minimized.

Although it is important and interesting to control Frenkel E_{eb} , there are also CT excitons that form at the DA interface that are likely influenced by adding CA. The next step in this study is to determine if the CT state energy is also manipulated by varying the permittivity of the active layers. Unfortunately, because the DA interfacial area is small in planar heterojunction devices, the CT state energy is difficult to measure due to the small signal-to-noise ratio. The CT exciton binding energy can more easily be measured in a BHJ, where the DA interfacial area is larger. Thus, I investigated the effect of CA concentration on the CT state energy in BHJ OSCs, as described in the next chapter.

Chapter 8

Controlling charge transfer exciton binding energy in organic bulk heterojunction photovoltaics

Adapted from manuscript:

Sibel Y. Leblebici, Alexander Weber-Bargioni, Biwu Ma. *Submitted*

8.1 Introduction

In OSCs, the process of exciton dissociation is critical for maximizing I_{SC} because free carriers need to be collected at the electrodes (29, 30). But, also allowing for efficient exciton dissociation with minimal energetic driving force is necessary to maintain high V_{OC} (59). PCE can be improved by reducing the Frenkel E_{eb} , as I showed in Chapter 7, but dissociation of the CT state that forms at the DA interface is also essential for high performance. There is still considerable debate about the process of CT state dissociation (see section 3.3), and it is a form of exciton dissociation and depends on several factors. As described by the Onsager-Braun model, the probability of exciton dissociation is dependent on exciton lifetime, permittivity, distance between the electron and hole, local electric field, and E_{eb} (64). In the case of CT states, E_{eb} is described by the Coulombic attraction of the electron in the acceptor and the hole in the donor: $e^2/4\pi\epsilon_r\epsilon_0a$, where e is the charge of an electron, ϵ_r is the relative permittivity, ϵ_0 is the permittivity of vacuum, and a is the distance between the charges (30). Many approaches have been used to either enhance η_{ES} or directly reduce the CT state energy and thus improve OSC performance. Doping the active layer with ferroelectric polymers to create localized electric fields (65, 66) and with small molecules to alter the density of states (67) have been used as strategies enhance η_{ES} . CT state energy has been reduced synthetically by increasing the dipole change between ground and excited states (69, 70). A prevalent method to decrease the CT state energy is to increase the permittivity through such methods as doping with salts (68), synthetically incorporating fluorine and high permittivity side chains in semiconducting polymers (71–74), and increasing the concentration of fullerenes in the BHJ (75–77). However, changing the concentration of fullerenes or changing the structure of a semiconducting polymer not only changes the permittivity but can significantly alter the phase separation in the BHJ layer, and thus convolute the change in OSC performance. In Chapter 7, I described my strategy to reduce E_{eb} of Frenkel excitons in small molecule layers for planar heterojunction devices by blending BO-ADPM with CA, a high permittivity molecule (217, 223, 231). I observed an increase in permittivity and IQE when CA was added to the donor film, and I concluded that this enhancement is due to a decrease in the donor E_{eb} . Permittivity can also impact the CT state energy, but the CT state could not be observed in the planar heterojunction devices because of the small interaction area between the donor and acceptor. I hypothesize that this method of increasing permittivity by incorporating CA into a polymer-fullerene BHJ will effectively increase PCE by reducing the CT state energy.

In this chapter, I apply the strategy of adding high permittivity CA to MDMO-PPV:PCBM BHJs to improve OSC performance. The MDMO-PPV:PCBM BHJ is used as a model system because the CT state energy can conveniently be observed via electroluminescence (EL) (232). See Figure 8.1 for molecular structures and energy level alignment of MDMO-PPV and PCBM. By increasing the permittivity of the active layer, I expect to observe lower CT state energies, leading to improved η_{ES} and PCE.

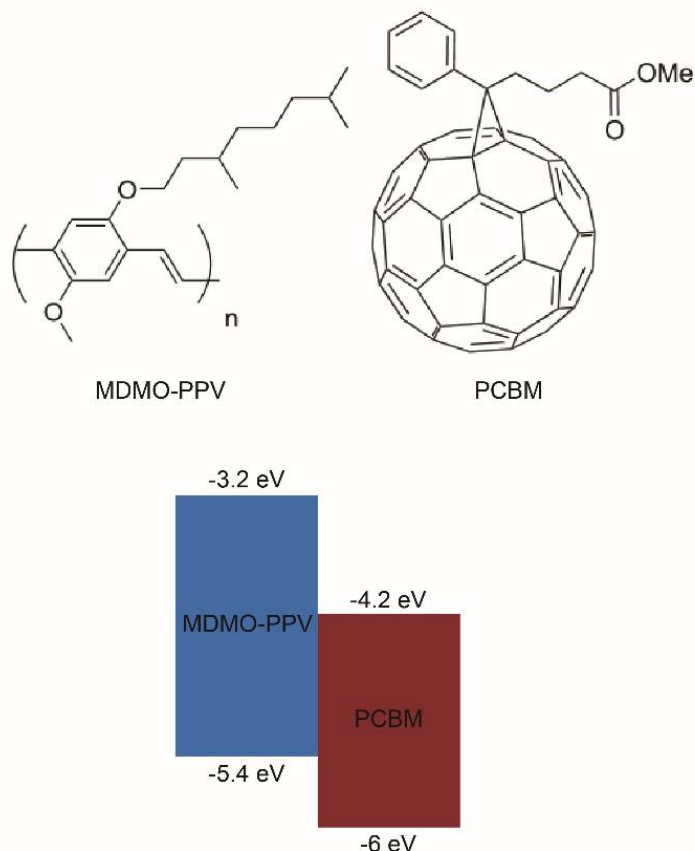


Figure 8.1. Molecular structures of MDMO-PPV and PCBM and their band alignment. Adapted from Ref. (233).

8.2 Film and device formation

The active layer for the OSCs, permittivity measurements, and EL devices were made using the same process. The MDMO-PPV, PCBM, and CA were purchased from H.W. Sands Corp., nano-c, and Alfa Aesar respectively. MDMO-PPV was dissolved in chlorobenzene by stirring overnight. PCBM and CA were dissolved in chlorobenzene and passed through a 0.2 μm polytetrafluoroethylene filter. The MDMO-PPV:PCBM:CA solutions were formed at a 1:1 weight ratio of MDMO-PPV:PCBM with CA added at the appropriate ratios to form solutions with various wt% CA. For all devices, pre-patterned ITO-coated glass substrates, from Thin Film Devices Inc., were cleaned by successive sonication in soap solution, deionized water, acetone, and isopropanol for 15 min at 40 $^{\circ}\text{C}$ and UV ozone cleaned for 10 min. PEDOT:PSS (Baytron PH 500) was spin cast onto the substrates at 4000 rpm and subsequently baked in air at 140 $^{\circ}\text{C}$ for 20 minutes. The MDMO-PPV:PCBM:CA solutions was spin coated onto the PEDOT:PSS layer to form the active layer.

The OSCs were fabricated in a BHJ structure of ITO/PEDOT:PSS (30 nm)/MDMO-PPV:PCBM:CA (90 nm)/LiF (7 \AA)/Al (100 nm). To maintain a thickness of 90 nm for all concentrations of CA, the MDMO-PPV:PCBM:CA solutions (15 mg/mL) were spin coated at rates from 4000 to 1400 rpm for 40 s. Subsequently, LiF/Al electrodes, which define the device area with a shadow mask of 0.03 cm^2 , were thermally evaporated under high vacuum ($\sim 2 \times 10^{-6}$ mbar) at a rate of 0.5 and 2 $\text{\AA}/\text{s}$. Parallel plate capacitors used to measure permittivity had the

structure as the OSCs except the MDMO-PPV:PCBM:CA solutions (20 mg/mL) were spin coated at 1000 rpm for 40 s to form thicker films.

Devices to measure EL had the structure ITO/PEDOT:PSS (30 nm)/MDMO-PPV:PCBM:CA/LiF (7 Å)/Al (70 nm). MDMO-PPV:PCBM:CA solutions (20 mg/mL) were spin cast at 1000 rpm for 60 s. The top electrode of LiF/Al was defined using a 1.4 cm² shadow mask. LiF and Al were evaporated under high vacuum ($\sim 2 \times 10^{-6}$ mbar) at rates of 0.5 and 2 Å/s. To minimize degradation during the EL measurements under high bias, the devices were encapsulated in the glovebox by capping with a second glass substrate and securing with UV curable epoxy (Epo-tek OG159-2).

8.3 Film characterization

Permittivity was measured via impedance spectroscopy of parallel plate capacitors using a VMP3 potentiostat from BioLogic without exposure to air and in the dark. The real and imaginary impedance were measured by sweeping the AC frequency from 10⁶ to 10 Hz and at an AC level of 100 mV. The permittivity was calculated from the impedance spectroscopy measurement using the methods and models described by Carr et al. (234). To accurately measure the geometric capacitance to extract the permittivity, the DC voltage must be sufficient to fully deplete the active layer. DC biases of 0, 1, and 2 V all showed similar capacitive behavior suggesting that there is a low doping level in the BHJ (234).

EL was measured using a Horiba Nanolog Spectrofluorometer with a R5509PMT visible/NIR detector and a 1200, 500 grating. An extech instruments DC power supply was used to excite the films in a nitrogen protecting environment. All samples were measured under an electric field of 1.8×10^5 V/cm.

Film thicknesses were measured using a Dektak 150 profilometer. AFM images were measured with a Park Systems NX10 AFM in tapping mode to acquire phase information. A single silicon NCHR AFM tip purchased from NanoWorld was used for all the images.

8.4 Results and discussion

The effect of enhancing the local permittivity on the CT state energy and device efficiency was studied by varying the concentration of CA in the BHJ active layer. The device structure is ITO/PEDOT:PSS/MDMO-PPV:PCBM:CA/LiF/Al. All solar cells were fabricated using a simple 1:1 weight ratio of MDMO-PPV to PCBM and CA was incorporated at different wt% of the BHJ mixture. I did not use the higher efficiency 1:4 MDMO-PPV:PCBM ratio (57), because the CA does not effectively mix with the BHJ at a that ratio. OSCs were tested under nitrogen with standard AM1.5G illumination. The permittivity of the MDMO-PPV:PCBM:CA films was measured with impedance spectroscopy of parallel plate capacitors and the CT state energy was measured using EL.

Figure 8.2a shows the change in MDMO-PPV:PCBM PCE with varying concentrations of CA; the average PCE of 8 devices are plotted and the standard deviation is represented by the error bars. Because the maximum reported PCE for MDMO-PPV:PCBM OSCs is only 2.5% and the EQE has a maximum of 50% (57), I assume that the excitons are not efficiently separated in MDMO-PPV:PCBM OSCs and that excitons will dissociate more efficiency by lowering the binding energy. The PCE initially increases when CA is added to the BHJ and continues to increase up to 20 wt% CA, where the PCE increases by 75%. However, the PCE rapidly decreases when the concentration of CA is greater than or equal to 30 wt%. As the concentration of CA increases, the V_{OC} decreases linearly from 0.90 to 0.85 V. However, J_{SC} and FF follow the same trend as the PCE: increase up to 20 wt% CA and then decrease rapidly with further

addition of CA. The standard deviation, represented by the error bars in Figure 8.2a, increases as more CA is added to the BHJ, suggesting that the film uniformity varies more significantly when more CA is added. The increase in film heterogeneity is also seen in J_{SC} and FF standard deviation. Device performance details including J - V curves and average values of V_{OC} , J_{SC} , and FF are available in Figure 8.3.

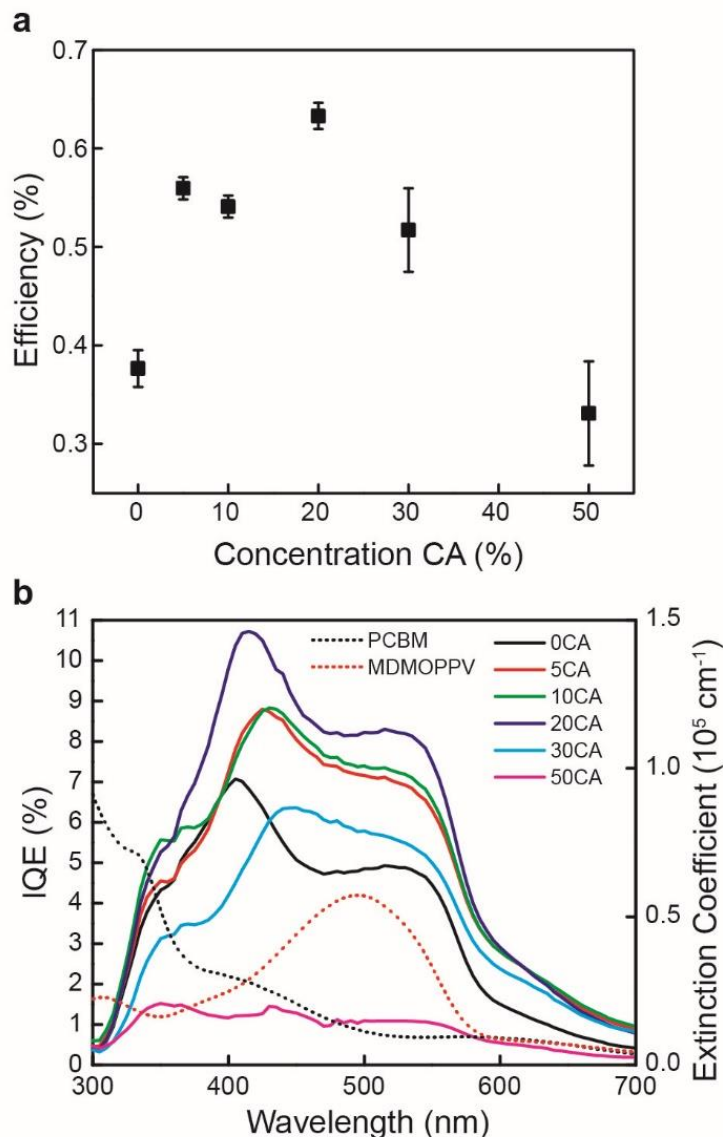


Figure 8.2. Performance of MDMO-PPV:PCBM solar cells blended with CA. a) Average PCE of 8 devices with increasing weight percent of CA blended in the BHJ. The error bars represent the PCE standard deviation. PCE initially increases to a 75% enhancement at 20 wt% CA. As the concentration of CA increases beyond 20 wt%, the efficiency decreases rapidly and the standard deviation increases substantially. b) IQE spectra of BHJ devices with CA in solid lines and extinction coefficients for MDMO-PPV and PCBM in dashed lines. The IQE increases throughout the spectrum up to 20 wt% CA and then quickly decreases at higher concentrations of CA.

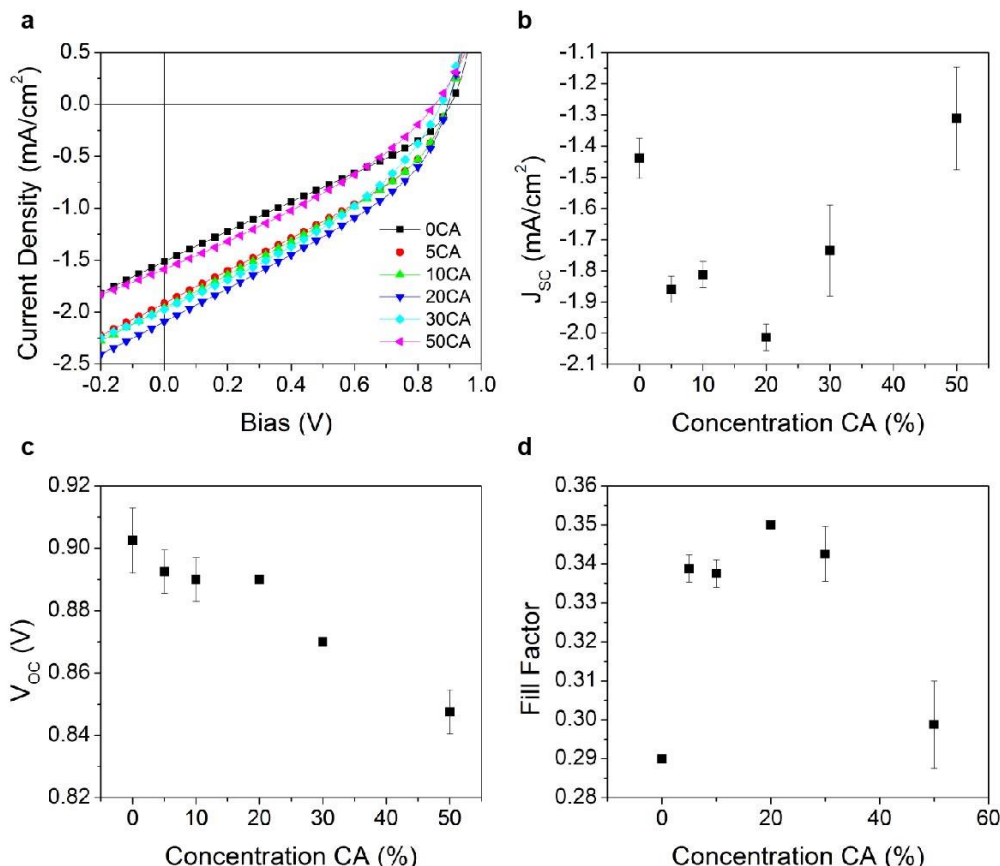


Figure 8.3. Efficiency parameters for MDMO-PPV:PCBM solar cells blended with CA. (a) Illuminated $J-V$ curves for MDMO-PPV:PCBM:CA BHJ solar cells with varying concentrations of CA. The highest performing cells for each concentration are plotted. The concentrations vary from 0 to 50 wt% CA. Average J_{SC} (b), FF (c), and V_{OC} (d) of 8 devices with increasing weight percent of CA blended in the BHJ. The error bars represent the standard deviation. Both FF and J_{SC} are optimized at 20 wt% CA. The V_{OC} decreases as more CA is added.

To provide deeper insight into the OSC optoelectronic processes, I measured the IQE, the ratio of the number of carriers collected to the number of photons absorbed. IQE is needed to assess OSC performance without the influence of absorption, since the absorption is reduced as CA displaces the absorbing donor and acceptor materials. IQE spectra of the best performing devices are plotted in Figure 8.2b along with the absorption spectra of MDMO-PPV and PCBM films for reference. The corresponding EQE spectra are available Figure 8.4. As expected, the majority of the photocurrent is generated at longer wavelengths where the MDMO-PPV absorbs (57). The IQE spectra reveal that the efficiency of the photocurrent generation increases rapidly from 0 to 5 wt% CA, increases at a slower rate from 5 to 20 wt% CA, and decreases rapidly for higher concentrations of CA. The change in IQE with increasing CA concentration is equivalent to the trend in PCE. IQE is the product of exciton diffusion, CT exciton dissociation, carrier transport, and carrier collection efficiencies. Simply based on the IQE spectra, I cannot deduce which of these photocurrent generation steps is responsible for the increase in PCE for concentrations of CA up to 20%.

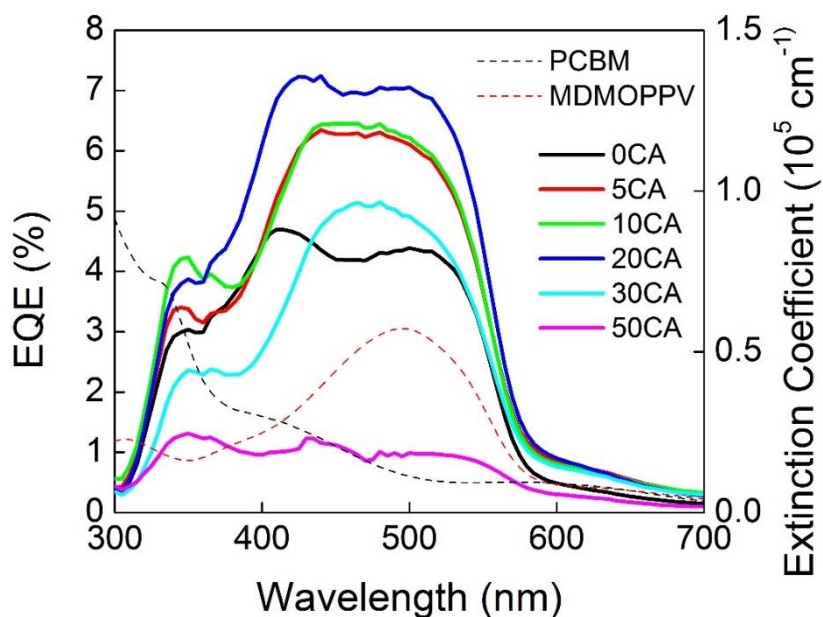


Figure 8.4. Raw EQE spectra of BHJ devices with CA in solid lines and extinction coefficients for MDMO-PPV and PCBM in dashed lines. The maximum EQE, across almost the entire spectrum, is achieved at 20% CA.

I expect that the CT state binding energy will be reduced by increasing the permittivity of the BHJ film. Hence, I measured the real and imaginary impedance of parallel plate capacitors with the BHJ layer as the dielectric between the two electrodes to calculate the relative permittivity (234). Figure 8.5 shows that the permittivity increases with added CA up to 10 wt%, stays relatively constant until 20 wt% CA, and rapidly decreases beyond 20 wt% CA. Thus, three regimes of behavior are observed in the MDMO-PPV:PCBM films as higher concentrations of CA are added: (1) linear increase in permittivity by weight addition of CA from 0 to 10 wt% CA, (2) the permittivity increases at a slower rate from 10 to 20 wt% CA, and (3) the permittivity decreases from 20 to 50 wt% CA. These three regimes are also found in the behavior of the PCE and IQE with increasing concentrations of CA. The dashed red line in Figure 8.5 represents the weighted average of the permittivity of each material, where the relative permittivity of the BHJ and CA are 4.7 and 24.8 respectively (231). Up to 10 wt% CA, the measured permittivity follows the expected behavior (223) before it begins to deviate. Beyond 20 wt% the permittivity drops rapidly towards the permittivity of crystalline CA of 3.2 at room temperature (231). As I will show below, the deviation from the expected trend is related to crystallization and phase separation of CA in the BHJ at high loading. However, within the first regime up to 10 wt% CA, the effect of permittivity increase should also modify the CT exciton binding energy, which is the goal of this work.

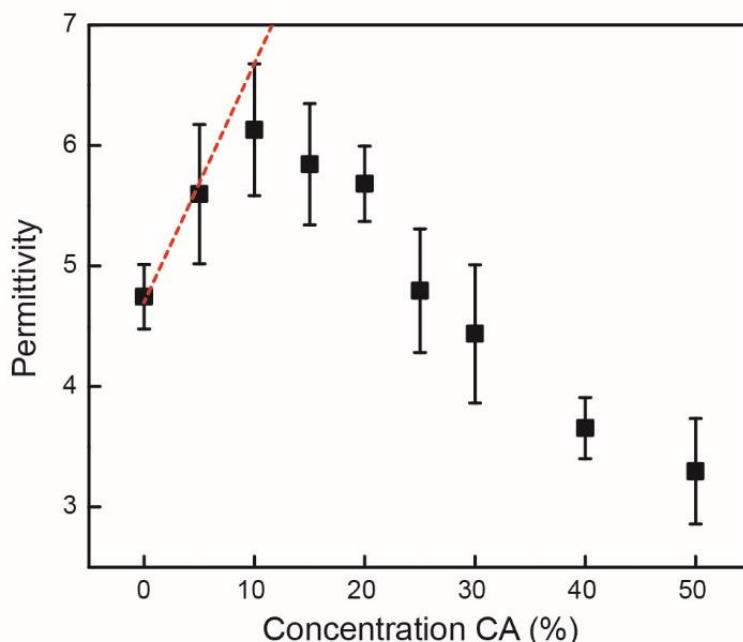


Figure 8.5. Permittivity of MDMO-PPV:PCBM BHJ films with increasing CA concentration in the BHJ. The dashed line indicates the expected permittivity based on the weighted average permittivity of each component. The permittivity unexpectedly decreases for CA concentrations above 10 wt% CA.

As described earlier, the CT exciton binding energy can be modeled by the screened Coulomb law; as the permittivity of the film increases, the CT state energy should decrease. However, van Duijnen et al. argue that the Coulomb description of the exciton does not apply in this case because the charges are closer than 10 nm (235). Alternatively, the CT state energy dependence on permittivity can also be modeled using solid state solvation effect (SSSE) (223), which accounts for the interaction of a solute with an electric field produced by the solvent molecules. The SSSE model predicts also that as the low frequency permittivity increases, the CT exciton binding energy will decrease. In the films here, the solvent is the CA and the solute that is effected is the CT exciton. The CT exciton binding energy was measured in the MDMO-PPV:PCBM:CA films via EL (232), as shown in Figure 8.6. In Figure 8.6a, the EL spectra of PCBM and MDMO-PPV peak at 730 and 590 nm respectively, which are distinct from the EL spectrum at 980 nm for the CT state in the MDMO-PPV:PCBM blend. Our results are corroborated by those of Tvingstedt et al. (232). The EL spectra for BHJ films incorporating CA are also shown in Figure 8.6a, though it is challenging to distinguish the peaks for each spectrum. To determine the peak maxima, the spectra were fit with an exponentially modified Gaussian function because it best described the data (236). The peak maxima and the full width at half maximum (FWHM) are shown in Figure 8.6b. The peak maxima and the FWHM behave very similarly: they increase significantly from 0 to 10 wt% CA and then begin to plateau beyond 20 wt% CA. This indicates that the CT exciton binding energy indeed decreases at least within the first wt% regime from 1.26 to 1.21 eV at 0 and 10 wt% CA respectively.

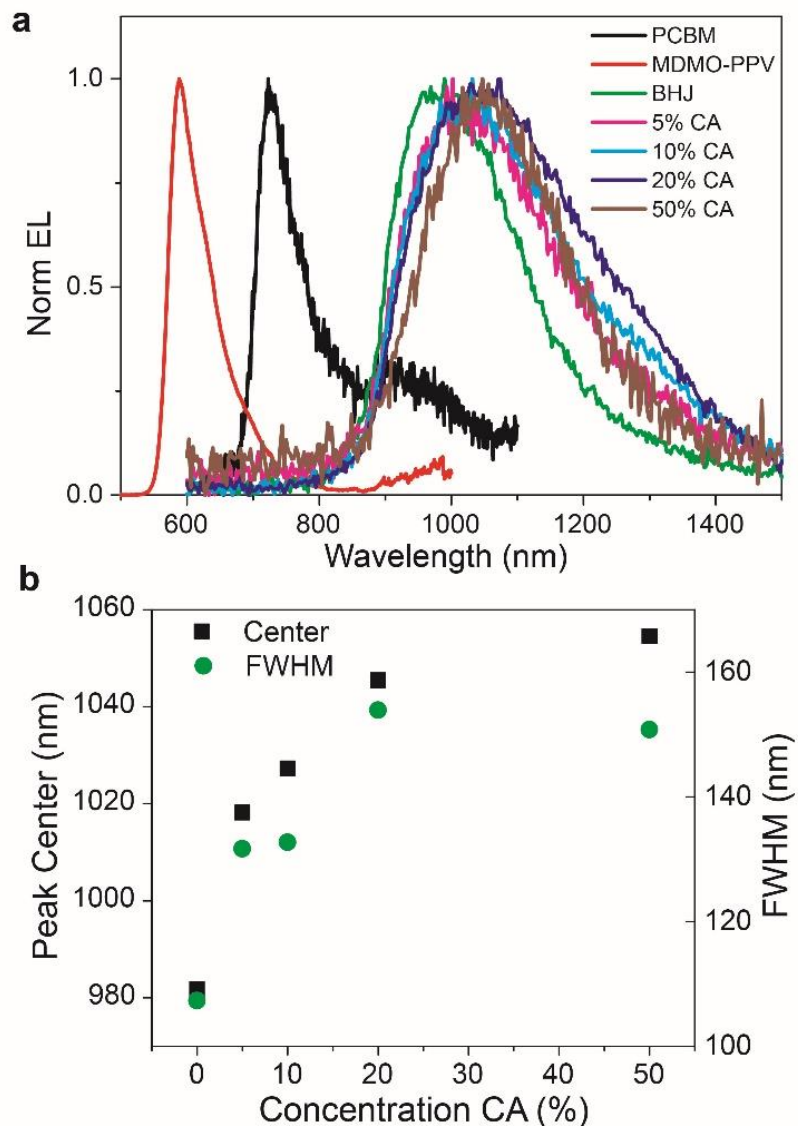


Figure 8.6. CT exciton energies measured with electroluminescence. (a) Normalized EL spectra of PCBM and MDMO-PPV individually are distinct from the CT exciton spectra of the MDMO-PPV:PCBM BHJ films. Spectra are also shown for all the concentrations of BHJ films with CA. (b) Peak maxima and FWHM of fits to EL spectra for each concentration of CA. As more CA is added to the BHJ, the CT exciton energy decreases and the FWHM increases.

To determine if the change in CT exciton binding energy follows the Coulombic or SSSE model, the EL peak maxima were compared to the measured permittivity values for the different concentrations of CA (Figure 8.7). But, I only considered the data up to 10 wt% CA since the behaviors of both the permittivity and EL spectral peak positions change significantly at higher concentrations. From the plots of permittivity versus CT state energy, both models appear to be valid. I show that increasing the concentration of CA up to 10 wt% indeed enhances the BHJ permittivity, reduces the CT state energy, causing the PCE to increase. The broadening of the EL spectra with higher concentrations of CA suggests that the films become less uniform over the 1.4 cm^2 active area, similar to the observed increase in standard deviation of the PCE. To

understand the increase in FWHM and why the CT state plateaus beyond 10 wt% of CA, I studied the morphology of the BHJ films at varying CA concentrations using high resolution AFM.

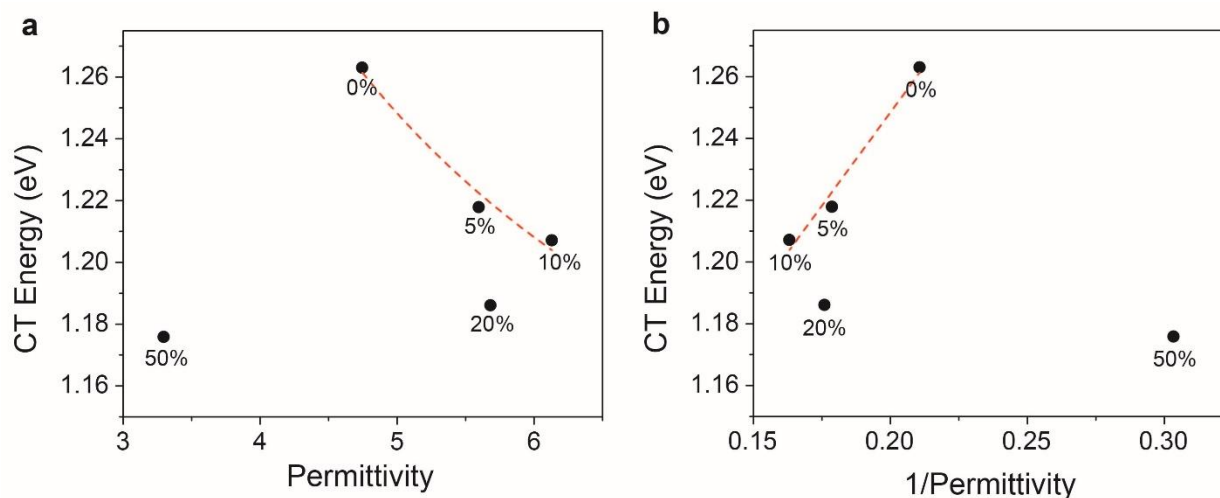


Figure 8.7. Fitting data to Coulombic and SSSE models. (a) CT state plotted against permittivity only shows a trend towards the SSSE behavior (dashed line) for the films with CA concentrations up to 10 wt% (223). (b) In the Coulombic model, the CT state energy is inversely related to the permittivity. The dashed line is a linear fit for data from films with CA concentrations up to 10 wt%. The wt% CA for each data point is labeled.

I employed AFM tapping mode imaging to differentiate material domains within the BHJ films (46, 237, 238). The phase images in Figure 8.8a-c show that although the domain size increases slightly from 0 to 10 wt% CA, the morphology does not change significantly when CA is added. These results are representative for many measured regions over these three films. I conclude from these results that CA is effectively incorporated into the BHJ when increasing the concentration up to 10 wt%. This observation fits the behavior in the first regime (0-10 wt% CA) where the permittivity increases, the CT state energy decreases, and the solar cell performance is enhanced. However, the phase images in Figure 8.8d,e show a drastic change in morphology with the formation of a new phase at 20 wt% CA, and the domains of the new phase becomes larger as more CA is added. Thus, in the regime between 10 and 20 wt% CA, I believe CA is beginning to phase separate out of the MDMO-PPV:PCBM BHJ. As a result, the CA does not interact as strongly with the excitons, which can describe the slower increase in permittivity and CT state energy in this second regime.

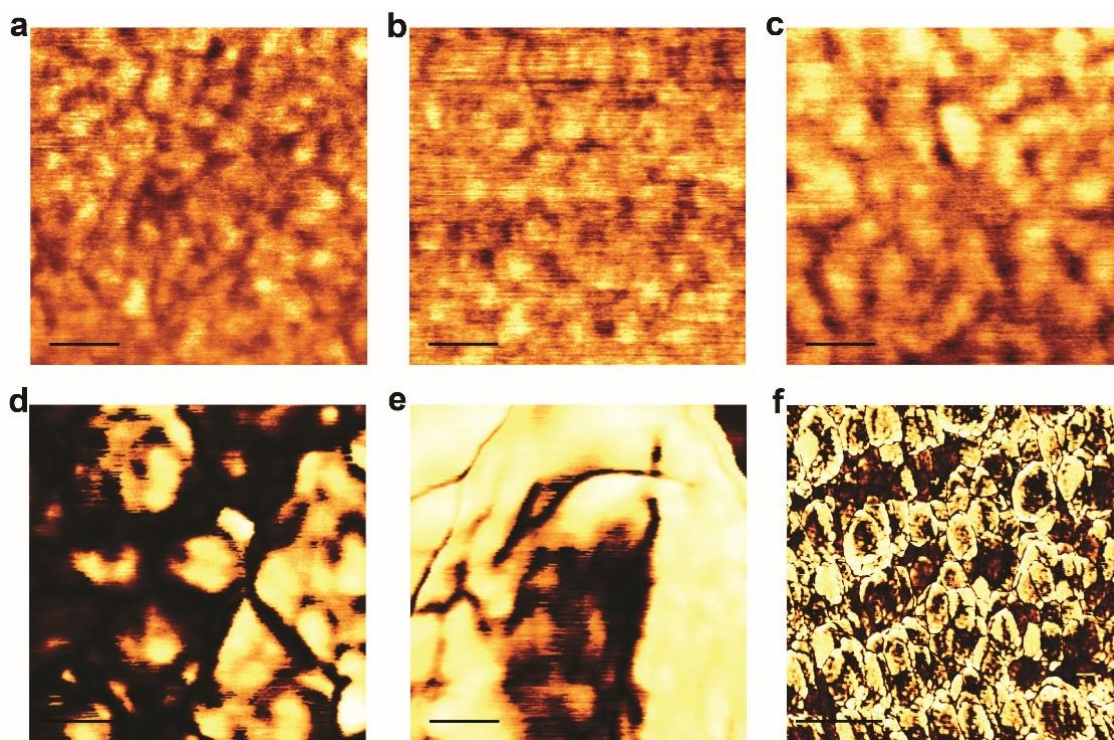


Figure 8.8. AFM phase images of MDMO-PPV:PCBM blended with increasing concentrations of CA. 0 wt% (a), 5 wt% (b), 10 wt% (c), 20 wt% (d), and 50 wt% (e) CA in BHJ films spin cast on PEDOT:PSS/ITO/glass substrates. Scale bars for a-e are 50 nm. At 20 wt% CA (d), the morphology changes significantly and large domains of a new phase form. At 50 wt% CA (e), the new phase domains become much larger. (f) An enlarged image of a 50 wt% CA film. Scale bar is 500 nm.

Above 20% CA, the CA begins to form very large domains, and it likely forms crystals, which have a low permittivity of 3.2 because the CA can no longer rotate to align its dipole to the electric field (231). This behavior was not observed in the previously studied small molecule films because the amorphous nature of BO-ADPM donor molecule used prevents phase separation (217), whereas phase separation is a known behavior in the MDMO-PPV:PCBM BHJ system (239, 240). Crystallization and reduced permittivity of CA at high concentrations explains the decrease in permittivity for the MDMO-PPV:PCMB:CA films in Figure 8.5. Because of the lower permittivity, I initially expected the CT state energy to increase in the third regime. But, based on the recent results from Deotare et al., I suspect that the CT state excitons are diffusing to the low energy sites where CA remains mixed in the BHJ (241), leading to a plateau in CT state energy.

8.5 Conclusion

In conclusion, I enhance OSC performance of polymer-fullerene BHJ devices by adding up to 20 wt% CA to the BHJ. The increase in PCE is due to the increase in permittivity and the resulting decrease in CT state energy when CA is added to the film. Beyond 20 wt% CA, the CA begins to phase separate out and form crystals, which results in lower permittivity and PV performance. Adding CA in low concentrations is an effective strategy to increase permittivity and, as a result, boost OSC efficiency in BHJ devices.

The ability to manipulate the CT state energy not only allows for improved solar cell performance but also provides insight into CT state behavior. However, there are still many unknowns in the steps leading up to the CT state dissociation. How mobile are these CT state excitons and the initial Frenkel excitons? How do the excitons move through the material to reach the DA interface? To better understand the exciton behavior in the MDMO-PPV:PCBM system leading up to charge transfer, we can use time resolved measurements to observe how the populations of excitons and free carriers change over time.

Chapter 9

Exciton mobility and charge transfer in organic solar cell bulk heterojunctions from femtosecond stimulated Raman spectroscopy

Adapted from Ref (242):

David P. Hoffman, Sibel Y. Leblebici, Adam M. Schwartzberg, Richard A. Mathies. *The Journal of Physical Chemistry Letters* 2015, 6, 2919-2923.

9.1 Introduction

Understanding and controlling the charge transfer process between donor and acceptor materials in OCSs is critical for improving photovoltaic performance because it is required for photocurrent generation. In the previous chapter, I showed that CT exciton binding energy in MDMO-PPV:PCBM BHJs can be manipulated by modifying the permittivity in the BHJ film, which corresponded to a change in PCE. However, there are critical factors, other than E_{eb} , for the process of exciton separation: long-range material order, electric fields, and hot excitons. Hot excitons occupy a high excitonic state after formation and then relax to the lowest exciton energy state. It is debated that hot excitons have a higher dissociation efficiency (see section 3.3 for more details). The femtosecond stimulated Raman spectroscopy (FSRS) experiments described in this chapter show that, for the MDMO-PPV:PCBM system studied, hot excitons are critical for enhancing charge carrier generation because they have greater mobility, greater probability of reaching the DA interface, before thermalization.

Ultra-fast time resolved spectroscopy is used to track exciton dynamics in OSCs. Conventional transient absorption spectroscopy has been used extensively (220, 243–247), but the broad overlapping electronic signals, especially those due to excitons, are difficult to distinguish and analyze. On the other hand, vibrational spectroscopy, in particular FSRS (248), can alleviate this problem because vibrational spectra are generally sparse and narrow and resonance conditions can be leveraged to enhance one species over another.

Raman spectroscopy probes vibrational, rotational, and other nuclear motions in materials, generally organic molecules where specific fingerprint vibrational modes, such as carbon-carbon double and single bond stretches, are observed. These molecular vibrations are sensitive to electronic and structural aspects of the system and last for 10 – 500 fs (248). Raman spectroscopy is an effective probe of changes in electron density in organic semiconductors because molecules reorganize due to the gain or loss of an electron during charge transfer (249). FSRS allows for the measurement of atomic motion via these Raman active vibrational modes to be studied on a time scale of 1 ps to 10 fs.

The process of FSRS is shown in Figure 9.1. An ultra-short actinic visible wavelength pulse excites the material and initiates the process of interest, in this case taking a molecule from the ground state (GS) to the excited state (ES). Then after some time delay, ΔT , the structural evolution of the system is probed with two pulses: a narrow bandwidth Raman pulse around 800 nm and a broadband continuum probe pulse from 830 - 960 nm. Because these two pulses interact both spatially and temporally, photons from the Raman pulse are transferred to the probe pulse at the vibrational frequencies of the molecule initiating vibrational coherence (248). Vibrational coherence can be described as driving the Raman-active modes in the molecule. More simply stated, the pump and probe pulse simultaneously prepare and stimulate the Raman transition in the material (250). More details on the theory of FSRS are available in Refs (248, 251).

FSRS has been used to study a wide variety of materials. For example, it has been used to directly measure lattice dynamics in optically excited semiconductor nanocrystals (252), investigate conformational relaxation dynamics in organic multi-electron acceptors (253), and to study isomerization dynamics in retinal pigments that initiate vision (254). Also, FSRS can

directly probe charge dynamics in organic semiconductors because a polaron forms in the polymer after charge transfer occurs, which causes a conformational change necessary to stabilize and delocalize the extra charge and results in vibrational signatures (255). To this end, FSRS has been used to investigate a variety of charge transfer phenomena (256–258) including a recent study of polaron formation in poly[*N*-9'-heptadecan-2,7-carbazole-*alt*-5,5-(4',7'-di-2-thienyl-2',1',3'-benzothiadiazole)]:PCBM films (255).

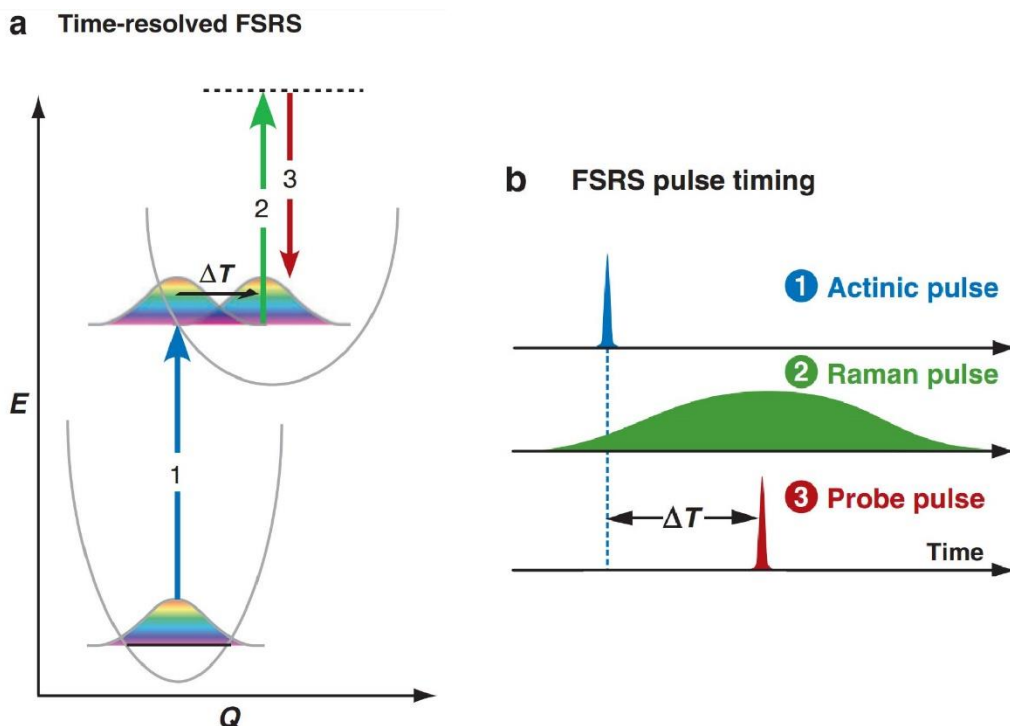


Figure 9.1. Schematics describing FSRS experiments. a) Energy level diagram and b) pulse timing for a FSRS experiment. (1) The actinic pulse excites the molecule from the GS to the ES. After some time delay, (2) the molecule is probed by the Raman pulse and (3) probe pulse which gives rise to the stimulated Raman transition. Adapted from Ref. (248)

We used FSRS to study the exciton dynamics in MDMO-PPV:PCBM BHJ solar cells. The FSRS signal of pure MDMO-PPV and pure PCBM films was measured to determine their signature features in the GS and ES. Then, the dynamics of the MDMO-PPV spectral features within a MDMO-PPV:PCBM BHJ film was probed with FSRS. Through a subtraction method, described below, the vibrations of the MDMO-PPV in the BHJ at the DA interface and MDMO-PPV only domains were differentiated. These are referred to as interfacial and bulk components, respectively. By using FSRS to disentangle and analyze signals from the bulk and interfacial regions in MDMO-PPV:PCBM BHJs, we found that excitons migrate to the interface primarily during the ~ 300 fs Franck–Condon (FC) relaxation time, before thermalization of the ES to the LUMO level.

9.2 Experimental methods

MDMO-PPV (H. W. Sands Corp.) and PCBM (Nano-C) were each dissolved into chlorobenzene at a concentration of 5 mg/mL. MDMO-PPV was stirred overnight at room temperature and PCBM was stirred at 50 °C. The PCBM solution was passed through a 0.45 μm

polytetrafluoroethylene filter prior to being mixed with the MDMO-PPV solution at a ratio of 1:0.6 MDMO-PPV:PCBM. Glass substrates were cleaned by successive sonication in soap solution, deionized water, acetone, and isopropanol for 15 minutes each at 40 °C and dried with nitrogen. The MDMO-PPV:PCBM solution was spin coated onto cleaned glass slides at 800 rpm for 60 s. All solutions and films were prepared in a nitrogen glovebox.

To minimize the damaging effect of pulsed laser excitation, the sample was raster scanned by a custom-built x-y translation stage. As a result, total sample degradation was never in excess of 10% as determined by comparing the ground and excited state stimulated Raman signal collected at different times throughout the experiment. The motorized stage was built by attaching two stepper motors to the x and y micrometers of the xyz sample translation stage via flexible drive shafts. Drive shafts were connected to the stage with 3D printed adapters. Flexible drive shafts introduce some hysteresis, thus this design is unsuitable for high precision positioning.

Samples were mounted in the custom-built x-y motorized translation stage placed at the focus of the actinic ($\lambda_{\text{max}} = 540$ nm, 60 fs, 30 nJ/pulse), Raman ($\lambda_{\text{max}} = 795$ nm, 2.8 cm^{-1} , 100 nJ/pulse,) and probe (830–940 nm, 8 fs, 10 nJ/pulse) beams of the femtosecond stimulated Raman spectrometer. For more details of the spectrometer please see Refs. (259, 260). During the measurement, the films were raster-scanned to mitigate sample degradation. On average, each molecule interacted with ~ 21 sets of pulses over the duration of the experiment.

9.3 Data processing

Data was acquired at different delay times between the actinic pump and the Raman probe pair with GS spectra acquired at regular intervals by shuttering the actinic pump. Raw GS and transient spectra from multiple acquisitions were averaged together. Cyclohexane was used as a reference to calibrate the Raman shift axis. Figure 9.2 presents raw GS spectra for the pure MDMO-PPV film (blue), the MDMOPP:PCBM BHJ (green) and the estimated interfacial component of the BHJ (red).

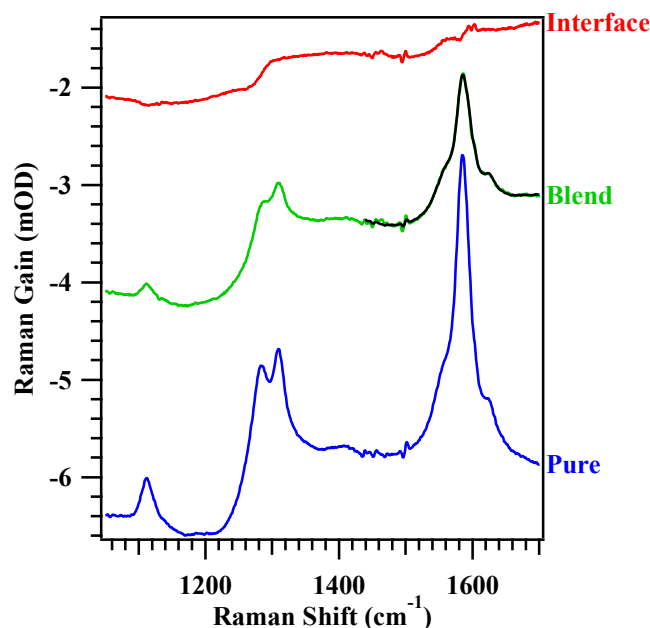


Figure 9.2. Estimating the ground state donor-acceptor interfacial spectrum. The raw GS spectrum of the BHJ (green) is fit to a combination of the GS spectrum of the MDMO-PPV film (blue) multiplied by a constant, a sum of three Lorentzian line shapes and a third order polynomial. The fit is shown as the black line. The extracted scale factor is used to subtract the bulk MDMO-PPV component from the BHJ spectrum revealing the interfacial component (red).

To isolate the GS spectrum of the DA interface, the C=C stretching region (1440-1750 cm^{-1}) of the GS spectrum of the BHJ film was fit to the sum of the GS spectrum of the pure MDMO-PPV film scaled by a constant (representing the bulk MDMO-PPV component), three line shape functions (representing the DA interfacial component) and a 3rd order polynomial (representing the background). The fit is shown as the black line in Figure 9.2. The extracted scaling factor was used to subtract the bulk MDMO-PPV component from the BHJ spectrum, yielding the interfacial spectrum. It is clear from this procedure that the spectrum of the BHJ films cannot simply be represented as an admixture of the pure MDMO-PPV and pure PCBM spectra. Note that PCBM has only one visible peak in the observable Raman window for this experiment at 1465 cm^{-1} , see Figure 9.3.

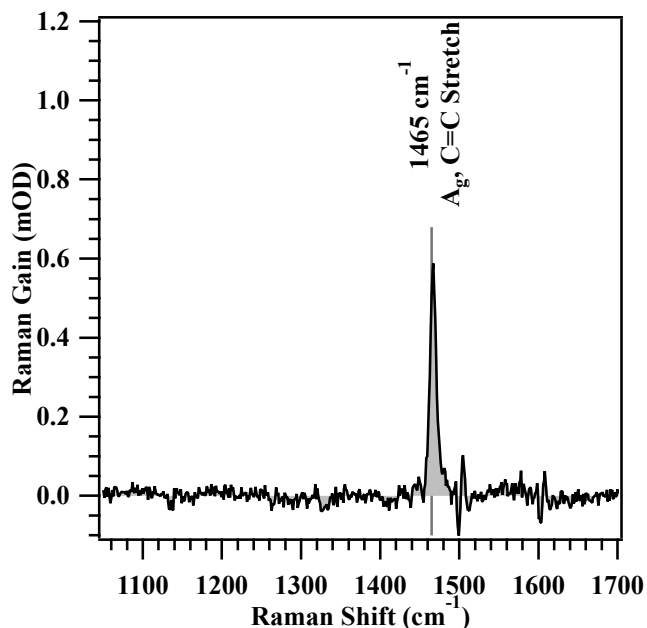


Figure 9.3. Stimulated Raman spectrum of a pure PCBM film taken under the same conditions as the MDMO-PPV and BHJ. Only one Raman mode is observable at 1465 cm^{-1} and it corresponds to a totally symmetric C=C stretch (261).

ES spectra were processed as follows. First, the GS spectrum was subtracted from all ES spectra yielding one-to-one subtracted spectra. The one-to-one subtracted spectra were fit in the C=C region to the sum of a scaled GS spectrum, a 3rd order polynomial, and two dispersive Lorentzian line shapes to optimize the subtraction process. To avoid additional noise, the extracted scale factors were then fit to a multi-exponential decay, and the fit curve was used to correct the over-subtracted GS revealing the pure ES spectra. To isolate the ES spectra of the DA interface, the MDMO-PPV film ES spectra were multiplied by the GS scale factor determined when isolating the GS interfacial spectrum and subtracted from the ES spectra of the BHJ film, yielding the ES spectra of the DA interface. Subsequently, the ES spectra of the MDMO-PPV in the bulk and at the DA interface were fit to a sum of dispersive Lorentzian line shapes and a 7th order polynomial, representing the baseline. All further data analysis was performed using spectra with the algorithmically estimated baseline removed and with peak parameters extracted from the fitting. Both the MDMO-PPV bulk and interfacial spectra have real and dispersive components, and the bulk species has two C=C stretches, one at 1586 cm^{-1} and one at 1563 cm^{-1} , while the interfacial species has only one at 1562 cm^{-1} . Figure 9.4 presents the ES spectra (black, shaded) of MDMO-PPV in the bulk (a) and at the interface (b), along with fits to the model function described above (red). The estimated baselines are shown in blue. Figures 9.5 (a) and (b) present the C=C stretching region of the bulk and interfacial components, respectively, with baselines removed and color coded according to time delay. To summarize, simultaneous analysis of both the BHJ and the pure MDMO-PPV and PCBM films allowed the MDMO-PPV signal from the DA interfacial region to be isolated from that of the MDMO-PPV in the bulk by subtraction.

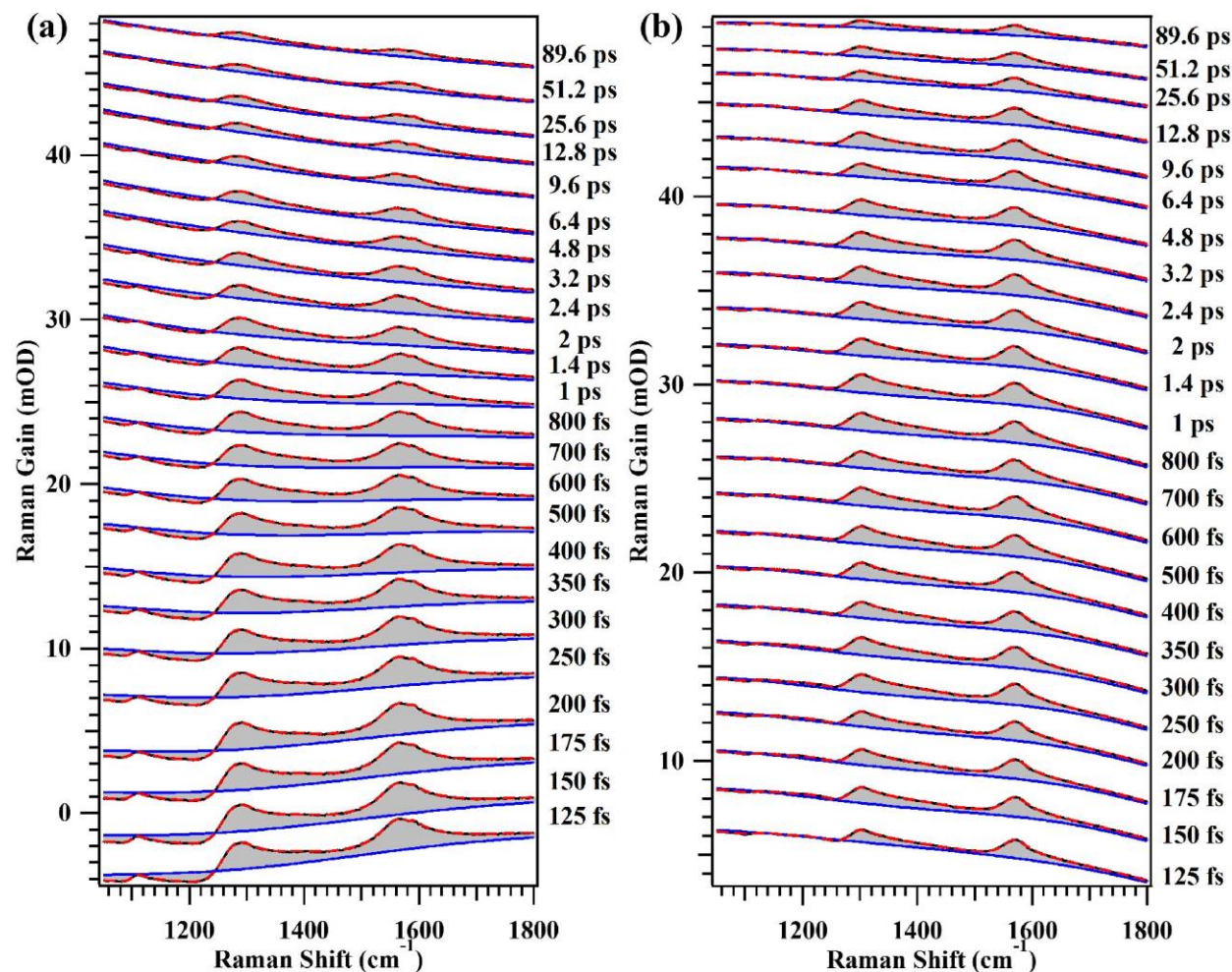


Figure 9.4. Data analysis of MDMO-PPV ES spectra. a) Transient spectra of the pure MDMO-PPV films with the GS contribution removed. b) Transient spectra of the interfacial component with the GS and bulk contributions removed. Data is shown as the black shaded curves and fits to a model function consisting of a 7th order polynomial baseline (representing the non-resonant background) and a sum of dispersive Lorentzians are shown as the red dashed curves. The estimated baselines are shown as blue lines.

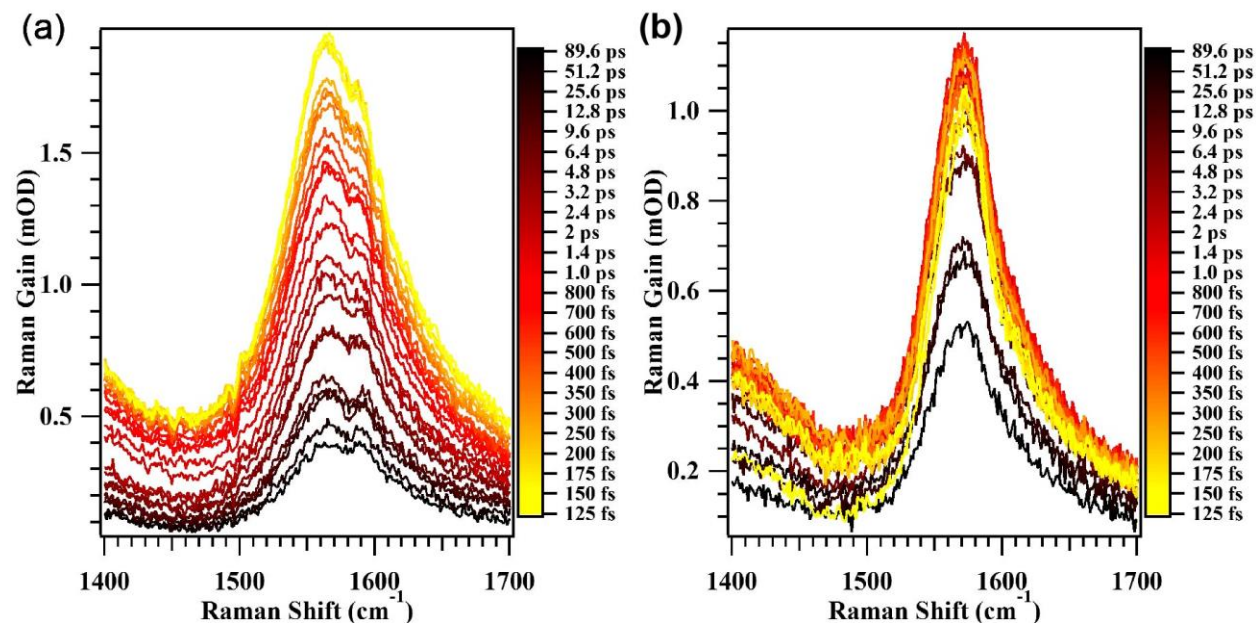


Figure 9.5. ES spectra of the C=C stretching region after data processing of the bulk films (a) and the interfacial (b) components presented with their estimated baselines removed. Note that the C=C intensity decay of the MDMO-PPV films is monotonic while that of the MDMO-PPV interfacial component is not.

9.3 Results and discussion

Figure 9.6 presents the GS (shaded) and ES (lines) stimulated Raman spectra of the MDMO-PPV in the bulk (blue) and at the interface (red) within the MDMO-PPV:PCBM BHJ at selected time delays. The PCBM GS Raman signal is barely visible in the GS interfacial spectrum at 1465 cm^{-1} (Figure 9.3), and no distinct PCBM ES Raman signal was observed, likely due to unfavorable resonance conditions. Dashed gray lines in Figure 9.6 mark the frequencies of the GS bulk spectrum. Assignment of these modes was facilitated by DFT calculations at the B3LYP/6-311G++(D,P) level performed on the monomer structure shown in Figure 9.6. Figure 9.7 presents a comparison between the bulk MDMO-PPV GS spectrum (black), the DFT predicted neutral (blue) and radical cation (red) monomer spectra, along with the ES interfacial spectrum at 4.8 ps delay (purple). Thick vertical lines indicate the calculated frequency and Raman intensity of the vibrational modes; spectra represent the convolution of these lines with a 20 cm^{-1} FWHM Lorentzian lineshape. Asterisks indicate artifacts that are the result of modeling the monomer in place of the polymer. Specifically, these marked modes are primarily due to different motions of the methyl groups put in place of the repeat monomer units. Another consequence of modeling the monomer rather than the polymer is that the intensity of the backbone C=C stretch at 1629 cm^{-1} is grossly overestimated. In spite of these artifacts, strong overall agreement is found between the neutral monomer calculation and the MDMO-PPV thin film spectrum. Correspondences between modes of different spectra are shown with black arrows. The radical cation calculation predicts a significant red shift in all C=C frequencies upon oxidation and a significant decrease in the 1629 cm^{-1} C=C backbone stretching mode. The GS interfacial spectrum has similar features albeit with much lower intensities, and the 1284 cm^{-1} ring stretch and backbone C-H rock mode is strongly dispersive. The final assignments of the vibrational modes are summarized in Figure 9.6.

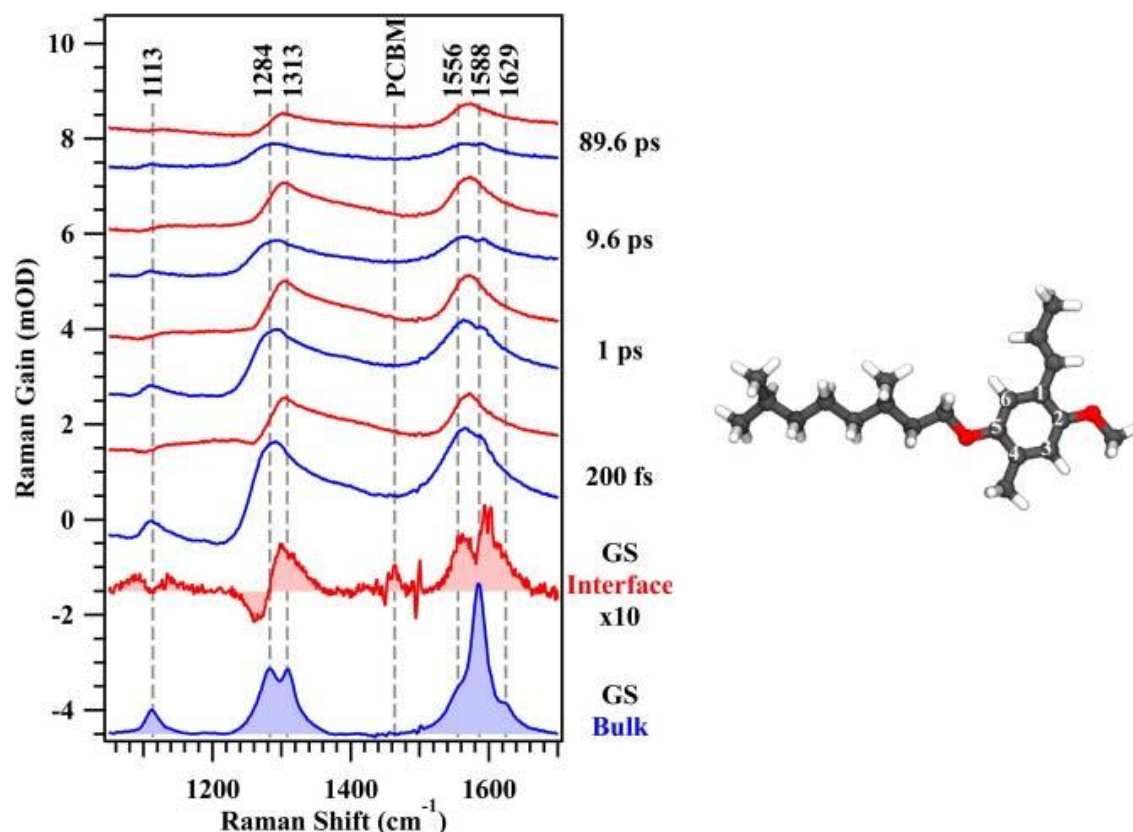


Figure 9.6. Ground state and transient MDMO-PPV stimulated Raman spectra. Steady-state (shaded) and transient (lines) stimulated Raman spectra of MDMO-PPV in the bulk (blue) and at the interface (red) in the BHJ film. Structure of the MDMO-PPV monomer is shown to the right. Mode frequencies are marked with dashed gray lines and have the following approximate characters: 1113 cm^{-1} , ring deformation (ϕ def.) and alkane H-rock; 1284 cm^{-1} , ϕ def. and backbone (bb) H-rock; 1313 cm^{-1} , ring breathing (ϕ br.) and bb H-rock; 1556 cm^{-1} , $\text{C}_1=\text{C}_6 + \text{C}_3=\text{C}_4$ stretch; 1588 cm^{-1} , $\text{C}_1=\text{C}_2 + \text{C}_4=\text{C}_5$ stretch; 1629 cm^{-1} , bb $\text{C}=\text{C}$ stretch. A PCBM Raman peak is visible at 1465 cm^{-1} .

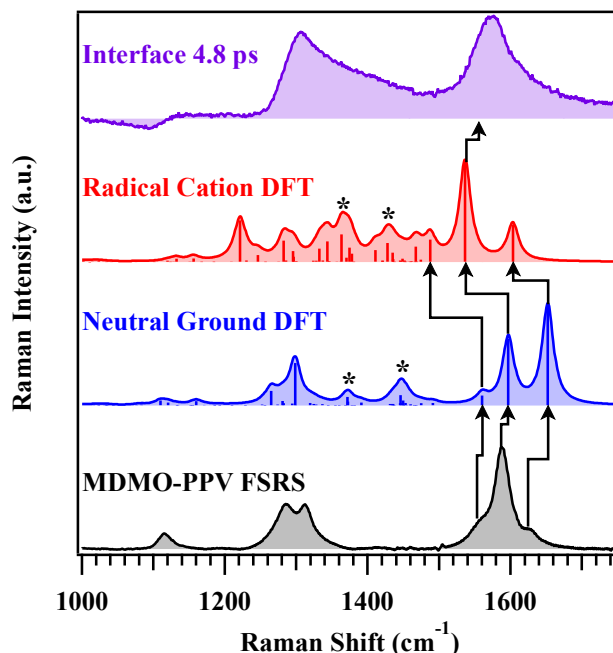


Figure 9.7. Comparing measured stimulated Raman spectra to calculated spectra to identify vibrational modes. Spectrum of the GS of pure MDMO-PPV (black), the predicted spectra of the neutral monomer (blue) and radical cation (red) along with the ES of MDMO-PPV at the DA interface at 4.8 ps delay (purple). Correspondences between spectra are shown by the black arrows. Predicted frequencies have been scaled by a factor of 0.97 to better agree with the experimental data. Features marked with asterisks are artifacts caused by modeling the monomer instead of the polymer. All C=C stretching frequencies are predicted to red shift by over 50 cm^{-1} upon oxidation, while the lower frequency modes are predicted to blue shift slightly. In addition, the 1588 cm^{-1} peak is predicted to gain significant intensity compared to the other C=C stretches, in agreement with the observations presented in Figure 9.6.

In Figure 9.6, MDMO-PPV ES spectra in the BHJ bulk (blue) and interface (red) differ significantly from the GS spectra and from each other. The ES spectra for both species are nearly twice as broad as the corresponding GS spectra, consistent with previous results (262), indicating that the ES vibrational dephasing time is significantly shorter than that of the GS. Furthermore, the 1629 cm^{-1} backbone C=C stretching mode has lost appreciable intensity in both ES spectra, to the point that it is no longer observable as a distinct peak, which is consistent with the system undergoing a $\pi \rightarrow \pi^*$ excitation. Finally, both the bulk and interfacial ES spectra contain a number of strongly dispersive features. Comparison of these with the aid of DFT calculations (see Figure 9.7) suggests that the interfacial spectra lack the 1556 cm^{-1} mode and that the 1588 cm^{-1} mode has strongly red-shifted to 1561 cm^{-1} ; both observations are consistent with the formation of a radical cation. Moreover, electrical and chemical oxidation of PPV has been shown to produce nearly identical spectral changes (263, 264).

The sum of the real and dispersive amplitudes of the C=C stretches for each species shown in Figure 9.5 is used to generate Figure 9.8, which presents the normalized C=C stretching intensities of both MDMO-PPV in the BHJ bulk (blue squares) and at the DA interface (red circles). Multiexponential fits to the data are shown as dashed lines, and the extracted model parameters are presented in the figure legend. The bulk MDMO-PPV in the BHJ

decays in a monotonic fashion with three characteristic time constants (0.28, 3.1, and 170 ps), each corresponding to approximately one-third of the decay. We attribute the decays to FC relaxation, meaning relaxation along low frequency degrees of freedom, and to internal conversion to the GS, respectively. However, the kinetics of MDMO-PPV at the DA interface are not monotonic, with a fast (280 fs) rise time and a slower overall decay composed of 7 and 170 ps components, with the latter comprising nearly two-thirds of the decay. We attribute the initial rise to fast exciton diffusion from the bulk to the interface. The slower decay dynamics of the interface signal could be the result of two phenomena: additional, slower, exciton diffusion from the bulk to the interface, or increased disorder at the interface and steric interactions with the PCBM layer, which would hinder the nuclear motion necessary for internal conversion. In the first case, the slower exciton diffusion would lead to an increase of the interfacial signal but would be convoluted with the natural decay of the ES, whereas in the second case the natural decay itself would be delayed.

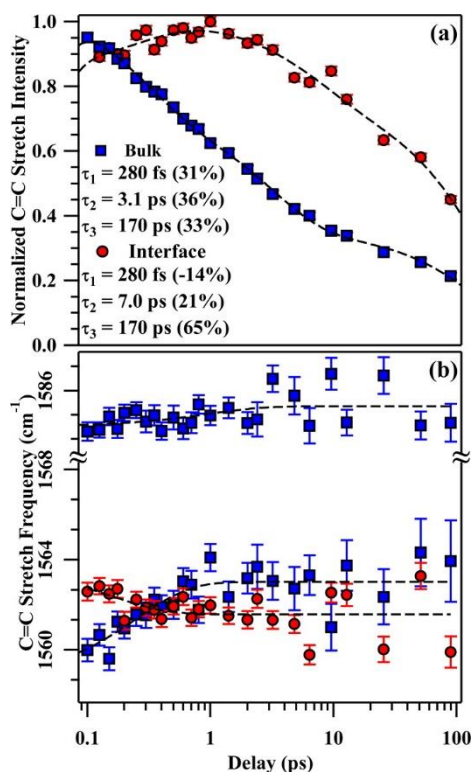


Figure 9.8. Variation in C=C stretch intensity and frequency with delay after excitation pulse. (a) Normalized C=C stretching intensities and (b) frequencies for the bulk (blue squares) and interfacial (red circles) species. Fits are shown as dashed lines; raw data is shown in Figure 9.4 and 9.5. The C=C intensity for the bulk decays monotonically while that of the interface has an initial 280 fs rise, which is attributed to exciton transport from the bulk to the interface. Both bulk C=C modes shift to higher frequencies, while that of the interface shifts to lower frequency on the picosecond time scale. On average, the interfacial species is much longer lived than that of the bulk.

Figure 9.8b presents the C=C stretching frequencies for MDMO-PV in the bulk (blue squares) and at the DA interface (red circles). On the picosecond time scale, both bulk modes blue shift slightly and the interface experiences a small red shift. The blue shift can be understood in terms of vibrational cooling of the ES. In contrast, the red shift of the interface

indicates that the molecular structure is reacting to the loss of a π -bonding electron after it has transferred to the PCBM LUMO.

These time-resolved stimulated Raman measurements on pure donor (MDMO-PPV) and blended (MDMO-PPV:PCBM) films reveal new information on exciton dynamics in BHJs. In particular, analysis of the Raman data allows the unique vibrational signal from the donor polymer in the interfacial region to be deconvoluted from that of the bulk within the BHJ, enabling analysis of the complex population dynamics. The kinetics of the isolated DA interfacial signal reveals that photogenerated excitons are primarily mobile early in the exciton lifetime, i.e., before thermalization.

This new understanding of exciton dynamics is summarized pictorially in Figure 9.9. Figure 9.9a presents a physical picture of the BHJ, and Figure 9.9b presents a schematic kinetic model based on the data obtained here. Initially, the actinic pump pulse excites both the bulk and interfacial components of the donor layer (green arrows). Excitons prepared in the interfacial region quickly (<50 fs) participate in charge transfer and dissociate into free charges (curved green arrow) (262). Within the BHJ, both the excited MDMO-PPV far from the interface and the radical cations at the interface relax out of the FC region within 280 fs along high frequency Raman active nuclear degrees of freedom. During this time, excitons in the MDMO-PPV bulk are highly mobile. This mobility has two possible origins: localized excitons that hop from one site to another, or delocalized excitons whose wave functions extend over a large volume (83, 265–270). The first case would result in diffusive (power law) kinetics, while the second would result in Fermi Golden Rule (exponential) kinetics. A ~ 280 fs rise in the interfacial signal is observed; unfortunately, the signal-to-noise ratio is insufficient to differentiate between the two possibilities and an exponential model was used to estimate the rise time. Regardless of the precise mechanism, it is clear that exciton mobility is only significant during FC relaxation (265, 266). Excitons that reach the interface quickly dissociate, leading to the observed increase in the radical cation (interfacial) signal. Following FC relaxation, the exciton diffusion rate is reduced dramatically. Bulk and interfacial MDMO-PPV in the BHJ continue to structurally relax via low-frequency motions for 3 and 7 ps, respectively, and internal conversion occurs on the 170 ps time scale (red arrows).

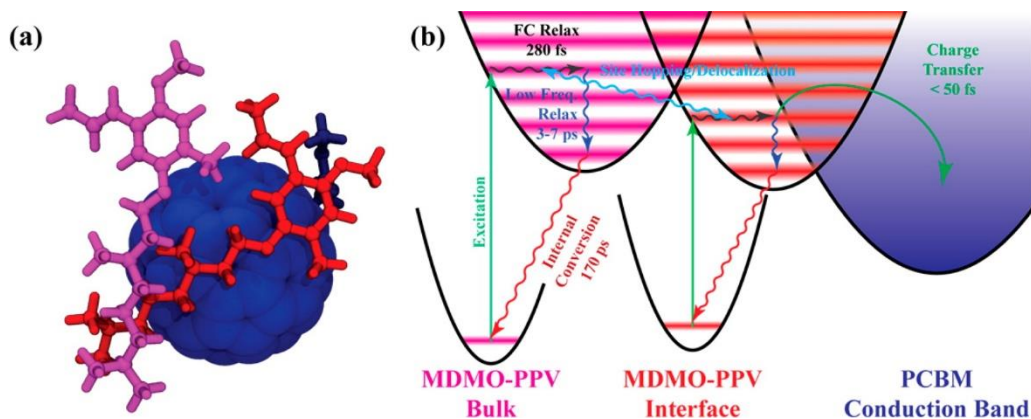


Figure 9.9. Schematic of exciton and carrier dynamics in MDMO-PPV:PCBM BHJs. a) Molecular depiction of the MDMO-PPV:PCBM system; PCBM, bulk, and interfacial MDMO-PPV are highlighted in blue, magenta, and red, respectively. (b) Depiction of the ground and excited state potential energy surfaces for the bulk and interfacial MDMO-PPV components along with the PCBM LUMO. The broadband pulse excites both MDMO-PPV components simultaneously (green arrows). Following excitation, each constituent relaxes out of its FC region along a few high-frequency Raman active degrees of freedom within 280 fs (wavy gray arrows). During this time, excitons created in the MDMO-PPV layer are relatively mobile (site hopping/delocalization, wavy cyan arrow). Additionally, excitons in the interfacial layer separate into free charge carriers (charge transfer, curved green arrow). However, once FC relaxation is complete, the diffusion becomes much slower. Structural relaxation along lower frequency degrees of freedom continues on the 3–7 ps time scale (wavy blue arrows) before internal conversion on the 170 ps time scale completes the photocycle.

Exciton mobility is a key component of the charge generation process in OSCs. Here, we have exploited the capabilities of FSRS to isolate the unique vibrational signature of the interface and have shown that prolonged exciton lifetimes do not necessarily imply high mobility. As excitons can only be split into free charge carriers at the DA interface, it is important to tailor mobility to domain size or vice versa. However, larger domains are beneficial for two reasons: first, more donor and acceptor domains would be contiguous from the charge carrier generation site to the electrodes, aiding charge collection, and second, larger domain sizes would provide fewer opportunities for charge recombination. Tailoring this parameter requires new and more sophisticated measurements (83, 255, 266, 270), such as FSRS, which are sensitive not only to the electronic state but also the nuclear configuration.

9.4 Conclusion

These FSRS experiments on BHJ films adds to a growing body of evidence that excitons are primarily mobile (either through hopping or delocalization) early in the ES lifetime (83, 265, 266, 269–272). Conversely, earlier reports measured exciton diffusion times of multiple picoseconds to nanoseconds and exciton diffusion lengths of 10 nm on average (273–275). These two bodies of work can be unified under the hypothesis that there are two different exciton diffusion regimes, evidence of which has been previously reported (266, 269): a fast regime occurring before thermalization (possibly driven by exciton delocalization), and a slow regime following FC relaxation. Through the FSRS experiments it was not possible to corroborate the existence of the slow diffusion process because such a signal would be convoluted with the natural decay of the interfacial ES. Even so, the results presented here, and in previous work, are

beginning to demonstrate that the fast diffusion regime occurring before ES thermalization is the greatest factor contributing to exciton diffusion and the resulting exciton separation (83, 265, 266, 269, 270, 272).

If this hypothesis is correct, then simply increasing the ES lifetime will not increase exciton mobility and exciton separation at the DA interface. Instead, focus should be placed on slowing FC relaxation and minimizing the reorganization energy. For instance, MDMO-PPV is a relatively poor OSC donor, and Wise and Gray have shown that it has large dimensionless displacements along the C=C stretch and phenyl deformation modes (264). However, it is difficult to maintain good conjugation (electrical conductivity) while reducing the ES equilibrium nuclear displacement (Δ) that drives the structural changes associated with FC relaxation. An associated problem lies in controlling the anharmonic couplings that allow energy to flow from the high energy modes to the low energy ones, thereby making FC relaxation irreversible (257, 276). Devising synthetic strategies to achieve these goals would be difficult but potentially fruitful. In the meantime, these results reveal a relatively simple and potentially effective empirical screening method: any molecule that experiences a pronounced resonance Raman effect and has a large fluorescence Stokes shift (i.e., has a large Δ) will likely be a less efficient OSC material.

As a future study, FSRS could be used to understand variations in hot exciton mobility among BHJ systems of various efficiencies. This experiment would provide insight into the importance of hot excitons in OSCs. Specifically, it would be interesting to observe the effect of crystallinity, via variable annealing times, on exciton mobility because many reports suggest that crystallinity is critical for improving η_{ES} . Additionally, FSRS could be used to determine if the exciton dynamics change when the permittivity of the BHJ increases. Does adding CA to the BHJ change only the CT state energy or also the exciton mobility?

My research in OSCs has focused on understanding and manipulating exciton behavior in organic semiconductors in order to develop design principles to improve PCE. Chapters 7 – 9 highlight the most significant challenge in OSCs: managing excitons. Excitons pose a major limitation because an efficient process must exist to dissociate the excitons to generate photocurrent while minimizing the energy lost in that process to achieve large V_{OC} (60, 222). My research in Chapters 7 and 8 investigate how increasing permittivity can lead to lower E_{eb} . And, Chapter 9 shows that understanding the dynamics of exciton diffusion and dissociation is challenging and complex. Even with a better understanding of excitons in organic semiconductors, each polymer or molecular semiconductor has unique behavior that is also dependent on processing conditions, meaning optimizing device performance is different for every material.

The challenges that excitons pose for OSCs provides excellent motivation for scientists interested in learning more about excitons. But, for efficient solar cells, is it ideal if EHPs, rather than excitons, are directly generated upon light absorption. Although the highest OSC efficiency of 11.5% is impressive for an excitonic solar cell (101), it is too low to encourage large scale commercialization due to issues such as forming high-quality large-area solution processed films and ensuring 25-year low cost oxygen encapsulation. Especially when the price of silicon is low, little motivation exists to work through these challenges to for the sake of low cost OSCs (277, 278). On the other hand, organic semiconductors are highly suitable for photodiodes, OFETs, and OLEDs, where they are already used commercially. For example, OLEDs are used for the display in many Samsung smartphones (279, 280).

During my Ph.D., I have been fascinated by critical properties of OSCs to improve PCE. But, a new exciting thin film solar cell material has recently emerged: hybrid organic-inorganic perovskites, which have exhibited exceptional PCEs within only a few years of research. I wanted to understand the properties that limit the efficiency in perovskite solar cells by using the expertise I developed in characterizing OSCs and manipulating properties to maximize PCE.

The next section of this dissertation describes my efforts to optimize a scanning probe microscopy technique to effectively characterize local optoelectronic processes that limit PCE in perovskite solar cells. By better understanding hybrid perovskites, I hope that the research community can learn to process and tune these materials such that these solar cells approach their maximum theoretical PCE.

Optoelectronic processes limiting power conversion efficiency in perovskite photovoltaics

Chapter 10

Facet-dependent photovoltaic efficiency variations in single hybrid halide perovskite grains

Adapted from manuscript:

Sibel Y. Leblebici, Linn Leppert, Yanbo Li, Sebastian E. Reyes-Lillo, Sebastian Wickenburg, Ed Wong, Jiye Lee, Mauro Melli, Dominik Ziegler, Daniel K. Angell, D. Frank Ogletree, Paul D. Ashby, Francesca M. Toma, Jeffrey B. Neaton, Ian D. Sharp, Alexander Weber-Bargioni. *Under review*.

10.1 Introduction

For hybrid organic-inorganic halide perovskite solar cells, the rapid increase in PCE is astounding considering that the origins of their highly efficient photovoltaic effect, as well as efficiency loss mechanisms, are not fully understood. The majority of initial reports on perovskite solar cells were focused on processing thin films to improve device efficiency through trial-and-error processing with little focus on understanding the material or device properties (113, 122, 130, 281–287). The main technique to characterize thin films was, and often still is, SEM, and it was assumed that larger grains led to better performance but with little direct evidence (123, 288, 289). To systematically increase solar cell efficiency, more information about the material's properties was needed, specifically about the exact photocurrent generation and photovoltaic loss mechanisms. Some of the most important discoveries on hybrid halide perovskite optoelectronic mechanisms revealed surprisingly high carrier mobilities (126, 137, 138) and long lifetimes (139) for a polycrystalline material. From these results, it was assumed that the processes within the solar cell active layer were homogenous (290), since these characterization techniques do not access the native spatial dimensions of I_{SC} and V_{OC} .

As I mentioned in Chapter 5, solar cell materials, particularly those that are polycrystalline, are ideally studied at a resolution that captures significant variations in morphology, e.g. grain boundaries and other defects, hence the nm scale. Systematic optimization of solar cells to improve PCE requires correlating the local morphology to local optoelectronic properties.

The need to understand nanoscale behavior has led to several recent nanoscale investigations of lead halide perovskites films and solar cells. Edri et al. established that perovskite solar cells function as p-i-n solar cells. EBIC was used on perovskite solar cell cross-sections to map charge separation efficiency and collection in the out-of-plane direction (134). This study provided the first realistic insight into the transport of charge in perovskite solar cells. Similarly, Bergmann et al. probed surface potential variations across perovskite solar cell cross-sections using KPFM and also found that these devices have p-i-n behavior. Also, the effect of grain boundaries has been investigated by scanning probe based techniques (145, 291, 292); however, the debate on the benefit or detriment of grain boundaries is still ongoing. Recent studies found surprisingly strong intergrain PL (142) and cathodoluminescence (143) heterogeneity, which suggests that optoelectronic properties, such as V_{OC} , may also exhibit strong local variation (293). These results highlight the pressing need to study not only various optoelectronic processes related to photovoltaics but also to directly measure local V_{OC} and I_{SC} to understand the factors affecting efficiency in these systems. However, while these properties in inorganic and polymer photovoltaic materials have been studied with nanoscale resolution using scanning probe techniques (182, 294, 295), no studies have yet determined the governing optoelectronic properties for perovskite photovoltaic devices at their native length scales (10 – 100 nm) or what limits their efficiency.

I locally probed and mapped the parameters that determine solar cell performance – V_{OC} , I_{SC} , and dark drift current (I_D) – close to their native length scales. This was accomplished by

employing a customized cAFM technique to provide insight into these critical performance-determining parameters with nm scale resolution and supported by DFT calculations. I found significant intragrain heterogeneities, which arise from facet-dependent variations of surface defect states that strongly impact device-scale PCE. As a result, the macroscopic solar cell and LED performance of lead halide perovskites could be optimized by controlling the crystal orientation and facets at interfaces for both polycrystalline and single crystal devices (126).

10.2 Sample preparation and device performance

The two-step low pressure vapor-assisted solution process to fabricate $\text{MAPbI}_{3-x}\text{Cl}_x$ films is described as follows (136). First, a $\text{PbI}_2/\text{PbCl}_2$ solution is spin coated onto TiO_2 coated FTO glass substrates. Second, the film is converted to $\text{MAPbI}_{3-x}\text{Cl}_x$ by annealing the film in $\text{CH}_3\text{NH}_3\text{I}$ vapor at low pressure for 2 hours. This fabrication technique creates continuous films and reduced hysteresis effects in a planar photovoltaic device architecture. Planar solar cells with the structure FTO/dense TiO_2 / $\text{MAPbI}_{3-x}\text{Cl}_x$ /spiro-OMeTAD/Au have an average PCE of 15.7%, V_{OC} of 1.0 V, and J_{SC} of 21.3 mA/cm^2 (136). A representative J - V curve is shown in Figure 10.1a. For the cAFM measurement, the $\text{MAPbI}_{3-x}\text{Cl}_x$ surface must be exposed to correlate morphology and current. Thus, to directly access the perovskite surface, the spiro-OMeTAD HTL and Au contact are omitted and the Pt coated AFM tip acts as the electrode. A macroscale solar cell with a structure mimicking the cAFM measurement (FTO/ TiO_2 / $\text{MAPbI}_{3-x}\text{Cl}_x$ /Pt) that was processed in parallel with the samples studied with cAFM has a V_{OC} of 0.51 V and J_{SC} of 16.2 mA/cm^2 . Figure 10.1b shows a representative J - V curve for the mimic device. The reduced V_{OC} is the result of removing the $\text{MAPbI}_{3-x}\text{Cl}_x$ /spiro-OMeTAD heterojunction, so only the TiO_2 / $\text{MAPbI}_{3-x}\text{Cl}_x$ heterojunction contributes to the V_{OC} (134).

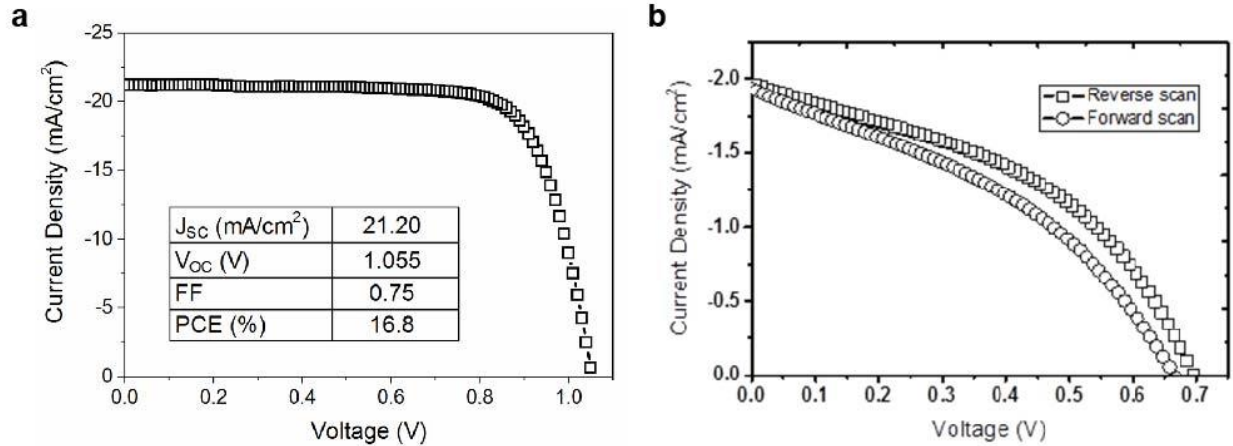


Figure 10.1. Current density – voltage curves for $\text{MAPbI}_{3-x}\text{Cl}_x$ solar cells. a) Representative J - V curve of a macroscale $\text{MAPbI}_{3-x}\text{Cl}_x$ solar cell. The solar cell has the structure FTO/dense TiO_2 / $\text{MAPbI}_{3-x}\text{Cl}_x$ /spiro-OMeTAD/Au and an active area of 0.16 cm^2 . b) J - V curve for a macroscale device mimicking the cAFM measurement. The device has the structure FTO/dense TiO_2 / $\text{MAPbI}_{3-x}\text{Cl}_x$ /Pt.

10.3 Python image analysis

The Python code for image registration utilizes the Oriented FAST and Rotated BRIEF binary descriptor to match objects in the images, and the RANSAC method is used to filter the

matches in order to determine the transform (296). Image registration allowed for careful comparisons of I_D , I_{SC} , and V_{OC} of the exact same region. To compare I_{SC} to the grain size, I used the watershed method to identify crystal grains and calculate the average I_{SC} per grain.

10.4 Conductive atomic force microscopy

cAFM allows for the simultaneous measurement of current and topography. Measurements were performed using a Park Systems NX10 AFM encased in a nitrogen filled glovebox to prevent sample degradation. Samples can be stored at least one week in a nitrogen atmosphere without degradation. All measurements were conducted with relative humidity less than 1%. MAPbI_{3-x}Cl_x thin films on glass/FTO/compact TiO₂ substrates were studied using scanning probe analysis, omitting the HTL and top electrode found in the full solar cell to directly access the bare MAPbI_{3-x}Cl_x surface. The large surface roughness of the perovskite material, together with strong tip-sample interactions, pose significant challenges to perform cAFM using contact mode topography feedback. I observed three main artifacts (Figure 10.2) that convolute the current measurement when employing traditional contact mode AFM for cAFM measurements, which could lead to substantial misinterpretation of local photocurrent maps. In one case, the tip dragging on the surface causes the tip to become coated with material due to frictional forces. This material is likely some form of precursor because it is non-conductive and thus causes the AFM tip to be non-conductive. I imaged the AFM tips via scanning electron microscopy before and after measuring the perovskite samples in traditional cAFM, and observed large pieces of material on the tip after scanning. The other two artifacts are both due to changes in the electrical contact area between the tip and the sample and can be seen in the error signal image. In the first artifact, if the integral gain is too high, the tip oscillates on the surface and more current is measured. The second artifact arises if the set point is such that the error signal varies significantly due to changes in the topography, no current is measured in areas with low error signal. Examples of these artifacts are shown in Figure 10.2.

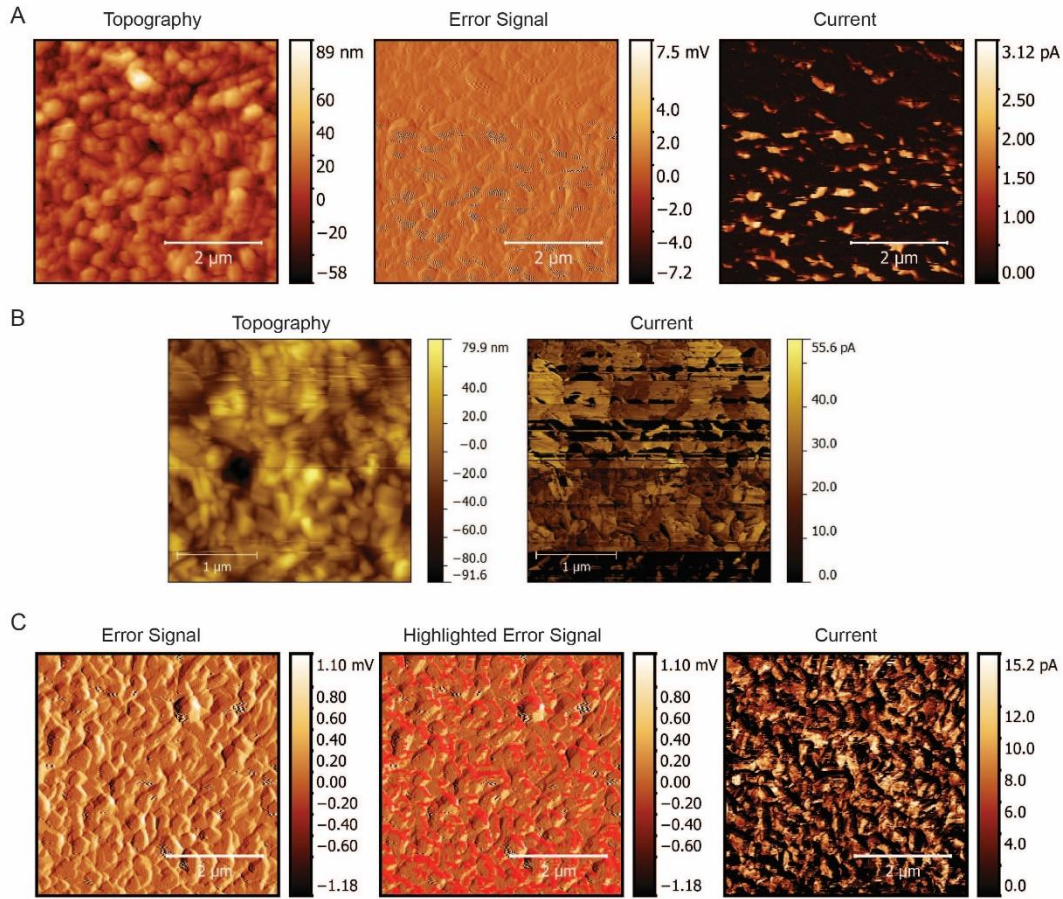


Figure 10.2. Artifacts caused by using standard cAFM with contact mode deflection. (a) High current due to tip oscillation. In the error signal image, the grey areas indicate where the tip was oscillating due to high gain in topography feedback mode. By comparing to the current map, it is clear that only those areas have high current. (b) No current is collected in certain areas because the tip becomes coated with non-conductive material and current is collected later in the scan when the material falls off the tip. (c) An artifact due to change in tip-sample contact area, which is shown in the error signal. In the error signal image, significant variations exist particularly at the grain boundaries where the gradient in the height image is largest. The areas of low current are marked in red in the highlighted error signal image. All areas with low error signal are highlighted. The extreme heterogeneity in current in this image is only an artifact.

To overcome the issues associated with traditional contact mode, I employed a modified cAFM technique in which, at each pixel, the tip approaches the surface, measures the photocurrent, retracts from the surface and moves to the next pixel, as shown in Figure 10.3a. More specifically, the tip approaches the surface over 5 ms to achieve an interaction force of 2 nN, the force is held constant while the current is sampled 80 times at 50 kHz, then the tip retracts over 5 ms and moves to the next pixel. This method, also referred to as PinPoint mode, differs significantly from tapping mode AFM because a contact mode tip is used, the tip is not oscillated, and the tip retracts and approaches at each pixel rather than adjusting the tip height to maintain a constant oscillation amplitude. In contrast to conventional cAFM, this technique eliminates friction, which reduces tip-sample deterioration, and maintains a constant contact area

while measuring current. Figure 10.3b shows a representative topography measurement of the $\text{MAPbI}_{3-x}\text{Cl}_x$ surface; the average surface roughness is 19.1 nm and grain size is 142 ± 38 nm.

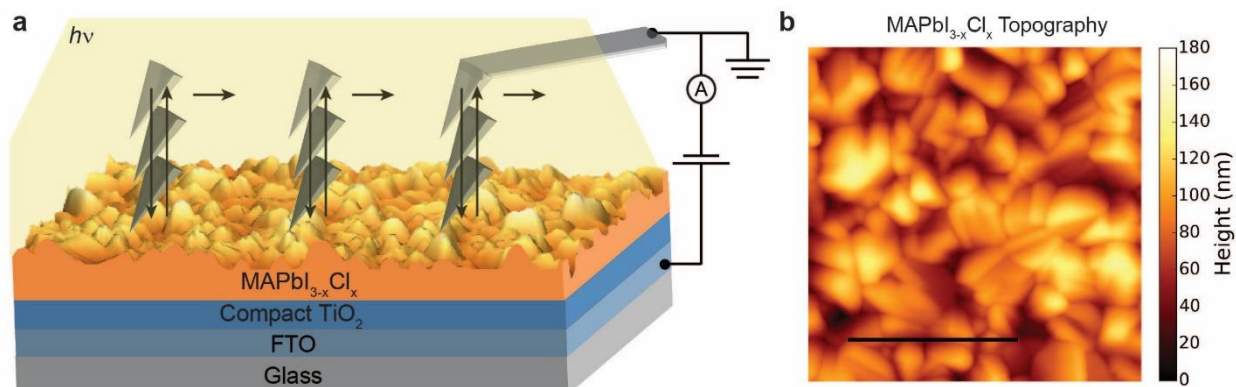


Figure 10.3. cAFM experiment on the surface of a $\text{MAPbI}_{3-x}\text{Cl}_x$ solar cell. (a) The entire sample surface is illuminated while a conductive AFM tip measures the photocurrent. Bias is applied to the FTO electrode and current is collected through the grounded platinum coated AFM tip. The arrows describe the approach-retract scan mode in which the tip approaches, measures, and retracts at each pixel, thereby minimizing potentially damaging tip-sample interactions. (b) A representative topography image of a $\text{MAPbI}_{3-x}\text{Cl}_x$ thin film illustrates the large surface roughness. The scale bar is 1 μm .

Again, the gentle PinPointTM mode was the key to perform reproducible and reliable topography and cAFM images on the rough $\text{MAPbI}_{3-x}\text{Cl}_x$ surfaces. As shown in Figure 10.4, height, error signal, adhesion, and surface gradient do not have an impact on the current measured in this mode, meaning the current measurements are free of any artifacts. This scan mode does require more measurement time (approximately 2 h for a 512×512 pixel image), but results in highly reproducible images (Figure 10.5). As shown in Figure 10.6, the drift on the Park NX10 microscope was typically 10 nm/h and successive scans were digitally aligned; thus, drift did not complicate interpretation of the results presented here.

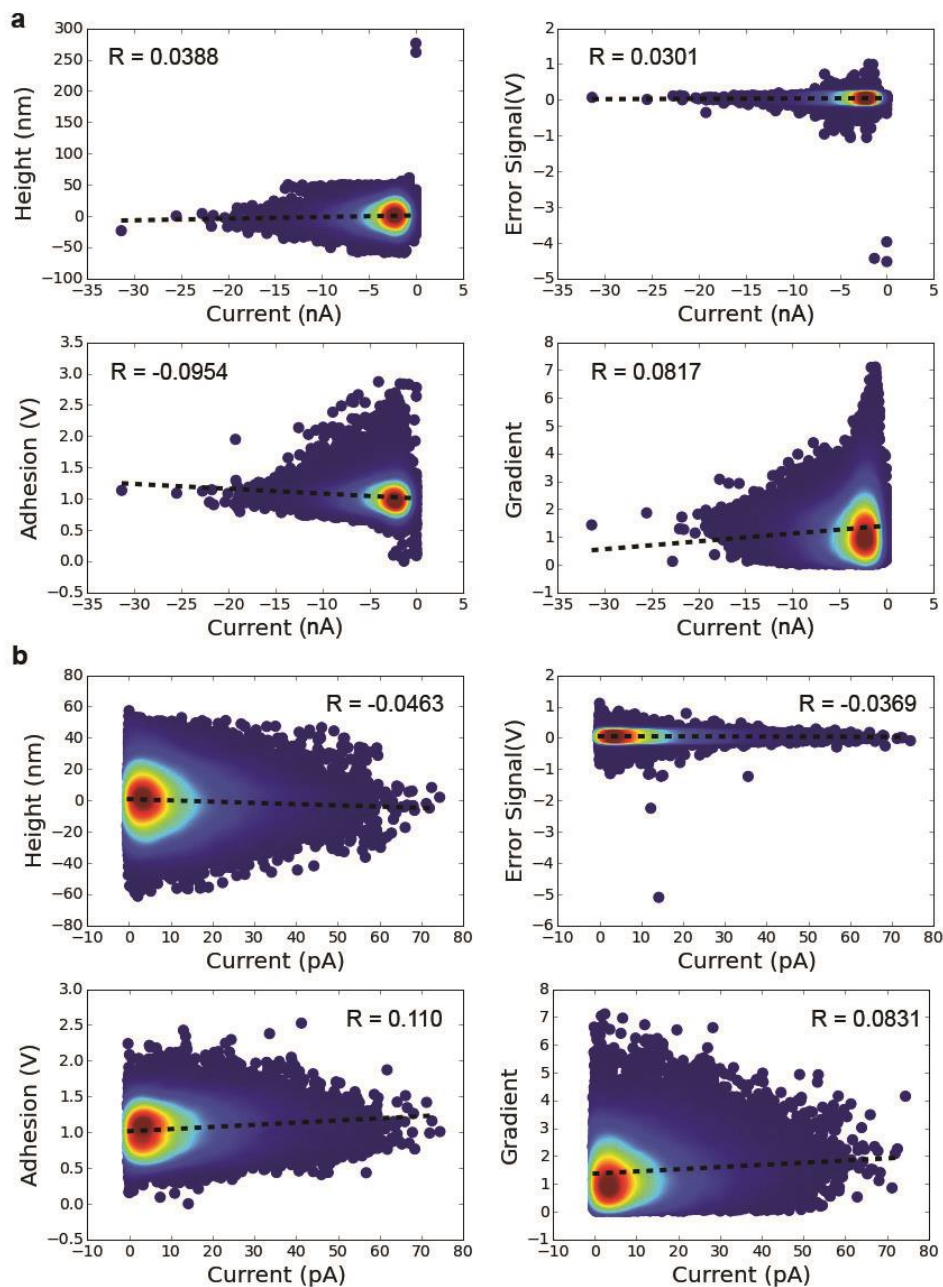


Figure 10.4. Scatter plots showing current measurements are not convoluted with other measured properties. Each point in the plot is the value of the pixel from the current map and the map designated by the y-axis. Scatter plots compare the I_D (a) and I_{SC} (b) to the simultaneously measured height, error signal, adhesion, and calculated slope. The dashed line is the linear regression and the correlation coefficient (R) is shown in the top right of each plot. The very small R values indicate that there is little to no correlation between current and other measured properties.

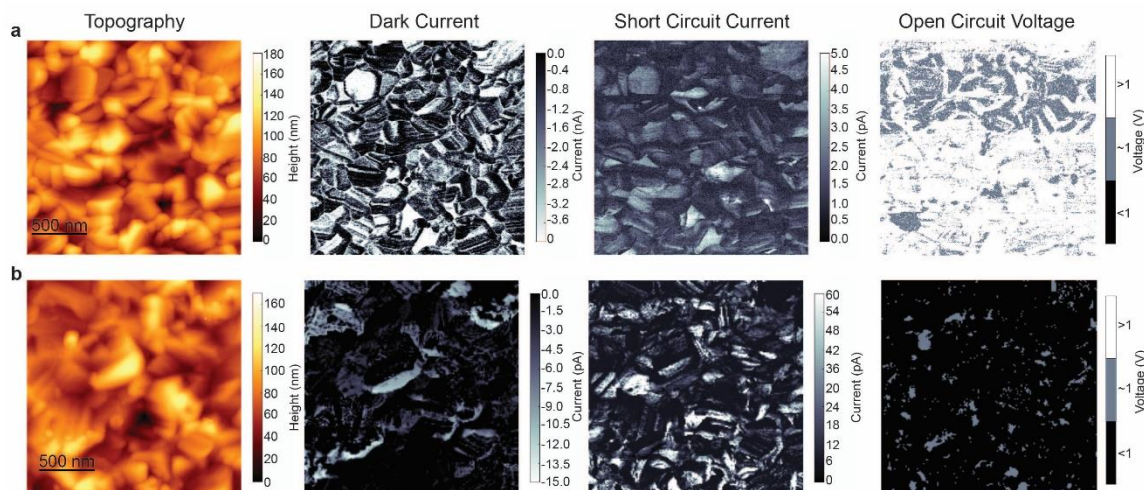


Figure 10.5. Topography, I_D , I_{SC} , and V_{OC} maps of other $\text{MAPbI}_{3-x}\text{Cl}_x$ samples. (a) Second sample where I_D was measured at -2 V and V_{OC} is relative to 1 V. (b) Third sample where I_D was measured at -2 V and V_{OC} is relative to 1 V. Significant heterogeneity is seen in different samples.

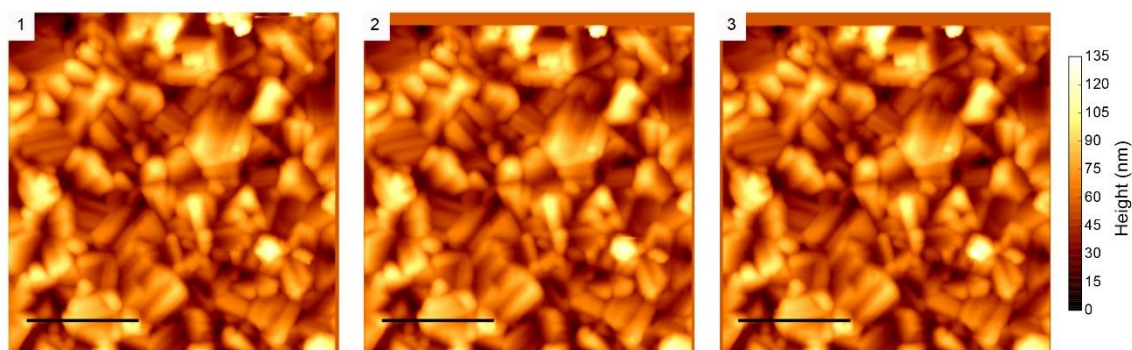


Figure 10.6. XY drift for three consecutively measured images. The images were measured in the order 1, 2, 3, with each imaging taking approximately 30 minutes to measure. The images have been aligned and the areas around the images indicate the drift. Though some minimal drift does occur, it is fully compensated for through the alignment of the images. The scale bar is 1 μm .

In the cAFM setup, the bias is applied to the FTO electrode, while the Pt tip is grounded. The current is measured directly after the tip using a preamplifier with 10^{10} gain. Because of this electrical configuration, negative voltage forward biases the solar cell and I_{SC} has a positive value. For the photocurrent maps, the sample is illuminated from above with a white LED having an output from 375 to 800 nm and a maximum power density of $24 \mu\text{W}/\text{cm}^2$ at 450 nm, see Figure 10.7 for the spectrum. Proper illumination of the tip apex/sample area was ensured using the following methods. I employed AdvancedTEC ContPt AFM probes (Nanosensors), often referred to as “elephant tips” because the tetrahedral tip protrudes from the end of the cantilever, which provides direct optical access to the point of contact between the tip apex and the sample. A 0.4 numerical aperture objective was used to focus the light onto the tip apex/sample from the top with a 24 degree half angle, ensuring uniform illumination of the tip/sample region. Employing a traditional rectangular AFM cantilever with top illumination did show shadowing

effects in the form of reduced signal-to-noise ratio. Since initial light exposure modifies the performance of lead halide perovskites, I light soaked the samples for an hour before characterizing the local performance under equilibrium conditions. The AdvancedTEC tips have a 25 nm radius of curvature and a 0.2 N/m force constant. Many tips were used to ensure that the tips were sharp and not contaminated by material from the perovskite surface. As soon as any tip modification was observed, I exchanged the tip. Data taken while the tip apex was modified were not considered for analysis.

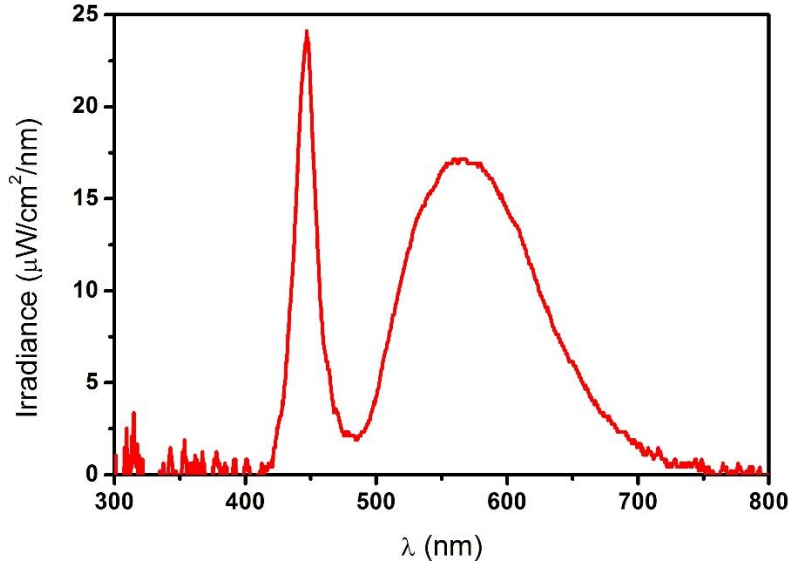


Figure 10.7. Power density spectrum of LED used to illuminate samples in cAFM.

To measure local PCE on the nanoscale using cAFM, I_{SC} , FF, and V_{OC} need to be measured. Ideally, V_{OC} and FF would be determined by measuring local IV curves with cAFM or V_{OC} would be measured using scanning potentiometry, but neither of these techniques were successful nor reproducible on $\text{MAPbI}_{3-x}\text{Cl}_x$. Applying a moderate bias between the FTO and the sharp AFM tip results in very large electric fields, which degrades the $\text{MAPbI}_{3-x}\text{Cl}_x$ surface and the AFM tip when the tip is at a single point for more than one second. The challenges in measuring local IV curves is also related to the issues of ion migration in lead halide perovskites, as was described in section 1.4.4. Ion migration is mitigated in the measurement of I_{SC} because no bias is applied. And, the electric field applied to measure V_{OC} opposes the built-in electric field, thus reducing the effective internal electric field even further, ensuring that the probed system remains far from the regime in which ion migration defines optoelectronic properties. Additionally, the tip is in contact with the sample for less than 2 ms, which is not long enough for ion migration at the biases used. Ion migration is expected to be reduced in these samples because the hysteresis is minimal (Figure 10.1b), the current is stable at P_{MAX} , and the V_{OC} is stable (Figure 10.8). These results suggest that ion migration in these films is not dominant in the bias range measured here.

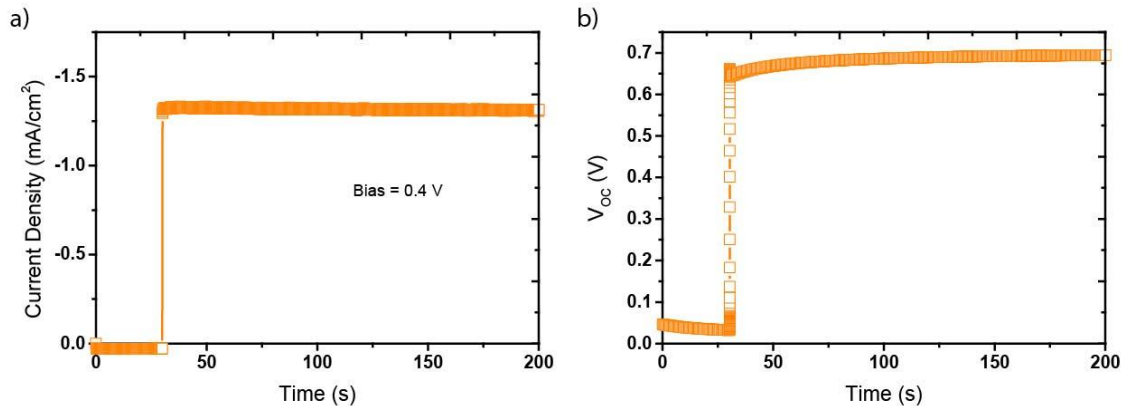


Figure 10.8. Stabilized current and V_{OC} for a device with the structure FTO/TiO₂/MAPbI_{3-x}Cl_x/Pt. a) Stabilized current density at the P_{MAX} (0.4 V). The current is very stable for approximately 200 s. b) Stabilized V_{OC} also shows highly stable voltage over approximately 200 s. The stable voltage and current suggest that ion migration during cAFM measurements is not a concern under these conditions.

10.5 First principles calculations

To understand the consequences of internal electric fields on the atomic and electronic structure of (CH₃NH₃)PbI₃, we performed first principles DFT calculations including spin-orbit coupling (SOC). DFT calculations were performed using the Perdew-Burke-Ernzerhof exchange correlation functional (297) and the projector augmented wave formalism (298) as implemented in the Vienna ab Initio Simulation Program (VASP) (299). Microscopically, (CH₃NH₃)PbI₃ takes up a perovskite-like phase, consisting of corner-sharing PbI₆ octahedra with the MA ions on the A sites (112, 300, 301). At room temperature, the MA molecules are randomly oriented and explore several local energy minima separated by small energy barriers on the order of 10 meV (302, 303), resulting, on average, in a vanishingly small macroscopic polarization and a centrosymmetric phase. However, at room temperature, an external electric field would be expected to simultaneously align the MA molecules and off-center the Pb ion in the inorganic cage. The displacement of the Pb cation relative to the I₆ octahedra causes a polar distortion in the structure that leads to the emergence of a significant polarization along the direction of the field.

The description of the experimental structure in the regime of low electric fields requires special attention. The tetragonal phase is described by a $\sqrt{2} \times \sqrt{2} \times 2$ unit cell with 4 formula units, corresponding to a total of 48 atoms. We use the experimentally reported room temperature tetragonal structure (136, 300) and compute the electronic band structure for antiparallel alignments of the MA ions in [001], [100] and [111] direction (structures 1-3). It is important to note that, given the rotational freedom of MA molecules at room temperature (303), none of these structures are expected to represent the actual experimental structure under a small or zero electric field. Finite temperatures, which play an important role in determining structural properties of MAPbI₃(300), are not considered in the calculations. Hence, we approximate the room temperature ground state of MAPbI₃ using locally stable low-energy structures in which the alignment of the MA molecule results in a small or vanishing polarization.

We performed geometry optimizations of three structures with parallel alignment of the MA molecules in [001], [100] and [111] directions, using a 4x4x4 Γ -centered k-point mesh and an energy cutoff of 500 eV. Starting from experimental lattice parameters (136), we performed

full structural relaxations where lattice constants and internal degrees of freedom were allowed to relax. No symmetry constraints were imposed in these calculations and forces were converged until smaller than 0.01 eV/Å. We refer to these fully relaxed geometries as structures 4-6. Band structures were calculated from charge densities obtained using a denser 6x6x6 Γ -centered k-point mesh, including semi-core states and spin-orbit interaction. Total energies and lattice parameters of structures 1-6 are shown in Table 10.1.

Table 10.1. Total energies, lattice parameters and cell volume of structures 1 – 6. The total energy refers to a single point calculation including SOC and a 6x6x6 k-point mesh.

#	E_{total} (eV)	a (Å)	b (Å)	c (Å)	V (Å ³)
1	-204.94	8.876	8.876	12.67	998.19
2	-205.47	8.876	8.876	12.67	998.19
3	-205.45	8.876	8.876	12.67	998.19
4	-206.26	9.078	9.088	12.816	1057.44
5	-206.49	9.203	8.865	12.565	1025.08
6	-206.42	9.044	9.043	12.586	1027.70

10.6 Results and discussion

I_{SC} , V_{OC} , and I_D were measured, in this order, on MAPbI_{3-x}Cl_x solar cells under three different conditions: I_{SC} under illumination at 0 V; V_{OC} relative to the bias voltage under illumination at forward biases between 0.1 and 0.7 V; and I_D in the dark at 2 and 3 V forward bias. The V_{OC} is measured relative to the applied bias. That is, when the photocurrent measured by cAFM is negative, positive, or approximately zero, the V_{OC} is less than, greater than, or approximately equal to the applied bias, respectively. It is important to note that the conditions used to map I_{SC} and V_{OC} mitigate ion migration (304) because the tip is in contact with the sample for less than 2 ms, while electrical current from analogous macroscale devices is stable for at least hundreds of seconds (Figure 10.8). Furthermore, the maximum internal electric field is given by the built-in field at zero bias and is reduced as the tip bias approaches V_{OC} .

The topography image in Figure 10.9a displays individual crystal grains and various crystal facets within these grains. To guide the eye, the image has been enlarged and the grains outlined in Figure 10.10. The range of different grain shapes observed in the topography image is due to the lack of preferential grain orientation in these MAPbI_{3-x}Cl_x films, as we have shown in a previous study using x-ray diffraction (136). Again, these measurements are reproducible (Figure 10.5) and free of artifacts from topography and tip-sample interactions (Figure 10.4).

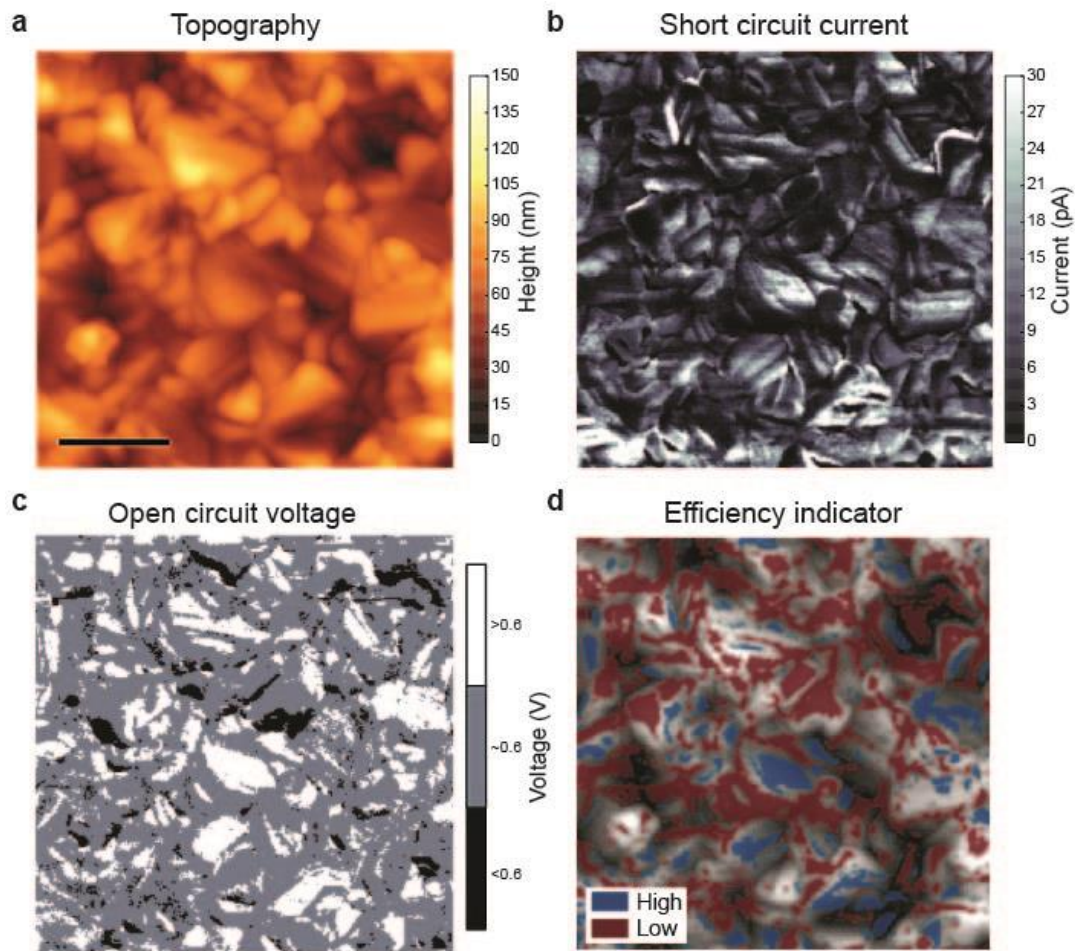


Figure 10.9. Intragrain heterogeneity of I_{sc} , V_{OC} , and efficiency indicator. (a) Topography image corresponding to all current maps. Individual crystal grains and their facets are clearly visible. The scale bar is 500 nm. (b) I_{sc} map is measured at 0 V bias under illumination. (c) Relative V_{OC} map measured at a forward bias of 0.6 V under illumination. (d) To compare heterogeneity of I_{sc} and V_{OC} to facets, areas in blue (high V_{OC} and I_{sc}) and areas in red (low V_{OC} and I_{sc}) are overlaid on the local topography indicating that many grains have a specific crystal facet that provides higher performance.

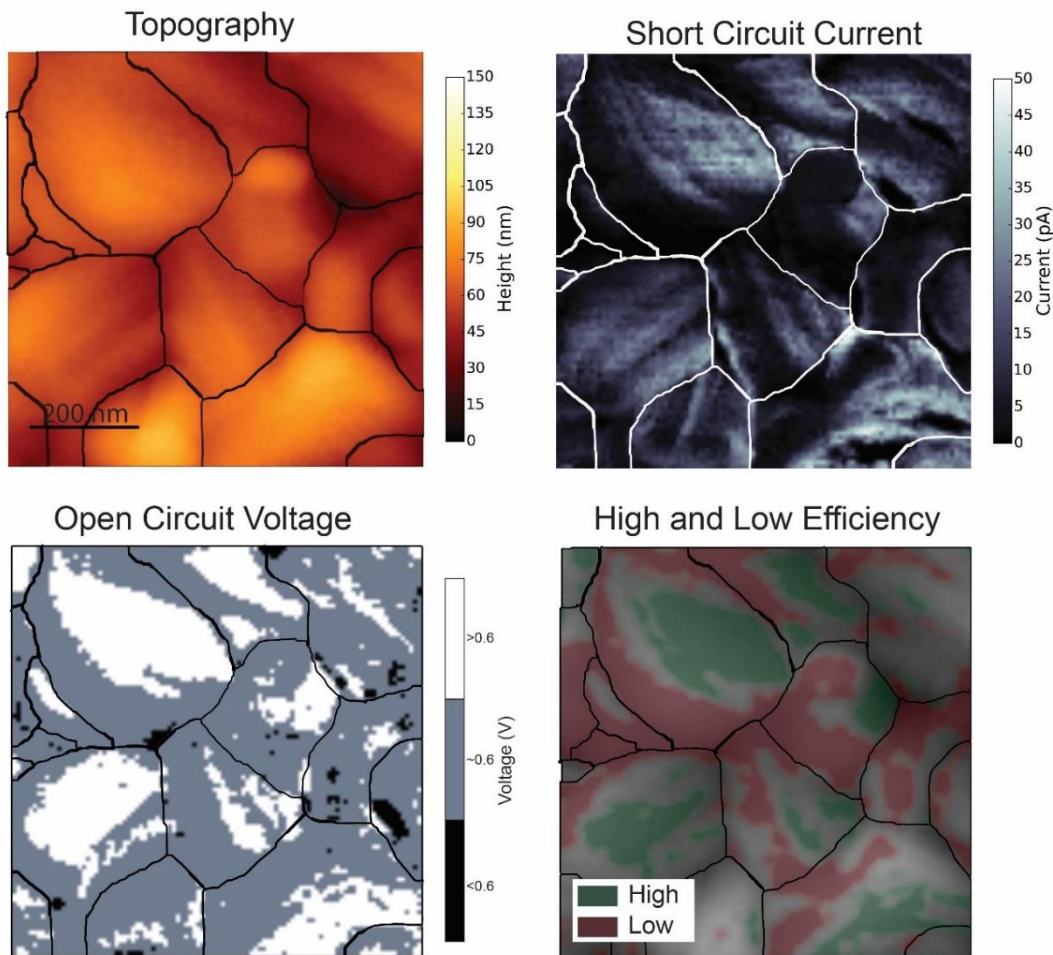


Figure 10.10. Topography, I_{SC} , relative V_{OC} , and efficiency indicator maps enlarged. The grains are outlined to help guide the eye. The variation between two facets of the same grain can easily be seen in these enlarged images.

Surprisingly, I_{SC} and V_{OC} (Figure 10.9b,c and Figure 10.10b,c) show not only strong local intergrain but also intragrain heterogeneity, which appear to be associated with individual grains and facets. The photocurrent varies by up to an order of magnitude within individual grains (I_{SC} map Figure 10.9b). Importantly, I found that the average I_{SC} for individual grains does not depend on grain size (Figure 10.11). This result contrasts with that of Nie et al. (288) and suggests that grain-size dependent I_{SC} may be different for the regime studied here, in which the grain size is smaller than the $\sim 1\mu\text{m}$ carrier diffusion length (137). To ensure that the measured heterogeneity is not due to tip-sample interaction artifacts, I verified that I_{SC} is not correlated with crystal height, different regions of constant slope, or lateral and adhesion forces (Figure 10.4).

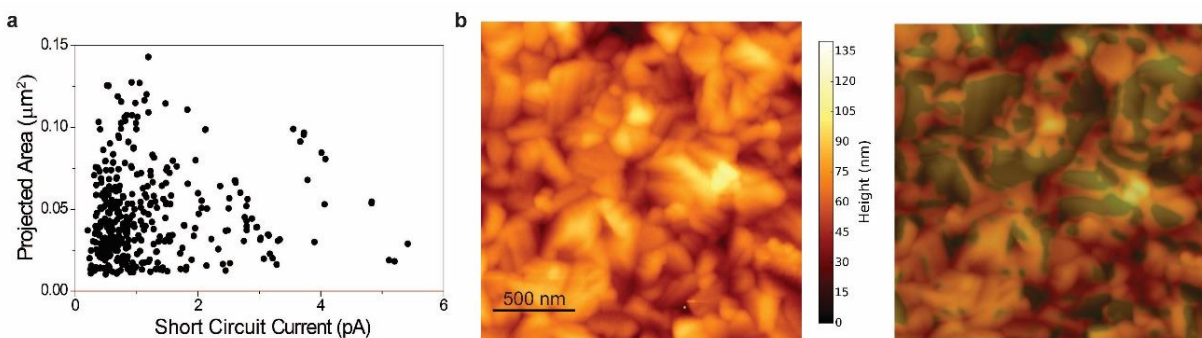


Figure 10.11. Grain size does not affect local short circuit current. (a) Scatter plot of grain area versus I_{SC} shows that there is no correlation between grain size and I_{SC} . (b) Topography image of MAPbI_{3-x}Cl_x and the topography image highlighted with areas of high I_{SC} ($I_{SC} > 15$ pA). The highlighted image shows that even small grains have regions of very high current.

The V_{OC} map shown in Figure 10.9c also reveals intragrain heterogeneity. This map was obtained by measuring current at a forward bias of 0.6 V, which is near the macroscale V_{OC} (0.51 V) obtained on a device made simultaneously with a Pt top contact in place of the HTL/Au to mimic the Pt cAFM tip. As a result, all V_{OC} values in the map are reported relative to the applied 0.6 V, as described above. As in the case of I_{SC} , the observed variation of V_{OC} is most pronounced within individual grains rather than between different grains.

Since the PCE for a solar cell is the product of V_{OC} , I_{SC} and FF, I spatially correlated regions of high and low V_{OC} and I_{SC} . I define the efficiency indicator as regions having a combination of either high or low V_{OC} and I_{SC} ; this is different from PCE because it does not incorporate FF. Figure 10.9d represents the efficiency indicator and shows that relative efficiency also varies significantly within grains. This map was generated by overlaying topography, in gray scale, with pixels representing high efficiency in blue ($V_{OC} > 0.6$ V, $I_{SC} > 12$ pA) and low efficiency in red ($V_{OC} \leq 0.6$ V, $I_{SC} < 5$ pA). To exclude tip-substrate effects as a cause for the heterogeneity I: (1) repeated I_{SC} and V_{OC} scans over the same region and observed no change in the heterogeneity; (2) used tips of different materials and observed similar heterogeneity (Figure 10.12); and (3) performed cAFM experiments on samples following deposition of a thin HTL layer of spiro-OMeTAD on the MAPbI_{3-x}Cl_x (Figure 10.13) and observed again similar heterogeneity in I_{SC} . These tests clearly indicate that the observed spatial variation is an inherent feature of these photovoltaic devices and not an artifact of interactions between the tip and the sample material.

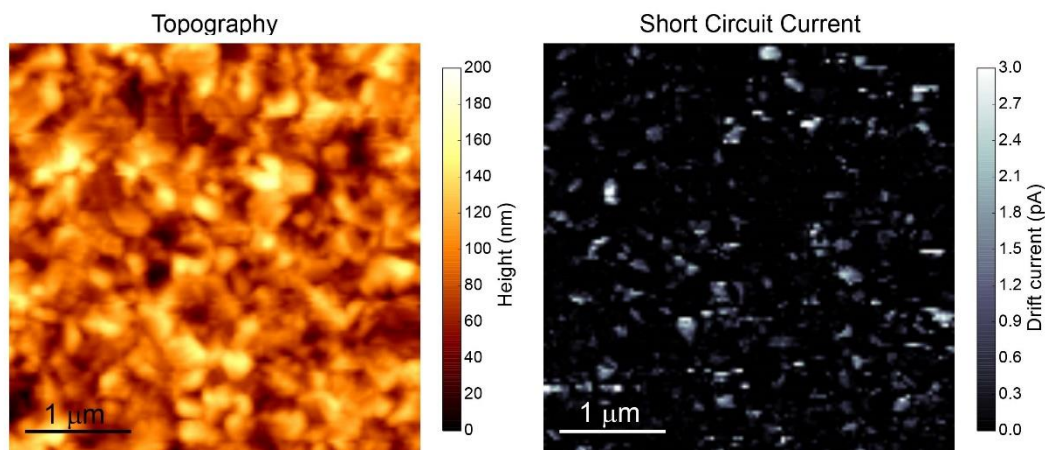


Figure 10.12. Topography and I_{SC} measured with a platinum silicide tip. The heterogeneity seen in the I_{SC} map is similar to that seen with a platinum-iridium tip.

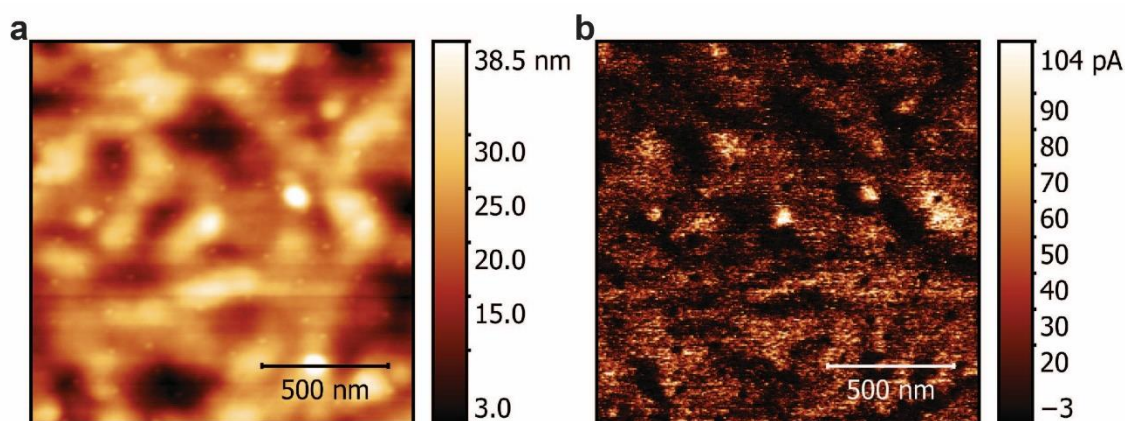


Figure 10.13. cAFM of $\text{MAPbI}_{3-x}\text{Cl}_x$ solar cell with spiro-OMeTAD HTL. To confirm that these heterogeneities exist with the addition of the HTL, local I_{SC} was measured with a thin layer of spiro-OMeTAD on the $\text{MAPbI}_{3-x}\text{Cl}_x$ film. The structure of this sample is FTO/dense TiO_2 / $\text{MAPbI}_{3-x}\text{Cl}_x$ /spiro-OMeTAD with a Pt coated AFM tip as the other electrode. (a) Topography image shows that the topography of the $\text{MAPbI}_{3-x}\text{Cl}_x$ grains is smoothed out with the spiro-OMeTAD on top. (b) I_{SC} image demonstrates that even with the spiro-OMeTAD layer there is significant heterogeneity in the current, although not as drastic, since the current gets laterally distributed by the HTL.

The observed intragrain heterogeneity in I_{SC} , V_{OC} , and efficiency indicator maps appear to be facet dependent when compared to the topography map. To confirm this observation analytically, the variance of I_{SC} within facets was determined and compared to the I_{SC} variance of facet-sized areas that were randomly placed over the I_{SC} map. The method used to identify the facets is shown in Figure 10.14. First the azimuthal gradient is calculated from the measured topography image. Then areas of approximately constant gradient, which is how I define facets, are outlined using a segmentation algorithm, and filled using the watershed algorithm to define each facet.

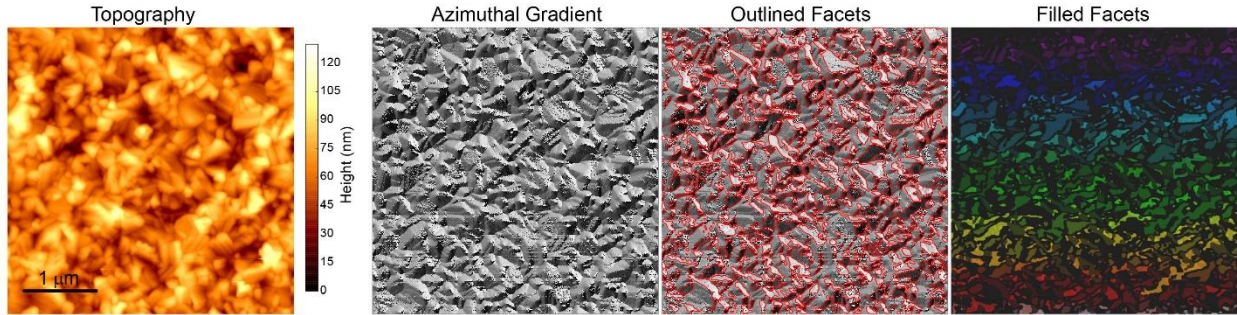


Figure 10.14. Identifying facets. Maps of topography, the calculated azimuthal gradient, the outlines of the facets overlaid onto the gradient image, and each facet defined by a separate color. The facets are defined as areas of constant gradient. The facets were identified by using a segmentation algorithm on the gradient image followed by the watershed algorithm.

The variance of I_{SC} values within each facet was calculated, and then averaged, yielding a mean of variances of 5.69 pA^2 . Variance, rather than standard deviation, was used to determine the spread in the I_{SC} values because the current distribution is not Gaussian due to the lower limit of 0 pA at short circuit conditions. To eliminate outliers from the variance calculation, a Gaussian blur ($\sigma=1.5$) was applied to the I_{SC} map. Then, for each facet area, the outlier current values (pixels) above and below the 75th and 25th percentile, respectively, were removed from the distribution. The variance was calculated for the remaining current values in that facet. Then, the mean was taken of the calculated variance values for each facet.

To determine the significance of this mean value, the same calculation was performed on randomly selected areas of the I_{SC} map that mimic the number and size of the identified facets. The following describes the details of how the histogram in Figure 10.15 was calculated. First, the number of facets identified from the gradient image and the number of pixels in each facet was determined. Then, for each identified facet, a square having an equivalent number of pixels was placed in a random position on the I_{SC} map; this was done for all the equivalent ‘facets’ at once. The variance was calculated for I_{SC} values in each of the squares and their mean was calculated. This process represents each data point plotted in the histogram. The process of randomly placing all the squares, calculating the variance of the current in each, and then taking the mean of the variances was performed 2000 times to generate all the data in the histogram. The majority of randomly placed areas exhibit a mean variance of 7.5 pA^2 . Since the current within the crystal facets has a mean variance significantly lower than the mean variance for randomly selected areas, the I_{SC} heterogeneity is correlated to the crystal facets ($p\text{-value} = 0.02$). The same calculation was performed on another set of topography and I_{SC} images for $\text{MAPbI}_{3-x}\text{Cl}_x$, and again the mean current variance for the facets is significantly less than for randomly selected areas (Figure 10.16). From this analysis, I conclude that the intragrain variations in I_{SC} and V_{OC} are indeed facet dependent.

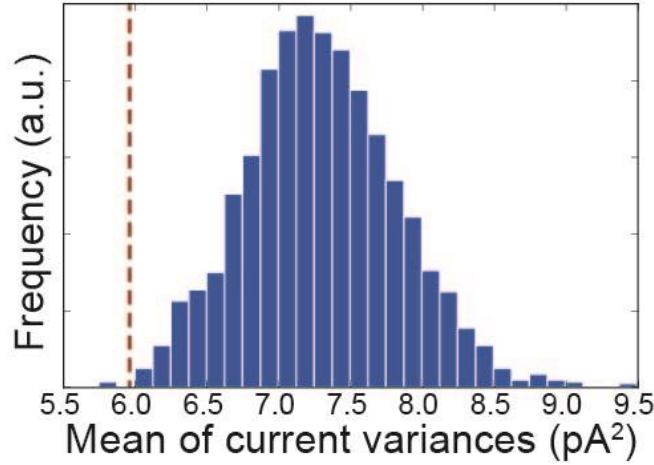


Figure 10.15. Facet dependent I_{SC} heterogeneity. Histogram of the mean of the I_{SC} variances calculated for 2000 sets of randomly placed squares that mimic the size and number of the identified facets in the gradient image. The red dashed line at 5.96 pA^2 is the mean of the I_{SC} variances within the identified facets. Based on the histogram, it is statistically unlikely that the mean of the current variances in the facets is random; the p-value is 0.02.

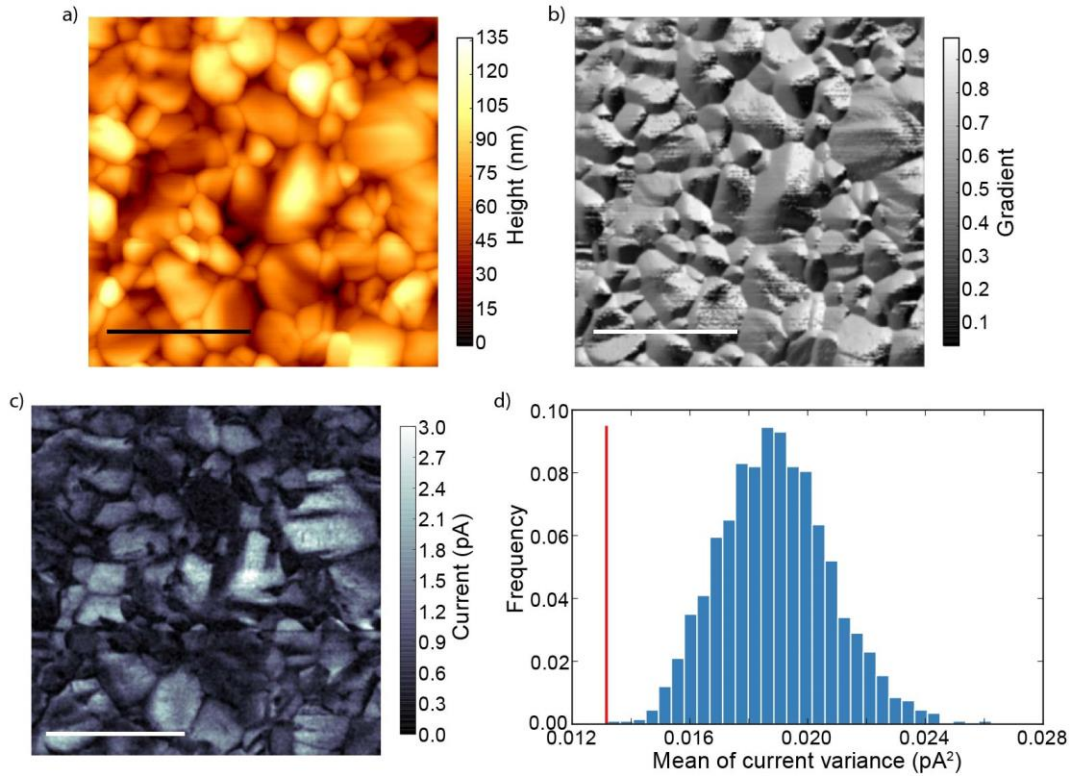


Figure 10.16. Identifying facets and establishing that the current is facet dependent in a second sample. Topography map (a), calculated azimuthal gradient image (b), and I_{SC} map with Gaussian blur ($\sigma=1.5$) of $\text{MAPbI}_{3-x}\text{Cl}_x$. The histogram (d) is calculated as described above and shown for a different sample than in Figure 10.15. Because the mean current variance for the identified facets is lower than any randomly placed ‘facets’, the current is determined to be facet dependent. Scale bars are 1 μm .

While the I_{SC} heterogeneity on the length scale probed here might be partially compensated by long charge carrier diffusion lengths, V_{OC} inhomogeneity is the performance determining factor for macroscale solar cells: MAPbI_{3-x}Cl_x grains can be approximated as individual photovoltaic elements wired in parallel, where the lowest V_{OC} will significantly reduce the macroscopic V_{OC} (134, 305). If simply considering two adjacent grains, charges will flow from the high to the low V_{OC} grain, reducing the overall V_{OC} . Hence, I investigated V_{OC} variation in more detail by collecting consecutive photocurrent maps of the same area at forward biases from 0.1 to 0.7 V with increments of 0.1 V, shown in Figure 10.17a. These images were aligned, and the voltage values assigned based on two factors: if the photocurrent is approximately zero, V_{OC} is set equal to the applied bias. If the current switches from positive (V_{OC} higher than applied bias) to negative (V_{OC} lower than applied bias) from one measurement to the next, I record V_{OC} to be between the two applied bias values. Values of V_{OC} above 0.7 V are marked in white. Some areas are likely to have a higher V_{OC} than 0.7 V, but I was not able to measure consecutive photocurrent maps for an applied bias range greater than 0.1 V to 0.7 V without tip modification. Any tip modification changes the tip substrate contact area and work function, making the current and voltage interpretation unreliable. I found a surprisingly large local variation in V_{OC} – over a range of 0.6 V – that has a dramatic impact on the macroscopic V_{OC} and, hence, PCE. Again, the variation in V_{OC} is highly dependent on the crystal facet that is being measured, as can be seen by comparing the local V_{OC} to the topography in Figure 10.17b.

The spatial correlation between V_{OC} and I_{SC} indicated in Figure 10.9 becomes more apparent when the full V_{OC} range map in Figure 10.17a is compared to the I_{SC} map for that area (Figure 10.17c), as illustrated in Figure 10.17d. Higher V_{OC} correlates with higher I_{SC} . Approximately 5% of the measured area was non-functioning with zero I_{SC} and V_{OC} , while 35% of the area produced V_{OC} greater than 0.7 V, suggesting that the efficiency in those areas was very high. If one would assume a uniform FF, and gauge PCE only by the product of V_{OC} and I_{SC} , high efficiency facets would perform up to 50% better than average, meaning that some grains with specific facets could approach the theoretical PCE limit.

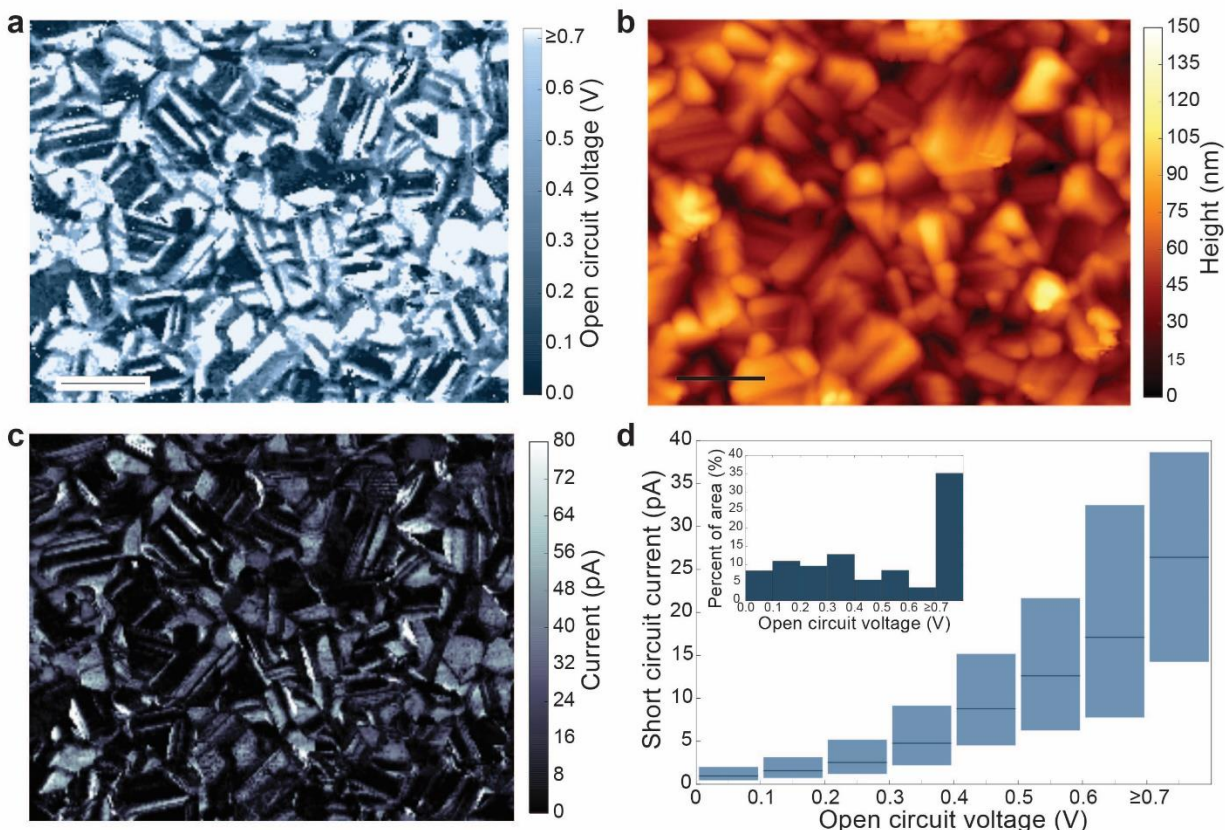


Figure 10.17. Heterogeneity in V_{OC} and its correlation to I_{SC} . (a) Local V_{OC} map generated by consecutively measuring photocurrent at biases from 0.1 to 0.7 V in increments of 0.1 V in the same area and aligning the images to assign V_{OC} values to individual pixels. The scale bar is 500 nm. (b) Topography image and (c) I_{SC} map for the same area as the V_{OC} map. (d) A box plot reveals the spatial correlation between V_{OC} and I_{SC} for the area shown in (a). Larger V_{OC} correlates with higher I_{SC} . Inset: Histogram of V_{OC} intervals.

So far, I was not able to specifically index the high and low efficiency facets: Electron backscatter diffraction mapping gave no meaningful results on facet orientation due to damage from the electron beam. Furthermore, spatially resolved elemental analysis by energy dispersive x-ray spectroscopy and by scanning Auger microscopy (Figure 10.19) failed to find differences in chemical composition with no detectable trace of chlorine across the surface, consistent with prior reports (116–118).

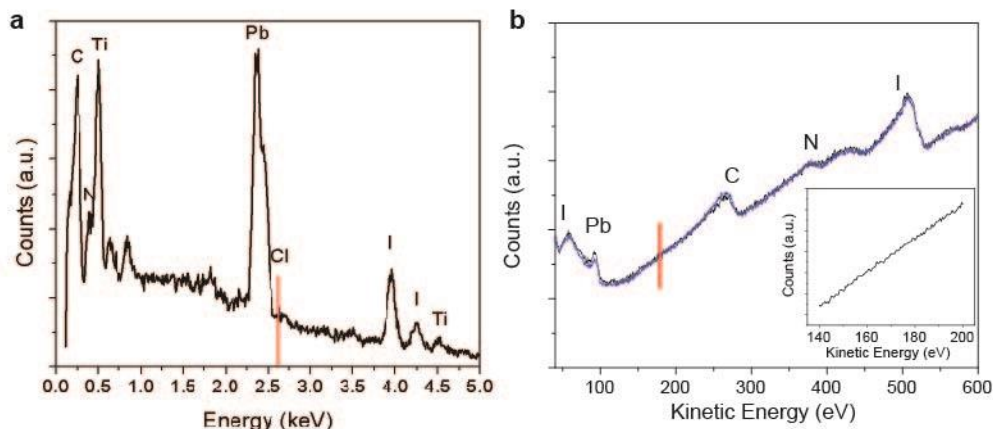


Figure 10.18. No chloride was detected with energy dispersive x-ray spectroscopy (EDS) or scanning auger microscopy. (a) Representative EDS spectrum shows no Cl peak. The red line marks where the Cl peak is expected. (b) Representative Auger spectrum, performed with a defocused electron beam to prevent sample damage, showing no Cl related peaks. The red line shows where the Cl peak is expected. Inset: Slow scan in the kinetic energy range where Cl peaks are expected. No Cl peaks are observed.

I considered a range of hypotheses to explain the observed heterogeneity, but most could not describe the experimentally observed facet dependence. However, recent findings from deQuilettes et al. showed that intergrain variation of PL intensity and lifetime are due to variations in trap state concentrations and that the traps can be passivated by surface treatment (142). Because PL efficiency is related to V_{OC} (293), I hypothesize that the observed intragrain heterogeneity in V_{OC} is a consequence of variations in trap state concentrations among crystal facets: a high density of trap states lowers V_{OC} due to Fermi level pinning. Also, trap states reduce I_{SC} due to higher recombination rates. This hypothesis is further supported by Noel et al. showing that surface passivation enhances I_{SC} , V_{OC} , and FF in photovoltaic devices equivalent in material and performance to those studied here (144). The simultaneous negative effect of trap states on V_{OC} and I_{SC} explains the strong spatial correlation I observed.

I also considered that the heterogeneity could be explained by local variations in surface potential, local doping, variations in mobility along different crystallographic directions, and variations in conductivity of the FTO and TiO_2 layers. I measured the surface potential using KPFM and did not observe any heterogeneity, but these measurements were performed under ambient conditions. Other reports of KPFM on perovskites also do not observe grain or facet dependent heterogeneity (145, 306). Thus, it is highly unlikely that variations in the surface potential exist. I also considered local variations in doping or carrier concentrations, but these variations would manifest as heterogeneity between grains rather than within a grain. Thus, variation in doping does not describe the facet dependence. I carefully considered variations in mobility to describe the facet dependent heterogeneity; however, there are two main reasons why mobility variations are not responsible: (i) First principles DFT was used to calculate effective masses along different crystallographic directions. The effective mass varies by less than a factor of 2 along different crystallographic directions. (ii) Without extreme variations in mobilities along different directions, the current should flow along a direct path between the TiO_2 and the AFM tip due to the electric field. Thus, variations in mobility would be observed as intergrain rather than intragrain heterogeneity. I also considered the TiO_2 and FTO layers. The FTO has a

much larger grain structure than the heterogeneity I observe in the perovskite. TiO_2 conformally coats the FTO layer, and the grains are much smaller than those in the perovskite. For both layers, the length scales of the grains do not match the observed V_{OC} and I_{SC} heterogeneity in the perovskite.

To experimentally confirm that the observed heterogeneity in V_{OC} and I_{SC} is not related to differences in mobility, I also mapped the local I_D , which is proportional to mobility. Figure 10.19a is a map of I_D at 2 V applied bias, which provides a sufficiently large electric field across the perovskite film to ensure that current is dominated by electronic transport (Figure 10.20) rather than recombination at trap states (134, 284, 307). The I_D map at 2 V shows very little heterogeneity and is mostly homogeneous throughout individual grains and between grains, which indicates a dominantly homogenous mobility at these length scales and bias conditions. This observation indicates that variations of mobility are not the cause of the I_{SC} and V_{OC} heterogeneity. However, at 3 V forward bias, the heterogeneities become much more pronounced and reveal a reoccurrence of the facet-dependent heterogeneity (Figure 10.19b).

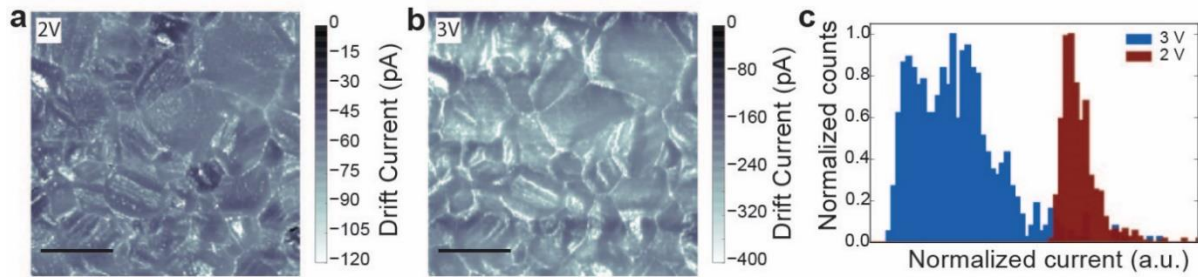


Figure 10.19. Heterogeneity in drift current due to changes in effective mass. (a) I_D map measured at a forward bias of 2 V indicates homogeneous electrical transport within grains. The scale bar is 500 nm. (b) I_D map measured at a forward bias of 3 V and in the same area reveals significant heterogeneity. The scale bar is 500 nm. (c) Histogram of the relative drift currents at each pixel within a representative grain measured at 2 and 3 V showing increased heterogeneity at 3 V.

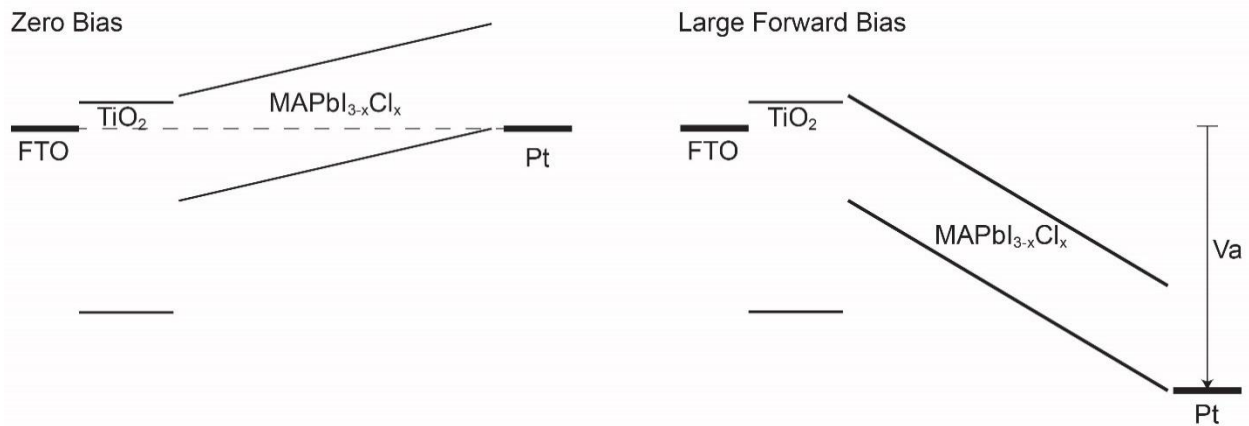


Figure 10.20. Band diagram of MAPbI_{3-x}Cl_x device in cAFM measurement. The band diagrams at 0 V and under a large applied bias (V_a) are shown. In both cases, an electric field exists across the intrinsic MAPbI_{3-x}Cl_x layer that causes I_D to dominate.

The enhancement of I_D heterogeneity when moving from 2 to 3 V forward bias is illustrated in the histogram in Figure 10.19c where the number of pixels is plotted versus the relative I_D for an individual grain. The blue histogram represents I_D at 3 V, the red histogram at 2 V. Due to the difference in I_D magnitude measured at 2 and 3 V and to enhance the comparison, the current values in the histograms are shifted and normalized to the respective mean currents and the histogram amplitudes were normalized to one. The I_D histogram at 3 V (blue) is very broad, with I_D values ranging over an order of magnitude for different pixels. It shows two distinct peaks at -0.22 and -0.15 nA, which stem from two different facets within one grain, with one facet allowing 1.5 times higher I_D . In contrast, the 2 V histogram (red) is narrow and has only one peak at -65 pA, representing the spatial homogeneity of the measured mobility. To ensure reproducibility, I measured at 2 V, 3 V, and back to 2 V showing no difference in the 2 V I_D maps or topography (Figure 10.21). Previously, ion migration was observed at comparable applied electric fields, by observing the modification of the topography (156). However, due to my measurement technique, the sample is exposed to the maximum electric field for only 1.6 ms when the tip is on the sample surface – too brief for ion migration (304) – while the field is one order of magnitude lower during the next 10 ms, when the tip retracts, moves to the next pixel, and re-approaches. Based on a diffusion coefficient of 10^{-12} cm²/s (308), iodine ions will only drift 0.062 nm under a bias of 3 V across a 300 nm film over 1.6 ms. Hence, I observe no topographic or I_D modification for biases up to 3 V. However, I did not apply a bias over 3 V due to observed modifications in sample morphology at higher bias. While the I_D homogeneity at 2 V supports the hypothesis that facet-dependent surface defect state concentrations give rise to local differences of I_{SC} and V_{OC} , the question remains: what causes the appearance of facet-dependent heterogeneity of I_D at higher bias?

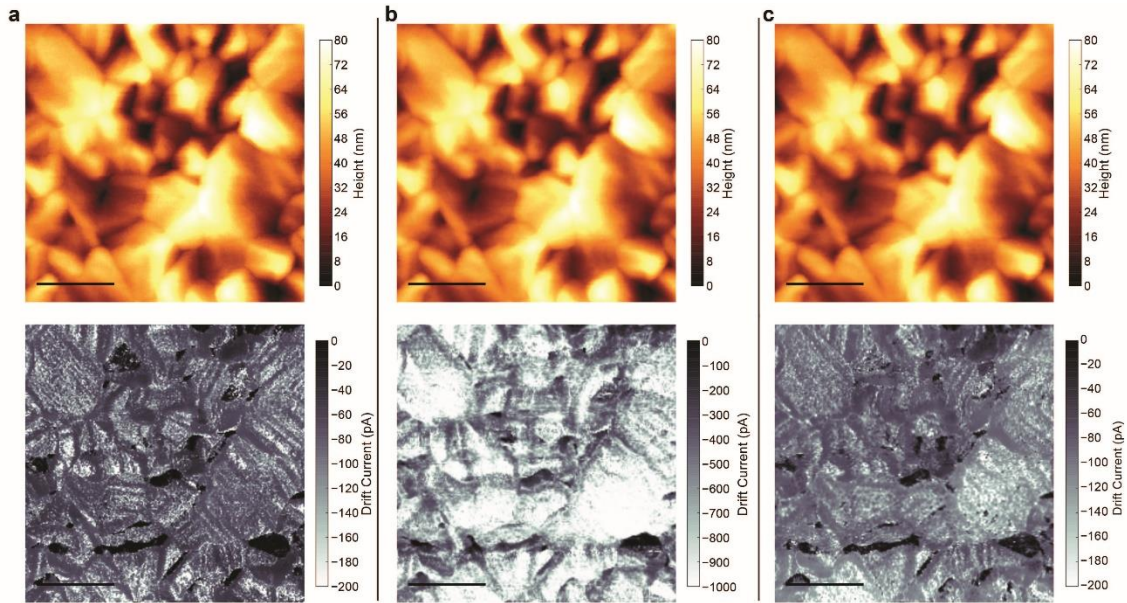


Figure 10.21. I_D at voltage up to 3 V does not cause ion migration. I_D was measured at 2 V (a), 3 V (b), and 2 V (c) consecutively in the same area. The topography and current measured before and after 3 V are approximately identical, thus a bias of 3 V with the PinPoint scan mode is not sufficient to alter the material via ion migration. All scale bars are 500 nm.

To address this question, we investigated the effect of large electric fields on the electronic structure of lead halide perovskites using first principles DFT calculations including SOC. From the band structures of the perovskite structures with the MA ions in parallel and antiparallel alignment (structures 1-6), we calculated the effective electron and hole masses by parabolic band fitting around the CBM and the VBM, respectively, along the crystallographic high symmetry directions. We report the factor by which the reduced effective mass changes along the direction of MA alignment, since we assume that transport takes place along the direction of the applied electric field. For example, we show the factor by which the reduced effective mass changes along the crystallographic [001] direction upon aligning the MA ions in this direction. This factor is defined as $m^{\alpha,*}_{001}/m^{\alpha=0^{\circ},*}_{001}$, where $m^{\alpha,*}_{001}=m^e_{001}m^h_{001}/(m^e_{001}+m^h_{001})$ is the reduced effective mass for alignment angle α . m^e_{001} and m^h_{001} are the respective electron and hole effective masses along the crystallographic [001] direction. The effective masses of all structures that we considered can be found in Table 10.2.

Table 10.2. Effective electron and hole masses and reduced effective masses (in units of the free electron mass m_e) for structures 1 – 6. The table lists the values for the crystallographic high symmetry directions and averages.

Structure 1, antiparallel alignment [001]

	m_e^*	m_h^*	μ
$\Gamma \rightarrow A$	0.11	0.13	0.060
$\Gamma \rightarrow X$	0.12	0.14	0.065
$\Gamma \rightarrow Z$	0.08	0.09	0.042
$\Gamma \rightarrow R$	0.10	0.11	0.052
$\Gamma \rightarrow M$	0.12	0.17	0.070
Avg	0.11	0.13	0.058

Structure 2, antiparallel alignment [100]

	m_e^*	m_h^*	μ
$\Gamma \rightarrow A$	0.11	0.13	0.060
$\Gamma \rightarrow X$	0.12	0.13	0.062
$\Gamma \rightarrow Z$	0.08	0.10	0.044
$\Gamma \rightarrow R$	0.10	0.11	0.052
$\Gamma \rightarrow M$	0.12	0.13	0.062
Avg	0.11	0.12	0.056

Structure 3, antiparallel alignment [111]

	m_e^*	m_h^*	μ
$\Gamma \rightarrow A$	0.10	0.12	0.055
$\Gamma \rightarrow X$	0.11	0.13	0.060
$\Gamma \rightarrow Z$	0.09	0.10	0.047
$\Gamma \rightarrow R$	0.10	0.12	0.055
$\Gamma \rightarrow M$	0.12	0.13	0.062
Avg	0.10	0.12	0.056

Structure 4, parallel alignment [001]

	m_e^*	m_h^*	μ
$\Gamma \rightarrow A$	0.11	0.16	0.065
$\Gamma \rightarrow X$	0.13	0.18	0.072
$\Gamma \rightarrow Z$	0.12	0.15	0.067
$\Gamma \rightarrow R$	0.11	0.16	0.065
$\Gamma \rightarrow M$	0.12	0.19	0.074
Avg	0.12	0.17	0.069

Structure 5, parallel alignment [100]

	m_e^*	m_h^*	μ
$\Gamma \rightarrow A$	0.15	0.22	0.089
$\Gamma \rightarrow X$	0.14	0.21	0.084
$\Gamma \rightarrow Z$	0.19	0.23	0.104
$\Gamma \rightarrow R$	0.16	0.24	0.096
$\Gamma \rightarrow M$	0.15	0.22	0.089
Avg	0.16	0.22	0.092

Structure 6, parallel alignment [111]

	m_e^*	m_h^*	μ
$\Gamma \rightarrow A$	0.16	0.27	0.100
$\Gamma \rightarrow X$	0.17	0.28	0.106
$\Gamma \rightarrow Z$	0.16	0.18	0.085
$\Gamma \rightarrow R$	0.16	0.21	0.091
$\Gamma \rightarrow M$	0.16	0.36	0.111
Avg	0.16	0.26	0.099

The total polarization was calculated using the modern theory of polarization (309) as implemented in VASP. For example, the macroscopic polarization of the polar structure 4 was calculated with respect to the experimentally observed room-temperature tetragonal structure 1 (136, 300). The path connecting the polar and the non-polar structures was subdivided in 20 structures. For three of these structures (with MA alignment angles α of 45°, 90° and 135°), we additionally determined the effective masses as described above. We compute a total polarization of 12.5 $\mu\text{C}/\text{cm}^2$, in agreement with previous calculations (310). We further estimated the contribution of the MA molecules to the polarization by constructing a path connecting structures with parallel and antiparallel alignment of MA (without octahedral rotations of the iodine cage). We calculate the molecular contribution to the macroscopic polarization to be 5.3 $\mu\text{C}/\text{cm}^2$ and use this value to estimate the electric field E_c required to align the MA molecules to be 10^5 V/cm using the relationship $E_c P \sim \Delta E/V$, where the volume V and polarization P are obtained from our first principles calculations and ΔE is an estimation of the energy that has to be overcome to polarize the system (302, 303).

For electric fields larger than $\sim 10^5$ V/cm, corresponding to 3 – 4 V across our thin films, we find that the MA ions align with the electric field. This alignment is accompanied by displacements of the Pb ions relative to the I_6 octahedra in each unit cell, leading to an overall polarization of the crystal lattice (Figure 10.22a) (303, 311, 312). As shown in Figure 10.22b and Table 10.2, this polarization results in an increase in the effective mass of electrons and holes along the direction of the electric field by a factor between 1.3 and 1.8 for the three directions of MA alignment examined. Assuming a constant charge density, I_D is proportional to mobility and, thus, inversely proportional to the reduced effective mass, which increases under sufficiently large electric fields according to our DFT calculations.

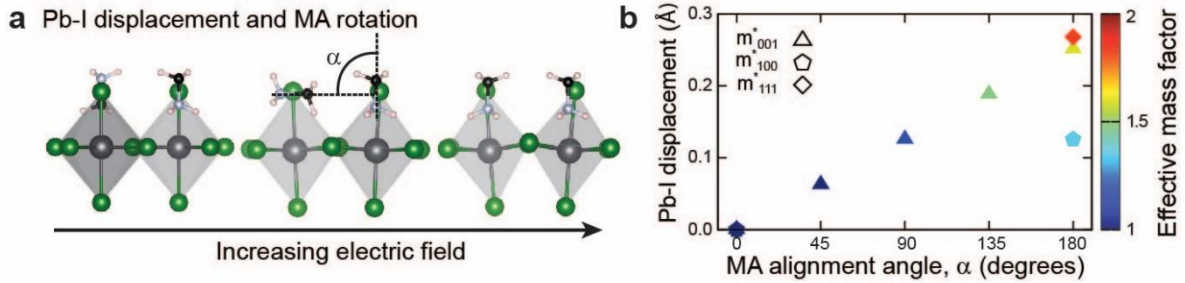


Figure 10.22. DFT calculated changes in the perovskite lattice and the resulting effective masses. a) Application of sufficiently high electric fields results in alignment of the MA molecules along the electric field direction and a displacement of the Pb cations relative to I_6 octahedra. The MA molecules are aligned in parallel at an alignment angle of $\alpha = 180^\circ$. b) The electron and hole effective masses increase as both the Pb ions are displaced and as the MA become more aligned with the electric field. The effective mass can increase by up to a factor of 1.8 depending on the electric field direction.

The internal electric field in $\text{MAPbI}_{3-x}\text{Cl}_x$ films is approximately equal to $(V_{app} - V_{oc})/d$, where V_{app} is the applied forward bias and d is the film thickness. Hence, I suggest that at a bias of 3 V, only facets with low V_{oc} (higher trap state density) have an internal electric field sufficiently high to induce complete MA alignment and the corresponding polar Pb and I displacements. The 1.3 to 1.8 times increase in effective mass, as predicted by our calculations, explains the reduction in I_D observed in the experiments of 1.5 times between different facets on

the same grain. On facets characterized by high V_{OC} , the internal electric fields do not surpass the necessary threshold and the mobility remains high. This model explains the facet dependent heterogeneity in I_D at large bias and its spatial correlation with V_{OC} (Figure 10.23). I did consider other hypotheses to describe the heterogeneity at high bias, such as variations in carrier concentration, scattering time, and ion migration because drift current density is defined as $J_d = qn\mu E = qn\frac{q\tau}{m^*}E$, where q is the charge of an electron, n is the carrier concentration, μ is the carrier mobility, E is the magnitude of the electric field, τ is the scattering time, and m^* is the effective mass. If the carrier concentration, n , was responsible for the heterogeneity, I would observe this effect at low biases and, as described above, it would not be a facet dependent effect. Thus, I can eliminate variations in carrier concentration as the cause of heterogeneity. The DFT calculations show that variations in mobility at high bias provide the best agreement with the experimental results can explain the effect I observe here. Ion migration may play a role, though, based on Figure 10.21, I expect it to be a minor effect below 3 V. Facets with high trap state density can modify local I_D , a particularly important insight for LED operation.

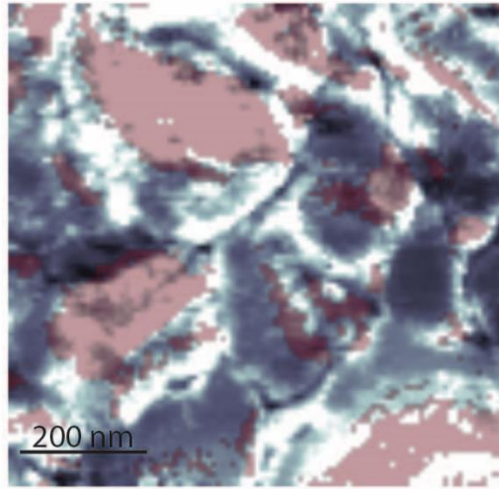


Figure 10.23. Overlay of V_{OC} higher than 0.6 V in red on the map of I_D at 4 V. The overlay shows that high V_{OC} corresponds to regions of more negative I_D (lighter).

10.7 Conclusion

I show significant intragrain heterogeneity in I_{SC} , V_{OC} , and high bias I_D , as well as spatial correlation between these parameters in state-of-the-art $\text{MAPbI}_{3-x}\text{Cl}_x$ solar cell materials. The intragrain heterogeneity in V_{OC} and I_{SC} is indicative of facet-dependent defect concentrations in these polycrystalline films. V_{OC} heterogeneity has a direct effect on macroscale solar cell performance, but can also indirectly affect mobility due to local polarization at high forward bias, which also affects LED applications. Based on the results of these nanoscale measurements using cAFM, the efficiency of single and polycrystalline halide perovskite solar cells and LEDs can be systematically improved by controlling the growth direction of the grains and the orientation of the facets at interfaces with electron and hole conducting layers. These findings also suggest that reproducible performance of devices at the scale of individual grains will rely on control of facet-specific defect properties. Without using a nanoscale characterization technique, it would not have been possible to detect intragrain differences in solar cell performance.

Conclusions and outlook

This dissertation focuses on understanding and manipulating emerging thin film solar cell materials: organic semiconductors and hybrid halide perovskite materials. Organic semiconductors and halide perovskites have many advantages compared to existing thin film inorganic solar cells: composed of inexpensive and abundant materials, strongly absorb visible light, are easily processed into thin films at low temperatures, and have tunable electronic properties. In my dissertation, I focused on identifying and overcoming critical loss pathways in both OSCs and perovskite solar cells to systematically improve their PCEs.

In OSCs, dissociating excitons is critical for high PCE. Thus, I worked on manipulating and reducing E_{eb} of Frenkel excitons in small molecule donor materials and CT excitons in polymer-fullerene BHJs. By adding a high permittivity small molecule, CA, to the BO-ADPM film, I successfully increased the permittivity of the film and reduced the BO-ADPM E_{eb} . As a result, IQE of the BO-ADPM:C₆₀ planar heterojunction increased by 30%. Similarly in MDMO-PPV:PCBM BHJs, the permittivity increased linearly, the CT state energy decreased, and the PCE increased when adding up to 20 wt% CA to the film. To better understand the exciton dynamics in MDMO-PPV:PCBM BHJs, we used FSRS to differentiate of the MDMO-PPV behavior in the bulk of the BHJ and at the interface with PCBM. We observed that the excitons are most mobile before thermalization. The implication of these results are that excitons can be controlled by modifying the permittivity in the film and that excitons are more likely to dissociate if they have a long thermalization time.

Based on the results of the above mentioned studies, there are several new insights into manipulating excitons that enable both new technical approaches to improve OSCs and lead to a new set of scientific questions to answer. In the case of increasing permittivity in OSCs, CA could be incorporated into a less crystalline BHJ system to prevent the CA from phase separating. This may allow for more CA to be mixed into the BHJ, higher permittivity to be achieved, and lower CT state energies leading to improved PCE. Alternatively, a higher permittivity material such as barium titanate could be incorporated into the film. If homogeneously incorporated, in the form of nanoparticles, higher permittivity could be achieved while displacing less of the active absorber material for improved PCE. Additionally, more data and statistics on the CT state energy as a function of permittivity would better explain the mechanism leading to lower CT state energy: SSSE or Coulombic attraction. Further studies for FSRS would include performing similar experiments on a range of BHJs with different PCEs. This would help answer the question, do longer thermalization times lead to improved performance because of greater exciton mobility?

A significant challenge in perovskite solar cells is identifying loss mechanisms and understanding how they are related to local morphology to then overcome them to achieve higher PCEs. To address this challenge, I developed a novel scanning probe technique to map local I_{SC} and V_{OC} . I found that heterogeneity in I_{SC} and V_{OC} are correlated and crystal facet dependent. The heterogeneity is attributed it to facet dependent surface trap state densities. These results indicate that the efficiency of hybrid halide perovskite solar cells can be systematically improved by controlling the growth direction of the grains such that the facets interfacing with the electrodes have a low density of trap states.

There are several opportunities for future work based on these preliminary cAFM results. Ideally, the facets with a high density of trap states would be identified to provide an optimal

grain growth direction. By growing larger grains, the facet orientation could be determined using electron backscatter diffraction and the same area could be measured with cAFM. Alternatively, the solar cell performance could be compared between films grown with different preferential grain orientations. cAFM can also be used to understand other critical aspects of perovskite solar cells. Ion migration in halide perovskite materials is known to exist, but how it occurs and migration pathways through the film are not understood. By applying a sufficiently high bias with cAFM and then observing the chemical species before and after with scanning auger microscopy could provide a strong understanding of ion migration pathways. Additionally, cAFM can be used to study the degradation mechanism in perovskite solar cells by controllably increasing the relative humidity in the AFM glovebox and observe changes to the surface and photocurrent. By understanding degradation and ion migration, the stability of perovskite solar cells can be improved for use in commercial applications.

Bibliography

1. United Nations, *Adoption of the Paris Agreement* (2015).
2. M. Z. Jacobson, M. A. Delucchi, Providing all global energy with wind, water, and solar power, Part I: Technologies, energy resources, quantities and areas of infrastructure, and materials. *Energy Policy*. **39**, 1154–1169 (2011).
3. G. Barbose, N. Garghouth, “Tracking the Sun VIII” (Lawrence Berkeley National Laboratory, 2015), (available at <http://www.seia.org/research-resources/tracking-sun-viii>).
4. “Micro-scale optimized solar-cell arrays with integrated concentration (MOSAIC)” (Financial Assistance Funding Opportunity Announcement 81.135, ARPA-E, 2014).
5. E. A. Alsema, E. Nieuwlaar, Energy viability of photovoltaic systems. *Energy Policy*. **28**, 999–1010 (2000).
6. “PV FAQs: What is the energy payback for PV?” (DOE Solar Energy Technologies Program), (available at <http://www.nrel.gov/docs/fy04osti/35489.pdf>).
7. A. Anctil, C. Babbitt, B. Landi, R. P. Raffaele, in *2010 35th IEEE Photovoltaic Specialists Conference (PVSC)* (2010), pp. 000742–000747.
8. G. D. Scholes, G. Rumbles, Excitons in nanoscale systems. *Nat. Mater.* **5**, 683–696 (2006).
9. M. A. Green, K. Emery, Y. Hishikawa, W. Warta, E. D. Dunlop, Solar cell efficiency tables (version 46). *Prog. Photovolt. Res. Appl.* **23**, 805–812 (2015).
10. J. Nelson, *The physics of solar cells* (Imperial College Press, London, 2003).
11. M. A. Green, *Solar cells: operating principles, technology, and system applications* (Prentice-Hall, Englewood Cliffs, NJ, 1982), *Prentice-Hall series in solid state physical electronics*.
12. W. Shockley, H. J. Queisser, Detailed Balance Limit of Efficiency of p-n Junction Solar Cells. *J. Appl. Phys.* **32**, 510–519 (1961).
13. S. E. Shaheen, D. S. Ginley, G. E. Jabbour, Organic-Based Photovoltaics: Toward Low-Cost Power Generation. *MRS Bull.* **30**, 10–19 (2005).
14. B. Kippelen, J.-L. Brédas, Organic photovoltaics. *Energy Environ. Sci.* **2**, 251 (2009).
15. T. Kim *et al.*, Flexible, highly efficient all-polymer solar cells. *Nat. Commun.* **6**, 8547 (2015).
16. M. Kaltenbrunner *et al.*, Ultrathin and lightweight organic solar cells with high flexibility. *Nat. Commun.* **3**, 770 (2012).
17. Y.-J. Cheng, S.-H. Yang, C.-S. Hsu, Synthesis of Conjugated Polymers for Organic Solar Cell Applications. *Chem. Rev.* **109**, 5868–5923 (2009).
18. C. N. Hoth, P. Schilinsky, S. A. Choulis, C. J. Brabec, Printing Highly Efficient Organic Solar Cells. *Nano Lett.* **8**, 2806–2813 (2008).
19. F. C. Krebs, Polymer solar cell modules prepared using roll-to-roll methods: Knife-over-edge coating, slot-die coating and screen printing. *Sol. Energy Mater. Sol. Cells.* **93**, 465–475 (2009).
20. J.-L. Brédas, J. E. Norton, J. Cornil, V. Coropceanu, Molecular Understanding of Organic Solar Cells: The Challenges. *Acc. Chem. Res.* **42**, 1691–1699 (2009).
21. N. Kim *et al.*, A correlation study between barrier film performance and shelf lifetime of encapsulated organic solar cells. *Sol. Energy Mater. Sol. Cells.* **101**, 140–146 (2012).
22. M. Hermenau *et al.*, The effect of barrier performance on the lifetime of small-molecule organic solar cells. *Sol. Energy Mater. Sol. Cells.* **97**, 102–108 (2012).

23. A. W. Hains, Z. Liang, M. A. Woodhouse, B. A. Gregg, Molecular semiconductors in organic photovoltaic cells. *Chem. Rev.* **110**, 6689–6735 (2010).
24. H. Hoppe, N. Sariciftci, Organic solar cells: An overview. *J. Mater. Res.* **19**, 1924–1945 (2004).
25. M. Knupfer, Exciton binding energies in organic semiconductors. *Appl. Phys. Mater. Sci. Process.* **77**, 623–626 (2003).
26. P. Peumans, A. Yakimov, S. R. Forrest, Small molecular weight organic thin-film photodetectors and solar cells. *J. Appl. Phys.* **93**, 3693–3723 (2003).
27. W. Brütting, in *Physics of Organic Semiconductors*, W. Brütting, Ed. (Wiley-VCH Verlag GmbH & Co. KGaA, 2006), pp. 1–14.
28. H. Hoppe, N. S. Sariciftci, in *Photoresponsive Polymers II*, S. R. Marder, K.-S. Lee, Eds. (Springer Berlin Heidelberg, 2007; http://link.springer.com/chapter/10.1007/12_2007_121), *Advances in Polymer Science*, pp. 1–86.
29. C. Deibel, T. Strobel, V. Dyakonov, Role of the Charge Transfer State in Organic Donor–Acceptor Solar Cells. *Adv. Mater.* **22**, 4097–4111 (2010).
30. T. M. Clarke, J. R. Durrant, Charge Photogeneration in Organic Solar Cells. *Chem. Rev.* **110**, 6736–6767 (2010).
31. F. Yang, S. R. Forrest, Photocurrent Generation in Nanostructured Organic Solar Cells. *ACS Nano*. **2**, 1022–1032 (2008).
32. A. K. Ghosh, T. Feng, Merocyanine organic solar cells. *J. Appl. Phys.* **49**, 5982–5989 (1978).
33. C. W. Tang, Two-layer organic photovoltaic cell. *Appl. Phys. Lett.* **48**, 183–185 (1986).
34. N. S. Sariciftci, L. Smilowitz, A. J. Heeger, F. Wudl, Photoinduced Electron Transfer from a Conducting Polymer to Buckminsterfullerene. *Science*. **258**, 1474–1476 (1992).
35. Picture Story - How Do Organic Solar Cells Function? *Notes Disord. Matter* (2008), (available at <http://blog.disorderedmatter.eu/2008/06/05/picture-story-how-do-organic-solar-cells-function/>).
36. R. N. Marks, J. J. M. Halls, D. D. C. Bradley, R. H. Friend, A. B. Holmes, The photovoltaic response in poly(p-phenylene vinylene) thin-film devices. *J. Phys. Condens. Matter*. **6**, 1379 (1994).
37. N. S. Sariciftci *et al.*, Semiconducting polymer-buckminsterfullerene heterojunctions: Diodes, photodiodes, and photovoltaic cells. *Appl. Phys. Lett.* **62**, 585–587 (1993).
38. G. Yu, A. J. Heeger, Charge separation and photovoltaic conversion in polymer composites with internal donor/acceptor heterojunctions. *J. Appl. Phys.* **78**, 4510–4515 (1995).
39. G. Yu, J. Gao, J. C. Hummelen, F. Wudl, A. J. Heeger, Polymer Photovoltaic Cells: Enhanced Efficiencies via a Network of Internal Donor-Acceptor Heterojunctions. *Science*. **270**, 1789–1791 (1995).
40. F. Padinger, R. s. Rittberger, N. s. Sariciftci, Effects of Postproduction Treatment on Plastic Solar Cells. *Adv. Funct. Mater.* **13**, 85–88 (2003).
41. C. J. Brabec *et al.*, Polymer–Fullerene Bulk-Heterojunction Solar Cells. *Adv. Mater.* **22**, 3839–3856 (2010).
42. J. J. M. Halls, K. Pichler, R. H. Friend, S. C. Moratti, A. B. Holmes, Exciton dissociation at a poly(p-phenylenevinylene)/C60 heterojunction. *Synth. Met.* **77**, 277–280 (1996).

43. J. J. M. Halls *et al.*, Efficient photodiodes from interpenetrating polymer networks. *Nature*. **376**, 498–500 (1995).
44. J. C. Hummelen *et al.*, Preparation and Characterization of Fulleroid and Methanofullerene Derivatives. *J. Org. Chem.* **60**, 532–538 (1995).
45. P. Schilinsky, C. Waldauf, C. J. Brabec, Recombination and loss analysis in polythiophene based bulk heterojunction photodetectors. *Appl. Phys. Lett.* **81**, 3885–3887 (2002).
46. B. Walker *et al.*, Nanoscale Phase Separation and High Photovoltaic Efficiency in Solution-Processed, Small-Molecule Bulk Heterojunction Solar Cells. *Adv. Funct. Mater.* **19**, 3063–3069 (2009).
47. J. Roncali *et al.*, Molecular and supramolecular engineering of π -conjugated systems for photovoltaic conversion. *Thin Solid Films*. **511–512**, 567–575 (2006).
48. X. Sun *et al.*, X-Shaped Oligothiophenes as a New Class of Electron Donors for Bulk-Heterojunction Solar Cells. *J. Phys. Chem. B*. **110**, 7702–7707 (2006).
49. N. Kopidakis *et al.*, Bulk heterojunction organic photovoltaic devices based on phenyl-cored thiophene dendrimers. *Appl. Phys. Lett.* **89**, 103524 (2006).
50. Y. Sun *et al.*, Solution-processed small-molecule solar cells with 6.7% efficiency. *Nat. Mater.* **11**, 44–48 (2011).
51. M. T. Lloyd, J. E. Anthony, G. G. Malliaras, Photovoltaics from soluble small molecules. *Mater. Today*. **10**, 34–41 (2007).
52. W. Cao, J. Xue, Recent progress in organic photovoltaics: device architecture and optical design. *Energy Environ. Sci.* **7**, 2123 (2014).
53. C. P. Brangwynne, P. Tompa, R. V. Pappu, Polymer physics of intracellular phase transitions. *Nat. Phys.* **11**, 899–904 (2015).
54. N. D. Treat, M. L. Chabinyc, Phase Separation in Bulk Heterojunctions of Semiconducting Polymers and Fullerenes for Photovoltaics. *Annu. Rev. Phys. Chem.* **65**, 59–81 (2014).
55. A. J. Heeger, 25th Anniversary Article: Bulk Heterojunction Solar Cells: Understanding the Mechanism of Operation. *Adv. Mater.* **26**, 10–28 (2014).
56. Y. Huang, E. J. Kramer, A. J. Heeger, G. C. Bazan, Bulk Heterojunction Solar Cells: Morphology and Performance Relationships. *Chem. Rev.* **114**, 7006–7043 (2014).
57. S. E. Shaheen *et al.*, 2.5% efficient organic plastic solar cells. *Appl. Phys. Lett.* **78**, 841–843 (2001).
58. M. Dante, J. Peet, T.-Q. Nguyen, Nanoscale Charge Transport and Internal Structure of Bulk Heterojunction Conjugated Polymer/Fullerene Solar Cells by Scanning Probe Microscopy. *J. Phys. Chem. C*. **112**, 7241–7249 (2008).
59. P. Erwin, M. E. Thompson, Elucidating the interplay between dark current coupling and open circuit voltage in organic photovoltaics. *Appl. Phys. Lett.* **98**, 223305 (2011).
60. L. J. A. Koster, S. E. Shaheen, J. C. Hummelen, Pathways to a New Efficiency Regime for Organic Solar Cells. *Adv. Energy Mater.* **2**, 1246–1253 (2012).
61. S. F. Alvarado, P. F. Seidler, D. G. Lidzey, D. D. C. Bradley, Direct Determination of the Exciton Binding Energy of Conjugated Polymers Using a Scanning Tunneling Microscope. *Phys. Rev. Lett.* **81**, 1082–1085 (1998).
62. R. G. Wilks, G. S. Chang, K. H. Kim, D. H. Choi, A. Moewes, Molecular orientation and optical luminescence properties of soluble star shaped oligothiophene molecules for organic electronic applications. *J. Electron Spectrosc. Relat. Phenom.* **184**, 355–359 (2011).

63. L. Onsager, Initial Recombination of Ions. *Phys. Rev.* **54**, 554–557 (1938).
64. C. L. Braun, Electric field assisted dissociation of charge transfer states as a mechanism of photocarrier production. *J. Chem. Phys.* **80**, 4157–4161 (1984).
65. K. S. Nalwa *et al.*, Enhanced charge separation in organic photovoltaic films doped with ferroelectric dipoles. *Energy Environ. Sci.* **5**, 7042–7049 (2012).
66. Y. Yuan *et al.*, Efficiency enhancement in organic solar cells with ferroelectric polymers. *Nat. Mater.* **10**, 296–302 (2011).
67. F. Deschler *et al.*, Reduced Charge Transfer Exciton Recombination in Organic Semiconductor Heterojunctions by Molecular Doping. *Phys. Rev. Lett.* **107**, 127402 (2011).
68. X. Liu *et al.*, Tuning the Dielectric Properties of Organic Semiconductors via Salt Doping. *J. Phys. Chem. B.* **117**, 15866–15874 (2013).
69. B. Carsten *et al.*, Mediating Solar Cell Performance by Controlling the Internal Dipole Change in Organic Photovoltaic Polymers. *Macromolecules.* **45**, 6390–6395 (2012).
70. B. Carsten *et al.*, Examining the Effect of the Dipole Moment on Charge Separation in Donor–Acceptor Polymers for Organic Photovoltaic Applications. *J. Am. Chem. Soc.* **133**, 20468–20475 (2011).
71. P. Yang *et al.*, Influence of fluorine substituents on the film dielectric constant and open-circuit voltage in organic photovoltaics. *J. Mater. Chem. C.* **2**, 3278–3284 (2014).
72. N. Cho *et al.*, High-Dielectric Constant Side-Chain Polymers Show Reduced Non-Geminate Recombination in Heterojunction Solar Cells. *Adv. Energy Mater.* **4**, 1301857 (2014).
73. S. Torabi *et al.*, Strategy for Enhancing the Dielectric Constant of Organic Semiconductors Without Sacrificing Charge Carrier Mobility and Solubility. *Adv. Funct. Mater.* **25**, 150–157 (2015).
74. J. E. Donaghey, A. Armin, P. L. Burn, P. Meredith, Dielectric constant enhancement of non-fullerene acceptors via side-chain modification. *Chem. Commun.* **51**, 14115–14118 (2015).
75. B. Bernardo *et al.*, Delocalization and dielectric screening of charge transfer states in organic photovoltaic cells. *Nat. Commun.* **5**, 3245 (2014).
76. M. Lenes *et al.*, Charge dissociation in polymer:fullerene bulk heterojunction solar cells with enhanced permittivity. *J. Appl. Phys.* **104**, 114517 (2008).
77. D. Veldman *et al.*, Compositional and Electric Field Dependence of the Dissociation of Charge Transfer Excitons in Alternating Polyfluorene Copolymer/Fullerene Blends. *J Am Chem Soc.* **130**, 7721–7735 (2008).
78. P. K. Nayak, K. L. Narasimhan, D. Cahen, Separating Charges at Organic Interfaces: Effects of Disorder, Hot States, and Electric Field. *J. Phys. Chem. Lett.* **4**, 1707–1717 (2013).
79. R. D. Pensack, J. B. Asbury, Beyond the Adiabatic Limit: Charge Photogeneration in Organic Photovoltaic Materials. *J. Phys. Chem. Lett.* **1**, 2255–2263 (2010).
80. A. E. Jailaubekov *et al.*, Hot charge-transfer excitons set the time limit for charge separation at donor/acceptor interfaces in organic photovoltaics. *Nat. Mater.* **12**, 66–73 (2013).
81. X. Shen, G. Han, D. Fan, Y. Xie, Y. Yi, Hot Charge-Transfer States Determine Exciton Dissociation in the DTDCTB/C60 Complex for Organic Solar Cells: A Theoretical Insight. *J. Phys. Chem. C.* **119**, 11320–11326 (2015).

82. H. van Eersel, R. A. J. Janssen, M. Kemerink, Mechanism for Efficient Photoinduced Charge Separation at Disordered Organic Heterointerfaces. *Adv. Funct. Mater.* **22**, 2700–2708 (2012).
83. A. A. Bakulin *et al.*, The Role of Driving Energy and Delocalized States for Charge Separation in Organic Semiconductors. *Science*. **335**, 1340–1344 (2012).
84. T. Drori *et al.*, Below-Gap Excitation of pi-Conjugated Polymer-Fullerene Blends: Implications for Bulk Organic Heterojunction Solar Cells. *Phys. Rev. Lett.* **101**, 037401 (2008).
85. G. Grancini *et al.*, Hot exciton dissociation in polymer solar cells. *Nat. Mater.* **12**, 29–33 (2013).
86. J. Lee *et al.*, Charge Transfer State Versus Hot Exciton Dissociation in Polymer–Fullerene Blended Solar Cells. *J. Am. Chem. Soc.* **132**, 11878–11880 (2010).
87. M. M. Mandoc, W. Veurman, J. Sweelssen, M. M. Koetse, P. W. M. Blom, Origin of the efficiency improvement in all-polymer solar cells upon annealing. *Appl. Phys. Lett.* **91**, 073518 (2007).
88. F. Ali, N. Periasamy, M. P. Patankar, K. L. Narasimhan, Photoluminescence Quenching and Photoconductivity in Devices Using 3,6-Diaryl-N-hexylcarbazole. *J. Phys. Chem. C*. **116**, 1298–1306 (2012).
89. A. R. Murphy, J. M. J. Fréchet, Organic Semiconducting Oligomers for Use in Thin Film Transistors. *Chem Rev.* **107**, 1066–1096 (2007).
90. J. Nelson, J. J. Kwiattkowski, J. Kirkpatrick, J. M. Frost, Modeling Charge Transport in Organic Photovoltaic Materials. *Acc Chem Res.* **42**, 1768–1778 (2009).
91. Y. Shirota, H. Kageyama, Charge Carrier Transporting Molecular Materials and Their Applications in Devices. *Chem Rev.* **107**, 953–1010 (2007).
92. C. D. Dimitrakopoulos, P. R. . Malenfant, Organic Thin Film Transistors for Large Area Electronics. *Adv. Mater.* **14**, 99–117 (2002).
93. G. Schweicher, Y. Olivier, V. Lemaure, Y. H. Geerts, What Currently Limits Charge Carrier Mobility in Crystals of Molecular Semiconductors? *Isr. J. Chem.* **54**, 595–620 (2014).
94. Y. Geng *et al.*, A theoretical discussion on the relationships among molecular packings, intermolecular interactions, and electron transport properties for naphthalene tetracarboxylic diimide derivatives. *J Mater Chem.* **21**, 15558–15566 (2011).
95. H. Bassler, G. Schonherr, M. Abkowitz, D. Pai, Hopping Transport in Prototypical Organic Glasses. *Phys. Rev. B*. **26**, 3105–3113 (1982).
96. D. Adam *et al.*, Transient Photoconductivity in a Discotic Liquid-Crystal. *Phys. Rev. Lett.* **70**, 457–460 (1993).
97. V. Coropceanu *et al.*, Charge Transport in Organic Semiconductors. *Chem Rev.* **107**, 926–952 (2007).
98. C. Goh, R. Kline, M. McGehee, E. Kadnikova, J. Frechet, Molecular-weight-dependent mobilities in regioregular poly(3-hexyl-thiophene) diodes. *Appl. Phys. Lett.* **86**, 122110 (2005).
99. P. Blom, M. deJong, J. Vleggaar, Electron and hole transport in poly(p-phenylene vinylene) devices. *Appl. Phys. Lett.* **68**, 3308–3310 (1996).
100. M. Mas-Torrent, C. Rovira, Role of Molecular Order and Solid-State Structure in Organic Field-Effect Transistors. *Chem. Rev.* **111**, 4833–4856 (2011).

101. “Best Research-Cell Efficiencies” (National Renewable Energy Laboratory, 2016), (available at http://www.nrel.gov/ncpv/images/efficiency_chart.jpg).
102. M. A. Green, A. Ho-Baillie, H. J. Snaith, The emergence of perovskite solar cells. *Nat. Photonics*. **8**, 506–514 (2014).
103. C. D. Bailie *et al.*, Semi-transparent perovskite solar cells for tandems with silicon and CIGS. *Energy Env. Sci.* **8**, 956–963 (2015).
104. G. E. Eperon, V. M. Burlakov, P. Docampo, A. Goriely, H. J. Snaith, Morphological Control for High Performance, Solution-Processed Planar Heterojunction Perovskite Solar Cells. *Adv. Funct. Mater.* **24**, 151–157 (2014).
105. J. G. Bednorz, K. A. Müller, Perovskite-type oxides - The new approach to high-Tc superconductivity. *Rev. Mod. Phys.* **60**, 585–600 (1988).
106. A. von Hippel, Ferroelectricity, Domain Structure, and Phase Transitions of Barium Titanate. *Rev. Mod. Phys.* **22**, 221–237 (1950).
107. T. He *et al.*, Superconductivity in the non-oxide perovskite MgCNi₃. *Nature*. **411**, 54–56 (2001).
108. C. C. Stoumpos, C. D. Malliakas, M. G. Kanatzidis, Semiconducting Tin and Lead Iodide Perovskites with Organic Cations: Phase Transitions, High Mobilities, and Near-Infrared Photoluminescent Properties. *Inorg. Chem.* **52**, 9019–9038 (2013).
109. H. S. Jung, N.-G. Park, Perovskite Solar Cells: From Materials to Devices. *Small*. **11**, 10–25 (2015).
110. S. De Wolf *et al.*, Organometallic Halide Perovskites: Sharp Optical Absorption Edge and Its Relation to Photovoltaic Performance. *J. Phys. Chem. Lett.* **5**, 1035–1039 (2014).
111. C. Quarti *et al.*, Structural and optical properties of methylammonium lead iodide across the tetragonal to cubic phase transition: implications for perovskite solar cells. *Energy Env. Sci.* **9**, 155–163 (2016).
112. A. Poglitsch, D. Weber, Dynamic disorder in methylammoniumtrihalogenoplumbates (II) observed by millimeter-wave spectroscopy. *J. Chem. Phys.* **87**, 6373–6378 (1987).
113. M. Liu, M. B. Johnston, H. J. Snaith, Efficient planar heterojunction perovskite solar cells by vapour deposition. *Nature*. **501**, 395–398 (2013).
114. S. D. Stranks, H. J. Snaith, Metal-halide perovskites for photovoltaic and light-emitting devices. *Nat. Nanotechnol.* **10**, 391–402 (2015).
115. J.-W. Lee *et al.*, Formamidinium and Cesium Hybridization for Photo- and Moisture-Stable Perovskite Solar Cell. *Adv. Energy Mater.* **5**, 1501310 (2015).
116. S. T. Williams *et al.*, Role of chloride in the morphological evolution of organo-lead halide perovskite thin films. *ACS Nano*. **8**, 10640–10654 (2014).
117. Y. Tidhar *et al.*, Crystallization of methyl ammonium lead halide perovskites: implications for photovoltaic applications. *J. Am. Chem. Soc.* **136**, 13249–13256 (2014).
118. H. Yu *et al.*, The role of chlorine in the formation process of “CH₃NH₃PbI_{3-x}Cl_x” perovskite. *Adv. Funct. Mater.* **24**, 7102–7108 (2014).
119. E. T. Hoke *et al.*, Reversible photo-induced trap formation in mixed-halide hybrid perovskites for photovoltaics. *Chem. Sci.* **6**, 613–617 (2014).
120. D. P. McMeekin *et al.*, A mixed-cation lead mixed-halide perovskite absorber for tandem solar cells. *Science*. **351**, 151–155 (2016).
121. S. D. Stranks, P. K. Nayak, W. Zhang, T. Stergiopoulos, H. J. Snaith, Formation of Thin Films of Organic–Inorganic Perovskites for High-Efficiency Solar Cells. *Angew. Chem. Int. Ed.*, 3240–3248 (2015).

122. J. Burschka *et al.*, Sequential deposition as a route to high-performance perovskite-sensitized solar cells. *Nature*. **499**, 316–319 (2013).
123. Q. Chen *et al.*, Planar Heterojunction Perovskite Solar Cells via Vapor-Assisted Solution Process. *J. Am. Chem. Soc.* **136**, 622–625 (2014).
124. M. I. Saidaminov *et al.*, High-quality bulk hybrid perovskite single crystals within minutes by inverse temperature crystallization. *Nat. Commun.* **6**, 7586 (2015).
125. D. Shi *et al.*, Low trap-state density and long carrier diffusion in organolead trihalide perovskite single crystals. *Science*. **347**, 519–522 (2015).
126. Q. Dong *et al.*, Electron-hole diffusion lengths >175 μm in solution grown $\text{CH}_3\text{NH}_3\text{PbI}_3$ single crystals. *Science*. **347**, 967–970 (2015).
127. A. Kojima, K. Teshima, Y. Shirai, T. Miyasaka, Organometal Halide Perovskites as Visible-Light Sensitizers for Photovoltaic Cells. *J. Am. Chem. Soc.* **131**, 6050–6051 (2009).
128. J.-H. Im, C.-R. Lee, J.-W. Lee, S.-W. Park, N.-G. Park, 6.5% efficient perovskite quantum-dot-sensitized solar cell. *Nanoscale*. **3**, 4088–4093 (2011).
129. H.-S. Kim *et al.*, Lead iodide perovskite sensitized all-solid-state submicron thin film mesoscopic solar cell with efficiency exceeding 9%. *Sci. Rep.* **2**, 591 (2012).
130. M. M. Lee, J. Teuscher, T. Miyasaka, T. N. Murakami, H. J. Snaith, Efficient Hybrid Solar Cells Based on Meso-Superstructured Organometal Halide Perovskites. *Science*. **338**, 643–647 (2012).
131. H. Zhou *et al.*, Interface engineering of highly efficient perovskite solar cells. *Science*. **345**, 542–546 (2014).
132. N. J. Jeon *et al.*, Compositional engineering of perovskite materials for high-performance solar cells. *Nature*. **517**, 476–480 (2015).
133. W.-J. Yin, T. Shi, Y. Yan, Unique Properties of Halide Perovskites as Possible Origins of the Superior Solar Cell Performance. *Adv. Mater.* **26**, 4653–4658 (2014).
134. E. Edri *et al.*, Elucidating the charge carrier separation and working mechanism of $\text{CH}_3\text{NH}_3\text{PbI}_3\text{-xClx}$ perovskite solar cells. *Nat. Commun.* **5**, 3461 (2014).
135. M. Grätzel, The light and shade of perovskite solar cells. *Nat. Mater.* **13**, 838–842 (2014).
136. Y. Li *et al.*, Fabrication of planar heterojunction perovskite solar cells by controlled low-pressure vapor annealing. *J. Phys. Chem. Lett.* **6**, 493–499 (2015).
137. S. D. Stranks *et al.*, Electron-hole diffusion lengths exceeding 1 micrometer in an organometal trihalide perovskite absorber. *Science*. **342**, 341–344 (2013).
138. G. Xing *et al.*, Long-range balanced electron- and hole-transport lengths in organic-inorganic $\text{CH}_3\text{NH}_3\text{PbI}_3$. *Science*. **342**, 344–347 (2013).
139. C. Wehrenfennig, G. E. Eperon, M. B. Johnston, H. J. Snaith, L. M. Herz, High charge carrier mobilities and lifetimes in organolead trihalide perovskites. *Adv. Mater.* **26**, 1584–1589 (2014).
140. C. S. Ponseca *et al.*, Organometal Halide Perovskite Solar Cell Materials Rationalized: Ultrafast Charge Generation, High and Microsecond-Long Balanced Mobilities, and Slow Recombination. *J. Am. Chem. Soc.* **136**, 5189–5192 (2014).
141. C. Motta, F. El-Mellouhi, S. Sanvito, Charge carrier mobility in hybrid halide perovskites. *Sci. Rep.* **5**, 12746 (2015).
142. D. W. deQuilettes *et al.*, Impact of microstructure on local carrier lifetime in perovskite solar cells. *Science*. **348**, 683–686 (2015).

143. C. G. Bischak, E. M. Sanehira, J. T. Precht, J. M. Luther, N. S. Ginsberg, Heterogeneous Charge Carrier Dynamics in Organic–Inorganic Hybrid Materials: Nanoscale Lateral and Depth-Dependent Variation of Recombination Rates in Methylammonium Lead Halide Perovskite Thin Films. *Nano Lett.* **15**, 4799–4807 (2015).
144. N. K. Noel *et al.*, Enhanced Photoluminescence and Solar Cell Performance via Lewis Base Passivation of Organic–Inorganic Lead Halide Perovskites. *ACS Nano*. **8**, 9815–9821 (2014).
145. E. Edri *et al.*, Why Lead Methylammonium Tri-Iodide Perovskite-Based Solar Cells Require a Mesoporous Electron Transporting Scaffold (but Not Necessarily a Hole Conductor). *Nano Lett.* **14**, 1000–1004 (2014).
146. J. H. Noh, S. H. Im, J. H. Heo, T. N. Mandal, S. I. Seok, Chemical management for colorful, efficient, and stable inorganic–organic hybrid nanostructured solar cells. *Nano Lett.* **13**, 1764–1769 (2013).
147. F. Hao, C. C. Stoumpos, R. P. H. Chang, M. G. Kanatzidis, Anomalous band gap behavior in mixed Sn and Pb perovskites enables broadening of absorption spectrum in solar cells. *J. Am. Chem. Soc.* **136**, 8094–8099 (2014).
148. F. Hao, C. C. Stoumpos, D. H. Cao, R. P. H. Chang, M. G. Kanatzidis, Lead-free solid-state organic-inorganic halide perovskite solar cells. *Nat. Photonics*. **8**, 489–494 (2014).
149. N. K. Noel *et al.*, Lead-free organic–inorganic tin halide perovskites for photovoltaic applications. *Energy Environ. Sci.* **7**, 3061–3068 (2014).
150. H. J. Snaith *et al.*, Anomalous Hysteresis in Perovskite Solar Cells. *J. Phys. Chem. Lett.* **5**, 1511–1515 (2014).
151. E. L. Unger *et al.*, Hysteresis and transient behavior in current–voltage measurements of hybrid-perovskite absorber solar cells. *Energy Environ. Sci.* **7**, 3690–3698 (2014).
152. A checklist for photovoltaic research. *Nat. Mater.* **14**, 1073–1073 (2015).
153. W. Tress *et al.*, Understanding the rate-dependent J–V hysteresis, slow time component, and aging in $\text{CH}_3\text{NH}_3\text{PbI}_3$ perovskite solar cells: the role of a compensated electric field. *Energy Env. Sci.* **8**, 995–1004 (2015).
154. A. Dualeh *et al.*, Impedance Spectroscopic Analysis of Lead Iodide Perovskite-Sensitized Solid-State Solar Cells. *ACS Nano*. **8**, 362–373 (2014).
155. Y. Zhang *et al.*, Charge selective contacts, mobile ions and anomalous hysteresis in organic–inorganic perovskite solar cells. *Mater Horiz.* **2**, 315–322 (2015).
156. Y. Yuan *et al.*, Photovoltaic Switching Mechanism in Lateral Structure Hybrid Perovskite Solar Cells. *Adv. Energy Mater.* **5**, 1500615 (2015).
157. M. De Bastiani *et al.*, Ion Migration and the Role of Preconditioning Cycles in the Stabilization of the J–V Characteristics of Inverted Hybrid Perovskite Solar Cells. *Adv. Energy Mater.* **6**, 1501453 (2016).
158. Y. Yuan, J. Huang, Ion Migration in Organometal Trihalide Perovskite and Its Impact on Photovoltaic Efficiency and Stability. *Acc. Chem. Res.* **49**, 286–293 (2016).
159. Z. Xiao *et al.*, Giant switchable photovoltaic effect in organometal trihalide perovskite devices. *Nat. Mater.* **14**, 193–198 (2015).
160. Y. Zhao *et al.*, Anomalously large interface charge in polarity-switchable photovoltaic devices: an indication of mobile ions in organic–inorganic halide perovskites. *Energy Environ. Sci.* **8**, 1256–1260 (2015).
161. L. N. Quan *et al.*, Ligand-Stabilized Reduced-Dimensionality Perovskites. *J. Am. Chem. Soc.* (2016), doi:10.1021/jacs.5b11740.

162. Dawn a. Bonnell, Sergei V. Kalinin, in *Scanning Probe Microscopy for Energy Research* (WORLD SCIENTIFIC, 2012; http://www.worldscientific.com/doi/abs/10.1142/9789814434713_0001), vol. Volume 7 of *World Scientific Series in Nanoscience and Nanotechnology*, pp. 3–35.
163. T. Glatzel, D. F. Marrón, T. Schedel-Niedrig, S. Sadewasser, M. C. Lux-Steiner, CuGaSe₂ solar cell cross section studied by Kelvin probe force microscopy in ultrahigh vacuum. *Appl. Phys. Lett.* **81**, 2017–2019 (2002).
164. H. Hoppe *et al.*, Kelvin Probe Force Microscopy Study on Conjugated Polymer/Fullerene Bulk Heterojunction Organic Solar Cells. *Nano Lett.* **5**, 269–274 (2005).
165. A. Kikukawa, S. Hosaka, R. Imura, Silicon pn junction imaging and characterizations using sensitivity enhanced Kelvin probe force microscopy. *Appl. Phys. Lett.* **66**, 3510–3512 (1995).
166. S. Sadewasser *et al.*, Kelvin probe force microscopy for the nano scale characterization of chalcopyrite solar cell materials and devices. *Thin Solid Films.* **431–432**, 257–261 (2003).
167. V. W. Bergmann *et al.*, Real-space observation of unbalanced charge distribution inside a perovskite-sensitized solar cell. *Nat. Commun.* **5**, 5001 (2014).
168. W. Bao *et al.*, Mapping Local Charge Recombination Heterogeneity by Multidimensional Nanospectroscopic Imaging. *Science.* **338**, 1317–1321 (2012).
169. P. R. Edwards, S. A. Galloway, K. Durose, EBIC and luminescence mapping of CdTe/CdS solar cells. *Thin Solid Films.* **372**, 284–291 (2000).
170. M. J. Romero *et al.*, Cathodoluminescence of Cu(In,Ga)Se₂ thin films used in high-efficiency solar cells. *Appl. Phys. Lett.* **83**, 4770–4772 (2003).
171. B. Voigtländer, in *Scanning Probe Microscopy* (Springer Berlin Heidelberg, 2015; http://link.springer.com/chapter/10.1007/978-3-662-45240-0_11), *NanoScience and Technology*, pp. 145–155.
172. E. Meyer, H. J. Hug, R. Bennewitz, *Scanning Probe Microscopy* (Springer Berlin Heidelberg, Berlin, Heidelberg, 2004; <http://link.springer.com/10.1007/978-3-662-09801-1>), *Advanced Texts in Physics*.
173. B. Voigtländer, in *Scanning Probe Microscopy* (Springer Berlin Heidelberg, 2015; http://link.springer.com/chapter/10.1007/978-3-662-45240-0_13), *NanoScience and Technology*, pp. 177–186.
174. D. Abou-Ras, T. Kirchartz, U. Rau, Eds., *Advanced Characterization Techniques for Thin Film Solar Cells* (2011; <http://onlinelibrary.wiley.com/book/10.1002/9783527636280>).
175. K. Akimoto *et al.*, Thin film deposition of Cu₂O and application for solar cells. *Sol. Energy.* **80**, 715–722 (2006).
176. Y. Nasuno, M. Kondo, A. Matsuda, Effects of Substrate Surface Morphology on Microcrystalline Silicon Solar Cells. *Jpn. J. Appl. Phys.* **40**, L303–L305 (2001).
177. L. S. C. Pingree, O. G. Reid, D. S. Ginger, Electrical Scanning Probe Microscopy on Active Organic Electronic Devices. *Adv. Mater.* **21**, 19–28 (2009).
178. R. H. Shin, W. Jo, D.-W. Kim, J. H. Yun, S. Ahn, Local current–voltage behaviors of preferentially and randomly textured Cu(In,Ga)Se₂ thin films investigated by conductive atomic force microscopy. *Appl. Phys. A.* **104**, 1189–1194 (2011).
179. D. Azulay *et al.*, Current routes in polycrystalline CuInSe₂ and Cu(In,Ga)Se₂ films. *Sol. Energy Mater. Sol. Cells.* **91**, 85–90 (2007).
180. S. Sadewasser *et al.*, Nanometer-scale electronic and microstructural properties of grain boundaries in Cu(In,Ga)Se₂. *Thin Solid Films.* **519**, 7341–7346 (2011).

181. R. Giridharagopal, G. E. Rayermann, D. S. Ginger, in *Scanning Probe Microscopy for Energy Research* (WORLD SCIENTIFIC, 2013; http://www.worldscientific.com/doi/abs/10.1142/9789814434713_0002), pp. 39–72.
182. C. Groves, O. G. Reid, D. S. Ginger, Heterogeneity in Polymer Solar Cells: Local Morphology and Performance in Organic Photovoltaics Studied with Scanning Probe Microscopy. *Acc. Chem. Res.* **43**, 612–620 (2010).
183. J. M. Mativetsky, Y.-L. Loo, P. Samorì, Elucidating the nanoscale origins of organic electronic function by conductive atomic force microscopy. *J. Mater. Chem. C*, **2**, 3118–3128 (2014).
184. X.-D. Dang, M. Dante, T.-Q. Nguyen, Morphology and conductivity modification of poly(3,4-ethylenedioxythiophene):poly(styrene sulfonate) films induced by conductive atomic force microscopy measurements. *Appl. Phys. Lett.* **93**, 241911 (2008).
185. O. Douhéret *et al.*, Nanoscale electrical characterization of organic photovoltaic blends by conductive atomic force microscopy. *Appl. Phys. Lett.* **89**, 032107 (2006).
186. D. C. Coffey, O. G. Reid, D. B. Rodovsky, G. P. Bartholomew, D. S. Ginger, Mapping local photocurrents in polymer/fullerene solar cells with photoconductive atomic force microscopy. *Nano Lett.* **7**, 738–744 (2007).
187. S. Y. Leblebici *et al.*, Near-Infrared Azadipyrrromethenes as Electron Donor for Efficient Planar Heterojunction Organic Solar Cells. *ACS Appl Mater Interfaces*, **3**, 4469–4474 (2011).
188. K. Vasseur, B. P. Rand, D. Cheyns, L. Froyen, P. Heremans, Structural Evolution of Evaporated Lead Phthalocyanine Thin Films for Near-Infrared Sensitive Solar Cells†. *Chem. Mater.* **23**, 886–895 (2011).
189. W. Wang, D. Placencia, N. R. Armstrong, Planar and textured heterojunction organic photovoltaics based on chloroindium phthalocyanine (ClInPc) versus titanyl phthalocyanine (TiOPc) donor layers. *Org. Electron.* **12**, 383–393 (2011).
190. B. P. Rand, J. Xue, F. Yang, S. R. Forrest, Organic solar cells with sensitivity extending into the near infrared. *Appl. Phys. Lett.* **87**, 233508 (2005).
191. B. Ma, C. H. Woo, Y. Miyamoto, J. M. J. Fréchet, Solution Processing of a Small Molecule, Subnaphthalocyanine, for Efficient Organic Photovoltaic Cells. *Chem. Mater.* **21**, 1413–1417 (2009).
192. H. Bürckstümmer, N. M. Kronenberg, K. Meerholz, F. Würthner, Near-Infrared Absorbing Merocyanine Dyes for Bulk Heterojunction Solar Cells. *Org. Lett.* **12**, 3666–3669 (2010).
193. G. Wei, S. Wang, K. Renshaw, M. E. Thompson, S. R. Forrest, Solution-Processed Squaraine Bulk Heterojunction Photovoltaic Cells. *ACS Nano*, **4**, 1927–1934 (2010).
194. G. Zhang, Y. Fu, Z. Xie, Q. Zhang, Synthesis and Photovoltaic Properties of New Low Bandgap Isoindigo-Based Conjugated Polymers. *Macromolecules*, **44**, 1414–1420 (2011).
195. J. Mei, K. R. Graham, R. Stalder, J. R. Reynolds, Synthesis of Isoindigo-Based Oligothiophenes for Molecular Bulk Heterojunction Solar Cells. *Org. Lett.* **12**, 660–663 (2010).
196. Y. Kubo *et al.*, Near-Infrared Absorbing Boron-dibenzopyrromethenes that Serve As Light-Harvesting Sensitizers for Polymeric Solar Cells. *Org. Lett.* **13**, 4574–4577 (2011).
197. A. B. Tamayo, B. Walker, T.-Q. Nguyen*, A Low Band Gap, Solution Processable Oligothiophene with a Diketopyrrolopyrrole Core for Use in Organic Solar Cells. *J. Phys. Chem. C*, **112**, 11545–11551 (2008).

198. M. D. Perez, C. Borek, S. R. Forrest, M. E. Thompson, Molecular and Morphological Influences on the Open Circuit Voltages of Organic Photovoltaic Devices. *J. Am. Chem. Soc.* **131**, 9281–9286 (2009).
199. W. Zhao, E. M. Carreira, Conformationally Restricted Aza-Bodipy: A Highly Fluorescent, Stable, Near-Infrared-Absorbing Dye. *Angew. Chem. Int. Ed.* **44**, 1677–1679 (2005).
200. J. Killoran, D. F. O'Shea, Impact of a conformationally restricted receptor on the BF₂ chelated azadipyrrromethene fluorosensing platform. *Chem. Commun.*, 1503 (2006).
201. M. J. Hall, L. T. Allen, D. F. O'Shea, PET modulated fluorescent sensing from the BF₂ chelated azadipyrrromethene platform. *Org. Biomol. Chem.* **4**, 776 (2006).
202. A. Gorman *et al.*, In vitro demonstration of the heavy-atom effect for photodynamic therapy. *J. Am. Chem. Soc.* **126**, 10619–10631 (2004).
203. W. M. Gallagher *et al.*, A potent nonporphyrin class of photodynamic therapeutic agent: cellular localisation, cytotoxic potential and influence of hypoxia. *Br J Cancer.* **92**, 1702–1710 (2005).
204. A. Loudet *et al.*, B,O-Chelated Azadipyrrromethenes as Near-IR Probes. *Org. Lett.* **10**, 4771–4774 (2008).
205. S. O. McDonnell, D. F. O'Shea, Near-Infrared Sensing Properties of Dimethylamino-Substituted BF₂-Azadipyrrromethenes. *Org. Lett.* **8**, 3493–3496 (2006).
206. G. Ulrich, R. Ziessel, A. Harriman, The Chemistry of Fluorescent Bodipy Dyes: Versatility Unsurpassed. *Angew. Chem. Int. Ed.* **47**, 1184–1201 (2008).
207. M. J. Hall, S. O. McDonnell, J. Killoran, D. F. O'Shea, A Modular Synthesis of Unsymmetrical Tetraarylazadipyrrromethenes. *J. Org. Chem.* **70**, 5571–5578 (2005).
208. C. J. Brabec *et al.*, Origin of the Open Circuit Voltage of Plastic Solar Cells. *Adv. Funct. Mater.* **11**, 374–380 (2001).
209. D. Kekuda, J.-H. Huang, K.-C. Ho, C.-W. Chu, Modulation of Donor–Acceptor Interface through Thermal Treatment for Efficient Bilayer Organic Solar Cells. *J. Phys. Chem. C.* **114**, 2764–2768 (2010).
210. T. W. Holcombe *et al.*, Steric Control of the Donor/Acceptor Interface: Implications in Organic Photovoltaic Charge Generation. *J. Am. Chem. Soc.* **133**, 12106–12114 (2011).
211. G. Li *et al.*, High-efficiency solution processable polymer photovoltaic cells by self-organization of polymer blends. *Nat. Mater.* **4**, 864–868 (2005).
212. S. K. Park, T. N. Jackson, J. E. Anthony, D. A. Mourey, High mobility solution processed 6,13-bis(triisopropyl-silylethynyl) pentacene organic thin film transistors. *Appl. Phys. Lett.* **91**, 063514 (2007).
213. P. C. Chang *et al.*, Film Morphology and Thin Film Transistor Performance of Solution-Processed Oligothiophenes. *Chem. Mater.* **16**, 4783–4789 (2004).
214. J.-F. Chang *et al.*, Enhanced Mobility of Poly(3-hexylthiophene) Transistors by Spin-Coating from High-Boiling-Point Solvents. *Chem. Mater.* **16**, 4772–4776 (2004).
215. B. Walker, C. Kim, T.-Q. Nguyen, Small Molecule Solution-Processed Bulk Heterojunction Solar Cells†. *Chem. Mater.* **23**, 470–482 (2011).
216. Y. Matsuo *et al.*, Columnar Structure in Bulk Heterojunction in Solution-Processable Three-Layered p-i-n Organic Photovoltaic Devices Using Tetrabenzoporphyrin Precursor and Silylmethyl[60]fullerene. *J. Am. Chem. Soc.* **131**, 16048–16050 (2009).
217. Sibel Y. Leblebici, Teresa L. Chen, Paul Olalde-Velasco, Wanli Yang, Biwu Ma, Reducing Exciton Binding Energy by Increasing Thin Film Permittivity: Effective

- Approach to Enhance Exciton Separation Efficiency in Organic Solar Cells. *Rev. ACS Nano* (2013).
218. B. A. Gregg, M. C. Hanna, Comparing organic to inorganic photovoltaic cells: Theory, experiment, and simulation. *J. Appl. Phys.* **93**, 3605–3614 (2003).
 219. X. Gong *et al.*, Bulk Heterojunction Solar Cells with Large Open-Circuit Voltage: Electron Transfer with Small Donor-Acceptor Energy Offset. *Adv. Mater.* **23**, 2272–2277 (2011).
 220. H. Ohkita *et al.*, Charge Carrier Formation in Polythiophene/Fullerene Blend Films Studied by Transient Absorption Spectroscopy. *J. Am. Chem. Soc.* **130**, 3030–3042 (2008).
 221. M. Engel, F. Kunze, D. C. Lupascu, N. Benson, R. Schmechel, Reduced exciton binding energy in organic semiconductors: Tailoring the Coulomb interaction. *Phys. Status Solidi RRL - Rapid Res. Lett.* **6**, 68–70 (2012).
 222. N. Camaioni, R. Po, Pushing the Envelope of the Intrinsic Limitation of Organic Solar Cells. *J. Phys. Chem. Lett.* **4**, 1821–1828 (2013).
 223. C. F. Madigan, V. Bulović, Solid State Solvation in Amorphous Organic Thin Films. *Phys. Rev. Lett.* **91**, 247403 (2003).
 224. Y. Zhong, J. Ma, K. Hashimoto, K. Tajima, Electric Field-Induced Dipole Switching at the Donor/Acceptor Interface in Organic Solar Cells. *Adv. Mater.* **25**, 1071–1075 (2012).
 225. P. K. Watkins, A. B. Walker, G. L. B. Verschoor, Dynamical Monte Carlo Modelling of Organic Solar Cells: The Dependence of Internal Quantum Efficiency on Morphology. *Nano Lett.* **5**, 1814–1818 (2005).
 226. P. Heremans, D. Cheyns, B. P. Rand, Strategies for Increasing the Efficiency of Heterojunction Organic Solar Cells: Material Selection and Device Architecture. *Acc. Chem. Res.* **42**, 1740–1747 (2009).
 227. L. F. J. Piper *et al.*, Soft x-ray spectroscopy study of the element and orbital contributions to the electronic structure of copper hexadecafluoro-phthalocyanine. *Phys. Rev. B.* **81**, 045201 (2010).
 228. J. H. Seo *et al.*, Electronic structure of NPB and BCP molecules probed by x-ray emission spectroscopy. *J. Chem. Phys.* **126**, 064706 (2007).
 229. J. H. Seo, Y. Jin, J. Z. Brzezinski, B. Walker, T.-Q. Nguyen, Exciton Binding Energies in Conjugated Polyelectrolyte Films. *ChemPhysChem.* **10**, 1023–1027 (2009).
 230. G. Angulo *et al.*, Ultrafast Decay of the Excited Singlet States of Thioxanthone by Internal Conversion and Intersystem Crossing. *ChemPhysChem.* **11**, 480–488 (2010).
 231. W. A. Yager, S. O. Morgan, Transitions in Camphor and Chemically Related Compounds. I. Dipole Rotation in Crystalline Solids. *J. Am. Chem. Soc.* **57**, 2071–2078 (1935).
 232. K. Tvingstedt *et al.*, Electroluminescence from Charge Transfer States in Polymer Solar Cells. *J. Am. Chem. Soc.* **131**, 11819–11824 (2009).
 233. B. C. Thompson, J. M. J. Fréchet, Polymer–Fullerene Composite Solar Cells. *Angew. Chem. Int. Ed.* **47**, 58–77 (2008).
 234. J. A. Carr, S. Chaudhary, On accurate capacitance characterization of organic photovoltaic cells. *Appl. Phys. Lett.* **100**, 213902 (2012).
 235. P. T. van Duijnen, H. D. de Gier, R. Broer, R. W. A. Havenith, The behaviour of charge distributions in dielectric media. *Chem. Phys. Lett.* **615**, 83–88 (2014).
 236. J. D. Gallagher *et al.*, Electroluminescence from GeSn heterostructure pin diodes at the indirect to direct transition. *Appl. Phys. Lett.* **106**, 091103 (2015).

237. Y. Yao, J. Hou, Z. Xu, G. Li, Y. Yang, Effects of Solvent Mixtures on the Nanoscale Phase Separation in Polymer Solar Cells. *Adv. Funct. Mater.* **18**, 1783–1789 (2008).
238. Z. Xu *et al.*, Vertical Phase Separation in Poly(3-hexylthiophene): Fullerene Derivative Blends and its Advantage for Inverted Structure Solar Cells. *Adv. Funct. Mater.* **19**, 1227–1234 (2009).
239. H. Hoppe *et al.*, Efficiency limiting morphological factors of MDMO-PPV:PCBM plastic solar cells. *Thin Solid Films.* **511–512**, 587–592 (2006).
240. T. Martens *et al.*, Disclosure of the nanostructure of MDMO-PPV:PCBM bulk heterojunction organic solar cells by a combination of SPM and TEM. *Synth. Met.* **138**, 243–247 (2003).
241. P. B. Deotare *et al.*, Nanoscale transport of charge-transfer states in organic donor-acceptor blends. *Nat. Mater.* **14**, 1130–1134 (2015).
242. D. P. Hoffman, S. Y. Leblebici, A. M. Schwartzberg, R. A. Mathies, Exciton Mobility in Organic Photovoltaic Heterojunctions from Femtosecond Stimulated Raman. *J. Phys. Chem. Lett.* **6**, 2919–2923 (2015).
243. I. Montanari *et al.*, Transient optical studies of charge recombination dynamics in a polymer/fullerene composite at room temperature. *Appl. Phys. Lett.* **81**, 3001–3003 (2002).
244. T. M. Clarke, A. M. Ballantyne, J. Nelson, D. D. C. Bradley, J. R. Durrant, Free Energy Control of Charge Photogeneration in Polythiophene/Fullerene Solar Cells: The Influence of Thermal Annealing on P3HT/PCBM Blends. *Adv. Funct. Mater.* **18**, 4029–4035 (2008).
245. C. G. Shuttle *et al.*, Bimolecular recombination losses in polythiophene: Fullerene solar cells. *Phys. Rev. B.* **78**, 113201 (2008).
246. A. F. Nogueira *et al.*, Charge Recombination in Conjugated Polymer/Fullerene Blended Films Studied by Transient Absorption Spectroscopy. *J. Phys. Chem. B.* **107**, 1567–1573 (2003).
247. H. Ohkita, S. Ito, Transient absorption spectroscopy of polymer-based thin-film solar cells. *Polymer.* **52**, 4397–4417 (2011).
248. P. Kukura, D. W. McCamant, R. A. Mathies, Femtosecond Stimulated Raman Spectroscopy. *Annu. Rev. Phys. Chem.* **58**, 461–488 (2007).
249. J.-L. Brédas, D. Beljonne, V. Coropceanu, J. Cornil, Charge-Transfer and Energy-Transfer Processes in π -Conjugated Oligomers and Polymers: A Molecular Picture. *Chem Rev.* **104**, 4971–5004 (2004).
250. J. V. Lockard, A. Butler Ricks, D. T. Co, M. R. Wasielewski, Interrogating the Intramolecular Charge-Transfer State of a Julolidine–Anthracene Donor–Acceptor Molecule with Femtosecond Stimulated Raman Spectroscopy. *J. Phys. Chem. Lett.* **1**, 215–218 (2010).
251. S.-Y. Lee, D. Zhang, D. W. McCamant, P. Kukura, R. A. Mathies, Theory of femtosecond stimulated Raman spectroscopy. *J. Chem. Phys.* **121**, 3632–3642 (2004).
252. D. C. Hannah *et al.*, Direct Measurement of Lattice Dynamics and Optical Phonon Excitation in Semiconductor Nanocrystals Using Femtosecond Stimulated Raman Spectroscopy. *Phys. Rev. Lett.* **111**, 107401 (2013).
253. R. M. Young *et al.*, Ultrafast Conformational Dynamics of Electron Transfer in ExBox4+ π Perylene. *J. Phys. Chem. A.* **117**, 12438–12448 (2013).

254. P. Kukura, D. W. McCamant, S. Yoon, D. B. Wandschneider, R. A. Mathies, Structural Observation of the Primary Isomerization in Vision with Femtosecond-Stimulated Raman. *Science*. **310**, 1006–1009 (2005).
255. F. Provencher *et al.*, Direct observation of ultrafast long-range charge separation at polymer–fullerene heterojunctions. *Nat. Commun.* **5**, 4288 (2014).
256. D. P. Hoffman *et al.*, Electron Transfer Dynamics of Triphenylamine Dyes Bound to TiO₂ Nanoparticles from Femtosecond Stimulated Raman Spectroscopy. *J. Phys. Chem. C*. **117**, 6990–6997 (2013).
257. D. P. Hoffman, S. R. Ellis, R. A. Mathies, Characterization of a Conical Intersection in a Charge-Transfer Dimer with Two-Dimensional Time-Resolved Stimulated Raman Spectroscopy. *J. Phys. Chem. A*. **118**, 4955–4965 (2014).
258. K. E. Brown, B. S. Veldkamp, D. T. Co, M. R. Wasielewski, Vibrational Dynamics of a Perylene–Perylenediimide Donor–Acceptor Dyad Probed with Femtosecond Stimulated Raman Spectroscopy. *J. Phys. Chem. Lett.* **3**, 2362–2366 (2012).
259. D. W. McCamant, P. Kukura, S. Yoon, R. A. Mathies, Femtosecond broadband stimulated Raman spectroscopy: Apparatus and methods. *Rev. Sci. Instrum.* **75**, 4971–4980 (2004).
260. D. P. Hoffman, D. Valley, S. R. Ellis, M. Creelman, R. A. Mathies, Optimally shaped narrowband picosecond pulses for femtosecond stimulated Raman spectroscopy. *Opt. Express*. **21**, 21685 (2013).
261. R. D. Johnson, G. Meijer, D. S. Bethune, C₆₀ has icosahedral symmetry. *J. Am. Chem. Soc.* **112**, 8983–8984 (1990).
262. C. J. Brabec *et al.*, Tracing photoinduced electron transfer process in conjugated polymer/fullerene bulk heterojunctions in real time. *Chem. Phys. Lett.* **340**, 232–236 (2001).
263. M. Baitoul *et al.*, In situ resonant Raman and optical investigations of p-doped poly (p-phenylene vinylene). *Polymer*. **41**, 6955–6964 (2000).
264. A. J. Wise, J. K. Grey, Resonance Raman studies of excited state structural displacements of conjugated polymers in donor/acceptor charge transfer complexes. *Phys. Chem. Chem. Phys.* **14**, 11273–11276 (2012).
265. G. Grancini *et al.*, Hot exciton dissociation in polymer solar cells. *Nat. Mater.* **12**, 29–33 (2013).
266. K. Chen, A. J. Barker, M. E. Reish, K. C. Gordon, J. M. Hodgkiss, Broadband Ultrafast Photoluminescence Spectroscopy Resolves Charge Photogeneration via Delocalized Hot Excitons in Polymer:Fullerene Photovoltaic Blends. *J. Am. Chem. Soc.* **135**, 18502–18512 (2013).
267. H. Tamura, I. Burghardt, Ultrafast Charge Separation in Organic Photovoltaics Enhanced by Charge Delocalization and Vibronically Hot Exciton Dissociation. *J. Am. Chem. Soc.* **135**, 16364–16367 (2013).
268. D. A. Vithanage *et al.*, Visualizing charge separation in bulk heterojunction organic solar cells. *Nat. Commun.* **4**, 2334 (2013).
269. H. M. Heitzer, B. M. Savoie, T. J. Marks, M. A. Ratner, Organic Photovoltaics: Elucidating the Ultra-Fast Exciton Dissociation Mechanism in Disordered Materials. *Angew. Chem. Int. Ed.* **53**, 7456–7460 (2014).
270. S. Gélinas *et al.*, Ultrafast Long-Range Charge Separation in Organic Semiconductor Photovoltaic Diodes. *Science*, 1239947 (2013).

271. J.-C. Denis *et al.*, Subpicosecond Exciton Dynamics in Polyfluorene Films from Experiment and Microscopic Theory. *J. Phys. Chem. C* **119**, 9734–9744 (2015).
272. A. Ruseckas *et al.*, Ultrafast depolarization of the fluorescence in a conjugated polymer. *Phys. Rev. B* **72**, 115214 (2005).
273. R. D. Pensack, K. M. Banyas, L. W. Barbour, M. Hegadorn, J. B. Asbury, Ultrafast vibrational spectroscopy of charge-carrier dynamics in organic photovoltaic materials. *Phys. Chem. Chem. Phys.* **11**, 2575–2591 (2009).
274. M. C. Heiber, A. Dhinojwala, Estimating the Magnitude of Exciton Delocalization in Regioregular P3HT. *J. Phys. Chem. C* **117**, 21627–21634 (2013).
275. T. Offermans, P. A. van Hal, S. C. J. Meskers, M. M. Koetse, R. A. J. Janssen, Exciplex dynamics in a blend of π -conjugated polymers with electron donating and accepting properties: MDMO-PPV and PCNEPV. *Phys. Rev. B* **72**, 045213 (2005).
276. D. T. Valley, D. P. Hoffman, R. A. Mathies, Reactive and unreactive pathways in a photochemical ring opening reaction from 2D femtosecond stimulated Raman. *Phys. Chem. Chem. Phys.* **17**, 9231–9240 (2015).
277. Printed solar cells poised for a breakthrough. *Cosm. Mag.* (2015), (available at <https://cosmosmagazine.com/technology/printed-solar-cells-poised-breakthrough>).
278. Y. Nakata, Organic EL for Saving Energy and Organic Solar Cells for Creating Energy Using the Printing Method. *J. Print. Sci. Technol.* **49**, 312–317 (2012).
279. H. S. Shin, J. K. Jeong, Y. G. Mo, D. U. Jin, Organic light emitting display (OLED) and its method of fabrication (2010), (available at <http://www.google.com/patents/US7663302>).
280. I. H. Lee, Organic electroluminescent device (2004), (available at <http://www.google.com/patents/US6803128>).
281. M. J. Carnie *et al.*, A one-step low temperature processing route for organolead halide perovskite solar cells. *Chem. Commun.* **49**, 7893–7895 (2013).
282. W. Li *et al.*, Post modification of perovskite sensitized solar cells by aluminum oxide for enhanced performance. *J. Mater. Chem. A* **1**, 11735–11740 (2013).
283. D. Bi, L. Yang, G. Boschloo, A. Hagfeldt, E. M. J. Johansson, Effect of Different Hole Transport Materials on Recombination in CH₃NH₃PbI₃ Perovskite-Sensitized Mesoscopic Solar Cells. *J. Phys. Chem. Lett.* **4**, 1532–1536 (2013).
284. J. M. Ball, M. M. Lee, A. Hey, H. J. Snaith, Low-temperature processed meso-superstructured to thin-film perovskite solar cells. *Energy Environ. Sci.* **6**, 1739–1743 (2013).
285. J. H. Heo *et al.*, Efficient inorganic-organic hybrid heterojunction solar cells containing perovskite compound and polymeric hole conductors. *Nat. Photonics* **7**, 486–491 (2013).
286. A. Abrusci *et al.*, High-Performance Perovskite-Polymer Hybrid Solar Cells via Electronic Coupling with Fullerene Monolayers. *Nano Lett.* **13**, 3124–3128 (2013).
287. J.-Y. Jeng *et al.*, CH₃NH₃PbI₃ Perovskite/Fullerene Planar-Heterojunction Hybrid Solar Cells. *Adv. Mater.* **25**, 3727–3732 (2013).
288. W. Nie *et al.*, High-efficiency solution-processed perovskite solar cells with millimeter-scale grains. *Science* **347**, 522–525 (2015).
289. H. D. Kim, H. Ohkita, H. Benten, S. Ito, Photovoltaic Performance of Perovskite Solar Cells with Different Grain Sizes. *Adv. Mater.* **28**, 917–922 (2016).
290. H. Oga, A. Saeki, Y. Ogomi, S. Hayase, S. Seki, Improved understanding of the electronic and energetic landscapes of perovskite solar cells: high local charge carrier mobility,

- reduced recombination, and extremely shallow traps. *J. Am. Chem. Soc.* **136**, 13818–13825 (2014).
291. J. S. Yun *et al.*, Benefit of grain boundaries in organic–inorganic halide planar perovskite solar cells. *J. Phys. Chem. Lett.* **6**, 875–880 (2015).
 292. J.-J. Li *et al.*, Microscopic Investigation of Grain Boundaries in Organolead Halide Perovskite Solar Cells. *ACS Appl. Mater. Interfaces.* **7**, 28518–28523 (2015).
 293. W. Tress *et al.*, Predicting the open-circuit voltage of CH₃NH₃PbI₃ perovskite solar cells using electroluminescence and photovoltaic quantum efficiency spectra: the role of radiative and non-radiative recombination. *Adv. Energy Mater.* **5**, 1400812 (2015).
 294. C. Ballif, H. R. Moutinho, M. M. Al-Jassim, Cross-sectional electrostatic force microscopy of thin-film solar cells. *J. Appl. Phys.* **89**, 1418–1424 (2001).
 295. I. Visoly-Fisher, S. R. Cohen, K. Gartsman, A. Ruzin, D. Cahen, Understanding the Beneficial Role of Grain Boundaries in Polycrystalline Solar Cells from Single-Grain-Boundary Scanning Probe Microscopy. *Adv. Funct. Mater.* **16**, 649–660 (2006).
 296. S. van der Walt *et al.*, scikit-image: image processing in Python. *PeerJ.* **2**, e453 (2014).
 297. J. P. Perdew, K. Burke, M. Ernzerhof, Generalized Gradient Approximation Made Simple. *Phys. Rev. Lett.* **77**, 3865–3868 (1996).
 298. P. E. Blöchl, Projector augmented-wave method. *Phys. Rev. B.* **50**, 17953–17979 (1994).
 299. G. Kresse, J. Furthmüller, Efficient iterative schemes for ab initio total-energy calculations using a plane-wave basis set. *Phys. Rev. B.* **54**, 11169–11186 (1996).
 300. Y. Kawamura, H. Mashiyama, K. Hasebe, Structural Study on Cubic-Tetragonal Transition of CH₃NH₃PbI₃. *J. Phys. Soc. Jpn.* **71**, 1694–1697 (2002).
 301. T. Baikie *et al.*, Synthesis and crystal chemistry of the hybrid perovskite (CH₃NH₃)PbI₃ for solid-state sensitised solar cell applications. *J. Mater. Chem. A.* **1**, 5628–5641 (2013).
 302. A. Mattoni, A. Filippetti, M. I. Saba, P. Delugas, Methylammonium Rotational Dynamics in Lead Halide Perovskite by Classical Molecular Dynamics: The Role of Temperature. *J. Phys. Chem. C.* **119**, 17421–17428 (2015).
 303. A. M. A. Leguy *et al.*, The dynamics of methylammonium ions in hybrid organic-inorganic perovskite solar cells. *Nat. Commun.* **6**, 7124 (2015).
 304. B. Chen *et al.*, Impact of Capacitive Effect and Ion Migration on the Hysteretic Behavior of Perovskite Solar Cells. *J. Phys. Chem. Lett.*, 4693–4700 (2015).
 305. A. Abass, D. V. Gestel, K. V. Wichelen, B. Maes, M. Burgelman, On the diffusion length and grain size homogeneity requirements for efficient thin-film polycrystalline silicon solar cells. *J. Phys. Appl. Phys.* **46**, 045105 (2013).
 306. Q. Chen *et al.*, Controllable self-induced passivation of hybrid lead iodide perovskites toward high performance solar cells. *Nano Lett.* **14**, 4158–4163 (2014).
 307. A. Guerrero, E. J. Juarez-Perez, J. Bisquert, I. Mora-Sero, G. Garcia-Belmonte, Electrical field profile and doping in planar lead halide perovskite solar cells. *Appl. Phys. Lett.* **105**, 133902 (2014).
 308. C. Eames *et al.*, Ionic transport in hybrid lead iodide perovskite solar cells. *Nat. Commun.* **6**, 7497 (2015).
 309. R. D. King-Smith, D. Vanderbilt, Theory of polarization of crystalline solids. *Phys. Rev. B.* **47**, 1651–1654 (1993).
 310. A. Stroppa, C. Quarti, F. De Angelis, S. Picozzi, Ferroelectric Polarization of CH₃NH₃PbI₃: A Detailed Study Based on Density Functional Theory and Symmetry Mode Analysis. *J. Phys. Chem. Lett.* **6**, 2223–2231 (2015).

311. J. Li, P. M. Haney, in *Photovoltaic Specialist Conference (PVSC), 2015 IEEE 42nd* (2015), pp. 1–4.
312. M. Coll *et al.*, Polarization Switching and Light-Enhanced Piezoelectricity in Lead Halide Perovskites. *J. Phys. Chem. Lett.* **6**, 1408–1413 (2015).